Spectroscopic Studies On Hybrid-Materials Of Medicinally Important Molecules For Enhanced Biological Activity

THESIS

SUBMITTED FOR THE DEGREE OF

DOCTOR OF PHILOSOPHY (SCIENCE)

IN CHEMISTRY

BY

DAMAYANTI BAGCHI

DEPARTMENT OF CHEMISTRY

UNIVERSITY OF CALCUTTA

2019

To My Family

Acknowledgements

This gives me enormous pleasure and satisfaction to pay my admiration to those who have helped, motivated and contributed to accomplish my dissertation work. I would like to thank all of them for their kind support.

First and foremost, I owe my deepest gratitude to my enthusiastic supervisor, Professor Samir Kumar Pal, for providing me the opportunity to work under his supervision. I am very grateful for his constant motivation, belief in my capabilities and his persistent availability to clarify my doubts despite his extremely busy schedule. His immense knowledge in multidisciplinary field of science and technology, commitment to the highest scientific standards, unconditional support during crisis that, taken together, make him an exemplary mentor. I feel to be fortunate enough to learn from his instrumental expertise and detail insight into various experimental problems. This work would not have been possible without his thoughtful guidance, warm encouragement, unconditional support, constructive criticism with simultaneous allocation to express my ideas to work independently and his inexhaustible help. His positive vibes, everlasting energy, disciplined nature, great leadership quality and enduring willingness for learning motivates me substantially and thank you very much Sir for inspiring me to believe in my dreams.

I am grateful to get the opportunity to actively work with talented researchers from various national and international institutes. I would like to thank Prof. Peter Lemmens of TU Braunschweig, Germany, Prof. Saleh A. Ahmed of Umm Al-Qura University, KSA, Dr. Debjani Karmakar of BARC, India, Dr. Indranil Banerjee, National Institute of Technology Rourkela, India, Prof. Partha Saha of SINP, India, Prof. Maitree Bhattacharyya, Department of Biochemistry, University of Calcutta, India and Dr. Chinmoy Bhattacharya of IIEST, India for fruitful collaborations.

I express my gratitude to all the faculty members and the office staffs of S. N. Bose National Centre for Basic Sciences for their assistances in my research career. A sincere appreciation to all other non-academic staffs and gardeners of SNBNCBS who have actively maintained the magnificent ambiance of the centre. I acknowledge Department of Science and Technology (DST), India for providing me INSPIRE fellowship as financial assistance.

I'd like to express my sincere gratitude to all my seniors and colleagues for providing an enriching work environment. I am especially thankful to Dr. Siddhi Chaudhuri and Dr. Samim Sardar for mentoring me at the initial stage of my research work. I am grateful to Dr. Shreyasi Dutta for helping me in the experiments related to biology. My sincere appreciation goes to all my seniors: Dr. Nabarun Polley, Dr. Susobhan Choudhury, Dr. Prasenjit Kar, Dr. Prasanna Kumar Mondal and earlier lab-member Mr. Ramesh Nandi. I acknowledge Dr. Tanushree Dutta for working with me on the topic of hybrid materials. My sincere admiration goes to all the present group members: Priya, Jayita, Aniruddha, Tuhin, Probir, Animesh da, Arko, Arpan, Susmita, Dipanjan, Nur, Dr. Gulmi Chakraborty, Dr. Tatini Rakshit, Dr. Soumendra Darbar, Soumendra da, Lopamudra, Deep Shikha, Amrita, Pritam, Ria, Sumana di, Anindita, Sayan, Oiendrila, Suman for providing a homely and a cheerful environment, and also for assisting me during research work. I am grateful to Abhijit da and Sudip da who have helped me during simulation and biological studies respectively. Special thanks to Priya & Jayita for their assistance in formatting and proof-reading of my thesis. A very special thanks to Priya with whom I shared many wonderful and glorious moments over the last five years. I also thank Anirudhha, Jayita and Tuhin with whom I shared many joyful moments in recent past. I pay tribute to all my teachers throughout my life. I also want to thank all my friends especially Subhodip, Dibbendu, Nabaruna and Ninni for their support and all the good times I shared with them.

Finally, I would like to pay high regards to my family and all of my relatives for their love, affection, praise, and good wishes. Without the enormous sacrifices of my mother, encouragement and support from my elder sister and brother-in-law, great motivation from my grandmother, fondness of my little niece and blessing from my father, this thesis would not have acquired its shape. I hereby acknowledge and thank all those who directly or indirectly supported me in this mesmerizing venture.

Dated:
Department of Chemical, Biological and Macromolecular Sciences,
S. N. Bose National Centre for Basic Sciences,
Salt Lake, Kolkata 700106, India *(Damayanti Bagchi)*

CONTENTS

Chapter 3: Instrumentation and Sample Preparation

Page

Chapter 1

Introduction

1.1. Background

Medicine is the science and practice of the diagnosis, prognosis, treatment, and prevention of disease. The Greek etymon of medicine is 'medome' which means 'to care for'. Although the practice of medicine is started long back at stone age, the modern medicinal era started from early 20th century with the discovery of antibiotics and biomedical devices. The huge technological advent of last two decades grant revolutionary breakthrough in the field of medical diagnosis offering ease of disease detection at early stage. However, conventional therapeutics appear to be incompetent to win the battle over several life-threatening diseases [1]. Another alarming issue of healthcare service is inception of drug resistance that is the reduction in effectiveness of a medication towards diseased site specially in case of bacterial infection and cancer. The development of drug resistance commences with any mutation in the target protein site of the cellular species. The lack of concerted effort by governments and the pharmaceutical industry, together with the intrinsic capacity of microbes to develop resistance at a rate that outpaces the development of new drugs, suggests that existing strategies for developing viable, long-term anti-microbial therapies are ultimately doomed to failure. The acquisition of drug resistance by pathogenic microorganisms emerge as one of the most significant public health threats that humanity is facing in the 21st century suggesting the urgency of alternative therapeutic strategies. Invention of smart functional materials possessing target specific action instigated through external stimuli such as light, pH, ions etc., could be considered as an effective substitute of conventional drugs and evaluation of such materials in terms of fabrication,

characterization and application, should be considered as an impactful new-age research topic.

1.2. Hybrid Materials: A Brief Overview

Hybrid materials are composites of two constituents at the molecular level [2]. The interactions at the microscopic level between the two constituents impart new characteristics in between the two original phases or can sometime provide altered properties in the hybrid. In case of hybrid materials, the primary interactions occur mainly at the microscopic or nanoscale region (10^{-9} m), and thus they often termed as nanohybrid materials or simply nanohybrids [3]. The molecular cross-talking at the interface between the two constituents often able to generate novel properties of the hybrid material and thus can improve their activities compared to their bulk counterpart [4]. The molecular level interaction can be classified into two section such as non-covalent (electrostatic, van der Waal etc.) interaction and covalent conjugation. The hybrids formed through non-covalent interaction is often termed as class-I hybrids and the covalently attached hybrids are classified in the class-II section. However, depending upon the nature and strength of interaction, the functionalities of the hybrids get altered. In most of the cases, hybrids impart new effectivity and thus often referred as new class of functional materials [5, 6].

The two parent counterparts of hybrid materials can be divided into various sections. In general, hybrids consist of one inorganic and another organic building block assembled at the nanoscale [7]. However, sometime one organic material interacts with another organic dye at the nanoscale, imparting alteration in the dye characteristics. Organic nanoparticles mainly focused on the generally coarse crystalline synthesis product into the finest particulate dispersion possible, with greater water stability which is essential for pharmaceutical activity [8]. These organic nanomaterials mainly consist of size between 50 to 500 nm [9]. The charge transport or energy transfer processes at the interfacial position present in organic

nano materials often improve its functionalities. The other important classification is the inorganic-organic nanohybrids which mainly interacts through covalent conjugation and surface attachment and thus can be included as class-II nanohybrids [10]. Hybrid organic-inorganic materials have been developed in the past 30 years or so, as intimate combinations of these dissimilar materials [11]. The quantum leap in behavior often possible with hybrids arises principally from two sources: the reduction of the domain size of the inorganic phase to 100 nm or below (often much less), and generation of enormous interfacial areas, which enable numerous covalent bonds or other compatibilization between the phases. In some hybrid materials, the individual component has not been detected as a distinct phase. The realm of quantum effects and tunable electronic, optical, and magnetic properties are readily accessible in hybrid materials which extend its applicability [7].

1.3. Hybrid Materials of Medicinally Important Molecules:

Medicines are most often organic compounds, which are divided into the broad classes of small organic molecules (e.g., furanocoumarins, penicillin, levulan, clopidogrel) and "biologics" (manufactured from any living sources and composed of sugars, proteins, or nucleic acids or complex combinations of these substances). Inorganic and organometallic compounds are also useful as drugs (e.g., lithium and platinum-based agents such as lithium carbonate and cisplatin as well as gallium) [12]. However, many drug molecules fail to attain its medicinal activity in clinics due to its molecular properties important for a drug's pharmacokinetics in the human body, including their absorption, distribution, metabolism and excretion ("ADME") [13]. Hence, there exists the possibility of fabrication of hybrid materials consisting of pharmaceutically relevant molecules as one of its primary components. Hybrid materials of medicinal molecules are more likely to satisfy Lipinski's rule of five (RO5) which evaluate drug-likeness of a compound with a certain pharmacological activity, due to their exceptional interfacial properties [14,

15]. The ability to combine a multitude of organic and inorganic components in a modular fashion allows for systematic tuning of various properties including tuneable size, high drug loading, tailorable surface properties, controllable or stimuli responsive drug release kinetics, improved bioavailability, pharmacokinetics, and biocompatibility of the resultant hybrid material [16]. In general, small organic drug molecules can be entrapped within organic nanoparticles (liposomes, dendrimers etc.) which led to formation of class-I hybrids that improve lipophilicity of drug with enhanced permeability and retention (EPR) effects [17]. On the other hand, using covalent conjugation strategy, medicines can form complexes or attached to the surface of an inorganic nano-dimensional system [18]. These class-II hybrids often lead to alteration of redox-modulatory properties with precise enhanced drug action.

1.4. Scope of the Spectroscopic Investigation on Hybrid Materials of Medicinally Important Molecules:

The biological activity of redox active drugs relies on two key parameters, namely redox potential/ability of electron transfer and their trans-cellular bioavailability or effective concentration of the drugs in biological cells. Both the parameters are expected to be influenced upon hybrid formation. Hybrid materials often offer modulated physico-chemical properties than the individual counterparts due to presence of interfacial junction [19]. Research on the transformed physicochemical properties of drug upon generation of hybrids has attracted attention of the scientific community as they have wide therapeutic applications to combat various life-threatening diseases.

In case of class I hybrids, multiple drug molecules bind to a single organic nanoparticle, that increases the bioavailability of the drug in the cells. Hence, appropriate localization of a drug and its structure/functional integrity in a delivery agent essentially dictates the efficacy of the vehicle and the medicinal

activity of the drug [20]. There lies the importance to study the interfacial dynamical properties. The class-II hybrids show even stronger conjugation and thus the inorganic-organic interfacial features dictate the overall activity of the composites. Besides, the proximity of the drug to the inorganic counterparts of diverse electronic bands would change the electron transfer properties (redox activity) of the drug [21]. There is an efficient transfer of photoexcited electrons from the LUMO of the dye to the vacant molecular orbital of inorganic systems which not only confirm the formation of hybrids but also depicts the nature of hybridization [22]. In case of photosensitive drugs, photoinduced charge transfer process from dye to nano-dimensional system results in generation of augmented reactive oxygen species (ROS). This leads to an increase in overall drug activity with diseased site-specific accomplishment. Hence, these hybrid formulations are superior to conventional medicine with respect to control release, targeted delivery and therapeutic effect. In this respect, the mechanism of altered drug action hybrid material formation is within the purview of our studies.

The molecular cross-talking at the interfacial area of the hybrids need to be evaluated in detail to further improve applicability and functionalities of hybrids. The available microscopic techniques namely electron microscopy such as scanning electron microscopy (SEM) [23], transmission electron microscopy (TEM) [24], scanning tunnelling microscopy (STM) [25] could provide the information on the inorganic parts of the hybrid. High resolution microscopic images can even provide the lattice fringes and also the crystal inter-planar distance. These techniques are of superior importance to understand crystal details of inorganic counterparts. X ray diffraction (XRD) could provide the crystal plane diffraction pattern of the inorganic portion. Atomic force microscopy (AFM) is often used for determining the surface topology of the hybrid materials. On the other hand, Fourier-transform infrared spectroscopy (FTIR) or nuclear paramagnetic resonance spectroscopy (NMR) can analyse the perturbation in the organic part. The change in signals of the hybrids

compare to the drug molecules help to predict the nature of covalent conjugation which is useful to understand the specific bonding characteristics in the hybrids. However, all the above-mentioned methods are able to only observe the nano-bio interface in an indirect manner, either information of inorganic crystals can be obtained, or the nature of organic bonds can be determined. There exists severe importance of direct observation of interfacial dynamical processes in hybrids which could be sufficient enough to completely understand the junctional properties. The quantum mechanical phenomenon present at the interfaces of the hybrids also manifest the necessity to study the interfacial processes using experimental tools and to fully understand the interfacial dynamics at the nano-junction. Electronic spectroscopy including steady-state and excited state spectroscopy could be considered as one of the best available tools to study the interfacial properties. Ultrafast laser spectroscopy is a spectroscopic technique that uses ultrashort pulsed lasers for the study of dynamics on extremely short time scales (attoseconds to nanoseconds) [26]. Different methods are used to examine dynamics of charge carriers, atoms and molecules. Time-correlated single photon counting (TCSPC) is used to analyse the relaxation of molecules from an excited state to a lower energy state. Since various molecules in a sample will emit photons at different times following their simultaneous excitation, the decay must be thought of as having a certain rate rather than occurring at a specific time after excitation. By observing how long individual molecules take to emit their photons, and then combining all these data points, an intensity vs. time graph can be generated that displays the exponential decay curve typical to these processes. The interface between the inorganic and organic parts can be visualized using various ultrafast techniques.

The key focus of this thesis is to investigate the photoinduced dynamical processes across the heterogeneous interface present in hybrid materials which is important from both fundamental and application perspectives. In one of our

studies, we have investigated the role of metal chelation in perspective of bioavailability issue of polyphenolic drug curcumin [27, 28]. The study reveals zinc, copper and other redox active ions possess electron transfer processes in the metallo-curcumin complexes that alters its solubility and medicinal activity. In another study, we have functionalized bimetallic nanoscale metal-organic framework (MOF) with curcumin using a facile wet chemistry route and duly prepared nanohybrids produce photoinduced charge separation depict greater stability as well as better drug activity [29, 30]. Ultrafast photoinduced charge separation and charge recombination processes at the semiconductor-metal-curcumin (ZnO-M-cur) interface are explored for efficient heavy metal sensing. The incorporation of photochromic ligand (DHI) into digestive enzyme can produce light sensitive enzyme through non-covalent interactions. In a recent study, we have explored efficient localization of a photo-therapeutic drug into a drug-delivery agent (ethosome) using the steady state and picosecond-resolved fluorescence studies. In order to facilitate alternative therapeutic strategies, we have explored photodynamic therapy (PDT) that employ a photosensitizer molecule which can be excited upon irradiation with specific light source and in presence of molecular oxygen, it will produce reactive species (ROS) that help to destroy diseased cell [31-34]. Hybrids of photosensitizer drug squaraine (SQ) that can be excited using red light illumination have been fabricated using semiconductor ZnO nanoparticle and zeolitic imidazolate framework (ZIF). The synergistic combination of pH responsive delivery using ZnO nanoparticles, photoinduced charge separation at semiconductor-drug (ZnO-SQ) interface and lesser drug aggregation are demonstrated to be responsible for unprecedented antibacterial and anticancer photo-responsive effects. In recent times, MOFs are employed for several bio-medicinal activities as therapeutic agent or imaging tools. The present research includes the exploration of the photoinduced ultrafast dynamics in a well-known photosensitizer, SQ entrapped within ZIF NPs (ZIF-SQ). We have successfully showed that the nanohybrid exhibits enhanced PDT activity compared to that of

only drug. The hybrids are shown to highly effective towards destruction of drug resistance bacterial infection and their biofilm.

The experimental tools used for studying the dynamical processes involve picosecond-resolved carrier relaxation dynamics, such as, photoinduced electron transfer (PET) [35] and Förster resonance energy transfer (FRET) [36, 37]. The different experimental techniques employed for the structural and functional characterization of the hybrid materials include steady-state UV-VIS absorption and fluorescence, thermogravimetric analysis (TGA), Fourier transform infrared spectroscopy (FTIR), Raman scattering, dynamic light scattering (DLS), powder X-ray diffraction (XRD), cyclic voltammetry (CV), field emission scanning electron microscopy (FESEM) and high-resolution transmission electron microscopy (HRTEM). Bacterial culture technique and human cell culture is used to study the photodynamic activity. Cytotoxicity assay is used to study effect of hybrids in cultured cell.

1.5. Objective:

The use of hybrid materials for its beneficial biological applications has attracted immense attention in the recent time in order to address the healthcare challenges worldwide. Among them, metal-drug complexes, organic nanoparticles encapsulating drug molecules and semiconductor inorganic nanoparticles attached to drugs need to be evaluated in detail to understand the interfacial properties that are responsible for betterment in medicinal activity which could give rise to design of heterostructures with efficient charge separation useful for various diseased condition. The objective of this thesis is to fabricate various types of hybrid materials, unravel the ultrafast dynamical processes across the interface of heterostructures to enhance the medicinal efficiency. The special emphasis has been given to the correlation between the ultrafast processes at the interface and their implications in terms of improved biological applications.

Depending upon the nature and strength of interaction, the functionalities of the hybrids get altered. Thus, there is necessity to study the interfacial processes using experimental tools and to fully understand the interfacial dynamics at the nano-junction. The hybrid materials with improved properties often depict superior functionalities. The current generation of hybrids formed using commercially available drug molecule with some inorganic counterparts often enhance bioavailability and activity of the drug with an enhanced permeability and retention (EPR) effect at the target site [38]. Besides, the fabricated hybrid materials can incorporate 'sense and act' like stimuli responsive drug action and thus lowers the side effects of treatment [39-41]. The precise knowledge of interfacial charge transfer properties is important to fully understand the mechanism of drug action and their alteration upon hybrid formation is within the scope of our studies.

In order to diminish the side-effects and cost of treatment, herbal medicines as curcumin, the active ingredient of turmeric, are in focus over synthesized drug in recent times [42]. Despite, its multiple action in *in-vitro* condition, it elicits poor activity in pre-clinical and clinical trials due to low bioavailability at the target site even when administered at a very high dose [43, 44]. To overcome the problem, several methods have been proposed including conjugation to water-soluble polymers [45, 46] or encapsulation in colloidal carriers such as gold nanoparticles, silver nanoparticles and polymer nanoparticles [47, 48]. The present research includes studies on metallo-curcumin complexes with Cu(II) and Zn(II) metal ions through class-II type interaction. The excited state interaction between the metal and ligands are thoroughly characterized using ultrafast spectroscopic tools and metal complexes are evaluated for improved aqueous stability and biological activity (antioxidant, antibacterial). Further, we have synthesized one single nanoscale metal-organic framework (MOF) to load curcumin and the hybrid material show greater bioavailability as well as better activity. However, metalation property of curcumin can diminish its multiple health benefits as it can effectively

chelates toxic heavy metal ions. Next, we have constructed one nanoprobe based system to determine heavy metal toxicity in curcumin. We have also explored the ultrafast photoinduced charge separation and charge recombination processes at the nanoprobe-metallo-curcumin interface which managed the specificity of the nanoprobe towards heavy metals only.

In order to impart stimuli responsive nature in biologically relevant systems, formation of hybrid materials can be one of the easiest approaches [49]. Among the varied range of extrinsic stimuli as heat, ion sensitivity, pH etc., electromagnetic radiation is the most advantageous stimulus because it can precisely provide high spatio-temporal selectivity with strong dosage control. In this direction, we have studied the photo-control (UV light control) of the enzymatic activity of the serine protease α-chymotrypsin (CHT) through a new class of photochromic material, dihydroindolizine (DHI). The various molecular level interactions, mainly electrostatic in nature, are thoroughly investigated to unravel photo-responsive activity of a light insensitive enzyme. In another study, we have explored the photoinduced dynamical events of a model phototherapeutic drug psoralen (PSO) in a potential delivery vehicle called an ethosome.

Besides, light-mediated treatment methodologies as photodynamic therapy (PDT) involves photosensitizer molecules, which could be activated by specific photon energy followed by production of reactive oxygen species (ROS) for therapeutic use. Therapeutic efficacy of photoactive drugs using near-infrared light (NIR) can provide new avenues by using biological window of optical transparency. This often suggests implication of a NIR-absorbing dye molecule or nanomaterials as a photosensitizer in PDT, which in turn improves the penetration potency of the light used. In this direction, we have employed red-light-absorbing dye squaraine (SQ) as the photosensitizer molecule and prepare its hybrids using various nanostructures as semiconductor zinc oxide (ZnO) or zeolitic imidazolate framework (ZIF MOF). The hybrids show pH responsive drug delivery and red-

light induced ROS generation capabilities which further manifested in destruction of bacterial infection as well as to inhibit cancer progression. The results obtained by all these studies of hybrid materials from synthesis to spectroscopic characterization to prevailing health benefits, could be incorporated in designing new-age hybrids for benefit of human health.

1.6. Summary of the Work Done:

1.6.1. Spectroscopic Studies on the Complexation of Various Metal Ions with a Medicinally Important Drug for Enhanced Biological Activity:

1.6.1.1. Modulation of Stability and Functionality of a Phyto-antioxidant by Weakly Interacting Metal Ions: Curcumin in Aqueous Solution [50]: The natural polyphenol curcumin and its metal coordinated complexes show obvious benefits in the medical therapies of cancer and several neurodegenerative diseases. On the other side, their stability and bioavailability are critical issues. This particular study is an attempt to address the stability and functionality of curcumin upon complexation with transition metal ions. We have synthesized and optically characterized metallo–curcumin complexes with Cu(II) and Zn(II). From femtosecond resolved upconversion studies, an interaction at the molecular level is revealed based on an observed photoinduced electron transfer from curcumin to the metal ions. In order to investigate the antioxidant activity of the complexes, we have performed 2,2-diphenyl-1-picrylhydrazyl (DPPH) assay in dark. The Cu(II)–curcumin complex exhibits an enhanced and recyclable activity, more pronounced compared to that of the Zn(II)–curcumin complex, which can be attributed to the weaker O–H bond present in the former case. In contrast, the Zn(II) complex has a higher solubility and stability in aqueous media than the Cu(II) complex. To address stability vs. functionality issues, we have suggested a facile method that enhances the solubility and stability of curcumin in aqueous media by metalation with Zn(II)

and a successional replacement of Zn(II) in the complex by Cu(II) through a simple route to enhance the activity prior to its use. We have also used the complex in a model anti-bacteriological assay experiment where it shows significantly higher activity compared to pure curcumin. The dichlorofluorescin (DCFH) oxidation indicates an enhancement in ROS generation, which in turn is responsible for the enhanced antioxidative property of the Cu(II)–curcumin complex. Our results provide a promising method to use metallo–curcumin complexes in diverse biological applications.

1.6.1.2. Bimetallic Zeolitic Imidazolate Framework as an Active Excipient of Curcumin under Physiological Condition [51]: Metal-organic frameworks (MOFs) hold great promises in biotechnological application. MOFs have been shown as efficient carriers of therapeutic drugs. Yet MOFs have not been used for simultaneous drug delivery and efficacy enhancement. In this study, a mixed metal MOF copper (Cu^{2+})-doped zeolitic imidazolate framework-8 (Cu/ZIF-8) was applied for the first time for simultaneous increment of drug stability (through metalation with zinc (Zn^{2+})) and functionality (via complexation with Cu^{2+}). Copper was introduced in the tetrahedral sites of ZIF-8 in reactions conducted with 25% and 10% Cu^{2+} by weight of Zn^{2+} and the reaction time, temperature and metal to ligand ratios were optimized to ensure minimum distortions of ZIF-8 crystallinity. Further experiments were conducted with ZIF-8 prepared by 25% of Cu^{2+}. The as synthesized (Cu Zn (2-methyl imidazolate)$_2$) crystals were loaded with curcumin following a facile route at room temperature. Spectroscopic study of Cur@Cu/ZIF-8 revealed the nature of interaction to be metal chelation with or without adsorption while picosecond-resolved spectroscopic measurement depicted greater charge separation in Cur@Cu/ZIF-8 than Cu/ZIF-8. Cu/ZIF-8 exhibits reasonably high drug loading capacity (22%) with exceptionally high efficiency (83%). Attachment with Cu/ZIF-8 increased the aqueous stability of curcumin by several orders of magnitude. Reactive oxygen species (ROS) generation was amplified due to

combined interactions of Zn^{2+} and Cu^{2+} representing d^{10} and d^{9} electronic configurations respectively and enhanced bond breaking tendency of peripheral −O−H bond of curcumin molecule. Note worthily, Cur@Cu/ZIF-8 also exhibits greater anti-bacterial and anti-biofilm effects than free curcumin, a combination that is best suited for biomedical application.

1.6.2. Experimental and Computational Studies on the Formation of Nanohybrid of a Medicinally Important Drug with Inorganic Nanostructure:

1.6.2.1. Sensitized ZnO Nanorod Assemblies to Detect Heavy Metal Contaminated Phytomedicines: Spectroscopic and Simulation Studies [52]: The immense pharmacological relevance of the herbal medicine curcumin including anti-cancer and anti-Alzheimer effects, suggests it to be a superior alternative to synthesised drugs. The diverse functionalities with minimal side effects intensify the use of curcumin not only as a dietary supplement but also as a therapeutic agent. Besides all this effectiveness, some recent literature reported the presence of deleterious heavy metal contaminants from various sources in curcumin leading to potential health hazards. In this regard, we attempt to fabricate ZnO based nanoprobes to detect metal conjugated curcumin. We have synthesized and structurally characterized the ZnO nanorods (NR). Three samples namely curcumin (pure), Zn–curcumin (non-toxic metal attached to curcumin) and Hg–curcumin (toxic heavy metal attached to curcumin) were prepared for consideration. The samples were electrochemically deposited onto ZnO surfaces and the attachment was confirmed by cyclic voltammetry experiments. Moreover, to confirm a molecular level interaction picosecond-resolved PL-quenching of ZnO NR due to Förster Resonance Energy Transfer (FRET) from donor ZnO NR to the acceptor curcumin moieties was employed. The attachment proximity of ZnO NR and curcumin moieties depends on the size of metals. First principles analysis suggests

a variance of attachment sites and heavy metal Hg conjugated curcumin binds through a peripheral hydroxy group to NR. We fabricated a facile photovoltaic device consisting of ZnO NR as the working electrode with Pt counter electrode and iodide-triiodide as the electrolyte. The trend in photocurrent under visible light illumination suggests an enhancement in the case of heavy metal ions due to long range interaction and greater accumulation of charge at the active electrode. Our results provide a detailed physical insight into interfacial processes that are crucial for detecting heavy-metal attached phytomedicines and are thus expected to find vast application as sensors for the detection of selective metal contaminants.

1.6.3. Spectroscopic Studies on the Photosensitization of an Enzyme through Specific Molecular Recognition:

1.6.3.1. Allosteric Inhibitory Molecular Recognition of a Photochromic Dye by a Digestive Enzyme: Dihydroindolizine Makes Alpha-chymotrypsin Photo-responsive [53]: The structural-functional regulation of enzymes by the administration of an external stimulus such as light could create photo-switches that exhibit unique biotechnological applications. However, molecular recognition of small ligands is a central phenomenon involved in all biological processes. We demonstrate herein that the molecular recognition of a photochromic ligand, dihydroindolizine (DHI), by serine protease α-chymotrypsin (CHT) leads to the photo-control of enzymatic activity. We synthesized and optically characterized the photochromic DHI. Light-induced reversible pyrroline ring opening and a consequent thermal back reaction via 1,5-electrocyclization are responsible for the photochromic behavior. Furthermore, DHI inhibits the enzymatic activity of CHT in a photo-controlled manner. Simultaneous binding of the well-known inhibitors 4-nitrophenyl anthranilate (NPA) or proflavin (PF) in the presence of DHI displays spectral overlap between the emission of CHT-NPA or CHT-PF with the respective absorption of cis or trans DHI. The results suggest an opportunity to explore the binding site of DHI using Förster resonance energy transfer (FRET). Moreover, to

more specifically evaluate the DHI binding interactions, we employed molecular docking calculations, which suggested binding near the hydrophobic site of Cys-1-Cys-122 residues. Variations in the electrostatic interactions of the two conformers of DHI adopt unfavorable conformations, leading to the allosteric inhibition of enzymatic activity.

1.6.4. Spectroscopic Studies on Photosensitization of a Drug Delivery Vehicle for Enhanced Biological Functionality:

1.6.4.1. Essential Dynamics of an Effective Phototherapeutic Drug in a Nanoscopic Delivery Vehicle: Psoralen in Ethosome for Biofilm Treatment [54]: Appropriate localization of a drug and its structure/functional integrity in a delivery agent essentially dictates the efficacy of the vehicle and the medicinal activity of the drug. In the case of a phototherapeutic drug, its photoinduced dynamics becomes an added parameter. Here, we have explored the photoinduced dynamical events of a model phototherapeutic drug psoralen (PSO) in a potential delivery vehicle called an ethosome. Dynamic light scattering confirms the structural integrity of the ethosome vehicle after the encapsulation of PSO. Steady state and picosecond resolved spectroscopy and Förster resonance energy transfer, reveal the localization of the drug in the vehicle and the environment in the proximity of PSO. We have also investigated the efficacy of drug delivery to various individual bacteria (Gram-negative: *Escherichia coli*; Gram-positive: *Staphylococcus aureus*) and bacterial biofilms. Our optical and electron microscopic studies reveal a significant reduction in bacterial survival (~70%) and the destruction of bacterial adherence following a change in the morphology of the biofilms after phototherapy. Our studies are expected to find relevance in the formulation of drug delivery agents in several skin diseases and biofilm formation in artificial implants.

1.6.5. Spectroscopic Studies on a Hybrid Material of Red-light Active Dye with an Inorganic Oxide Material for Potential Photo-medicinal Application:

1.6.5.1. NIR Light Active ZnO Based Nanohybrids for Bacterial Biofilm Treatment [55]: Nanomaterials with antimicrobial properties triggered by external stimuli appear to be a promising and innovative substitute for the destruction of antibiotic-resistant superbugs as they can induce multiple disruptions in the cellular mechanism. This study demonstrates the use of squaraine (SQ) dye as the photosensitive material, activated in the near-infrared tissue-transparent therapeutic window. The dye has been covalently attached to the ZnO nanoparticle surface, forming ZnO-SQ nanohybrids. The formation of the nanohybrids is confirmed using Fourier transform infrared and other optical spectroscopic methods. The photoinduced interfacial electron transfer process (as confirmed using the time-resolved fluorescence technique) from the excited state of SQ to the conduction band of ZnO is responsible for the greater reactive oxygen species (ROS) generation ability of the nanohybrid. The production of photoactivated ROS (especially singlet oxygen species) by ZnO-SQ provides remarkable antimicrobial action against clinically significant *Staphylococcus aureus*. Detailed investigations suggest synergistic involvement of cell membrane disruption and nanoparticle internalization followed by photoinduced intracellular ROS generation, which result in an unprecedented 95% bacterial killing activity by the nanohybrid. Moreover, the efficacy of the nanohybrid for disruption of bacterial biofilms has been examined. The electron microscopic images suggest significant bacterial cell death following structural alteration and reduced adherence property of the biofilms. Nano-dimension-driven greater internalization of ZnO-SQ followed by an improved dissolution of ZnO in an acidic environment of the biofilm as well as red-light-driven interfacial charge separation and ROS generation improves the efficacy of the material for biofilm destruction. An artificial medical implant mimicking

titanium sheets coated with ZnO-SQ depicts light-triggered disruption in the adherence property of matured biofilms. The cytotoxicity and hemolysis assays show inherent biocompatibility of the photoactive nanohybrid. This study is notably promising for the treatment of life-threatening drug-resistant infections and eradication of biofilms formed within artificial implants.

1.6.5.2. Exploration of Interfacial Dynamics in Squaraine Based Nanohybrids for Potential Photodynamic Action [56]: Photodynamic therapy (PDT) is a clinically approved, minimally invasive therapeutic procedure exhibiting cytotoxic effects toward malignant cells. Hydrophobic nature of most photosensitizers used in PDT with lower light absorption ability restricts practical use of PDT. Herein, we have employed a squaraine drug (SQ) with 665 nm absorbance peak maxima as the photosensitizing agent and evaluate its photo-physical properties. The tendency of aggregation formation in aqueous media limits its practical usefulness. Thus, we have synthesised wide band gap semiconductor zinc oxide (ZnO) nanoparticles and functionalized the surface using squaraine molecules. The molecular cross-talking was evaluated using excited state fluorescence lifetime decay profiles and by employing Förster resonance energy transfer (FRET) technique. The nanohybrids show improvement in three aspects compared to bare SQ molecule such as lesser aggregate formation in aqueous media, pH responsive precipitation of the drug and improvement of photo-induced reactive oxygen species (ROS) generation. Ultrafast dynamical study at the inorganic (ZnO) - organic (SQ) interface depicts presence of photo-induced charge transfer process at the junction which indeed improves the ROS generation capability. Finally, the photodynamic action has been evaluated in human breast cancer cell line MCF-7. The nanohybrids depict enhanced photo toxicity in cancer cell with loss of adherence and typical morphology of cancerous cell depicting controlled cell death. The present study employ characterization of nanohybrids for potential use in PDT for cancer treatment.

1.6.6. Spectroscopic Studies on a Porous Metal-organic Framework for Enhanced Drug Loading and Near Infra-red Sensitized Drug Activity:

1.6.6.1. Nano MOF Entrapping Hydrophobic Photosensitizer for Dual-stimuli Responsive Unprecedented Therapeutic Action against Drug-resistant Bacteria [57]: Multi-drug resistance (MDR) of bacteria is a major threat to public health globally and its unprecedented increase calls for immediate alternative medical strategies. Antimicrobial photodynamic therapy (aPDT) offers alternative modalities to combat the growing MDR typically by means of targeted cellular internalization of a photosensitizer (PS) capable of producing photo-induced reactive oxygen species (ROS). However, aPDT is severely limited by the self-aggregation behaviour and hydrophobicity of PS molecules which significantly curbs its viability for clinical application. The present study reports the use of modified nanoscale metal-organic frameworks (NMOFs) encapsulating a hydrophobic PS drug squaraine (SQ) to enhance aPDT efficacy against drug resistant planktonic bacteria and its biofilm for the first time. Zeolitic imidazolate framework (ZIF-8) NMOF nanocrystals are attached post-synthetically with SQ (designated as ZIF8-SQ) and the resultant drug-doped NMOF is characterized by TEM, FESEM, PXRD, Raman spectroscopy, UV-Vis spectroscopy as well as steady-state and time-resolved fluorescence techniques. The microporous structure of ZIF-8 behave as molecular cages ceasing the self-aggregation of hydrophobic SQ. In addition, the formulated ZIF8-SQ produces cytotoxic ROS under red light irradiation (650 nm) in a pH sensitive way primarily due to molecular level interaction and charge separation between ZIF-8 and SQ depicting dual stimuli responsive nature. Most notably, ZIF8-SQ provides an unparallel aPDT action against methicillin resistant *Staphylococcus aureus* (MRSA) and leads to complete loss of adherence of structurally robust bacterial biofilms. Finally, the non-toxic nature of the nanoconjugate towards human cells holds great promise for effective

treatment of MRSA and other detrimental antibiotic-resistance microbes in clinical models.

1.7. Plan of Thesis:

The plan of the thesis is as follows:

Chapter 1: This chapter gives a brief introduction to the scope and motivation behind the thesis work. A brief summary of the work done is also included in this chapter.

Chapter 2: This chapter provides a brief overview of the steady-state and dynamical tools, the structural aspects of dyes and fluorescent probes used in the experiments.

Chapter 3: Details of instrumentation, data analysis and experimental procedures have been discussed in this chapter.

Chapter 4: In this chapter, the bioavailability and activity issue of herbal medicine have been investigated. The role of metallation in curcumin is explored in view of enhancement of its solubility and stability in aqueous media. Finally, bimetallic metal organic framework has been fabricated and curcumin is attached to it which provide better stability as well as activity.

Chapter 5: Dynamical processes in ZnO-metal-curcumin assemblies are evaluated upon photoexcitation and their implications in sensing heavy metal contamination is elaborated in this chapter.

Chapter 6: Molecular recognition of a synthesized photochromic dye with a digestive enzyme is explored using various spectroscopic tools and the induced photo-responsive enzymatic activity is discussed in the chapter.

Chapter 7: In order to enhance drug efficiency, organic drug delivery agent has been employed which provide better activity in terms of killing bacterial infection. UV mediated improved drug action within delivery agent have been described in this chapter.

Chapter 8: In this chapter, the use of different sized ZnO NPs to sensitize red light absorbing photosensitizer has been presented. The hybrid material is shown to produce photoinduced charge transfer with improved biological activities. The altered photo-induced activity is tested to destruct bacterial infection and cancer cell.

Chapter 9: The use of nanoscale zeolitic imidazolate framework ZIF NPs as drug delivery vehicle of a well-known red light activatable drug molecule and its ability to kill drug-resistant bacteria has been described in this chapter.

References

[1] C.J. Murray, A.D. Lopez, Measuring the global burden of disease, *N. Engl. J. Med.,* 369 (2013) 448-457.

[2] C. Kagan, D. Mitzi, C. Dimitrakopoulos, Organic-inorganic hybrid materials as semiconducting channels in thin-film field-effect transistors, *Science,* 286 (1999) 945-947.

[3] G.Z. Chen, Understanding supercapacitors based on nano-hybrid materials with interfacial conjugation, *Pro. Nat. Sci-Mater,* 23 (2013) 245-255.

[4] P. Gómez-Romero, C. Sanchez, Functional hybrid materials, John Wiley & Sons, 2006.

[5] A.E. Nel, L. Mädler, D. Velegol, T. Xia, E.M. Hoek, P. Somasundaran, F. Klaessig, V. Castranova, M. Thompson, Understanding biophysicochemical interactions at the nano–bio interface, *Nat. Mater.,* 8 (2009) 543-557.

[6] J.E. Gagner, S. Shrivastava, X. Qian, J.S. Dordick, R.W. Siegel, Engineering nanomaterials for biomedical applications requires understanding the nano-bio interface: a perspective, *J. Phys. Chem. Lett.,* 3 (2012) 3149-3158.

[7] P.J. Hagrman, D. Hagrman, J. Zubieta, Organic–inorganic hybrid materials: from "simple" coordination polymers to organodiamine-templated molybdenum oxides, *Angew. Chem.,* 38 (1999) 2638-2684.

[8] D. Horn, J. Rieger, Organic nanoparticles in the aqueous phase—theory, experiment, and use, *Angew. Chem.,* 40 (2001) 4330-4361.

[9] S. Kango, S. Kalia, A. Celli, J. Njuguna, Y. Habibi, R. Kumar, Surface modification of inorganic nanoparticles for development of organic–inorganic nanocomposites—a review, *Prog. Polym. Sci.,* 38 (2013) 1232-1261.

[10] H. Ishii, K. Sugiyama, E. Ito, K. Seki, Energy level alignment and interfacial electronic structures at organic/metal and organic/organic interfaces, *Adv. Mater.,* 11 (1999) 605-625.

[11] K.G. Sharp, Inorganic/organic hybrid materials, *Adv. Mater.,* 10 (1998) 1243-1248.

[12] D.S. Alberts, P. Liu, E.V. Hannigan, R. O'toole, S.D. Williams, J.A. Young, E.W. Franklin, D.L. Clarke-Pearson, V.K. Malviya, B. DuBeshter, Intraperitoneal cisplatin plus intravenous cyclophosphamide versus intravenous cisplatin plus intravenous cyclophosphamide for stage III ovarian cancer, *N. Engl. J. Med.,* 335 (1996) 1950-1955.

[13] A. Urtti, Challenges and obstacles of ocular pharmacokinetics and drug delivery, *Adv. Drug Deliv. Rev.,* 58 (2006) 1131-1135.

[14] C.A. Lipinski, Lead-and drug-like compounds: the rule-of-five revolution, *Drug Discov. Today,* 1 (2004) 337-341.

[15] M.-Q. Zhang, B. Wilkinson, Drug discovery beyond the 'rule-of-five', *Curr Opin Biotechnol,* 18 (2007) 478-488.

[16] E. Ruiz-Hitzky, K. Ariga, Y.M. Lvov, Bio-inorganic hybrid nanomaterials: strategies, synthesis, characterization and applications, John Wiley & Sons, 2008.

[17] S. Mitragotri, P. Stayton, Organic nanoparticles for drug delivery and imaging, *MRS Bull.,* 39 (2014) 219-223.

[18] T.Y. Ohulchanskyy, I. Roy, L.N. Goswami, Y. Chen, E.J. Bergey, R.K. Pandey, A.R. Oseroff, P.N. Prasad, Organically modified silica nanoparticles with covalently incorporated photosensitizer for photodynamic therapy of cancer, *Nano. Lett,* 7 (2007) 2835-2842.

[19] J.B. Hall, M.A. Dobrovolskaia, A.K. Patri, S.E. McNeil, Characterization of nanoparticles for therapeutics, *Nanomedicine,* 2 (2007) 789-803.

[20] T.S. Hauck, S. Giri, Y. Gao, W.C. Chan, Nanotechnology diagnostics for infectious diseases prevalent in developing countries, *Adv. Drug Deliv. Rev.,* 62 (2010) 438-448.

[21] J.S. Walsh, G.T. Miwa, Bioactivation of drugs: risk and drug design, *Annu. Rev. Pharmacol. Toxicol.,* 51 (2011) 145-167.

[22] M.E. Davis, Z. Chen, D.M. Shin, Nanoparticle therapeutics: an emerging treatment modality for cancer, in, World Scientific, 2010, pp. 239-250.

[23] J.-K.F. Suh, H.W. Matthew, Application of chitosan-based polysaccharide biomaterials in cartilage tissue engineering: a review, *Biomaterials,* 21 (2000) 2589-2598.

[24] T.K. Maji, D. Bagchi, P. Kar, D. Karmakar, S.K. Pal, Enhanced charge separation through modulation of defect-state in wide band-gap semiconductor for potential photocatalysis application: Ultrafast spectroscopy and computational studies, *J. Photochem. Photobiol. A,* 332 (2017) 391-398.

[25] M.-C. Shih, S.-S. Li, C.-H. Hsieh, Y.-C. Wang, H.-D. Yang, Y.-P. Chiu, C.-S. Chang, C.-W. Chen, Spatially resolved imaging on photocarrier generations and band alignments at perovskite/PbI2 heterointerfaces of perovskite solar cells by light-modulated scanning tunneling microscopy, *Nano. Lett,* 17 (2017) 1154-1160.

[26] S.K. Pal, A.H. Zewail, Dynamics of water in biological recognition, *Chem. Rev.,* 104 (2004) 2099-2124.

[27] T. Ak, İ. Gülçin, Antioxidant and radical scavenging properties of curcumin, *Chem. Biol. Interact.,* 174 (2008) 27-37.

[28] K. Priyadarsini, The chemistry of curcumin: from extraction to therapeutic agent, *Molecules,* 19 (2014) 20091-20112.

[29] A. Tiwari, A. Singh, N. Garg, J.K. Randhawa, Curcumin encapsulated zeolitic imidazolate frameworks as stimuli responsive drug delivery system and their interaction with biomimetic environment, *Sci. Rep.,* 7 (2017) 12598.

[30] M. Zheng, S. Liu, X. Guan, Z. Xie, One-step synthesis of nanoscale zeolitic imidazolate frameworks with high curcumin loading for treatment of cervical cancer, *ACS Appl. Mater. Interfaces,* 7 (2015) 22181-22187.

[31] T.J. Dougherty, C.J. Gomer, B.W. Henderson, G. Jori, D. Kessel, M. Korbelik, J. Moan, Q. Peng, Photodynamic therapy, *J. Natl. Cancer. Inst* 90 (1998) 889-905.

[32] D.E. Dolmans, D. Fukumura, R.K. Jain, Photodynamic therapy for cancer, *Nat. Rev. Cancer,* 3 (2003) 380-387.

[33] B.W. Henderson, T.J. Dougherty, How does photodynamic therapy work?, *Photochem. Photobiol.,* 55 (1992) 145-157.

[34] I.J. Macdonald, T.J. Dougherty, Basic principles of photodynamic therapy, *J. Porphyr. Phthalocyanines,* 5 (2001) 105-129.

[35] G.J. Kavarnos, Fundamentals of photoinduced electron transfer, VCH New York, 1993.

[36] J.R. Lakowicz, Topics in fluorescence spectroscopy: principles, Springer Science & Business Media, 1992.

[37] A. Periasamy, Fluorescence resonance energy transfer microscopy: a mini review, *J. Biomed. Opt.,* 6 (2001) 287-292.

[38] H. Kobayashi, R. Watanabe, P.L. Choyke, Improving conventional enhanced permeability and retention (EPR) effects; what is the appropriate target?, *Theranostics,* 4 (2014) 81-89.

[39] S. Mura, J. Nicolas, P. Couvreur, Stimuli-responsive nanocarriers for drug delivery, *Nat. Mater.,* 12 (2013) 991-1003.

[40] M.A.C. Stuart, W.T. Huck, J. Genzer, M. Müller, C. Ober, M. Stamm, G.B. Sukhorukov, I. Szleifer, V.V. Tsukruk, M. Urban, Emerging applications of stimuli-responsive polymer materials, *Nat. Mater.,* 9 (2010) 101-113.

[41] R. Cheng, F. Meng, C. Deng, H.-A. Klok, Z. Zhong, Dual and multi-stimuli responsive polymeric nanoparticles for programmed site-specific drug delivery, *Biomaterials,* 34 (2013) 3647-3657.

[42] A.K. Drew, S.P. Myers, Safety issues in herbal medicine: implications for the health professions, *Med. J. Aust.,* 166 (1997) 538-541.

[43] P. Anand, A.B. Kunnumakkara, R.A. Newman, B.B. Aggarwal, Bioavailability of curcumin: problems and promises, *Mol. Pharm.,* 4 (2007) 807-818.

[44] H. Yu, Q. Huang, Improving the oral bioavailability of curcumin using novel organogel-based nanoemulsions, *J. Agric. Food Chem.,* 60 (2012) 5373-5379.

[45] S. Bisht, G. Feldmann, S. Soni, R. Ravi, C. Karikar, A. Maitra, A. Maitra, Polymeric nanoparticle-encapsulated curcumin (" nanocurcumin"): a novel strategy for human cancer therapy, *J. Nanobiotechnology,* 5 (2007) 1-18.

[46] L. Li, F.S. Braiteh, R. Kurzrock, Liposome-encapsulated curcumin, *Cancer,* 104 (2005) 1322-1331.

[47] K. Varaprasad, K. Vimala, S. Ravindra, N.N. Reddy, G.V.S. Reddy, K.M. Raju, Fabrication of silver nanocomposite films impregnated with curcumin for superior antibacterial applications, *J. Mater. Sci. Mater. Med.,* 22 (2011) 1863-1872.

[48] C. Sreelakshmi, N. Goel, K. Datta, A. Addlagatta, R. Ummanni, B. Reddy, Green synthesis of curcumin capped gold nanoparticles and evaluation of their cytotoxicity, *Nanosci. Nanotechnol. Lett,* 5 (2013) 1258-1265.

[49] R.J. Mart, R.D. Osborne, M.M. Stevens, R.V. Ulijn, Peptide-based stimuli-responsive biomaterials, *Soft Matter,* 2 (2006) 822-835.

[50] D. Bagchi, S. Chaudhuri, S. Sardar, S. Choudhury, N. Polley, P. Lemmens, S.K. Pal, Modulation of stability and functionality of a phyto-antioxidant by weakly interacting metal ions: curcumin in aqueous solution, *RSC Adv,* 5 (2015) 102516-102524.

[51] T. Dutta, D. Bagchi, S.K. Pal, Bimetallic zeolitic imidazolate framework as an active excipient of curcumin under physiological condition, *Biomed. Phys. Eng. Express,* 4 (2018) 055004.

[52] D. Bagchi, T.K. Maji, S. Sardar, P. Lemmens, C. Bhattacharya, D. Karmakar, S.K. Pal, Sensitized ZnO nanorod assemblies to detect heavy metal contaminated phytomedicines: spectroscopic and simulation studies, *Phys. Chem. Chem. Phys.,* 19 (2017) 2503-2513.

[53] D. Bagchi, A. Ghosh, P. Singh, S. Dutta, N. Polley, I.I. Althagafi, R.S. Jassas, S.A. Ahmed, S.K. Pal, Allosteric inhibitory molecular recognition of a photochromic dye by a digestive enzyme: dihydroindolizine makes α-chymotrypsin photo-responsive, *Sci. Rep.,* 6 (2016) 34399.

[54] D. Bagchi, S. Dutta, P. Singh, S. Chaudhuri, S.K. Pal, Essential dynamics of an effective phototherapeutic drug in a nanoscopic delivery vehicle: psoralen in ethosomes for biofilm treatment, *ACS Omega,* 2 (2017) 1850-1857.

[55] D. Bagchi, V.S. Rathnam, P. Lemmens, I. Banerjee, S.K. Pal, NIR-light-active ZnO-based nanohybrids for bacterial biofilm treatment, *ACS Omega,* 3 (2018) 10877-10885.

[56] D. Bagchi, A. Halder, S. Debnath, P. Saha, S. K Pal, Exploration of interfacial dynamics in squaraine based nanohybrids for potential photodynamic action, *J. Photochem. Photobiol. A,* (2019) doi.org/10.1016/j.jphotochem.2019.1005.1005.

[57] D. Bagchi, A. Bhattacharya, T. Dutta, S. Nag, D. Wulferding, P. Lemmens, S.K. Pal, Nano MOF entrapping hydrophobic photosensitizer for dal-stimuli responsive unprecedented therapeutic action against drug-resistant bacteria, *ACS Appl. Bio Mater.,* 2 (2019) 1772-1780.

Chapter 2

An Overview of Experimental Techniques and Systems

In order to investigate the dynamical processes involved in hybrid materials, different steady-state and dynamical tools have been employed. These include photoinduced electron transfer (PET), Förster resonance energy transfer (FRET), distance distribution from FRET, photovoltage decay measurement and circular dichroism. In this chapter, we have included a brief discussion about the above-mentioned tools. Overviews of the various systems, probes and dyes used in the studies have also been provided.

2.1. Steady-state and Dynamical Tools:

2.1.1. Photoinduced Electron Transfer (PET): PET can be described as the movement of an electron caused by the absorption of light from an electron-rich species (D) to an electron deficient species (A), as shown in equation 2.1.

$$D + A \rightarrow D^+ + A^- \tag{2.1}$$

The first law of photochemistry tells us that a photoinduced process must be initiated by the absorption of light. In PET, the absorbing species can either be a donor, the acceptor, or a ground-state complex between the donor and acceptor, often referred to as a charge transfer complex. These possibilities are shown in equations 2.2−2.4.

$$D \xrightarrow{h\upsilon} D^* + A \longrightarrow D^+ + A^- \tag{2.2}$$

$$A \xrightarrow{h\upsilon} A^* + D \longrightarrow D^+ + A^- \tag{2.3}$$

$$(D \cdots A) \xrightarrow{h\upsilon} (D \cdots A)^* \longrightarrow D^+ + A^- \tag{2.4}$$

Transport of charges or excitons are commonly seen as fundamental processes in many optoelectronic devices as well as biological systems. The creation,

diffusion, and annihilation of excitons and the mobility of charges are some of the key processes in many light-responsive assemble structures of biological significance [1]. PET is an important process in many biochemical systems, such as those in respiration and photosynthesis [2, 3]. To gain a deep understanding for these systems, it is important to describe the rates of these processes with a few empirically derived parameters [4]. Therefore, it has become increasingly important to develop computational techniques that allow us to calculate the rate of charge or energy transport. In our systems the apparent rate constants, k_{nr}, were determined for the nonradiative processes by comparing the lifetimes of donor in the absence (τ_0) and in the presence (τ) of an acceptor, using equation 2.5.

$$k_{nr} = 1/\langle \tau \rangle - 1/\langle \tau_0 \rangle \tag{2.5}$$

The direction of electron transfer in the excited state is determined by the oxidation and reduction potential of the ground and excited states. Upon excitation the electron donor transfers an electron to the acceptor with a rate k_{nr}, forming the charge transfer complex. This complex may emit as an exciplex ($h\nu_E$) or be quenched and return to the ground state. The important part of this process is the decrease in total energy of the charge transfer complex. The energy decreases because the ability to donate or accept electrons changes when a fluorophore is in the excited state. Excitation provides the energy to drive charge separation. D and A do not form a complex when both are in the ground state because this is energetically unfavorable. The energy released by electron transfer can also change if the ions become solvated and/or separated in a solvent with a high dielectric constant. This thesis demonstrates several PET processes, particularly in hybrid materials and discusses the consequences of various interfacial electron transfer processes in dye/semiconductor system including a series of charge transfer processes which occur cooperatively.

2.1.2. Förster Resonance Energy Transfer (FRET): FRET is an electrodynamic phenomenon involving the nonradiative transfer of the excited state energy from

the donor dipole (D) to an acceptor dipole (A) in the ground state (Figure 2.1a). Basically, FRET is of two types: (i) homo-molecular FRET and (ii) hetero-molecular FRET. In the former case the same fluorophore acts both as energy donor and acceptor, while in the latter case two different molecules act as donor and acceptor [5].

Each donor-acceptor (D-A) pair participating in FRET is characterized by a distance known as Förster distance (R_0) i.e., the D-A separation at which energy transfer is 50% efficient. The rate of resonance energy transfer (k_T) from donor to an acceptor is given by [6],

$$k_T = \frac{1}{\tau_D}\left(\frac{R_0}{r}\right)^6 \tag{2.6}$$

where τ_D is the lifetime of the donor in the absence of acceptor and r is the donor to acceptor (D-A) distance. The rate of transfer of donor energy depends upon the extent of overlap of the emission spectrum of the donor with the absorption spectrum of the acceptor ($J(\lambda)$), the quantum yield of the donor (Q_D), the relative orientation of the donor and acceptor transition dipoles (κ^2) and the distance between the donor and acceptor molecules (r) (Figure 2.1b). In order to estimate FRET efficiency of the donor and hence to determine distances between donor-acceptor pairs, the methodology described below is followed [7]. R_0 is given by,

$$R_0 = 0.211\left[\kappa^2 n^{-4} Q_D J(\lambda)\right]^{1/6} \text{ (in Å)} \tag{2.7}$$

where n is the refractive index of the medium, Q_D is the quantum yield of the donor and $J(\lambda)$ is the overlap integral. κ^2 is defined as,

$$\kappa^2 = \left(\cos\theta_T - 3\cos\theta_D \cos\theta_A\right)^2 = \left(\sin\theta_D \sin\theta_A \cos\varphi - 2\cos\theta_D \cos\theta_A\right)^2 \tag{2.8}$$

where θ_T is the angle between the emission transition dipole of the donor and the absorption transition dipole of the acceptor, θ_D and θ_A are the angles between these dipoles and the vector joining the donor and acceptor and φ is angle between the planes of the donor and acceptor (Figure 2.1b). κ^2 value can vary from 0 to 4. For

collinear and parallel transition dipoles, $\kappa^2 = 4$; for parallel dipoles, $\kappa^2 = 1$; and for perpendicularly oriented dipoles, $\kappa^2 = 0$. For donor and acceptors that randomize

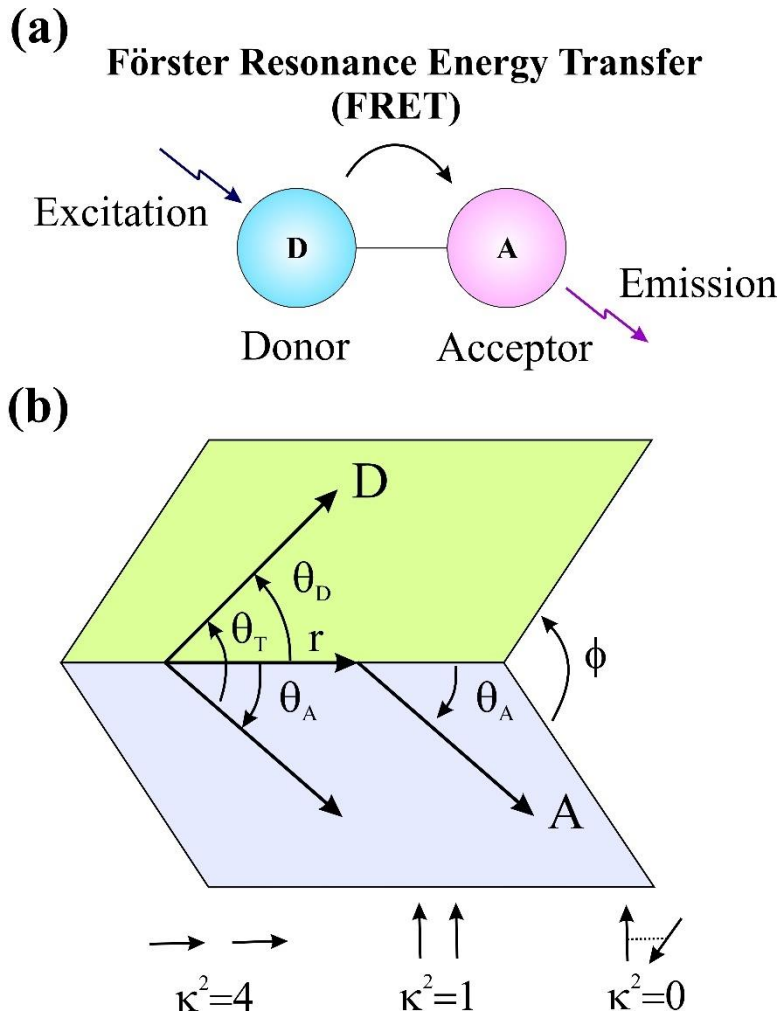

Figure 2.1. *(a) Schematic illustration of the FRET process (b) Dependence of the orientation factor κ^2 on the directions of the emission and absorption dipoles of the donor and acceptor, respectively.*

by rotational diffusion prior to energy transfer, the magnitude of κ^2 is assumed to be 2/3. However, in systems where there is a definite site of attachment of the donor and acceptor molecules, to get physically relevant results, the value of κ^2 has to be estimated from the angle between the donor emission and acceptor absorption dipoles. $J(\lambda)$, the overlap integral, which expresses the degree of spectral overlap between the donor emission and the acceptor absorption, is given by [8],

$$J(\lambda) = \frac{\int_0^\infty F_D(\lambda)\varepsilon_A(\lambda)\lambda^4 d\lambda}{\int_0^\infty F_D(\lambda)d\lambda} \tag{2.9}$$

where $F_D(\lambda)$ is the fluorescence intensity of the donor in the wavelength range of λ to $\lambda+d\lambda$ and is dimensionless. $\varepsilon_A(\lambda)$ is the extinction coefficient (in $M^{-1}cm^{-1}$) of the acceptor at λ. If λ is in nm, then $J(\lambda)$ is in units of $M^{-1}\,cm^{-1}\,nm^4$.

Once the value of R_0 is known, the efficiency of energy transfer can be calculated. The efficiency of energy transfer (E) is the fraction of photons absorbed by the donor which are transferred to the acceptor and is defined as,

$$E = \frac{k_T(r)}{\tau_D^{-1} + k_T(r)} \tag{2.10}$$

$$\text{Or, } E = \frac{R_0^6}{r^6 + R_0^6} \tag{2.11}$$

For D-A systems decaying with multiexponential lifetimes, E is calculated from the amplitude weighted lifetimes $\langle\tau\rangle = \sum_i \alpha_i\tau_i$ of the donor in absence (τ_D) and presence (τ_{DA}) of the acceptor as,

$$E = 1 - \frac{\tau_{DA}}{\tau_D} \tag{2.12}$$

The D-A distances can be measured using equations (2.11) and (2.12).

2.1.3. Data Analysis of Time-Resolved Fluorescence Transients: Curve fitting of the time-resolved fluorescence transients was carried out using a nonlinear least square fitting procedure to a function (2.13) comprised of convolution of the IRF

$$(X(t) = \int_0^t E(t')R(t-t')dt') \tag{2.13}$$

(E(t)) with a sum of exponentials (2.14) with pre-exponential factors (B_i),

$$(R(t) = A + \sum_{i=1}^{N} B_i e^{-t/\tau_i}) \tag{2.14}$$

characteristic lifetimes (τ_i) and a background (A). Relative concentration in a multiexponential decay is expressed as (2.15).

$$c_n = \frac{B_n}{\sum_{i=1}^{N} B_i} \times 100 \tag{2.15}$$

The average lifetime (amplitude-weighted) of a multiexponential decay is expressed as,

$$\tau_{av} = \sum_{i=1}^{N} c_i \tau_i \tag{2.16}$$

2.1.4. Distance Distribution between Donor and Acceptor: Distance distribution between donor and acceptor was estimated according to the procedure described in the literature [8]. The observed fluorescence transients of the donor molecules in absence of acceptor were fitted using a nonlinear least-squares fitting procedure (software SCIENTIST) to the following function,

$$I_D(t) = \int_0^t E(t')\, p(t'-t) dt' \tag{2.17}$$

which comprises the convolution of the instrument response function (IRF) ($(E(t)$) with exponential $(p(t) = \sum_i \alpha_{Di} \exp(-t/\tau_{Di}))$. The convolution of the distance distribution function $P(r)$ in the fluorescence transients of donor in presence of acceptor in the system under studies is estimated using the same software (SCIENTIST) in the following way.

The intensity decay of D-A pair, spaced at a distance r, is given by

$$I_{DA}(r,t) = \sum_i \alpha_{Di} \exp\left[-\frac{t}{\tau_{Di}} - \frac{t}{\tau_{Di}} \left(\frac{R_0}{r} \right)^6 \right] \tag{2.18}$$

and the intensity decay of the sample considering distance distribution probablity function, $P(r)$ is given by,

$$I_{DA}(t) = \int_{r=0}^{\infty} P(r) I_{DA}(r,t) dr \tag{2.19}$$

where *P(r)* consist of the folowing terms:

$$P(r) = \frac{1}{\sigma\sqrt{2\pi}} \exp\left[-\frac{1}{2}\left(\frac{\bar{r} - r}{\sigma} \right)^2 \right] \tag{2.20}$$

In this equation $\bar{r}$ is the mean of the Gaussian with a standard deviation of σ. Usually, distance distributions are described by the full width at half maxima (*hw*). This half width is given by $hw = 2.354\sigma$.

2.1.5. Photovoltaic Device: Photovoltaic device is fabricated using the platinum (Pt) nanoparticles deposited on the FTO substrates. This is used as counter electrode. Dye sensitized ZnO NR were used as the active electrodes and the two electrodes were placed on top of each other with a single layered spacer between the two electrodes. A liquid electrolyte in acetonitrile was used as the hole conductor and filled in the inter-electrode space by using capillary force, through two small holes (diameter = 1 mm) pre-drilled on the counter electrode. Finally, the two holes were sealed by using another piece of Surlyn to prevent the leakage of electrolyte from the cell.

2.1.5.1. Photovoltage Decay Measurement: The open circuit voltage of photovoltaic device generated under illumination is equivalent to the separation between the quasi-Fermi level of electrons in the ZnO film and the rest potential of the counter electrode, which remains in equilibrium with the redox couple. The forward electron injection from sensitizer to ZnO is terminated upon stopping the illumination, thus discharging of electrons occurs through the back-electron transfer or recombination with the oxidized electrolytes. The open circuit voltage decay reflects the timescales for the recombination processes.

2.1.6. Circular Dichroism (CD): CD is now a routine tool in many laboratories with applications to determine whether a chiral molecule has been synthesized or

resolved into pure enantiomers and probing the structures of biomolecules, in particular determining the α-helical content of proteins [9, 10].

2.1.6.1. Theory: When a plane polarized light passes through an optically active substance, not only do the left (*L*) and right (*R*) circularly polarized light rays travel at different speeds, $c_L \neq c_R$, but these two rays are absorbed to a different extent, i.e. $A_L \neq A_R$. The difference in the absorbance of the left and right circularly polarized light, i.e., $\Delta A = A_L - A_R$, is defined as circular dichroism (CD). Circular dichroism spectroscopy follows Beer-Lambert law. If I_0 is the intensity of light incident on the cell, and *I*, that of emergent light, then absorbance is given by,

$$A = \log_{10}\left(\frac{I_0}{I}\right) = \varepsilon c l \tag{2.21}$$

i.e., *A* is proportional to concentration (*c*) of optically active substance and optical path length (*l*). If '*c*' is in moles litre^{-1} and '*l*' is in cm, then ε is called the molar absorptivity or molar extinction coefficient. In an optically active medium, two absorbances, A_L and A_R are considered, where $A_L = \log_{10}\left(I_0/I_L\right)$ and $A_R = \log_{10}\left(I_0/I_R\right)$. At the time of incidence on the sample, intensity of left and right circularly polarized light are same, i.e. $I_0 = I_L = I_R$. Any dictograph passes periodically changing light through the medium, oscillating between left and right circular polarization, and the difference in absorbances are recorded directly.

$$\Delta A = A_L - A_R = \log_{10}\left(\frac{I_0}{I_L}\right) - \log_{10}\left(\frac{I_0}{I_R}\right) = \log_{10}\left(\frac{I_R}{I_L}\right) \tag{2.22}$$

$$\Delta A = \left(\Delta\varepsilon\right) c l \tag{2.23}$$

As seen from equation (2.22), I_0 does not appear in this final equation, so there is no need for a reference beam. The instruments are, therefore, of single beam type.

After passing through an optically active substance, light is changed in two aspects. The maximal amplitude of intensity is no longer confined to a plane; instead it traces out an ellipse. Ellipticity is defined as the arctangent of the ratio of minor

axis to the major axis of the ellipse (Figure 2.2). The orientation of ellipse is another aspect. The major axis of the ellipse no longer remains parallel to the polarization of the incident light. Thus, after passing through an optically active substance, neither do the absorbance nor do the radii of the emergent left and right circularly polarized light remains same. Hence, CD is equivalent to ellipticity.

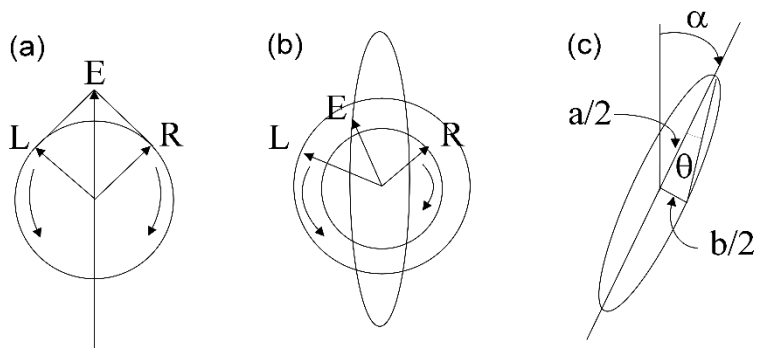

Figure 2.2. *(a) Left (L) and right (R) circularly polarized light component having same intensities and phases lying in one plane and oscillating with same magnitude, (b) R component being less intense (more absorbed) than L component leading to elliptically polarized light and (c) θ, ellipticity is the angle made by semi-major and semi-minor axes of the ellipse. The major axis has rotated through angle α corresponding to optical rotation.*

Most of the CD spectropolarimeters, although they measure differential absorption, produce a CD spectrum in units of ellipticity (θ) expressed in milli-degrees versus λ, rather than ΔA versus λ. The relation between ellipticity and CD is given by,

$$\theta = \frac{2.303 \times 180 \times \left(A_L - A_R\right)}{4\pi} \text{ (in degrees)} \tag{2.24}$$

to compare the results from different samples, optical activity is computed on a molar or residue basis. Molar ellipticity, $[\theta]$ is defined as,

$$[\theta] = \frac{\theta}{cl} \tag{2.25}$$

where (θ) is in degrees, 'c' is in moles per litre and 'l' is in cm. The unit of molar ellipticity is deg.M^{-1}.cm^{-1}. Sometimes, CD is reported as $\Delta\varepsilon = \Delta\varepsilon_L - \Delta\varepsilon_R$. From Beer-Lambert law and molar ellipticity relation it can be shown that,

$$[\theta] = 3300.\Delta\varepsilon \quad (2.26)$$

2.1.6.2. Experimental Methods: In biophysical studies, CD is mostly used to determine the secondary structures of proteins and nucleic acids and the changes in secondary structures upon recognition by small molecules and other biomolecules. Through CD spectropolarimeter, we obtain CD spectrograph having a plot of optical rotation in millidegrees versus wavelength in nm. In order to obtain information about the secondary structures of proteins, the graph is fitted with non-linear least square fitting method using freely available software. The percentages of different secondary structures are calculated by matching the experimental data with that of reference standard. In proteins, the secondary structural content includes α–helix, β–sheet, β–turn and random coil. The CD spectrum of α–helix contains two negative peaks, one at 208 nm (π–π* transition) and 222 nm (n–π* transition). β–sheet has a negative band at 216 nm and a positive band of similar magnitude at 195 nm. β–turn has weak negative peak at 225 nm (n–π* transition), a strong positive peak between 200 nm and 205 nm due to π–π* transition and a strong negative band between 180 nm and 190 nm. Random coil or unordered conformation has a strong negative band below 200 nm; a positive band at 218 nm and in some cases has a very weak negative band at 235 nm.

2.2. Systems:

2.2.1. Organized Assemblies (Biomimetics): Amphiphilic lipid molecules aggregates to form macromolecular assemblies, like liposomes, which very often useful for nanotechnology and biological applications. In the following section, we will discuss about these entities.

2.2.1.1. Ethosomes: Ethosomes are phospholipid nanovesicles used for dermal and transdermal delivery of molecules. Ethosomes are mainly composed of multiple, concentric layers of flexible phospholipid bilayers, with a relative high concentration of ethanol (20-45%), glycols and water [11]. Ethosomes are

noninvasive delivery carriers that enable drugs to reach the deep skin layers and/or the systemic circulation. These are soft, malleable vesicles tailored for enhanced delivery of active agents [12]. They are composed mainly of phospholipids, (phosphatidylcholine, phosphatidylserine), high concentration of ethanol and

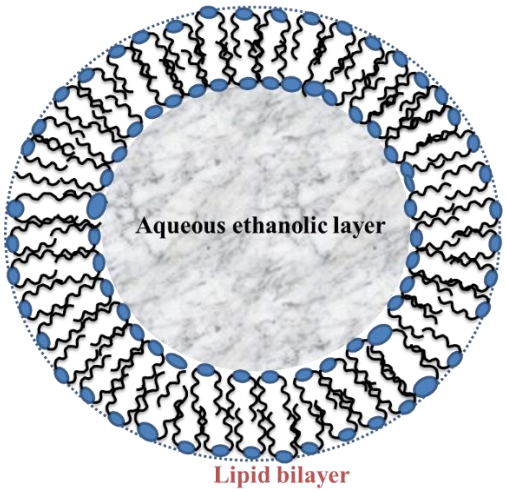

Figure 2.3. *Schematic representation of ethosomes structure.*

water. The high concentration of ethanol makes the ethosomes unique, as ethanol is known for its disturbance of skin lipid bilayer organization; therefore, when integrated into a vesicle membrane, it gives that vesicle the ability to penetrate the stratum corneum. Also, because of their high ethanol concentration, the lipid membrane is packed less tightly than conventional vesicles but has equivalent stability, allowing a more malleable structure and improves drug distribution ability in stratum corneum lipids. Because of their unique structure, ethosomes are able to efficiently encapsulate and deliver into the skin highly lipophilic molecules such as testosterone, cannabinoids and ibuprofen, as well as hydrophilic drugs such as clindamycin phosphate, buspirone hydrochloride [13]. They have been studied for the transdermal and intradermal delivery of peptides, steroids, antibiotics, prostaglandins, antivirals and anti-pyretic.

2.2.2. Proteins: In the study, alpha chymotrypsin (CHT) have been used.

2.2.2.1. α-Chymotrypsin (CHT): α-Chymotrypsin (Figure 2.4) isolated from bovine pancreas, is a member of the family serine endopeptidase (molecular weight of 25,191 Da) catalyzing the hydrolysis of peptides in the small intestine [14]. The three-dimensional structure of CHT was solved by David Blow. The molecule is a three-dimensional ellipsoid of dimensions 51 × 40 × 40 Å and comprises of 245 amino acid residues. CHT contains several antiparallel β-pleated sheet regions and little α-helix. Physiological activity of CHT is determined by the pH [15]. The enzyme is not active at lower pH, but the activity increases nonmonotonically with pH; in the duodenum (low pH), it is inactive, whereas in the lower small intestinal track (high pH), it becomes active [16]. The inactivity of the enzyme at lower pH is known to be related to the protonation of the residues of the catalytic triad. From spectroscopic studies, it was suggested that the degree of mobility of water molecules, not hydrophobicity, may be the important factor for the change with pH [17].

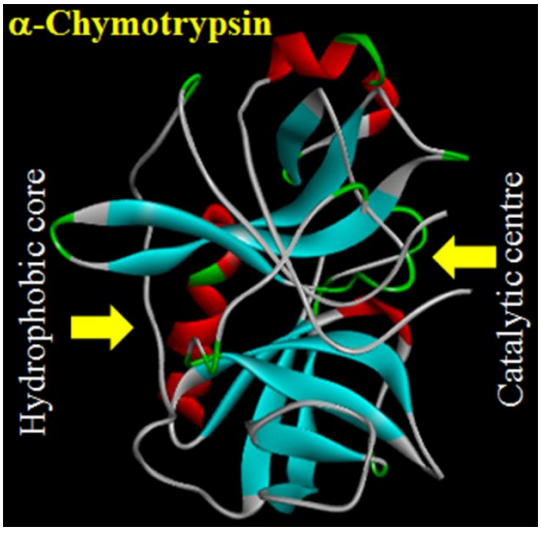

Figure 2.4. *X-ray crystallographic structure (PDB code: 2CHA) of CHT depicting the different domains.*

2.2.3. Molecular Probes: In this section, we will discuss about the different probe molecules that have been used in the course of study.

2.2.3.1. Curcumin (Cur): Curcumin is a natural yellowish orange diarylheptanoid derived from the rhizomes of *Curcuma longa L.* popularly known as turmeric, a member of the ginger family [18]. The diverse pharmacological applications of curcumin towards various diseases includes Alzheimer's disease, breast cancer, pancreatic cancer, colon cancer, arthritis and oxidative stress induced pathogenesis [19, 20]. Furthermore, its promising antioxidant activity anticipates its possible use as a novel drug also for other lethal diseases. Curcumin is a linear polyphenol consisting of two o-methoxy phenolic groups which are connected by a seven-carbon linker consisting of an α, β-unsaturated β-diketo moiety (Figure 2.5). The diketo group exhibits keto-enol tautomerism and can exist in different types of conformers depending on the nature of the solvent [21]. In most of non-polar and moderately polar solvents, the enol form is generally more stable than the keto form by 5 to 8 kcal/mol due to strong intramolecular H-bonding. Curcumin is hydrophobic in nature and almost insoluble in water at physiological pH values. This may be due to the presence of β-diketone linkers in the seven-carbon chain. This leads to poor bio-availability, limited absorption in body, rapid metabolism and excretion.

2.2.3.2. 2,5-Cyclohexadiene-1,4-dione (*p*-Benzoquinone, BQ): BQ (Figure 2.5) is a well-known probe for electron accepting and shuttling for any electron rich material/compound [22], which readily accepts electron and adapted to be resonance species hydroquinone. Large doses could induce local irritation, clonic convulsions, decreased blood pressure and death due to paralysis of the medullary centres.

2.2.3.3. 2,2-Diphenyl-1-picrylhydrazyl (DPPH): DPPH is a well-known radical and a trap ("scavenger") for other radicals. Therefore, rate reduction of a chemical reaction upon addition of DPPH is used as an indicator of the radical nature of that reaction [23]. Because of a strong absorption band centered at about 520 nm, the DPPH radical has a deep violet color in solution, and it becomes colorless or pale

yellow when neutralized. This property allows visual monitoring of the reaction, and the number of initial radicals can be counted from the change in the optical absorption at 520 nm.

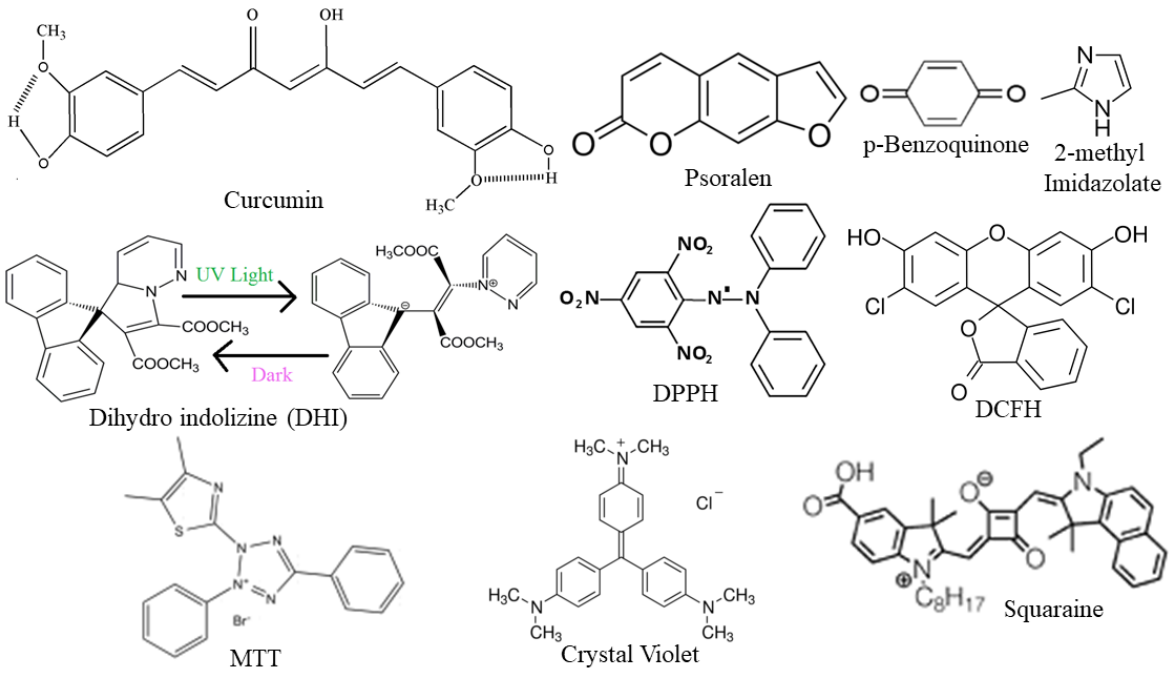

***Figure* 2.5.** *Schematic representation of the molecular probes used.*

2.2.3.4. Dichlorofluorescin (DCFH): Dichlorofluorescin (DCFH) is a probe that is trapped within cells and is easily oxidized to fluorescent dichlorofluorescein (DCF) [24]. Dichlorofluorescin (DCFH) is non-fluorescent which convert to fluorescent DCF upon oxidation through reacting with reactive oxygen species (ROS). This quantifies amount of ROS as well as cellular oxidative stress.

2.2.3.5. 7H-furo[3,2-g] chromen-7-one (Psoralen, PSO): The family of linear furocoumarins and their derivatives, more customarily known as psoralen (PSO) [25], have been shown to be active dermal photosensitizing agents in the presence of UVA. PSO intercalates with DNA upon irradiation with UVA and subsequently forms adducts with pyrimidine bases in the opposite strand of DNA, resulting in DNA strand crosslinking [26]. These result in the inhibition of cell division; thus, PSO followed by UV radiation is widely used for the treatment of psoriasis [27].

2.2.3.6. Tris(4-(dimethylamino) phenyl) methylium chloride (Crystal violet, CV): Crystal violet is a triarylmethane dye used as a histological stain and in Gram's method of classifying bacteria. Crystal violet has antibacterial, antifungal, and anthelmintic properties and was formerly important as a topical antiseptic [28]. The medical use of the dye has been largely superseded by more modern drugs, although it is still listed by the World Health Organization. When dissolved in water, the dye has a blue-violet color with an absorbance maximum at 590 nm and an extinction coefficient of 87,000 M^{-1} cm^{-1} [29]. The color of the dye depends on the acidity of the solution.

2.2.3.7. Dihydroindolizine (DHI): Photochromic DHI has received much attention owing to its remarkable photo-fatigue resistance and broad range of absorption [30]. Moreover, photochromic DHI is used to tether peptides and proteins via a maleimide functional group, which corresponds to absorption in the red region of the visible spectrum and in the near-IR spectral domain, indicating the potential for future use in *in vivo* applications. The basis of the photochromic behavior of DHI is light-induced reversible pyrroline ring opening, which transforms the molecule from a light-yellow colored form (cis) to a red colored betaine form (trans). Betaines undergo a thermal back reaction to their corresponding DHI cis form by 1,5-electrocyclization [31, 32].

2.2.3.8. Acridine-3,6-diamine (Proflavine): Proflavine is an acriflavine derivative, a disinfectant bacteriostatic against many gram-positive bacteria. It has been used in the form of the dihydrochloride and hemisulfate salts as a topical antiseptic and was formerly used as a urinary antiseptic. Proflavine is also known to have a mutagenic effect on DNA by intercalating between nucleic acid base pairs. It differs from most other mutagenic components by causing base pair-deletions or base pair-insertions and not substitutions. In the presence of light, proflavine can induce double-stranded breaks in DNA. Proflavine absorbs strongly in the blue region at 445 nm (in water at pH 7) [33].

2.2.3.9. Squaraine (SQ): Squaraine, condensation products of electron-rich substrates and squaric acid derivatives, with a four-membered squaraine ring present into the polymethine chain structure consist of absorption maxima in longer wavelength region [34]. Besides large applications in dye sensitized solar cell, squaraine dyes impose greater light-absorption ability at low-energy region and higher photo-stability with respect to other available commercial dye and can be considered as photomedicine [35].

2.2.3.10. 3-(4,5-dimethylthiazol-2-yl)-2,5-diphenyltetrazolium bromide (MTT): Tetrazolium dye MTT converted into its insoluble formazan through NAD(P)H-dependent cellular oxidoreductase enzymes under defined conditions that reflect the number of viable cells present [36]. Tetrazolium dye reduction is generally assumed to be dependent on NAD(P)H-dependent oxidoreductase enzymes largely in the cytosolic compartment of the cell. Therefore, reduction of MTT depends on the cellular metabolic activity due to NAD(P)H flux [37]. Cells with a low metabolism such as thymocytes and splenocytes reduce very little MTT. In contrast, rapidly dividing cells exhibit high rates of MTT reduction. It is important to keep in mind that assay conditions can alter metabolic activity and thus tetrazolium dye reduction without affecting cell viability.

References

[1] Y. Shirota, H. Kageyama, Charge carrier transporting molecular materials and their applications in devices, *Chem. Rev.,* 107 (2007) 953-1010.

[2] H.B. Gray, J.R. Winkler, Electron tunneling through proteins, *Q. Rev. Biophys,* 36 (2003) 341-372.

[3] G. McLendon, R. Hake, Interprotein electron transfer, *Chem. Rev.,* 92 (1992) 481-490.

[4] V. Kenkre, J.D. Andersen, D. Dunlap, C. Duke, Unified theory of the mobilities of photoinjected electrons in naphthalene, *Phys. Rev. Lett.,* 62 (1989) 1165.

[5] L. Stryer, Fluorescence energy transfer as a spectroscopic ruler, *Annu. Rev. Biochem.* , 47 (1978) 819-846.

[6] J.R. Lakowicz, Principles of fluorescence spectroscopy, Springer Science & Business Media, 2013.

[7] D. Banerjee, S.K. Pal, Simultaneous binding of minor groove binder and intercalator to dodecamer DNA: importance of relative orientation of donor and acceptor in FRET, *J. Phys. Chem. B,* 111 (2007) 5047-5052.

[8] S. Batabyal, T. Mondol, S.K. Pal, Picosecond-resolved solvent reorganization and energy transfer in biological and model cavities, *Biochimie,* 95 (2013) 1127-1135.

[9] A. Rodger, B. Nordén, B. Nordén, Circular dichroism and linear dichroism, Oxford University Press, USA, 1997.

[10] N.J. Greenfield, G.D. Fasman, Computed circular dichroism spectra for the evaluation of protein conformation, *Biochemistry,* 8 (1969) 4108-4116.

[11] Y.-P. Fang, Y.-H. Tsai, P.-C. Wu, Y.-B. Huang, Comparison of 5-aminolevulinic acid-encapsulated liposome versus ethosome for skin delivery for photodynamic therapy, *Int. J. Pharm.,* 356 (2008) 144-152.

[12] V. Dave, D. Kumar, S. Lewis, S. Paliwal, Ethosome for enhanced transdermal drug delivery of aceclofenac, *Int. J. Drug. Deliv,* 2 (2010).

[13] Z. Zhang, Y. Wo, Y. Zhang, D. Wang, R. He, H. Chen, D. Cui, In vitro study of ethosome penetration in human skin and hypertrophic scar tissue, *Nanomedicine,* 8 (2012) 1026-1033.

[14] R.A. Blevins, A. Tulinsky, The refinement and the structure of the dimer of alpha-chymotrypsin at 1.67-A resolution, *J. Biol. Chem.,* 260 (1985) 4264-4275.

[15] S.K. Pal, J. Peon, A.H. Zewail, Ultrafast surface hydration dynamics and expression of protein functionality: α-chymotrypsin, *Proc. Natl. Acad. Sci. U.S.A.*, 99 (2002) 15297-15302.

[16] S.K. Pal, J. Peon, A.H. Zewail, Biological water at the protein surface: dynamical solvation probed directly with femtosecond resolution, *Proc. Natl. Acad. Sci. U.S.A.,* 99 (2002) 1763-1768.

[17] S. Choudhury, S. Batabyal, P.K. Mondal, P. Singh, P. Lemmens, S.K. Pal, Direct observation of kinetic pathways of biomolecular recognition, *Chem.: Eur. J.,* 21 (2015) 16172-16177.

[18] K.M. Nelson, J.L. Dahlin, J. Bisson, J. Graham, G.F. Pauli, M.A. Walters, The essential medicinal chemistry of curcumin: miniperspective, *J. Med. Chem.,* 60 (2017) 1620-1637.

[19] D. Perrone, F. Ardito, G. Giannatempo, M. Dioguardi, G. Troiano, L. Lo Russo, A. De Lillo, L. Laino, L. Lo Muzio, Biological and therapeutic activities, and anticancer properties of curcumin, *Exp. Ther. Med,* 10 (2015) 1615-1623.

[20] S. Wanninger, V. Lorenz, A. Subhan, F.T. Edelmann, Metal complexes of curcumin–synthetic strategies, structures and medicinal applications, *Chem. Soc. Rev.,* 44 (2015) 4986-5002.

[21] M. Pröhl, U.S. Schubert, W. Weigand, M. Gottschaldt, Metal complexes of curcumin and curcumin derivatives for molecular imaging and anticancer therapy, *Coord. Chem. Rev.,* 307 (2016) 32-41.

[22] D.A. Horke, Q. Li, L. Blancafort, J.R. Verlet, Ultrafast above-threshold dynamics of the radical anion of a prototypical quinone electron-acceptor, *Nat. Chem.,* 5 (2013) 711-717.

[23] M. Szabo, D. Radu, S. Gavrilas, D. Chambre, C. Iditoiu, Antioxidant and antimicrobial properties of selected spice extracts, *Int. J. Food. Prop,* 13 (2010) 535-545.

[24] S. Sardar, S. Chaudhuri, P. Kar, S. Sarkar, P. Lemmens, S.K. Pal, Direct observation of key photoinduced dynamics in a potential nano-delivery vehicle of cancer drugs, *Phys. Chem. Chem. Phys.,* 17 (2015) 166-177.

[25] A.K. Gupta, T.F. Anderson, Psoralen photochemotherapy, *J. Am. Acad. Dermatol.,* 17 (1987) 703-734.

[26] W. Westerhof, L. Nieuweboer-Krobotova, Treatment of vitiligo with UV-B radiation vs topical psoralen plus UV-A, *Arch. Dermatol.,* 133 (1997) 1525-1528.

[27] B. Parsons, Psoralen photochemistry, *Photochem. Photobiol.,* 32 (1980) 813-821.

[28] M. Ishiyama, H. Tominaga, M. Shiga, K. Sasamoto, Y. Ohkura, K. Ueno, A combined assay of cell vability and in vitro cytotoxicity with a highly water-soluble tetrazolium salt, neutral red and crystal violet, *Biol. Pharm. Bull.,* 19 (1996) 1518-1520.

[29] J. Korppi-Tommola, R. Yip, Solvent effects on the visible absorption spectrum of crystal violet, *Can. J. Chem.,* 59 (1981) 191-194.

[30] T.B. Shrestha, J. Melin, Y. Liu, O. Dolgounitcheva, V.G. Zakrzewski, M.R. Pokhrel, E. Gogritchiani, J.V. Ortiz, C. Turró, S.H. Bossmann, New insights in the photochromic spiro-dihydroindolizine/betaine-system, *Photochem. Photobiol. Sci.* , 7 (2008) 1449-1456.

[31] A. Raghuvanshi, A.K. Jha, A. Sharma, S. Umar, S. Mishra, R. Kant, A. Goel, A nonarchetypal 5, 6-dihydro-2H-pyrano [3, 2-g] indolizine-based solution-solid dual emissive AIEgen with multicolor tunability, *Chem.: Eur. J.,* 23 (2017) 4527-4531.

[32] O.F. Mohammed, S.A. Ahmed, E. Vauthey, E.T. Nibbering, Photoinduced ring-opening of a photochromic dihydroindolizine derivative monitored with femtosecond visible and infrared spectroscopy, *J. Phys. Chem. A,* 113 (2009) 5061-5065.

[33] H.J. Li, D.M. Crothers, Relaxation studies of the proflavine-DNA complex: the kinetics of an intercalation reaction, *J. Mol. Biol.,* 39 (1969) 461-477.

[34] S. Sreejith, P. Carol, P. Chithra, A. Ajayaghosh, Squaraine dyes: a mine of molecular materials, *J. Mater. Chem.,* 18 (2008) 264-274.

[35] J.-H. Yum, P. Walter, S. Huber, D. Rentsch, T. Geiger, F. Nüesch, F. De Angelis, M. Grätzel, M.K. Nazeeruddin, Efficient far red sensitization of nanocrystalline TiO2 films by an unsymmetrical squaraine dye, *J. Am. Chem. Soc.,* 129 (2007) 10320-10321.

[36] J. Van Meerloo, G.J. Kaspers, J. Cloos, Cell sensitivity assays: the MTT assay, in: Cancer Cell Culture, Springer, 2011, pp. 237-245.

[37] D. Gerlier, N. Thomasset, Use of MTT colorimetric assay to measure cell activation, *J. Immunol. Methods,* 94 (1986) 57-63.

Chapter 3

Instrumentation and Sample Preparation

In this chapter, the details of instrumental setup and sample preparation techniques used in the thesis work have been described.

3.1. Instrumental Setups:

3.1.1. Steady-state UV-Vis Absorption and Emission Measurement: Steady-state UV-Vis absorption and emission spectra were measured with Shimadzu UV-2600 spectrophotometer and Horiba Fluorolog, respectively. Schematic ray diagrams of these two instruments are shown in Figures 3.1 and 3.2.

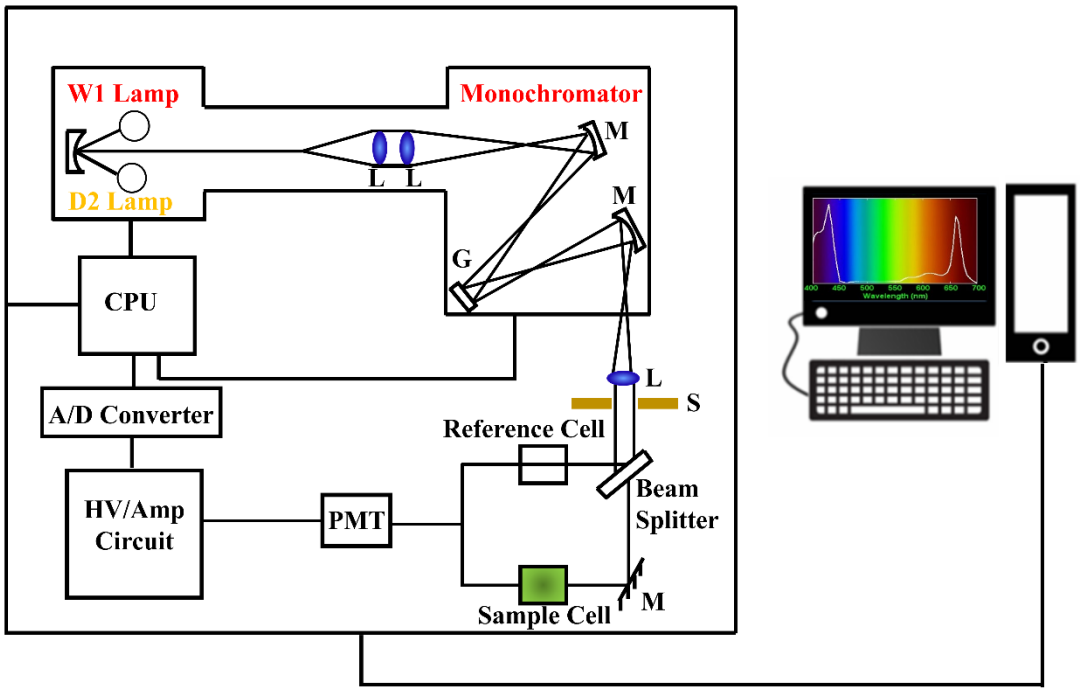

Figure 3.1. *Schematic ray diagram of an absorption spectrophotometer. Tungsten halogen (W1) and deuterium lamps (D2) are used as light sources in the visible and UV regions, respectively. M, G, L, S, PMT designate mirror, grating, lens, shutter and photomultiplier tube, respectively. CPU, A/D converter and HV/amp indicate central processing unit, analog to digital converter and high-voltage/amplifier circuit, respectively.*

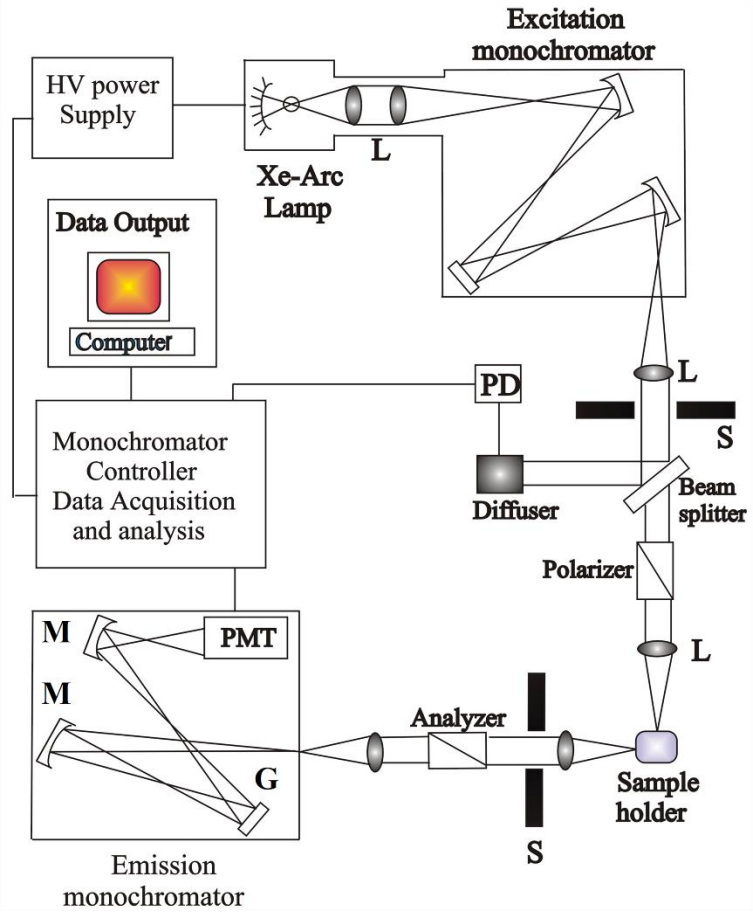

Figure 3.2. *Schematic ray diagram of an emission spectrofluorometer. M, G, L, S, PMT and PD represent mirror, grating, lens, shutter, and photomultiplier tube and reference photodiode, respectively.*

3.1.2. Time-correlated Single Photon Counting (TCSPC) Technique: All the picosecond-resolved fluorescence transients were recorded using TCSPC technique. The schematic block diagram of a TCSPC system is shown in Figure 3.3. TCSPC setup from Edinburgh instruments, U.K., was used during fluorescence decay acquisitions. The instrument response functions (IRFs) of the laser sources at different excitation wavelengths varied between 70 ps to 80 ps. The fluorescence from the sample was detected by a photomultiplier after dispersion through a grating monochromator [1]. For all transients, the polarizer in the emission side was adjusted to be at 54.70 (magic angle) with respect to the polarization axis of excitation beam.

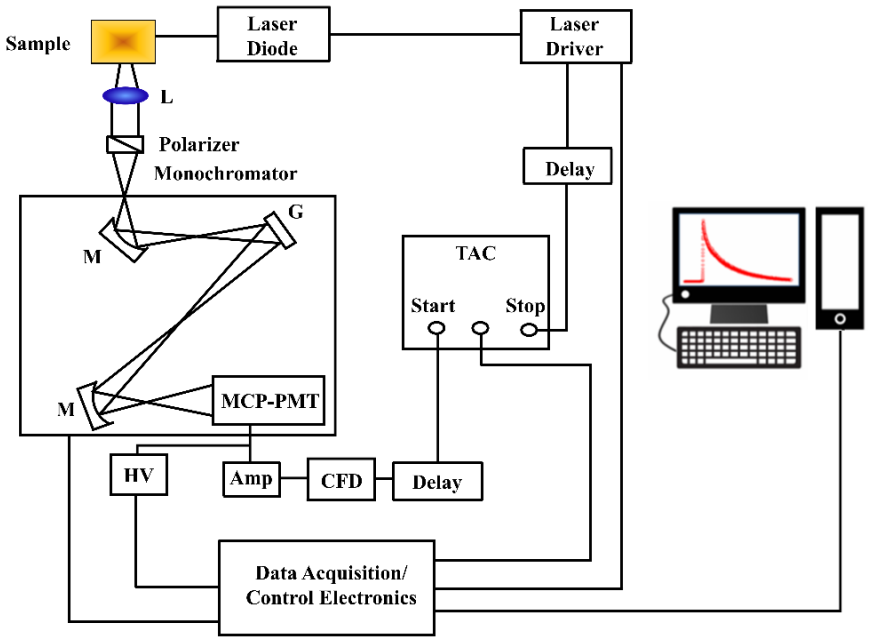

Figure 3.3. *Schematic ray diagram of a time correlated single photon counting (TCSPC) spectrophotometer. A signal from microchannel plate photomultiplier tube (MCP-PMT) is amplified (Amp) and connected to start channel of time to amplitude converter (TAC) via constant fraction discriminator (CFD) and delay. The stop channel of the TAC is connected to the laser driver via a delay line. L, M, G and HV represent lens, mirror, grating and high voltage source, respectively.*

3.1.3. Femtosecond Resolved Fluorescence Upconversion Technique: The femtosecond-resolved fluorescence spectroscopy was carried out using a femtosecond upconversion setup (FOG 100, CDP, Figure 3.4) in which the sample was excited at 400 nm, using the second harmonic of a mode-locked Ti-sapphire laser with 80 MHz repetition rate (Tsunami, Spectra Physics), pumped by 10 W Millennia (Spectra Physics). The fundamental beam was passed through a periscopic arrangement (P) (Figure 3.4) before getting frequency doubled in a nonlinear crystal, NC1 (1 mm BBO, $\theta = 25°$, $\phi = 90°$). This beam was then sent into a rotating circular cell of 1 mm thickness containing the sample via a dichroic mirror (DM), a polarizer and a mirror (M6). The resulting fluorescence emission was collected, refocused with a pair of lenses (L4 and L5) and mixed with the fundamental beam (770 nm) coming through a delay line to yield an upconverted photon signal in a nonlinear crystal, NC2 (0.5 mm BBO (β-barium borate), $\theta = 10°$, $\phi = 90°$). The upconverted light was dispersed in a double monochromator and

detected using photon counting electronics. A cross-correlation function obtained using the Raman scattering from water displayed a full width at half maximum (FWHM) of 195 fs. The femtosecond fluorescence decays were fitted using a Gaussian shape for the exciting pulse.

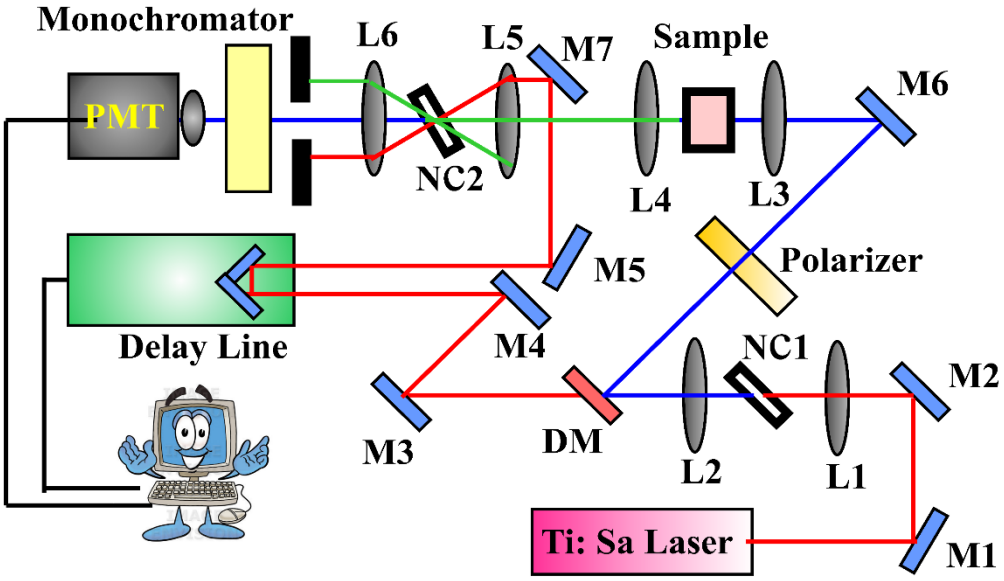

Figure 3.4. *Schematic diagram of a femtosecond fluorescence upconversion experimental setup. A BBO crystal (NC1) is used for second harmonic generation, which provides a pump beam in the UV region. Another BBO crystal (NC2) generates the upconversion signal of pump and probe beams. L and M indicate lenses and mirrors, respectively. M1, M2, M3, M4, M5, and M7 are IR mirrors whereas M6 is a UV mirror. DM is dichroic mirror, and P is periscope.*

3.1.4. Circular Dichroism (CD) Measurement: CD is a form of spectroscopy based on the differential absorption of left and right-handed circularly polarized light. It can be used to determine the structure of macromolecules (including the secondary structure of proteins). The CD measurements were done in a JASCO spectropolarimeter with a temperature controller attachment (Peltier) (Figure 3.5). The CD spectra were acquired using quartz cells of 0.1 and 1.0 cm path length.

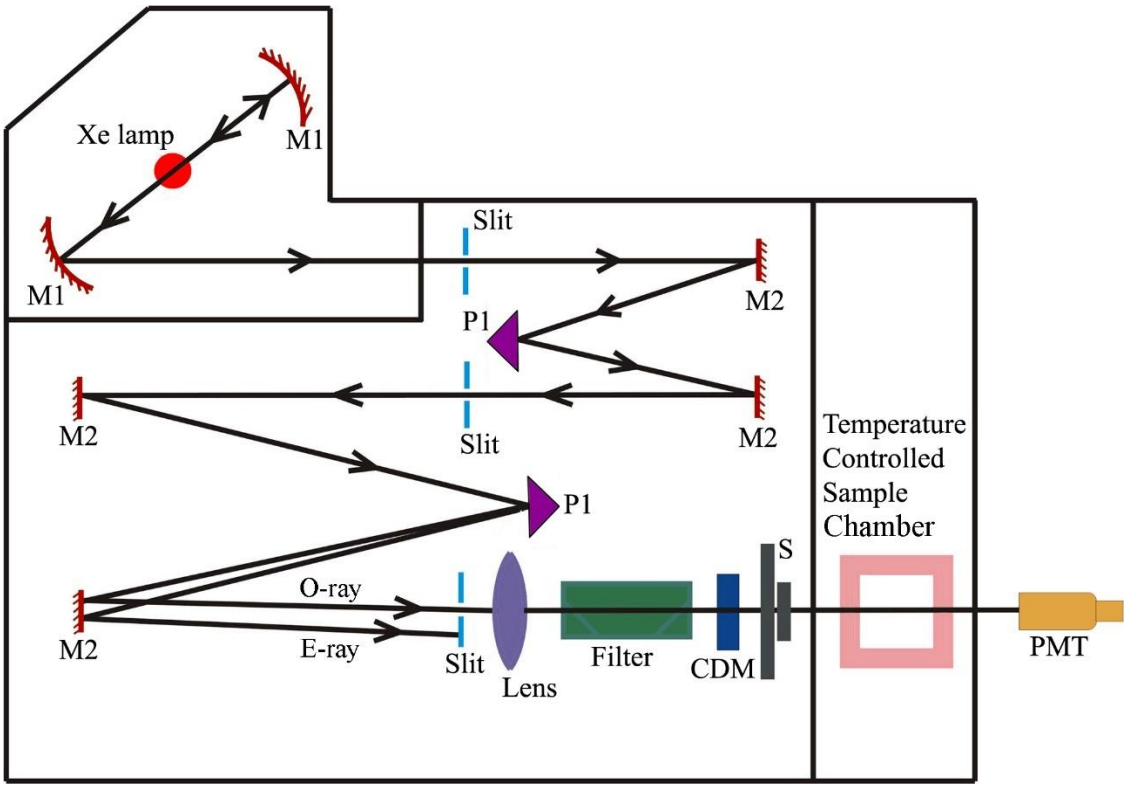

Figure 3.5. *Schematic ray diagram of a circular dichroism (CD) spectropolarimeter. M1, M2, P1, S, PMT, CDM, O-ray and E-ray represent concave mirror, plain mirror, reflecting prism, shutter, photomultiplier tube, CD-modulator, ordinary ray and extraordinary ray, respectively.*

3.1.5. Transmission Electron Microscopy (TEM): A FEI TecnaiTF-20 field-emission

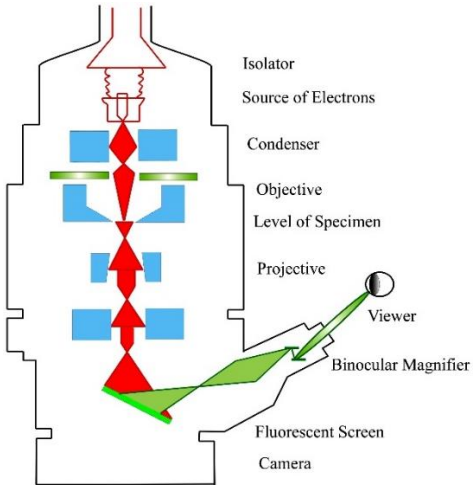

Figure 3.6. *Schematic diagram of a typical transmission electron microscope (TEM). After the transmission of electron beam through a specimen, the magnified image is formed either in the fluorescent screen or can be detected by a CCD camera.*

high-resolution TEM (Figure 3.6) equipped with energy dispersive X-ray (EDAX) spectrometer was used to characterize the microscopic structures of samples and to analyze their elemental composition. The sizes of the nanostructures were determined from the TEM images obtained at 200 kV acceleration voltage of the microscope. Samples for TEM were prepared by placing a drop of the colloidal solution on a carbon-coated copper grid and allowing the film to evaporate overnight at room-temperature.

3.1.6. Scanning Electron Microscopy (SEM): Surface characterization of nanomaterials were done by scanning electron microscope FE (field emission)-SEM; JEOL. Ltd., JSM-6500F. An electron-gun is attached to SEM and the electrons from filament triggered by 0 KV to 30 KV voltages. These electrons go first through a condenser lens and then through an objective lens, then through an aperture and finally reach to the specimen. The high energy electrons go a bit in the sample and back again give secondary electrons. The signal from secondary electrons are detected by detector and amplified. The ray diagram of the SEM setup is shown in Figure 3.7.

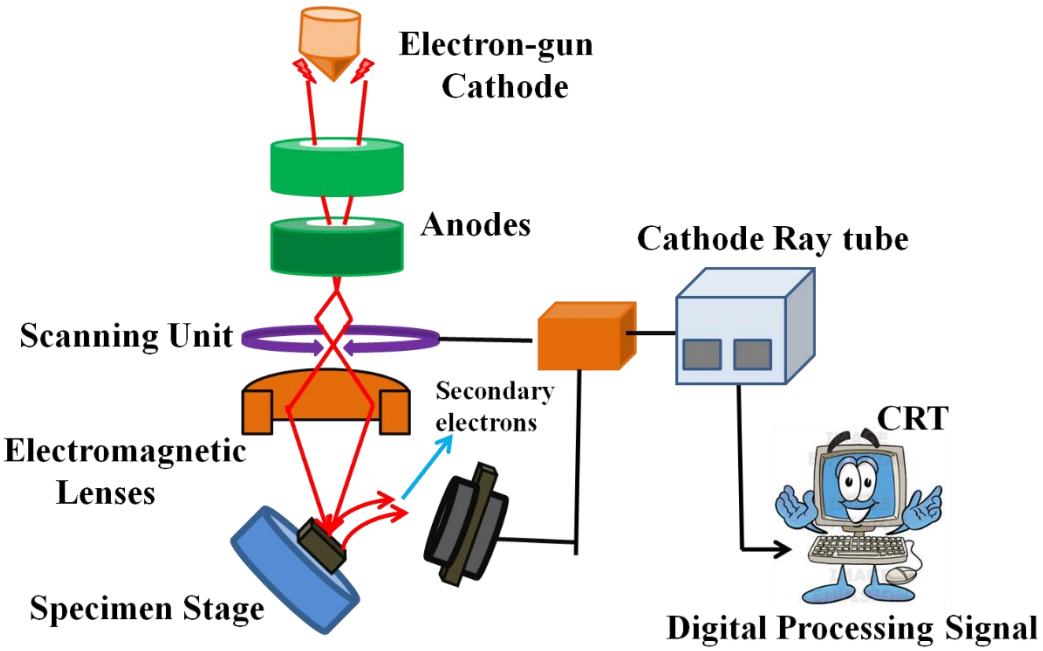

Figure 3.7. *Schematic diagram of typical scanning electron microscope (SEM).*

3.1.7. Dynamic Light Scattering (DLS): Dynamic light scattering (DLS), also known as Photon Correlation Spectroscopy (PCS) or Quasi-Elastic Light Scattering (QELS), is one of the most popular techniques used to determine the hydrodynamic size of the particle. DLS measurements were performed on a Nano S Malvern instruments, U.K. employing a 4 mW He-Ne laser (λ= 632.8 nm) and equipped with a thermostatic sample chamber. The instrument allows DLS measurements in which all the scattered photons are collected at 173˚ scattering angle (Figure 3.8). The instrument measures the time-dependent fluctuation in intensity of light scattered from the particles in solution at a fixed scattering angle. The ray diagram of the DLS setup is shown in Figure 3.8.

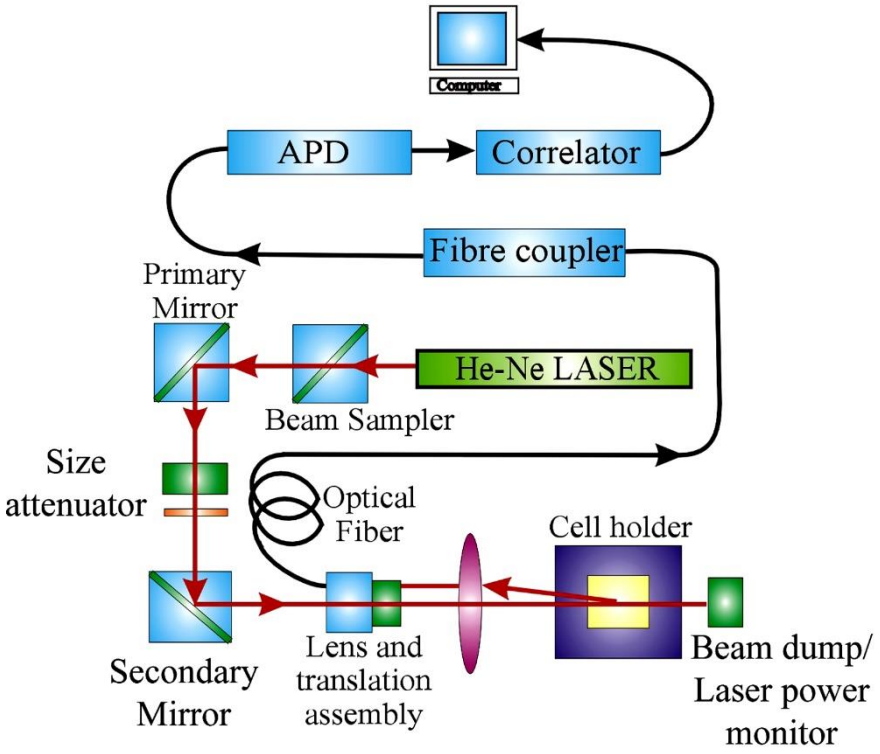

Figure 3.8. *Schematic ray diagram of dynamic light scattering (DLS) instrument. The avalanche photo diode (APD) is connected to preamplifier/amplifier assembly and finally to correlator. It has to be noted that lens and translational assembly, laser power monitor, size attenuator, laser are controlled by the computer.*

It has been seen that particles in dispersion are in a constant, random Brownian motion and this causes the intensity of scattered light to fluctuate as a

function of time. The correlator used in a DLS instrument constructs the intensity autocorrelation function G(τ) of the scattered intensity,

$$G(\tau) = \langle I(t)I(t+\tau)\rangle \tag{3.1}$$

where τ is the time difference (the sample time) of the correlator. For a large number of monodisperse particles in Brownian motion, the correlation function (given the symbol G) is an exponential decay function of the correlator time delay τ,

$$G(\tau) = A[1 + B\exp(-2\Gamma\tau)] \tag{3.2}$$

where A is the baseline of the correlation function, B is the intercept of the correlation function. Γ is the first cumulant and is related to the translational diffusion coefficient as, $\Gamma = Dq^2$, where q is the scattering vector and its magnitude is defined as,

$$q = \left(\frac{4\pi n}{\lambda_0}\right)\sin\left(\frac{\theta}{2}\right) \tag{3.3}$$

where n is the refractive index of dispersant, λ_0 is the wavelength of the laser and θ, the scattering angle. For polydisperse samples, the equation can be written as,

$$G(\tau) = A\left[1 + B\left|g^{(1)}(\tau)\right|^2\right] \tag{3.4}$$

where the correlation function $g^{(1)}(\tau)$ is no longer a single exponential decay and can be written as the Laplace transform of a continuous distribution G(Γ) of decay times,

$$g^{(1)}(\tau) = \int_0^\infty G(\Gamma)\exp(-\Gamma\tau)d\Gamma \tag{3.5}$$

The scattering intensity data in DLS are processed using the instrumental software to obtain the hydrodynamic diameter (d_H) and the size distribution of the scatterer in each sample. In a typical size distribution graph from the DLS measurement, X-

axis shows a distribution of size classes in nm, while the Y-axis shows the relative intensity of the scattered light. The diffusion coefficient (D) can be calculated using the hydrodynamic diameter (d_H) of the particle by using the Stoke-Einstein relation,

$$D = \frac{k_B T}{3\pi\eta d_H} \tag{3.6}$$

where k_B, T, d_H, η are Boltzmann constant, temperature in Kelvin, hydrodynamic diameter and viscosity, respectively.

3.1.8. X-ray Diffraction (XRD) Measurement: XRD is a popular and a powerful technique for determining crystal structure of crystalline materials. By examining the diffraction pattern, one can identify the crystalline phase of the material. Small angle scattering is useful for evaluating the average interparticle distance while wide-angle diffraction is useful for refining the atomic structure of nanoclusters. The widths of the diffraction lines are closely related to strain and defect size and distribution in nanocrystals. As the size of the nanocrystals decreases, the line width is broadened due to loss of long-range order relative to the bulk. This XRD line width can be used to estimate the size of the particle by using the Debye-Scherrer formula,

$$D = \frac{0.9\lambda}{\beta \cos\theta} \tag{3.7}$$

where, D is the nanocrystal diameter, λ is the wavelength of light, β is the full-width half-maximum (FWHM) of the peak in radians, and θ is the Bragg angle. XRD measurements were performed on a PANalytical XPERT-PRO diffractometer (Figure 3.9) equipped with CuKα radiation (λ = 1.5418 Å at 40 mA, 40 kV). XRD patterns were obtained by employing a scanning rate of 0.02° s^{-1} in the 2θ range from 15° to 75°.

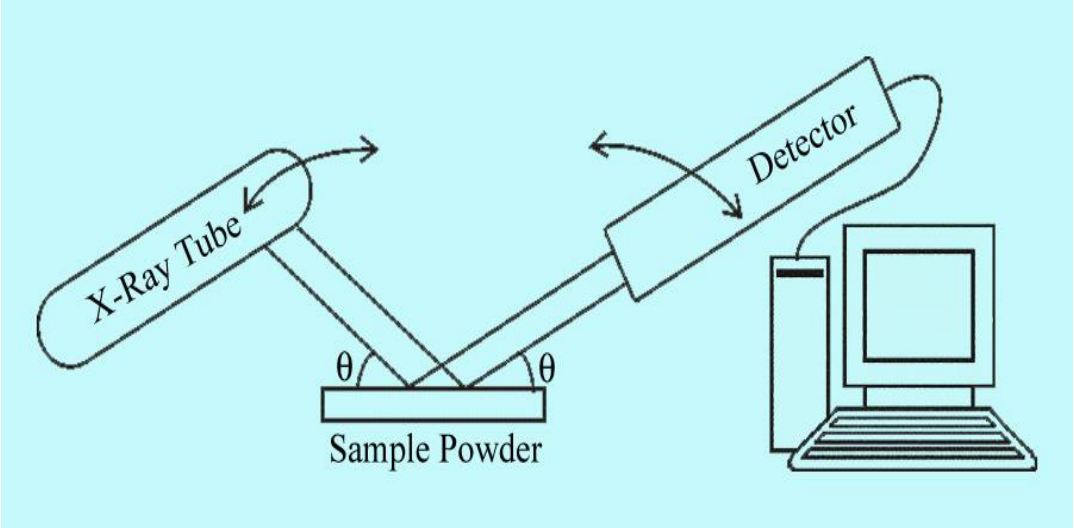

Figure 3.9. *Schematic diagram of X-ray Diffraction (XRD) instrument. By varying the angle θ, the Bragg's Law conditions, nλ=2dsinθ are satisfied by different d-spacings in polycrystalline materials. Plotting the angular positions and intensities of the resultant diffracted peaks of radiation produces a pattern, which is characteristic of the sample.*

3.1.9. Thermogravimetric-Differential Thermal Analyzer (TG-DTA) Setup: The thermogravimetric (TG) analysis was carried out using Diamond thermogravimetric (TG)-differential thermal analyzer (DTA) from Perkin Elmer. The TG determines the weight change of a sample whereas the DTA measures the change in temperature between a sample and the reference as a function of temperature and/or time. The schematic of the TG-DTA setup is shown in Figure 3.10. When a weight change occurs on the sample side, the beam holding the platinum pans is displaced. This movement is detected optically and the driving coil current is changed to return the displacement to zero. The detected driving coil current change is proportional to the sample weight change and the output is the TG signal. The DTA detects the temperature difference between the sample holder and the reference holder using the electromotive force of thermocouples, which are attached to the holders. This difference is measured as the DTA signal.

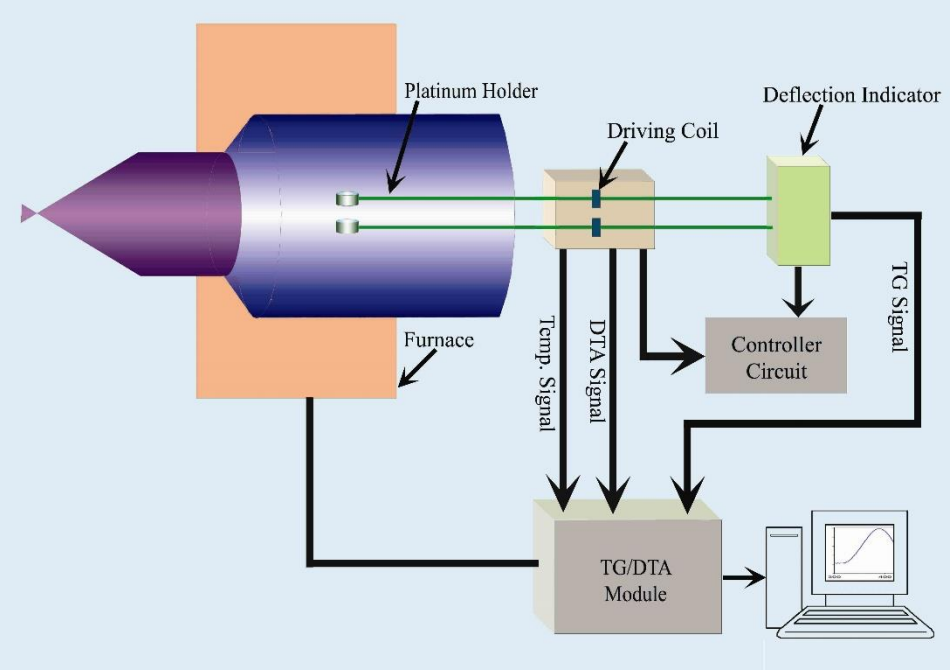

Figure 3.10. *The schematic representation of TG-DTA setup.*

3.1.10. Fourier Transform Infrared (FTIR) Measurement: FTIR spectroscopy is a technique that can provide very useful information about functional groups in a sample. An infrared spectrum represents the fingerprint of a sample with absorption peaks which correspond to the frequencies of vibrations between the bonds of the atoms making up the material. Because each different material is a unique combination of atoms, no two compounds produce the exact same infrared spectrum. Therefore, infrared spectroscopy can result in a positive identification (qualitative analysis) of every different kind of material. In addition, the size of the peaks in the spectrum is a direct indication of the amount of material present. The two-beam Michelson interferometer is the heart of FTIR spectrometer. It consists of a fixed mirror (M4), a moving mirror (M5) and a beam-splitter (BS1), as illustrated in Figure 3.11. The beam-splitter is a laminate material that reflects and transmits light equally. The collimated IR beam from the source is partially transmitted to the moving mirror and partially reflected to the fixed mirror by the beam-splitter. The two IR beams are then reflected back to the beam-splitter by the mirrors. The detector then sees the transmitted beam from the fixed mirror and reflected beam

from the moving mirror, simultaneously. The two combined beams interfere constructively or destructively depending on the wavelength of the light (or frequency in wavenumbers) and the optical path difference introduced by the moving mirror. The resulting signal is called an interferogram which has the unique property that every data point (a function of the moving mirror position) which makes up the signal has information about every infrared frequency which comes from the source. Because the analyst requires a frequency spectrum (a plot of the intensity at each individual frequency) in order to make identification, the measured interferogram signal cannot be interpreted directly. A means of "decoding" the individual frequencies is required. This can be accomplished *via* a well-known mathematical technique called the Fourier transformation. This transformation is performed by the computer which then presents the user with the desired spectral information for analysis. FTIR measurements were performed on a JASCO FTIR-6300 spectrometer (transmission mode). For the FTIR measurements, powdered samples were mixed with KBr powder and pelletized. The background correction was made using a reference blank of KBr pellet.

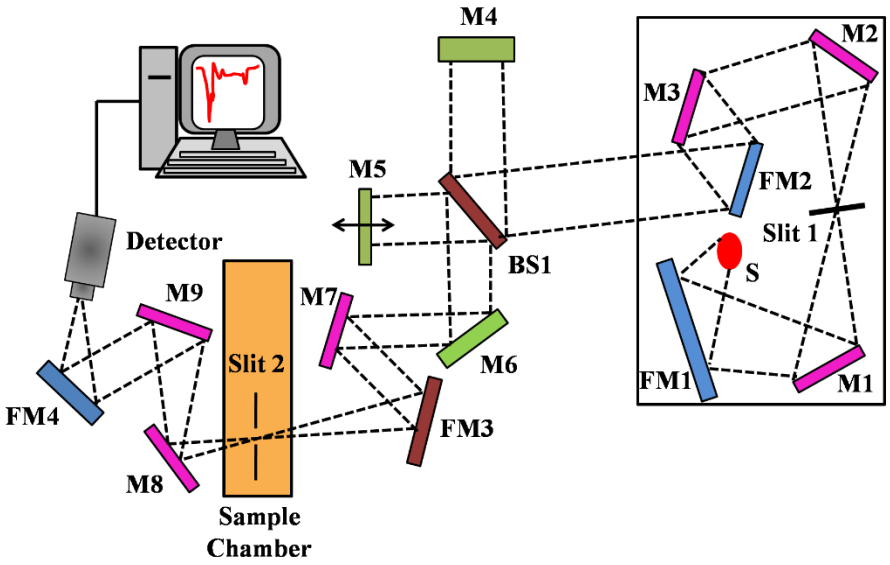

Figure 3.11. *Schematic of Fourier Transform Infrared (FTIR) spectrometer. It is basically a Michelson interferometer in which one of the two fully-reflecting mirrors is movable, allowing a variable delay (in the travel-time of the light) to be included in one of the beams. M, FM and BS1 represent the mirror, focussing mirror and beam splitter, respectively. M5 is a moving mirror.*

3.1.11. Laser Raman Spectroscopy: Raman spectroscopy is a useful technique for the identification of a wide range of substances− solids, liquids, and gases. It is a straightforward, non-destructive technique requiring no sample preparation. Raman spectroscopy involves illuminating a sample with monochromatic light and using a spectrometer to examine light scattered by the sample.

At the molecular level photons can interact with matter by absorption or scattering processes. Scattering may occur either elastically, or inelastically. The elastic process is termed Rayleigh scattering, whilst the inelastic process is termed Raman scattering. The electric field component of the scattering photon perturbs the electron cloud of the molecule and may be regarded as exciting the system to a 'virtual' state. Raman scattering occurs when the system exchanges energy with the photon and the system subsequently decays to vibrational energy levels above or below that of the initial state. The frequency shift corresponding to the energy difference between the incident and scattered photon is termed the Raman shift. Depending on whether the system has lost or gained vibrational energy, the Raman shift occurs either as an up or down-shift of the scattered photon frequency relative to that of the incident photon. The down-shifted and up-shifted components are called, respectively, the Stokes and anti-Stokes lines. A plot of detected number of photons versus Raman shift from the incident laser energy gives a Raman spectrum. Different materials have different vibrational modes, and therefore characteristic Raman spectra. This makes Raman spectroscopy a useful technique for material identification. There is one important distinction to make between the Raman spectra of gases and liquids, and those taken from solids− in particular, crystals. For gases and liquids it is meaningful to speak of the vibrational energy levels of the individual molecules which make up the material. Crystals do not behave as if composed of molecules with specific vibrational energy levels; instead the crystal lattice undergoes vibration. These macroscopic vibrational modes are called phonons.

In modern Raman spectrometers (Horiba LabRAM set up), lasers are used as a photon source due to their highly monochromatic nature, and high beam fluxes (Figure 3.12). This is necessary as the Raman effect is weak, typically the Stokes lines are ~10^5 times weaker than the Rayleigh scattered component. In the visible spectral range, Raman spectrometers use notch filters to cut out the signal from a very narrow range centred on the frequency corresponding to the laser radiation. Most Raman spectrometers for material characterization use a microscope to focus the laser beam to a small spot (<1−100 μm diameter). Light from the sample passes back through the microscope optics into the spectrometer. Raman shifted radiation is detected with a charge-coupled device (CCD) detector, and a computer is used for data acquisition and curve fitting. These factors have helped Raman spectroscopy to become a very sensitive and accurate technique.

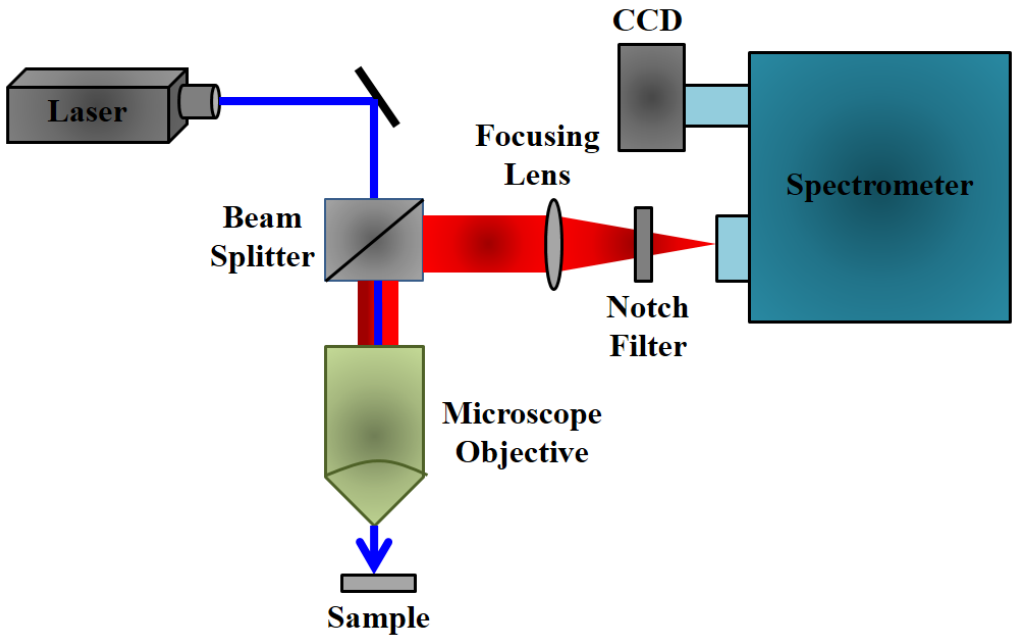

Figure 3.12. *Schematic diagram of a Raman spectrometer is shown.*

3.1.12. Fluorescence Microscope: Commercially available fluorescence microscope (Leica digital inverted microscopes DMI8.) was used in our study. The light source is usually a mercury-vapor lamp. For bright field, Tungsten-halogen lamp was

used. In particular, an inverted setup with a mercury-vapor lamp as light source is shown in Figure 3.13.

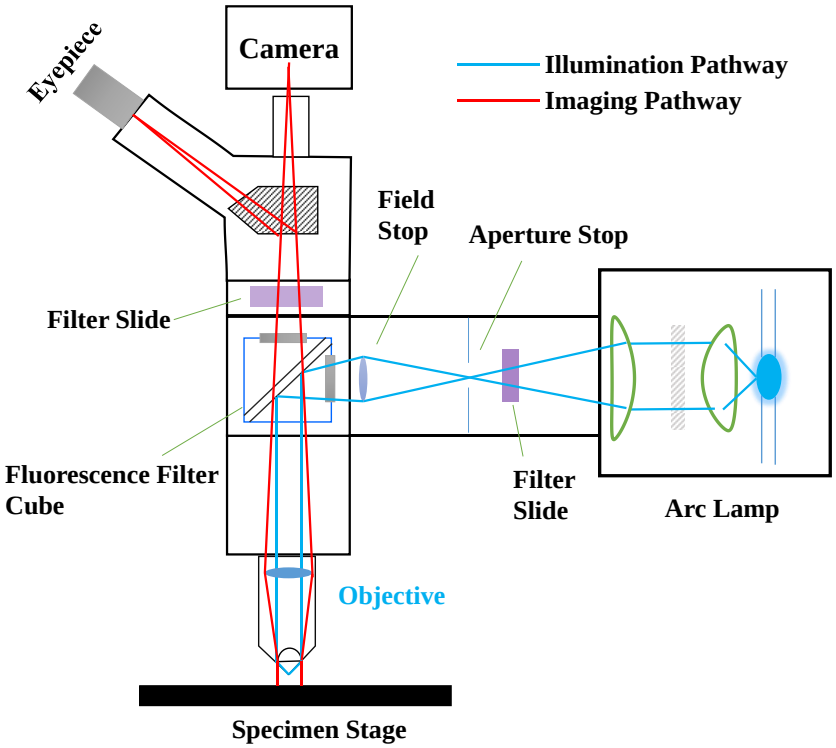

Figure 3.13. *Schematic presentation of the fluorescence microscope.*

The dichroic mirror, excitation and emission filter are joined together within the filter cube (Figure 3.13). Since mercury-vapor lamps emit light over the whole optical spectrum as well as in the ultraviolet range, an optical excitation filter is used to isolate one specific wavelength. Due to the Stokes shift, it is possible to separate excitation and emission light in the same light path optically via a dichroic mirror. This way, only the emission light is collected by the objective. An emission filter helps to suppress unwanted background light.

3.1.13. Cyclic Voltammetry (CV): CV is a useful technique for studying electrochemical reactions. In case of CV, the voltage is swept between two potential values (V_1 and V_2) at a fixed rate, however now when the voltage reaches V_2 from V_1, the scan is reversed and the voltage is swept back to V_1. The current response is plotted as a function of the applied potential. Electrochemical experiments were

performed using a CH analyser potentiostat (CHI1110C). A three electrode system consisting of a platinum working electrode, a platinum counter electrode and a reference electrode were employed. All the potentials reported in this thesis are referenced to the Ag/Ag+ couple. Electrolyte is usually added to the sample solution to ensure sufficient conductivity. The solvent, electrolyte, and material composition of the working electrode will determine the potential range that can be accessed during the experiment. The schematic presentation of the CV set up is shown in Figure 3.14.

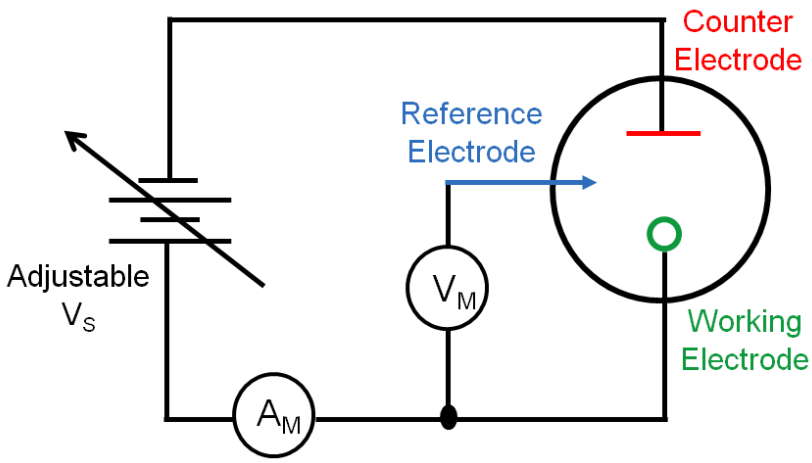

Figure 3.14. *Schematic diagram of a simplified measurement circuit for performing cyclic voltammetry (CV).*

A typical electrochemical measurement circuit made up of an electrochemical cell, an adjustable voltage source (V_S), an ammeter (A_M) and a voltmeter (V_M). The three electrodes of the electrochemical cell are the working electrode (WE), reference electrode (RE) and the counter (or auxiliary) electrode (CE). The voltage source (V_S) for the potential scan is applied between the working electrode and the counter electrode. The potential (E) between the reference electrode and the working electrode is measured with the voltmeter and the overall voltage (Vs) is adjusted to maintain the desired potential at the working electrode with respect to the reference electrode. The resulting current (I) flowing to or from the working electrode is measured with the ammeter (A_M).

3.1.14. Electrochemical Impedance Spectroscopy (EIS): Electrochemical Impedance Spectroscopy (EIS) is a powerful technique to investigate the electronic and ionic processes in photovoltaic devices. Electrochemical impedance is usually measured by applying an AC potential to an electrochemical cell and then measuring the current through the cell. An important advantage of EIS over other techniques is the possibility of using tiny AC voltage amplitudes exerting a very small perturbation on the system. A Nyquist plot can be made by plotting the real part of the transfer function on the X-axis and the imaginary part on the Y-axis. The Nyquist diagram features typically three semicircles that in the order of increasing frequency are attributed to the Nernst diffusion within the electrolyte, the electron transfer at the oxide/electrolyte interface and the redox reaction at the platinum counter electrode. From applying appropriate equivalent circuits, the transport rate

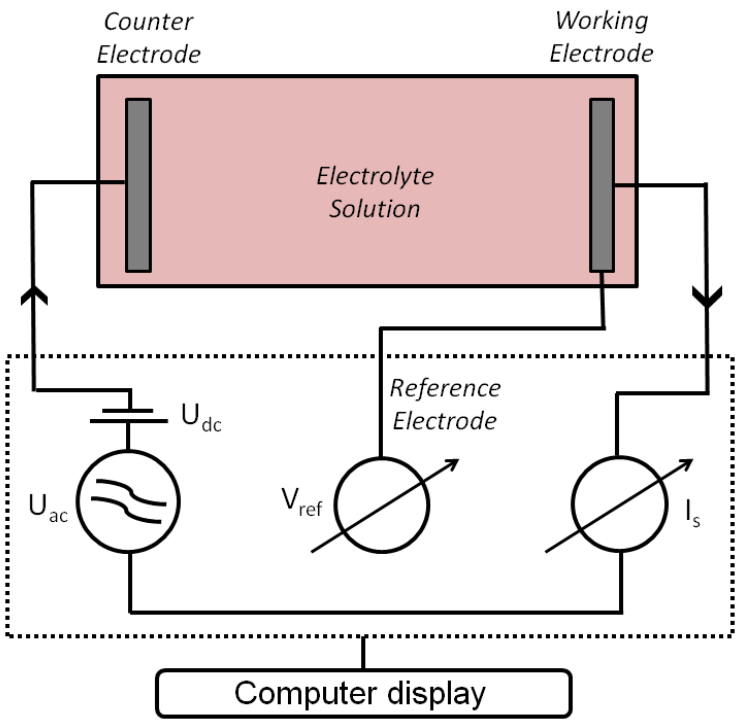

Figure 3.15. *Schematic diagram of a simplified measurement circuit for performing Electrochemical Impedance Spectroscopy (EIS).*

and lifetime of the electron in the mesoscopic film are derived. Electrochemical impedance spectroscopy (EIS) were performed on an electrochemical workstation CHI650E (CH instruments) with a frequency range from 100 kHz to 0.1 Hz in the open circuit condition. The schematic presentation of the EIS set up is shown in Figure 3.15. All impedance measurements were carried out under a bias illumination of 100mW/cm^2. The obtained spectra were fitted using the CHI650E software in terms of appropriate equivalent circuits.

3.1.15. Photovoltage Decay Measurements: Photovoltage decay measurements were carried out after illuminating the cells under 1 Sun condition. The photovoltage decays after switching off the irradiation were monitored by an oscilloscope (Owon) through computer interface as shown in Figure 3.16. The decays were fitted with exponential decay functions using Origin software.

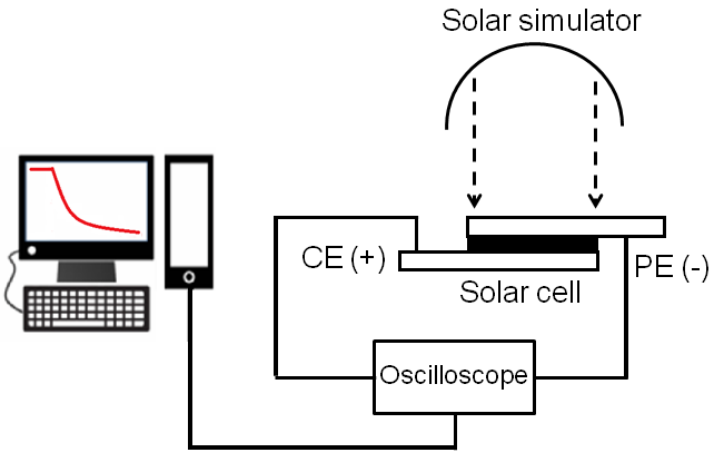

Figure 3.16. *Schematic diagram of the photovoltage decay measurement setup.*

3.1.16. Light Source Used for Irradiation: For red light activated experiments, a red light-emitting diode (LED) source (λ_{max} = 640 nm and power = 3 mW/cm^2) was used. A UV light source (LED) of 390 nm – 400 nm was used to irradiate samples under UV-blue light source.

3.2. Sample Preparation: In this section the different sample preparation methods have been discussed.

3.2.1. Chemicals Used: The chemicals and spectroscopic probes were procured from the following sources. Analytical-grade chemicals were used for synthesis without further purification. Deionized (DI) water, obtained from Millipore, was used to prepare all aqueous solutions. The probes DPPH (Sigma Aldrich), 2-methyl imidazole (Sigma Aldrich), dichloro-fuorescin diacetate (Calbiochem), benzoquinone (Alfa Aesar) and the dyes squaraine (Solaronix, Switzerland), curcumin (Sigma Aldrich), psoralen (Sigma Aldrich), crystal violet (Sigma Aldrich), DCM (Exciton, USA), protein bovine pancreatic α-chymotrypsin (CHT) (Sigma Aldrich) and L-α-phosphatidylcholin (PC) from soybean (Sigma Aldrich) were used without any further purification. ZnO NPs (~ 30 nm) was purchased from Sigma Aldrich.

3.2.2. Synthesis of Metallo–curcumin Complexes: The complex was synthesized by mixing methanolic solution of curcumin with metal salts (zinc acetate, copper acetate or mercury nitrate) at a molar ratio of 1: 1 [2]. 50 mL of 2 mM methanolic solution of curcumin was prepared and heated at 60°C for dissolution. Metal salts (2 mmol) were dissolved in 100 mL methanol by heating. The solution was added into the curcumin solution and an immediate precipitation was produced. The mixture was refluxed for 2 h at 180°C. The solid product was filtered and washed firstly by cold methanol and then by water to remove the residue reactants. The purified product was dried in vacuum overnight. The final appearance of the Zn product was red powder and dark brown crystalline for Cu. The synthesized metal curcumin complexes are kept in dark under closed vessels until further use.

3.2.3. Synthesis of Cu(II)–curcumin Complex from Zn(II)– curcumin Complex: The synthesized Zn(II)–curcumin complex was dissolved in water by using successive cyclo-mixing and bath-sonication for 3 h. The solution was centrifuged at 5000 rpm for 5 min and the supernatant (orangish-red) solution was separated. An aqueous solution of $CuCl_2.2H_2O$ was added to the collected supernatant solution and vortexed for 2 h. A brown solution was generated [3].

3.2.4. Synthesis of Cu/ZIF-8 and Cur@Cu/ZIF-8: Cu Zn (2-methyl imidazolate)$_2$ or Cu/ZIF-8 nanocrystals were prepared by doping the Cu^{2+} ions in a one-step reaction conducted with 25 and 10% Cu^{2+} by weight of Zn^{2+}. The doping percentages are chosen based on the previously reported results of Cu/ZIF-8 synthesis [4]. As higher dopant percentages (around 50%) reportedly cause complete structural collapse of ZIF-8, we optimized the Cu to Zn ratio (in the synthesis reaction) at 25%. The synthesis procedure was conducted through a facile and simple route following a one-pot synthesis procedure. In a typical synthesis, metal and ligand solutions were prepared separately in the same volume of methanol. To prepare the metal solution, 131.6 mg $Zn(NO_3)_2$, $6H_2O$ and 32.9 mg $Cu(OAc)_2$, H_2O (higher doping percentage) and 131.6 mg $Zn(NO_3)_2$, $6H_2O$ and 13.2 $Cu(OAc)_2$, H_2O (lower doping percentage) were dissolved in 5 ml methanol. Ligand solution was prepared by dissolving 292 mg Hmim separately in 5 ml methanol. The two solutions were mixed in a three-neck round bottom flask and the synthesis was carried out under N_2 flow at room temperature under stirring condition for 1 h. The resultant solid products were separated by centrifuging (at 4000 rpm, 3 min), washed three times with methanol to remove excess Hmim, dried overnight at room temperature. A pale-brownish colored powder (Cu/ ZIF-8) was formed. As a control experiment, ZIF-8 nanocrystals were synthesized under the same condition using the previously reported colloidal chemistry synthesis route [5]. 10 mg Cu/ZIF-8 was mixed with a methanol solution of curcumin (prepared by adding 1 mg curcumin in 5 ml methanol) and stirred overnight. The product was centrifuged (4000 rpm, 3 min), washed three times to remove free curcumin, dried at room temperature and stored in closed vials. Subsequently, 10 mg of as-synthesized ZIF-8 crystals were mixed with 5 ml methanol solution of curcumin and stirred overnight at room temperature. The reaction conditions were optimized with respect to reaction time and the weight ratio of curcumin to Cu/ZIF-8 to realize maximum drug loading efficiency.

3.2.5. Synthesis of ZnO Nanorods (NRs): Zinc acetate dihydrate, $Zn(CH_3COO)_2$ $2H_2O$ (Merck), zinc nitrate hexahydrate, $Zn(NO_3)_2$, $6H_2O$ (Sigma-Aldrich), hexamethylenetetramine, and $C_6H_{12}N_4$ (Aldrich) were used as the starting materials for a low temperature hydrothermal synthesis of ZnO NRs on FTO substrates. Detailed processes for the hydrothermal growth of single-crystal ZnO NRs are described in our previous reports [6]. In brief, a ZnO seed layer was initially deposited on cleaned glass substrates by the spray-pyrolysis method at 100 ^{0}C using 10 mM zinc acetate solution in isopropanol. The seeded glass substrates were then annealed in air at 350^{0}C for 5 h and used for the hydrothermal growth of the ZnO NRs. An aqueous solution of zinc nitrate (20 mM) and hexamethylenetetramine (20 mM) was used as the precursor solution for the ZnO NR growth, which was carried out at 90^{0}C for 40 h. This led to the growth of ZnO NRs with a length of approximately 2–3 µm and diameter of 80–100 nm. To maintain a constant growth rate of the ZnO NRs during the hydrothermal process, the old precursor solution was replaced with a fresh solution every 1 h [7]. The as-obtained ZnO NR samples were then taken out of the reaction vessel and rinsed thoroughly with DI water to remove unreacted residues. Finally, the samples were annealed in air at 350 ^{0}C for 1 h prior to the study.

3.2.6. Electrochemical Deposition of Cur and M–Cur Complexes on ZnO NRs: A stock solution of 1 mM Cur and 1 mM M–Cur was prepared in DMSO and complete dissolution of the solid was ensured by subsequent cyclo-mixing and sonication. 200 mL of the stock solution of Cur or M–Cur is added into 50 mL phosphate buffer solution (PBS) containing 5 g of KCl. To this solution, FTO plate with the grown ZnO NR was dipped, which acts as the working electrode. A Pt counter electrode was used with an Ag/Ag+ reference couple. The dipped solution was electrochemically deposited applying an open circuit potential method using a potential range of -2 to +2 volts for a time window of 4 h with consecutive monitoring of the deposition by cyclic voltammetry (CV) initially and at an interval

of 2 h. Finally, after 4 h of deposition, the plates were taken out of the solution, washed with PBS several times and analyzed using CV and spectroscopic methods [8].

3.2.7. Synthesis of PSO- and DCM-Containing Ethosomes: PSO and DCM were completely soluble in ethanol, and their concentrations were estimated from known extinction coefficients. 5 mg of PC was dissolved in 40 µL of an ethanolic solution of PSO or DCM and injected rapidly in warm water (~40 °C) followed by vigorous stirring. The solution was filtered through a 0.22 µm syringe filter (MillexGP, USA).

3.2.8. Synthesis of Photochromic Dihydroindolizine (DHI): The photochromic DHI was synthesized by the electrophilic addition of electron-deficient spiro-cyclopropenes through the nitrogen atom of the N-heterocyclic pyridazines in dry ether in the absence of light under nitrogen atmosphere for 24 h [9]. The final photochromic DHI was obtained as pale yellow crystals after recrystallization from the proper solvent. Pure products were obtained after purification by column chromatography on silica gel using dichloromethane as eluent [10].

3.2.9. Preparation of Protein-DHI (CHT-DHI) Solution: Enzyme-DHI solutions were prepared by adding a requisite amount of DHI to the enzyme solution with stirring for 2 h. To ensure complete complexation of DHI with the enzyme, the DHI concentration was kept much lower (20µM) than the CHT concentration (100µM). For energy transfer studies, the probes (NPA and PF; 20 µM concentration) were added to the CHT-DHI solution and stirred for 2h. For the enzymatic activity studies, the enzyme concentration was 5 µM in all cases, and the concentration of the substrate AMC was 125µM [11].

3.2.10. Preparation of SQ-Sensitized ZnO Nanohybrids: The nanohybrids were prepared using overnight incubation of 0.5 mM SQ with ZnO NPs under dark conditions. After the sensitization process, the solution was centrifuged and washed

with DMSO four times to separate any unattached dye. The nanohybrid was then dried in an oven and stored in the dark until further use.

3.2.11. Synthesis of ZIF-8 and ZIF8-SQ: ZIF-8 nanocrystals were prepared following the previously reported room temperature sol-gel method [12]. In brief, 3.44 mg of zinc nitrate and 81 mg Hmim were dissolved in 5 mL methanol separately. After complete dissolution, ligand was added to metal ion solution under stirring condition and kept for 24 hr in standing condition. The precipitates were collected by centrifugation followed by washing with methanol and dried at room temperature. 10 mg of prepared ZIF-8 was added to 0.5 mM SQ solution using DMSO as the solvent and stirred overnight followed by centrifugation, washing and drying. Synthesized ZIF8-SQ were kept in dark under closed environment until further use.

3.2.12. Determination of Antioxidant Property: DPPH degradation kinetics under dark conditions was monitored using spectrophotometer and data were collected at 3 min interval for a total time-window of 30 min. DPPH has a characteristic absorbance maximum at 520 nm. The decrease in this characteristic absorption peak of DPPH was chosen to monitor degradation. Finally, the DPPH absorbance at 520 nm was plotted as a function of time.

3.2.13. Preparation of Dichlorofluorescein and ROS Measurements: DCFH was prepared from DCFH-DA (dichlorofluorescin diacetate obtained from Calbiochem) by mixing 0.5 mL of 1.0 mM DCFH-DA in methanol with 2.0 mL of 0.01 N NaOH. This deesterification of DCFH-DA proceeded at room temperature for 30 min and the mixture was then neutralized with 10 mL of 25 mM NaH_2PO_4, pH 7.4. This solution was kept on ice in the dark until use. All the measurements were performed in a total volume of 2.0 mL water that contained 10 µL of DCFH solution, dye, ZnO dye-ZnO (individual concentrations of dye and ZnO in the nanohybrid are same).

3.2.14. Bacterial Strain and Culture Conditions: The viable count assay was performed with *E. coli* XL1-Blue cells. The cells were cultured at 37°C in a liquid Luria–Bertani (LB) medium. When the optical density reached 0.5, the inoculum was serially diluted one lakhs times with the LB medium. Samples of curcumin, Cu(II)–curcumin, Cu(II)-acetate dihydrate and DMSO were added to the diluted culture and incubated for 6 h in dark. The amount of curcumin in Cu(II)–curcumin sample was quantified from the absorption spectra after baseline correction and the absorbance at 430 nm was kept at 0.1 for each samples. The cultures were plated on LB agar plate, and the colonies were counted after overnight incubation. In another case also, ZIF-8, Cu/ZIF-8, Cur@ZIF-8 and Cur@Cu/ZIF-8 were evaluated for antimicrobial effect in a similar manner [13].

3.2.15. Development of Bacterial Biofilms: *E. coli* and *S. aureus* biofilms were cultured in their prescribed media (LB and liquid grade 3 medium, respectively) on 60 mm polycarbonate Petri dishes. Two milliliters of bacterial inoculum with an optical density of 0.8 was spread on the Petri dishes and incubated for 2 days at 37°C. Quantification of the biofilms was done using CV [0.1% (w/v)] staining after washing the attached cells. Briefly, unattached cells were aspirated from the Petri dishes, which were subsequently washed with 1 mL of water. CV solution (2 mL) was added to the dishes and removed after 30 min by aspiration. Petri dishes were washed with 1 mL of water, and the remaining CV was solubilized in 95% ethanol. The degree of CV staining was evaluated from the absorbance at 595 nm (A_{595}). A_{595} values are considered to be an index of bacteria adherence to the polycarbonate surface and forming a biofilm. To study the morphological changes in the biofilms upon different treatment conditions, 200 µL of the respective bacterial broth was kept over coverslips for 24 h at 37 °C, followed by washing in water. The samples were fixed with 2.5% glutaraldehyde followed by successive dehydration in alcohol and air. A qualitative assessment of the appearance of the biofilms was performed

by scanning electron microscopy. The coverslips were coated with gold and scanned in a field emission scanning electron microscope [14].

3.2.16. Cytotoxicity Assay: The MTT assay was used to check the biocompatibility of the ZnO-SQ nanohybrid. MG-63 cells were grown in Dulbecco's modified Eagle's medium (DMEM; HiMedia) supplemented with 10% fetal bovine serum (FBS; Gibco) and 1.0% penicillin/streptomycin (HiMedia) and cultured at 37°C, 5.0% CO_2, and 95% humidity [15]. These cells (1.0×10^4) were seeded in each well of a 96-well plate and cultured in 10% FBS-supplemented DMEM. The cells were incubated with various concentrations of ZnO-SQ (0−300 nM wrt SQ) for 2 h. The media have been changed with fresh media to remove excess particles, and cells were exposed to the red LED source for 30 min. After 24 h of incubation, the MTT assay was performed using an MTT assay kit (CCK003, Himedia) following the manufacture's instruction.

3.2.17. Hemolysis Assay: The hemolysis assay was performed on human RBCs. Ethylenediaminetetraacetate stabilized human whole blood was centrifuged five times and redispersed in 10 mL of phosphate-buffered saline (PBS) buffer. Then, 0.1 mL of RBC solution was mixed with variable concentrations of nanohybrids [16]. The samples were incubated at 37°C and 100 rpm for 30 min, and then the mixture was centrifuged at 5000 rpm for 5 min. The absorption of the supernatant solution was measured at 570 nm. RBCs incubated with PBS and 1% Triton X-100 were used as negative and positive controls, respectively. All sets were prepared in triplicate. The hemolysis percentage was calculated following the reported equation.

3.2.18. Propidium Iodide Staining Assay: *S. aureus* (1×10^8) cells were treated with 140 nM ZnO-SQ nanohybrid in the dark at 37 °C and 300 rpm for 3 h. Then, bacterial solutions were divided into two parts and one part was exposed to red light. After the treatment, samples were incubated with 2 µM PI for 15 min in the dark. The samples (10 µL) were observed under a fluorescence microscope [16].

3.2.19. Internalization of Nanohybrids into Bacterial Cells by TEM Observations: The nanohybrid-treated bacterial solution was applied to a carbon-coated Cu grid. After settlement of the solution in the grid, cells were stained with 2 µL of 1% uranyl acetate for 1 min. It was observed using a FEI Technai S-Twin microscope with an accelerating voltage of 200 kV.

3.2.20. Fabrication of a Photovoltaic Device for Photocurrent Measurements: Photocurrent measurements were carried out in a photovoltaic device set up under 1 sun condition. The platinum (Pt) nanoparticles were deposited on the FTO substrates via thermal decomposition of 5 mM platinum chloride, H_2PtCl_6,H_2O (Sigma-Aldrich) solution in isopropanol at 385°C for 30 min. This is used as the counter electrode. Cur or M–Cur sensitized ZnO NR was used as the active electrodes and the two electrodes were placed on top of each other with a single layered 60 mm thick Surlyn (Solaronix) as a spacer between the two electrodes. Cur and M–Cur solution were deposited on the ZnO NRs following the same electrochemical method. A liquid electrolyte composed of 0.5 M lithium iodide (LiI), 0.05 M iodine (I_2) and 0.5 M 4-tertbutylpyridine (TBP) in acetonitrile was used as the hole conductor and filled in the inter-electrode space by using capillary force, through two small holes (diameter = 1 mm) pre-drilled on the counter electrode. Finally, the two holes were sealed by using another piece of Surlyn to prevent the leakage of the electrolyte from the cell. In all our experiments, the active area was fixed at 1 cm^2 [8].

3.2.21. Details of Molecular Docking Calculations: The crystal structure of CHT was obtained from the Protein Data Bank (entry code 1YPH). The ligand files were prepared and optimized using the Avogadro software package. All molecular docking simulations of CHT-DHI (cis and trans) were performed with the AutoDock Tools-1.5.6 program. Blind grid computation was performed with a grid box of 126×126×126A with 0.375Å spacing, covering all of the active site residues and allowing rotatable ligand bond flexibility with 10 GA runs, and finally,

terminating after a maximum of 25× 106 energy evaluations. The population size was set to 150 with a crossover rate of 0.8 (Lamarckian Genetic Algorithm). For the site-specific flexible docking, a grid box of 58×62×64A with 0.375Å spacing covering the lowest energy ligand binding site obtained in the blind docking calculation was used, and all other parameters were the same as the earlier blind docking case [17]. The lowest energy conformation in the largest cluster of each docking simulation was extracted and analyzed. The hydrogen bonds and hydrophobic interactions between the ligands and the protein were visualized with Ligplot+ version 1.4.5. The Ligplot images show hydrogen bond interaction in green and hydrophobic interactions in red.

3.2.22. Details of Density Functional Calculations: For density functional calculations, we have used projector augmented wave (PAW) potentials under generalized gradient approximation (GGA) with Perdew–Burke–Ernzerhoff exchange correlation functional as implemented in the Vienna ab initio simulation package (VASP). The plane wave cut-off energy was set to 500 eV. All control and assembled systems are placed in a rectangular box of dimension 30 x 20 x 20 Å, with sufficient vacuum so as to avoid influence from periodic replication. Due to a large volume of the simulation cell for these cluster systems, single *k*-point (Γ point) calculations are performed for these systems with ionic optimization under conjugate gradient algorithm until the Hellmann–Feynmann force on each ion is less than 0.01 eV $Å^{-1}$. van der Waals corrections are incorporated in this calculation using the Grimme DFT-D2 formalism [18].

References

[1] D. O'Connor, Time-correlated single photon counting, Academic Press, 2012.

[2] S. Wanninger, V. Lorenz, A. Subhan, F.T. Edelmann, Metal complexes of curcumin–synthetic strategies, structures and medicinal applications, *Chem. Soc. Rev,* 44 (2015) 4986-5002.

[3] D. Bagchi, S. Chaudhuri, S. Sardar, S. Choudhury, N. Polley, P. Lemmens, S.K. Pal, Modulation of stability and functionality of a phyto-antioxidant by weakly interacting metal ions: curcumin in aqueous solution, *RSC Adv,* 5 (2015) 102516-102524.

[4] A. Schejn, A. Aboulaich, L. Balan, V. Falk, J. Lalevée, G. Medjahdi, L. Aranda, K. Mozet, R. Schneider, Cu 2+-doped zeolitic imidazolate frameworks (ZIF-8): efficient and stable catalysts for cycloadditions and condensation reactions, *Catal. Sci. Technol.,* 5 (2015) 1829-1839.

[5] J. Cravillon, S. Mu̇nzer, S.-J. Lohmeier, A. Feldhoff, K. Huber, M. Wiebcke, Rapid room-temperature synthesis and characterization of nanocrystals of a prototypical zeolitic imidazolate framework, *Chem. Mater.,* 21 (2009) 1410-1412.

[6] S. Baruah, J. Dutta, pH-dependent growth of zinc oxide nanorods, *J. Cryst. Growth.,* 311 (2009) 2549-2554.

[7] S. Baruah, J. Dutta, Effect of seeded substrates on hydrothermally grown ZnO nanorods, *J. Sol-Gel Sci. Technol.,* 50 (2009) 456-464.

[8] D. Bagchi, T.K. Maji, S. Sardar, P. Lemmens, C. Bhattacharya, D. Karmakar, S.K. Pal, Sensitized ZnO nanorod assemblies to detect heavy metal contaminated phytomedicines: spectroscopic and simulation studies, *Phys. Chem. Chem. Phys,* 19 (2017) 2503-2513.

[9] H. Dürr, Perspectives in Photochromism: A Novel System Based on the 1, 5-Electrocyclization of Heteroanalogous Pentadienyl Anions, *Angew. Chem.,* 28 (1989) 413-431.

[10] T.B. Shrestha, J. Melin, Y. Liu, O. Dolgounitcheva, V.G. Zakrzewski, M.R. Pokhrel, E. Gogritchiani, J.V. Ortiz, C. Turró, S.H. Bossmann, New insights in the photochromic spiro-dihydroindolizine/betaine-system, *Photochem. Photobiol. Sci.*, 7 (2008) 1449-1456.

[11] D. Banerjee, S.K. Srivastava, S.K. Pal, Spectroscopic Studies on Ligand− Enzyme Interactions: Complexation of α-chymotrypsin with 4,6-Diamidino-2-phenylindole (DAPI), *J. Phys. Chem. B,* 112 (2008) 1828-1833.

[12] K.S. Park, Z. Ni, A.P. Côté, J.Y. Choi, R. Huang, F.J. Uribe-Romo, H.K. Chae, M. O'Keeffe, O.M. Yaghi, Exceptional chemical and thermal stability of zeolitic imidazolate frameworks, *Proc. Natl. Acad. Sci. U.S.A.,* 103 (2006) 10186-10191.

[13] S. Chaudhuri, S. Sardar, D. Bagchi, S. Dutta, S. Debnath, P. Saha, P. Lemmens, S.K. Pal, Photoinduced dynamics and toxicity of a cancer drug in proximity of inorganic nanoparticles under visible light, *ChemPhysChem,* 17 (2016) 270-277.

[14] D. Bagchi, S. Dutta, P. Singh, S. Chaudhuri, S.K. Pal, Essential Dynamics of an Effective Phototherapeutic Drug in a Nanoscopic Delivery Vehicle: Psoralen in Ethosomes for Biofilm Treatment, *ACS Omega,* 2 (2017) 1850-1857.

[15] T.L. Riss, R.A. Moravec, A.L. Niles, S. Duellman, H.A. Benink, T.J. Worzella, L. Minor, Cell viability assays, Eli Lilly & Company and the National Center for Advancing Translational Sciences, 2016.

[16] B. Duncan, X. Li, R.F. Landis, S.T. Kim, A. Gupta, L.-S. Wang, R. Ramanathan, R. Tang, J.A. Boerth, V.M. Rotello, Nanoparticle-stabilized capsules for the treatment of bacterial biofilms, *ACS Nano,* 9 (2015) 7775-7782.

[17] M.F. Sanner, Python: a programming language for software integration and development, *J. Mol. Graph. Model,* 17 (1999) 57-61.

[18] S. Grimme, Semiempirical GGA-type density functional constructed with a long-range dispersion correction, *J. Comput. Chem.,* 27 (2006) 1787-1799.

Chapter 4

Spectroscopic Studies on the Complexation of Various Metal Ions with a Medicinally Important Drug for Enhanced Biological Activity

4.1. Introduction: Natural product drugs play a dominant role in pharmaceutical care. The medicinal use of plant derived compounds or their derivatives are well documented as exemplified by paclitaxel (Taxol®), vincristine (Oncovin®), vinorelbine (Navelbine®), teniposide (Vumon®) etc. often employed in cancer treatment [1]. In this view, curcumin, derived from turmeric (vernacular name: Haldi), is a rhizome of the plant *Curcuma longa* commonly used as a food-coloring agent, spices, food-preservatives or for decoration exhibit lot of medicinal activities [2]. The diverse pharmacological applications of curcumin towards various diseases includes Alzheimer's disease [3], breast cancer [4], pancreatic cancer, colon cancer, arthritis [5] and oxidative stress induced pathogenesis [6]. Furthermore, its promising antioxidant activity anticipates its possible use as a novel drug for other lethal diseases [7]. Curcumin is a linear polyphenol consisting of two o-methoxy phenolic groups which are connected by a seven-carbon linker consisting of an α, β-unsaturated β-diketo moiety (Scheme 4.1.a) [8]. The diketo group exhibits keto-enol tautomerism (Scheme 4.1.b) and can exist in different types of conformers depending on the nature of the solvent [9]. In most of non-polar and moderately polar solvents, the enol form is generally more stable than the keto form by 5 to 8 kcal/mol due to strong intramolecular H-bonding [10]. Curcumin is hydrophobic in nature and almost insoluble in water at physiological pH values [11]. This may be due to the presence of β-diketone linkers in the seven-carbon chain. This leads to poor bio-availability, limited absorption in body, rapid metabolism and excretion [12]. Therefore, it is an important task to improve the

bio-availability and solubility of curcumin in water in order to further exploit its medicinal benefits.

To overcome the problem of low bioavailability of curcumin, several methods have been proposed including conjugation to water-soluble polymers or encapsulation in colloidal carriers such as gold nanoparticles, and polymer nanoparticles [13, 14]. Recent report suggests that the introduction of dimethyl-amino-methyl group as substituents on aromatic rings in curcumin improves their aqueous solubility as the basic nitrogen atom will be responsible for converting the target compounds into the salt forms [15]. Another efficient strategy to improve the bioavailability of curcumin is the formation of complexes with transition metal ions, such as Zn^{2+}, Cu^{2+}, Mn^{2+} and Fe^{2+} which attract interest in the contemporary literature [16]. Some of these complexes are of much higher stability compare to free curcumin. Curcumin acts as a monobasic bidentate ligand in which the α, β-unsaturated β-diketo moiety acts as a chelating agent for complexation with metal ions [17]. Moreover, the stability of curcumin is increased by a factor of 20 after its complexation with Zn (II) ions at a buffer pH of 7.0 [18]. Stable metallo-curcumin complexes are useful in a dual manner: firstly, the complexations increase the drug solubility and can also act as new metal-based antioxidants which reduce the cytotoxicity of metal ions [19]. Moreover, complexation of curcumin to palladium (II) metal centre and its conjugation to another functionalized bioactive ligand, significantly enhance cell-death in prostate cancer cell line through apoptosis signal transduction route due to increased aqueous solubility and hence indicate the possibility of use of metallo-curcumin complexes as potential metal based anti-cancer drugs [20]. Recent studies reveal that deprotonation of the hydroxyl group in the keto-enol moiety leads to the formation of a bidentate β-diketonate which strongly chelates with transitional metal ions namely Cu (II) and Zn (II) in two different square planer geometries forming 1:1 and 1:2 complexes respectively (Scheme 4.1.c) [21].

Among the different metal bound complexes of curcumin, Zn (II) and Cu (II) complexes received immense importance for their diverse biological applications. The latest studies have shown that the Cu (II) and curcumin interaction may be important for its anti-cancer [22] and anti-amyloid properties [23]. It has also been reported that due to the reversible electron transfer reactions with superoxide ions, Cu (II) complexes of curcumin can act as superoxide dismutase enzyme mimics [24]. Zn(II)-curcumin complexes show anti-cancer, gastro-protective and antidepressant effects and are also very much effective for oxidative stress reduction [25]. These metallo-curcumin complexes are receiving increasing attentions due to their enhanced antioxidant activity. However, the complexes can induce DNA damage due to binding and consequently showing pro-oxidant activity [26]. Therefore, detailed mechanistic investigation of activity of metal complexes is needed. Moreover, both the aqueous solubility and stability are not profoundly altered for a particular metallo-curcumin complex and an alternative approach is required.

In the first work of this chapter, we have synthesized and optically characterized two metallo-curcumin complexes of Zn (II) and Cu (II). Femtosecond resolved fluorescence transient studies of the complexes have clearly depicted the key time components associated with the excited state electron transfer dynamics. The role of metal ions in antioxidant activity of the complex is evaluated in detail using well-known radical scavenger 2,2-diphenyl-1-picrylhydrazyl (DPPH) for aqueous media in dark condition. Herein, we suggest a new method for both increasing aqueous solubility by incorporation of Zn (II) and then to enhance the activity, where the metal ion can effectively be altered by Cu (II). Thus, we propose a novel approach in which both stability for storage and activity prior to use can be achieved in aqueous solvent. We have also used the active Cu-curcumin complex in a model bacteriological culture experiment to evaluate the effect of the synthesized complex as an antimicrobial agent. Our

studies on ROS marker including dichlorofluorescin (DCFH) in aqueous solution is in consonance with the antibacterial activity of the complex. This study clearly indicates the mechanism of higher free-radical scavenging activity by incorporation of Cu (II) ions in curcumin followed by its action as an antimicrobial agent. The newly suggested method to first increase the water solubility by incorporation of Zn (II) and then replacing it by Cu (II) for higher activity of the metallo-curcumin complex might be useful in future for further *in-vivo* experiments.

However, one single platform incorporating both Zn (II) and Cu (II) ions is the ideal candidate to improve both bioavailability and functionalities of curcumin improving real application. Metal-organic frameworks (MOFs), a class of porous hybrid materials comprised of metal ions and organic bridging ligands, are regarded widely for their exceptionally high surface area, tunable pore structure, and controllable surface functionalities [27, 28]. MOFs show great potential for sensing [29], adsorption [30], separation of gases [31], catalysis [32], and are also emerging as a powerful platform for the controlled release of therapeutic drugs [33, 34]. Zeolitic imidazolate frameworks (ZIFs) are a subclass of MOFs composed of divalent metal ions linked by imidazolate linkers in a tetrahedral framework of multitudes of structures, topologies, and pore matrices [35, 36]. The 3D structural network of ZIF with interconnected pores serves as an ideal template for synthesis of metal-doped composites. Specifically, ZIF-8, consisting of zinc (Zn) metal ions tetrahedrally coordinated with nitrogen atoms of 2-methyl imidazole (Hmim) linkers, are known to exhibit remarkably large surface area (Langmuir surface area = 1,810 m^2/g), high porosity (diameter of largest cavity ~11.6 Å), exceptional thermal (upto 550 ^oC) and chemical stability, and pH-sensitive behavior [37, 38]. ZIF-8 is hydrothermally almost as stable as a covalent solid which makes it an outstanding candidate for applications in natural systems involving ubiquitous presence of water molecules [39]. Previous studies have demonstrated the use of

ZIF-8 as a stimuli-responsive delivery system for a model anticancer drug doxorubicin (DOX) [40]. It was also demonstrated in some recent reports that loading of phytomedicines as curcumin onto ZIF-8 increases its chemical stability [41, 42]. While these studies suggest the use of ZIF systems for increasing aqueous stability and cellular uptake of curcumin, amplification of both stability and functionality in a single drug delivery system has not been considered.

This motivates the other work in this chapter where we have explored the possibility of chelation of a therapeutic drug through more than one transitional metal ions by using a hetero-metallic ZIF-8, i.e., $Cu_{0.25}Zn_{0.75}$(2-methyl imidazolate)$_2$ system as a drug carrier. Cu^{2+} ions were doped into ZIF-8 at two different doping percentages, i.e., 10% and 25% by weight of Zn^{2+} in a one-step synthesis procedure at room temperature. The as-synthesized Cu (II) doped ZIF-8 (Cu/ZIF-8) was loaded with curcumin post-synthetically following a facile route under mild conditions at room temperature. The as-synthesized mixed metal-organic hybrid was characterized using electron microscopic and diffraction methods. Steady and time-resolved fluorescence spectroscopic methods were employed to confirm molecular cross-talking. The water-stability and *in vitro* ROS generation by Cur@Cu/ZIF-8, was evaluated using UV-Visible spectroscopic methods and DCFH oxidation assay respectively. Finally, the efficacy of Cur@Cu/ZIF-8 was explored for its antibacterial application and ability to eradicate mature bacterial biofilms.

4.2. Results and Discussion:

4.2.1. Modulation of Stability and Functionality of a Phyto-antioxidant by Weakly Interacting Metal Ions: Curcumin in Aqueous Solution [43]: Metalation of organic ligands causes significant changes in their electronic structures. UV-visible spectroscopy is a useful technique to understand the complexation due to

metalation. Figure 4.1.b shows the absorption maxima of

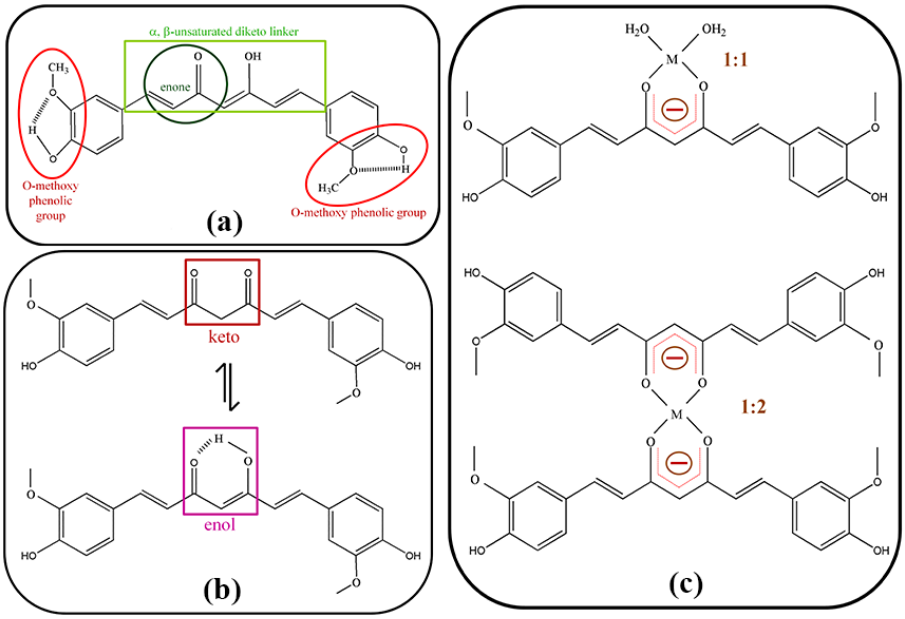

Scheme 4.1. *(a) Structure of curcumin (b) Keto–enol tautomerism of curcumin (c) Structure of metallo–curcumin complexes.*

curcumin at 422 nm with a shoulder at 348 nm in water. The absorption peak can be attributed to electronic transition typically a π-π* in nature from (HOMO) to (LUMO) and (HOMO-1) to (LUMO) respectively [44]. With extensively delocalized π-electrons curcumin exhibits a bright yellow color (Figure 4.1.a). After successful attachment of a metal ion to curcumin, a distinct red shift is observed in the absorption spectra. For the Zn(II)-curcumin, a sharp peak was observed at 440 nm, with a small peak at 485 nm. The dark brown Cu(II)-curcumin complex shows more prominent red shift with a broad peak at 512 nm. The red shift may be correlated with the formation of a new, lower energy charge-transfer state by electronic transition from the ligand curcumin to the metal ions. The delocalized π-electron density over the ligand curcumin moiety behaves as a donor to positively charged metal centres with empty d-orbitals behaving as an acceptor, exhibiting a ligand to metal charge transfer band (LMCT) [45]. The extent of interaction can be explained on the basis of number of d-electrons

present in the system. Zn(II) having a filled d-orbital shows lower interactions compared to Cu(II), a d^9 system which is prone to be involved in LMCT due to the presence of low-lying empty d orbitals [46].

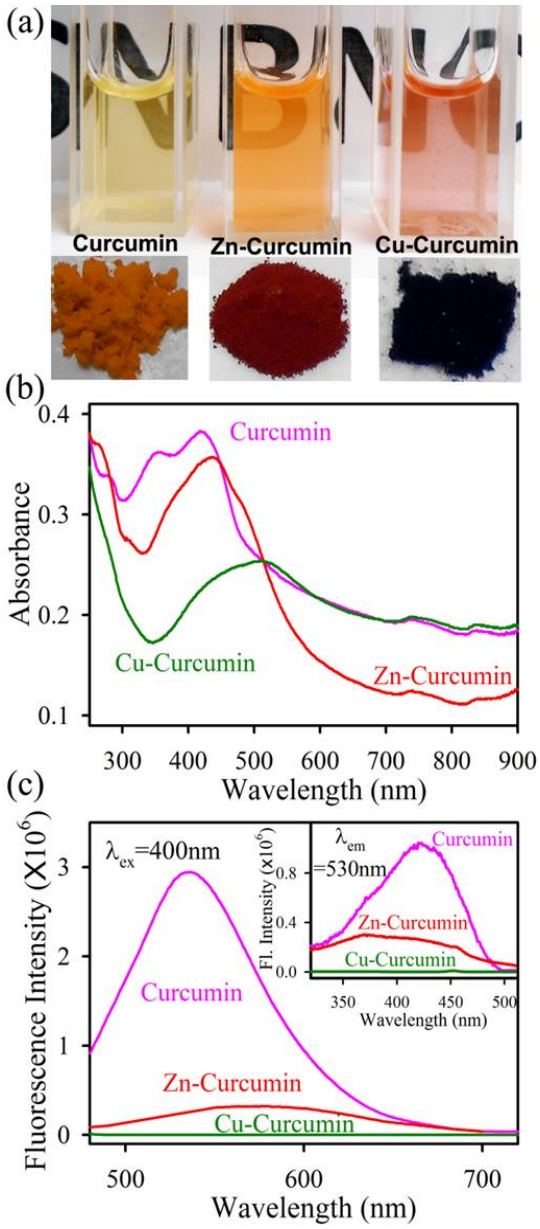

Figure 4.1. *(a) Photographs of Curcumin, Zn-Curcumin and Cu-Curcumin in water under visible light (b) Absorption spectra of Curcumin (pink), Zn-Curcumin (red), Cu-Curcumin (green) (c) Room temperature emission spectra of Curcumin (pink), Zn-Curcumin (red) and Cu-Curcumin (green) in water are shown. The excitation wavelength was at 400 nm. Inset shows excitation spectra of Curcumin (pink), Zn-Curcumin (red) and Cu-Curcumin (green).*

Moreover, Figure 4.1.b demonstrates curcumin and its metal complexes show extended absorbance in near infra-red region. The room temperature PL spectra (Figure 4.1.c) of curcumin depict a peak at 530 nm upon excitation at 400 nm. However, after metalation with Zn (II) and Cu (II), steady-state emission was significantly decreased although the corresponding absorbance of these solution are similar. This indicates involvement of non-radiative processes. The inset of Figure 4.1.c shows excitation spectra of all the samples and a clear quenching is observed. The significant quenching in both emission and excitation spectra suggest internal quenching due to complexation.

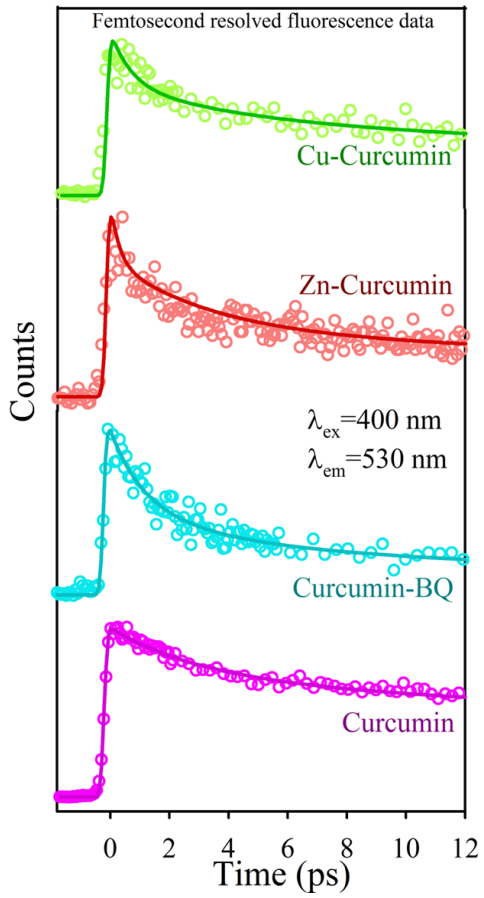

Figure 4.2. *Femtosecond resolved fluorescence transients of Curcumin (pink), Curcumin-BQ (cyan), Zn-Curcumin (red) and Cu-Curcumin (green) in DMSO. Excitation wavelength was at 400 nm and detection wavelength was at 530 nm. The circles are experimental data, and the solid lines are best multiexponential fit.*

Femtosecond resolved fluorescence decay transients of metallo-curcumin samples have been collected to understand the excited state interaction between metal and curcumin. The decay of curcumin was monitored at 530 nm upon excitation at 400 nm, in absence and presence of Cu (II) and Zn (II) in DMSO. The decay profiles are shown in Figure 4.2. The fluorescence transient of curcumin is fitted with biexponential decay with lifetime of 3.2 ps (shorter component: signature of solvation dynamics) and 73.5 ps (longer component: indication for excited state intramolecular H atom transfer ESIHT) [47], with an average lifetime of 50.4 ps. The decay profile of curcumin in presence of Cu (II) and Zn (II) show shorter time component of 0.7 ps with an average lifetime of 30.8 ps and 23.0 ps, respectively. The shorter excited state lifetime for Cu (II)-curcumin and Zn (II)-curcumin suggest the photoinduced electron-transfer process from curcumin to metal ions. In order to confirm the electron migration process, well-known electron acceptor benzoquinone (BQ) has been attached to curcumin. The possible excited state interaction in curcumin-BQ was monitored and the electron transfer timescale (~0.7 ps) was found to be similar to that of metallo-curcumin samples.

Table 4.1. *Femtosecond resolved fluorescence transient data of Curcumin and Metallo-Curcumin Samples*[a]

Sample	τ_1 (ps)	τ_2 (ps)	τ_3 (ps)	τ_{avg} (ps)
Curcumin	-	3.2 (32.8%)	73.5 (67.2%)	50.4
Cu-Curcumin	0.7 (35.5%)	5.0 (25.5%)	75.0 (39.0)	30.8
Zn-Curcumin	0.7 (52.6%)	7.5 (20.5%)	78.9 (26.9%)	23.0
Curcumin-BQ	0.7 (45.5%)	5.0 (38.9%)	75.0 (15.6%)	14.0

[a]*The emission (monitored at 530 nm) was detected with 400 nm laser excitation. Numbers in parentheses indicate relative contributions.*

It has to be noted that BQ attached curcumin structure might not be similar to that of metallo curcumin complexes, but excited state electron transfer timescale is similar due to proximity between two entities in both the cases. Thus, the shorter timescale in presence of metal ions can be rationalized as an electron transfer from

curcumin to the attached metal ion. The lifetime components of transients with their relative percentages are presented in a tabular form (Table 4.1).

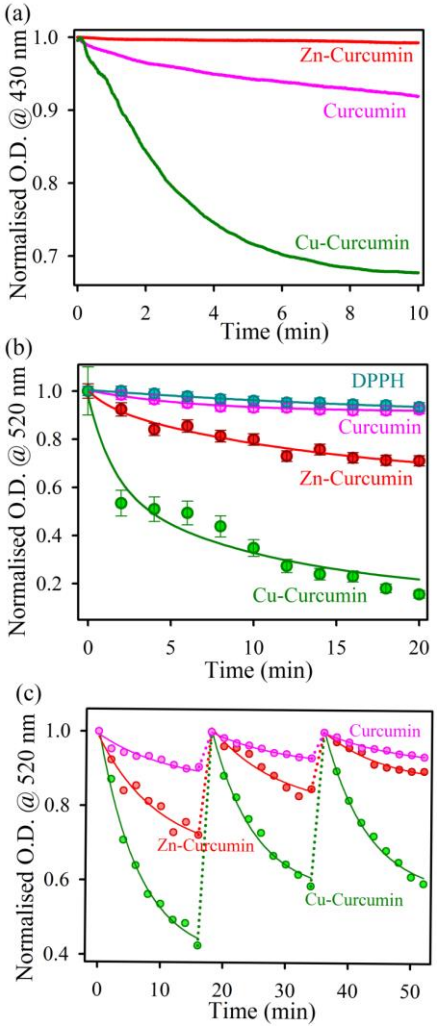

Figure 4.3. *(a) Stability of Curcumin (pink), Zn-Curcumin (red) and Cu-Curcumin (green) from absorbance at 430 nm in water at 10 mins time-window (b) Depicts the absorption kinetics of DPPH degradation (monitored at 520 nm) in presence of Curcumin (pink), Zn-Curcumin (red) and Cu-Curcumin (green) under stirring condition. The circles are experimental data and the solid lines represent the best biexponential fit with 10% error bar (c) Cycling curves of DPPH degradation (monitored at 520 nm) in presence of Curcumin (pink), Zn-Curcumin (red) and Cu-Curcumin (green) under stirring condition.*

The analysis regarding the stability and antioxidant activity of metallo-curcumin complexes in bio-compatible solvent water is essential for application purposes. In this regard, the UV-Vis peak maxima at 430 nm for curcumin in the presence and absence of metal ions were monitored in kinetic mode for 10 mins

(Figure 4.3.a) to establish aqueous stability of the complexes. All the solutions under consideration are clear and there is no scattering effect. Zn(II)-curcumin complex shows maximum stability followed by curcumin whereas Cu(II)-curcumin solution shows lowest stability. Figure 4.3.b demonstrates antioxidant activity of curcumin and metallo-curcumin complexes in dark under stirring condition. Antioxidant activities of the samples are monitored by the decolorization kinetics of stable free radical 2,2-diphenyl-1-picrylhydrazyl (DPPH) in ethanol-water mixture [48]. DPPH, a violet colored radical is reduced to $DPPH_2$ which is yellow in color due to donation of an H-atom from the polyphenolic antioxidant to the radical [49]. The absorbance of all the samples is maintained to 0.1 at 430 nm and DPPH is added in such a manner so that the absorbance at 520 nm becomes 0.5 just after addition of DPPH which is much higher compared to self-absorption of the complexes at that particular wavelength. Moreover, the assays were performed under stirring conditions which suggest that there is no decrease in absorbance due to precipitation of the complexes. The free radical quenching kinetics data have been fitted with biexponential decay functions. The time constants are calculated to be 46.5 min, 38.5 min and 6.5 min for curcumin, Zn(II)-curcumin and Cu(II)-curcumin, respectively (Table 4.2). The increase in the radical scavenging activity for metallo-curcumin samples is clearly evident from Figure 4.3.b. The enhanced anti-oxidant property for Cu(II)-curcumin can be attributed to weaker ArO-H bond present in o-methoxy phenolic group (red circled in Scheme 4.1.a) and a consequent easier H-atom loss process. Due to the presence of stronger O-H bond in case of Zn(II) complex, the radical scavenging activity is many folds lesser compared to Cu(II)-complex. Furthermore, to confirm the reusability of the highly active radical scavenger Cu(II)-curcumin, recycling experiments have been performed. Three consecutive cycles were conducted (Figure 4.3.c) which show that the rate of radical scavenging remains almost constant indicating the high activity of Cu(II)-curcumin. Moreover, curcumin and Zn(II)-curcumin complex did not produce any such recyclability. This observation

suggests that only for Cu(II)-curcumin complex, radical scavenging activity become rejuvenated after each cycle. Figure 4.3.c depicts that in the first cycle, the

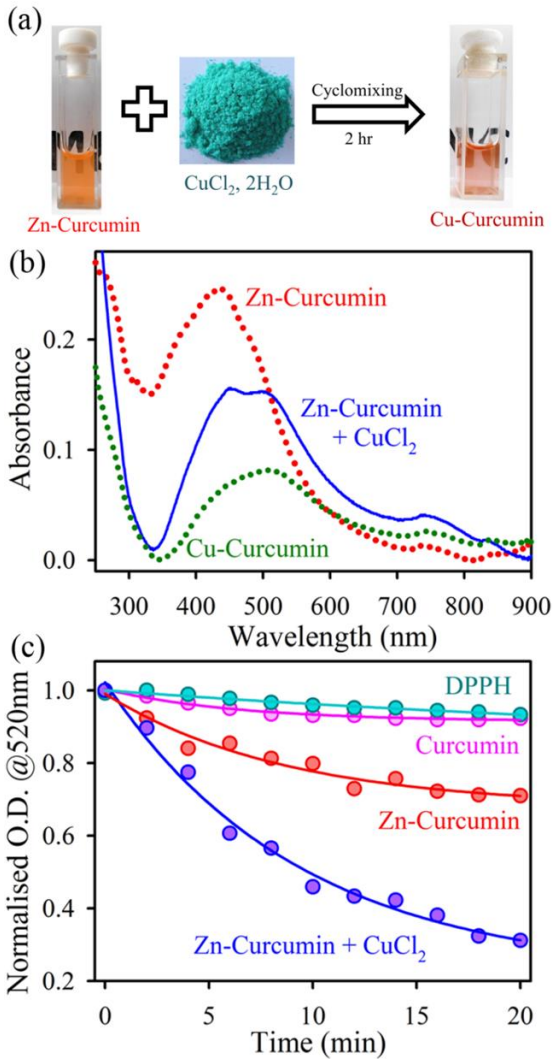

Figure 4.4. *(a) Pictorial representation of Cu replacement in Zn-Curcumin which leads to formation of Cu-Curcumin. (b) Absorption spectra of Zn-Curcumin (red dotted), Cu-Curcumin (green dotted) and Zn-Curcumin+$CuCl_2$ (blue solid line) (c) shows the kinetics of DPPH degradation (monitored at 520 nm) in presence of Curcumin (pink), Zn-Curcumin (red) and Zn-Curcumin+$CuCl_2$ (blue) under stirring condition.*

scavenging activity (57% DPPH degradation) is obtained in the presence of a very small amount of Cu(II)-curcumin (OD at 430 nm=0.1), and the degradation become 41% after third cycle. The time constants are shown in Table 4.3. The

results demonstrate that Cu(II)-curcumin serve as a highly effective recyclable free-radical scavenger than Zn(II)-curcumin and curcumin in water.

From Figure 4.3, it is clear that Zn(II)-curcumin complex is more stable in water whereas the less stable Cu(II)-curcumin is more active. In order to clarify this issue, an alternative approach is followed. Before using as an antioxidant more stable Zn-curcumin should be kept for greater aqueous stability and then addition of $CuCl_2.2H_2O$ followed by vortex for 2hr can replace Zn(II) by Cu(II) which eventually enhances the activity. Figure 4.4.a illustrate the visible color change by addition of $CuCl_2.2H_2O$ in Zn(II)-complex from orange to brown, indicating formation of Cu(II)-complex. Figure 4.4.b shows the UV-Vis spectra of Zn-curcumin after addition of $CuCl_2$ solution, which is distinctly different from Zn(II)-curcumin and $CuCl_2.2H_2O$ (data not shown) and more likely to the absorbance spectra of Cu(II)-curcumin complex. To evaluate the antioxidant properties, DPPH degradation kinetics was monitored. Figure 4.4.c indicates that there is a clear increase in antioxidant property compared to Zn-curcumin and $CuCl_2.2H_2O$ (data not shown). The time constant is calculated to be 8.3 min (fitted with biexponential function) for the complex which is comparable to that of

Table 4.2. *Time-constants for DPPH degradation in presence of Curcumin and Metallo-Curcumin samples*[b]

Sample	t_1 (min.)	t_2 (min.)	t_{avg} (min.)
DPPH	30.0 (25%)	75.0 (75%)	63.8
Curcumin	4.7 (36%)	70.0 (64%)	46.5
Zn-Curcumin	4.1 (25%)	50.0 (75%)	38.5
Cu-Curcumin	1.5 (46%)	10.8 (54%)	6.5
Zn-Curcumin+$CuCl_2$	6.3 (27%)	9.1 (73%)	8.3

[b] *Numbers in parentheses indicate relative contributions.*

Cu(II)-curcumin (Table 4.2). This result is in agreement with the fact that Cu(II) has higher affinity for complexation than Zn(II), due to d-electron density distribution. Altogether, Figure 4.4 suggests a simple methodology for both the

enhancement of aqueous stability and antioxidant property in metallo-curcumin complexes.

In the view to investigate the anti-microbial action, highly active Cu(II)-curcumin was used as a potential antibacterial agent in dark for the inhibition of growth of *Escherichia coli (E. coli)*. The upper panel of Figure 4.5 shows picture of *E. coli* cultures treated with DMSO, $Cu(OAc)_2.H_2O$, curcumin and Cu(II)-curcumin in dark. The inhibition in growth of the bacterial culture for Cu(II)-complex is clearly visible. The culture treated with Cu(II)-curcumin complex contains a smaller number of colonies with respect to the control samples and cultures containing curcumin and $Cu(OAc)_2$. In control and $Cu(OAc)_2$ treated samples, the colony forming units (CFU) are almost similar. In case of curcumin treated samples, the bacterial growth was inhibited to 35% whereas maximum inhibition is obtained for Cu(II)-curcumin treated samples. The decrease of CFU is 60%.

Table 4.3. *DPPH degradation efficiency data for cycling curves in presence of Curcumin and Metallo-Curcumin samples*[c]

Sample	Cycle	Efficiency			
		t_1 (min.)	t_2 (min.)	t_{avg} (min.)	Degradation percentage (%)
Curcumin	1st	6.8 (28.6%)	70.0 (71.4%)	52.0	11.0
	2nd	7.8 (29.4%)	70.5 (70.6%)	52.1	7.0
	3rd	6.5 (28.6%)	71 (71.4%)	52.6	6.0
Zn-curcumin	1st	4.6 (26.0%)	50.3 (74.0%)	38.5	28.0
	2nd	33.7 (80.4%)	45.1 (19.6%)	36.0	15.0
	3rd	4.1 (18.0%)	51.0 (82.0%)	42.6	10.0
Cu-curcumin	1st	6.6 (50.0%)	6.6 (50.0%)	6.6	57.0
	2nd	6.9 (5.0%)	9.9 (95.0%)	9.8	41.0
	3rd	9.0 (50.0%)	9.0 (50.0%)	9.1	41.0

[c]*Numbers in parentheses indicate relative contributions.*

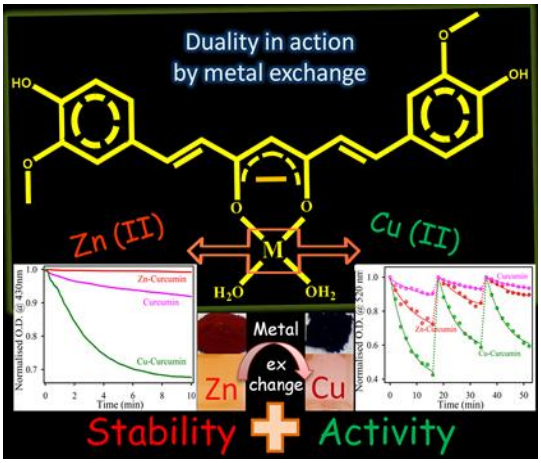

Scheme 4.2: *Schematic representation of metal exchange process leading to duality in action: enhancement of both aqueous stability and anti-oxidant property.*

In order to explain the detailed mechanistic view of both antioxidant and antimicrobial action of Cu(II)-curcumin complex, the ROS generation was investigated directly by dichlorofluorescin-dichlorofluorecein (DCFH-DCF) conversion in aqueous medium. Nonfluorescent DCFH is a well-known ROS marker, which is oxidized to fluorescent DCF in presence of ROS [50]. The emission intensity at 520nm of DCF was monitored with time to evaluate the extent of ROS generation. Figure 4.6.a shows that there is maximum increase in fluorescence intensity in presence of Cu(II)-curcumin complex. Moreover, no significant enhancement of fluorescence intensity was observed for both curcumin and its Zn(II) complex. To confirm the ROS generation, H_2O_2, which is a proper electron acceptor can act as a source of $OH^{\bullet}$ radical was added to the system. This results in a huge enhancement of fluorescence intensity in case of the Cu(II)-curcumin complex (Figure 4.6.b). The enhancement of ROS formation can be anticipated with the chain reaction in presence of H_2O_2 [51]. The antioxidant effect of ROS generator Cu(II)-curcumin can be explained by the fact that the ROS influence the activity of electron releasing substituents present in the phenolic anti-oxidant like Cu(II)-curcumin (ArOH). This results in breaking of the O-H

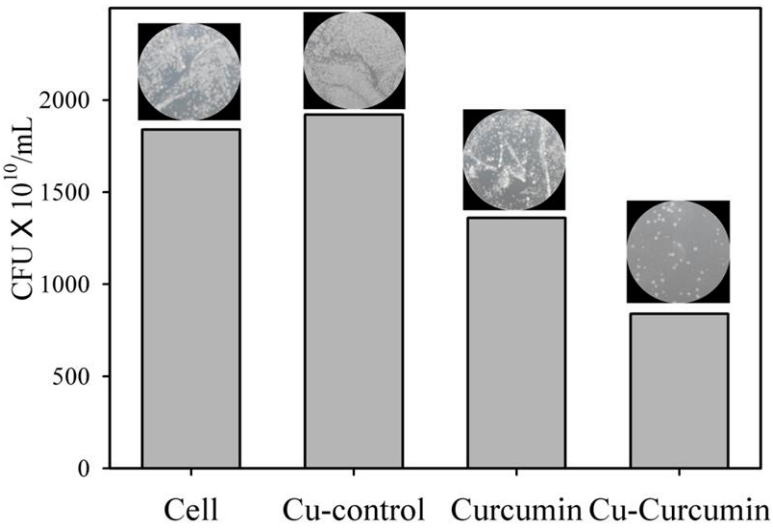

Figure 4.5. *Bacteriological assay of Cell, Cu-control, Curcumin and Cu-Curcumin in dark. The upper panel shows images of E. coli plates in presence of the corresponding samples.*

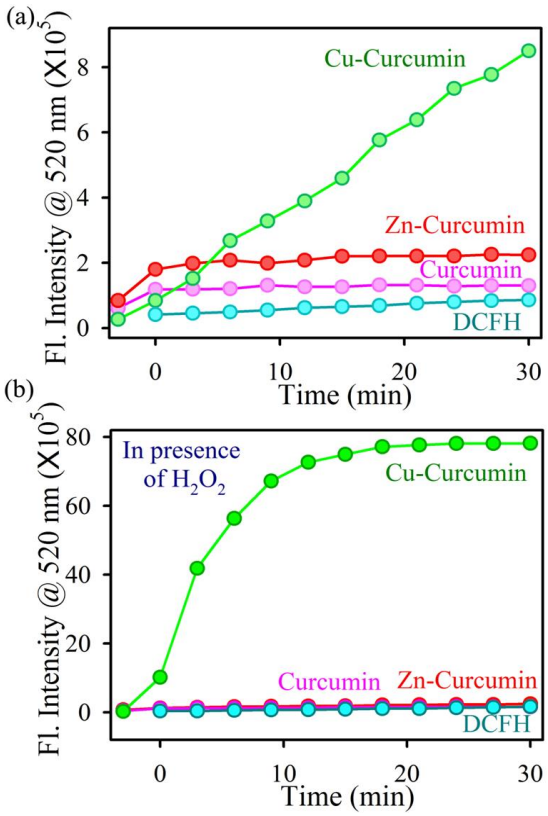

Figure 4.6. *(a) The DCFH oxidation (monitored at 520 nm) with time in presence of Curcumin (pink), Zn-Curcumin (red) and Cu-Curcumin (green) and DCFH only (cyan) in water under dark condition. The excitation was at 488 nm (b) The DCFH oxidation in presence of H_2O_2(monitored at 520 nm) with the samples of Curcumin (pink), Zn-Curcumin (red) and Cu-Curcumin (green) and DCFH only (cyan) in water under dark condition. The excitation was at 488 nm.*

bond and release of hydrogen radical as reported in the earlier literature [52]. The hydrogen radicals can react with nucleophilic free-radicals like DPPH and quench their activity as shown in the following equation:

$$ArOH + X^{\cdot} = ArO^{\cdot} + XH \ (X^{\cdot} = DPPH^{\cdot}) \qquad (4.1)$$

Thus Cu(II)-curcumin can act as a ROS generator as well as the by- product during ROS generation ($H^{\cdot}$) can quench the free radicals to show antioxidant activity.

4.2.2. Bimetallic Zeolitic Imidazolate Framework as an Active Excipient of Curcumin under Physiological Condition [53]: The fabrication strategy to synthesize bimetallic ZIF followed by curcumin loading into its pores are shown in Scheme 4.3.

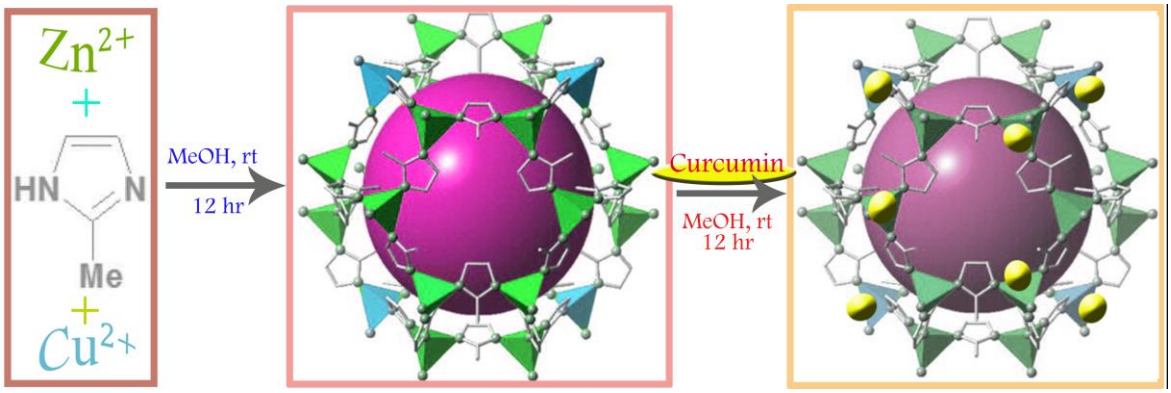

Scheme 4.3. *Fabrication strategy of the synthesis of Cu/ZIF-8 and Cur@Cu/ZIF-8.*

Transmission electron microscopy (TEM) and scanning electron microscopy (SEM) were used for the characterization of $Cu_{0.25}$ $Zn_{0.75}$ (2-methyl imidazolate)$_2$ and $Cu_{0.1}$ $Zn_{0.9}$ (2-methyl imidazolate)$_2$ nanocrystals which were prepared by doping ZIF-8 with Cu^{2+} at 10 and 25% by weight of Zn^{2+}. TEM and SEM results revealed the size and morphology of Cu^{2+} doped ZIF-8 crystals as uniform rhombic dodecahedral shaped crystals with an average diameter of 0.4 µm (Figure. 4.7.a and b). To investigate the chemical composition of Cu/ZIF-8, we performed Energy Filtered TEM (EFTEM) mapping analysis [54] of ZIF-8 doped at the percentages of 25%. The EFTEM map of a single crystal of Cu/ZIF-8 (Figure 4.7.c)

depicts the distribution of Zn^{2+} and Cu^{2+} ions throughout the crystal. Quantitative analyses of Zn and Cu L shell maps obtained using the Energy dispersive X-ray (EDX) elemental mapping analysis shows that the concentration of Cu in the crystal is slightly less than the respective doping percentages used for the synthesis (the Cu^{2+} doping percentages in the crystals were 3.6 and 11.5% for reactions conducted with 10 and 25% Cu^{2+}, respectively). The same disparity between the ratio of Cu/Zn in the Cu/ZIF-8 crystal and the ratio used in the synthesis, was reported previously. Next, we selected ZIF-8 doped by Cu^{2+} at 25% by weight of Zn for further experiments. The drug curcumin was loaded, and the structural characterization of the resultant product was estimated. TEM and SEM images showed that the sizes of Cu/ZIF-8 crystals were not altered significantly by the loading of curcumin molecules (Figure 4.7.d and e). Also, XRD patterns of the

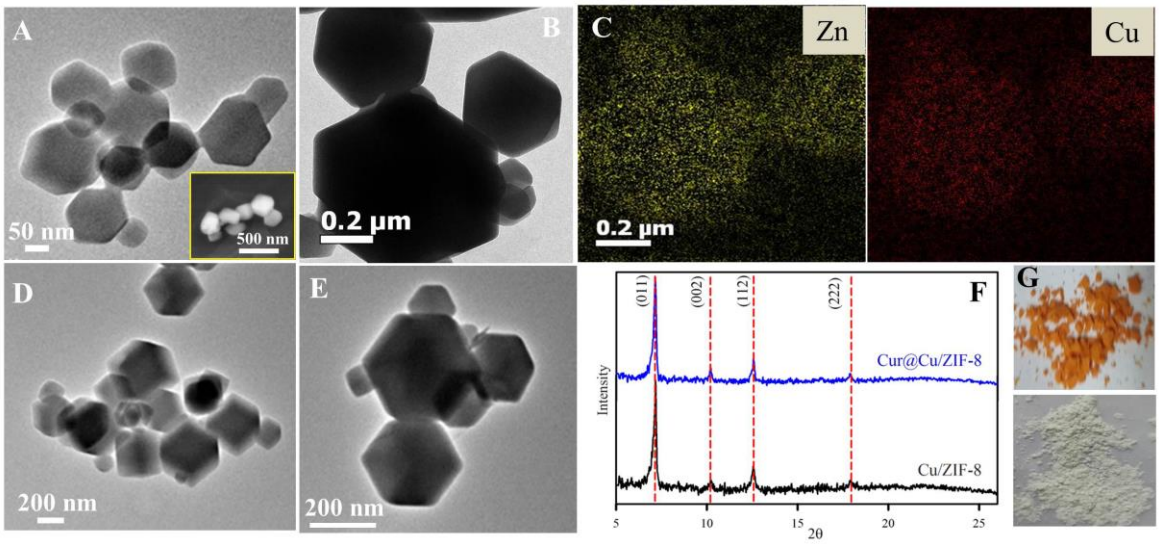

Figure 4.7. *(a) TEM images of Cu/ZIF-8 NPs. Inset shows SEM images of Cu/ZIF-8 (b) TEM images of Cu/ZIF-8 NPs of a particular area (c) EFTEM compositional analysis of Cu/ZIF-8 NPs (d) & (e) TEM images of Cur@Cu/ZIF-8 (f) PXRD patterns of Cu/ZIF-8 (black line) and Cur@Cu/ZIF-8 (blue line). (g) Photographs of Cur@Cu/ZIF-8 and Cu/ZIF-8 NPs.*

powdered samples of Cu/ZIF-8 recorded pre-and post-loading with curcumin as shown in Figure 4.7.f, depicted no change in the diffraction patterns. Moreover,

the recorded PXRD patterns demonstrate that the products are single phase materials [55] with sharp diffraction peaks indicative of high crystallinity of Cu/ZIF-8. A visible color change of Cu/ZIF-8 was observed after curcumin loading (Figure 4.7.g). To re-confirm the structural integrity of ZIF after Cu^{2+} doping, we analyzed the structural properties of ZIF-8 as a control of Cu/ZIF-8 and Cur@ZIF-8 as a control of Cur@Cu/ZIF-8.

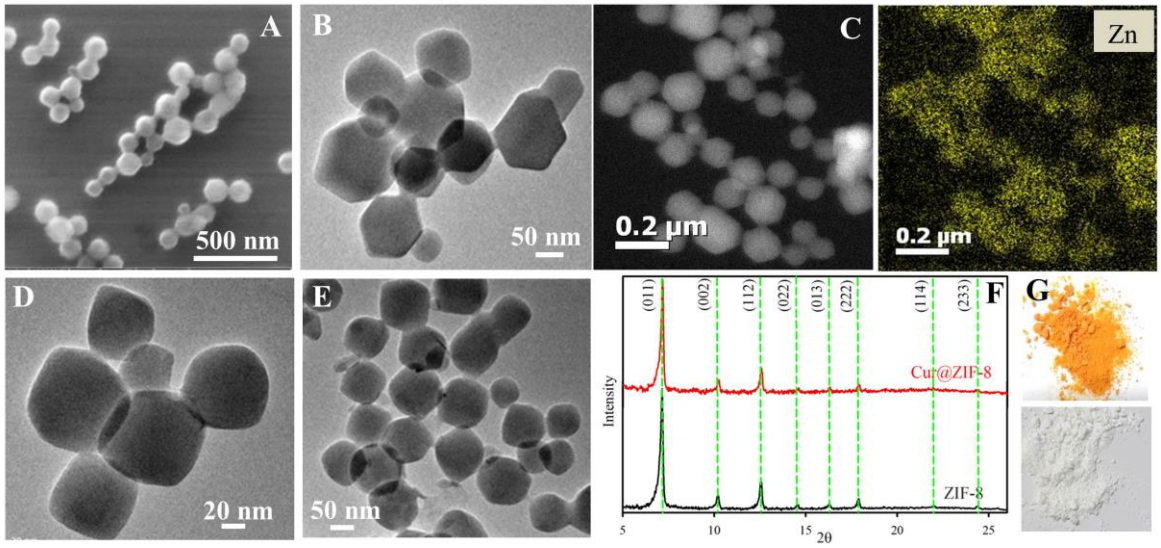

Figure 4.8. *(a) SEM image of ZIF-8 NPs, (b) TEM image of ZIF-8 NPs (c) EFTEM compositional analysis of ZIF-8 NPs (d) & (e) TEM image of Cur@ZIF-8 (f) PXRD patterns of ZIF-8 (black line) and Cur@ZIF-8 (red line). (g) Photographs of Cur@ZIF-8 and ZIF-8 NPs.*

ZIF-8 nanocrystals with an average diameter of 0.1 µm were synthesized via previously reported mild and facile colloidal chemistry route. Comparison of the SEM images depicted that the size of the ZIF-8 nanocrystals was inflated after the inclusion of Cu^{2+} ions (Figure. 4.8.a). We attribute this phenomenon to the disparity between the rate of nucleation and growth of ZIF and Cu/ZIF-8 crystals [56]. SEM and TEM images (Figure 4.8.a and b) show typical rhombic dodecahedron shape of ZIF-8 and EFTEM composition analysis shows uniform distribution of Zn^{2+} (Figure 4.8.c). However, after curcumin loading, there was a change in sharp edges of ZIF-8 which was not present in Cu/ZIF-8 system (Figure 4.8.d and e). The PXRD pattern shows no perturbation of crystal structure of ZIF-8

after curcumin loading (Figure 4.8.f). This implies greater structural stability of ZIF-8 after Cu^{2+} doping. Similar to Cu/ZIF-8, there was a visible change in the color of ZIF-8 after curcumin loading (Figure 4.8.g).

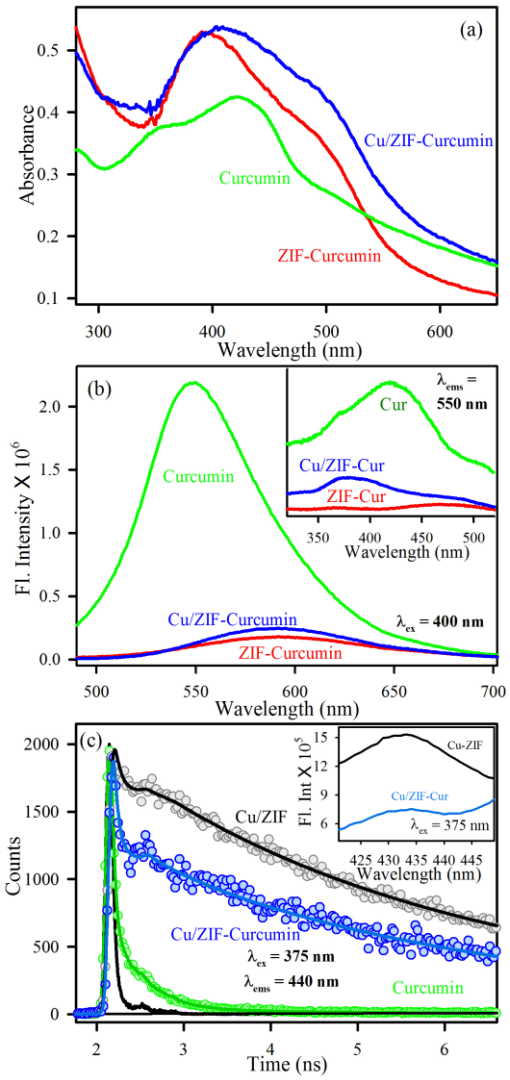

Figure 4.9. *(a) UV-Visible absorption spectra of Cur (green line), Cur@ZIF-8 (red line), Cur@Cu/ZIF-8 (blue line) (b) Fluorescence spectra of Curcumin (green line), Cur@ZIF-8 (red line), Cur@Cu/ZIF-8 (blue line). The excitation wavelength was 400 nm. Inset shows the excitation spectra (λ_{em} = 590 nm) of Cur (green line), Cur@ZIF-8 (red line), Cur@Cu/ZIF-8 (blue line) (c) Picosecond-resolved fluorescence transients of Cu/ZIF-8 (excited at 375 nm) in the absence (grey) and presence (blue) of Curcumin collected at 440 nm.*

The UV-Visible absorption spectra of free curcumin in aqueous media, as shown in Figure 4.9.a, comprises of two absorption bands, one centered at 422 nm and another relatively weak band at 348 nm. These two peaks can be attributed to

π-π* electronic transition from HOMO to LUMO and (HOMO-1) to LUMO, respectively. Post-attachment of curcumin to Cu/ZIF-8 crystals, a distinct red shift in its absorption maxima was observed, indicating metalation of curcumin molecules. The red shift may be assigned to the electronic transition from curcumin moiety with extensively delocalized π-electrons serving as a donor to the metal acceptors with partially empty d orbitals. Earlier reports suggested that the ZIF-8-curcumin attachment occurs only through surface adsorption process [42]. However, the significant red shift of the absorption maxima of curcumin post-attachment to ZIF clearly indicates a covalent type of interaction between curcumin and ZIF moiety. So, we confirm the nature of interaction as M-curcumin covalent bond formation with or without surface adsorption. To reconfirm this interaction, we used steady state and time-resolved fluorescence spectroscopic methods. The room temperature photoluminescence (PL) spectrum of free curcumin in Figure 4.9.b shows a peak at 530 nm upon excitation at 400 nm. After metalation with Zn^{2+} and Cu^{2+} in Cu/ZIF-8, a red shift in the emission band of curcumin was observed with a considerable decrease in its intensity. Given the similarity of their corresponding absorbance spectra, this quenching phenomenon suggests internal quenching due to metalation of curcumin molecule. Excitation spectra (Figure 4.9.b (inset)) was also recorded by selecting a particular emission wavelength (i.e., 550 nm) showing a similar pattern of quenching as observed in emission spectra.

We analyzed the intrinsic emission property of Cu/ZIF-8 after excitation with 375 nm laser source. It shows emission maxima at 430 nm which showed significant quenching after curcumin encapsulation. However, time-resolved fluorescence lifetime study revealed the presence of a faster decay component in Cu/ZIF-8 than ZIF-8. The fitting parameters listed in Table 4.4 after exponential fitting depicts the presence of a 45 ps component in Cu/ZIF-8 which is much faster than that of ZIF-8 (100 ps). Thus, we anticipate internal charge transfer between Zn^{2+} (featuring d^{10} electronic configuration) to vacant d orbital of Cu^{2+} (a

d^9 system) inside the secondary building unit (SBU) of Cu/ZIF-8. According to

Table 4.4. *Dynamics of picosecond-resolved luminescence transients* [d]

Systems (ex-375-ems-440)	τ_1 (ps)	τ_2 (ps)	τ_3 (ps)	τ_{avg} (ps)
ZIF-8	100 (27.1%)	1620 (17.4%)	5587 (55.5%)	3410.3
Cu/ZIF-8	45 (48.5%)	1620 (5.2%)	4484 (46.3%)	2183.1
Cur@ZIF-8	40 (59.8%)	2000 (7.04%)	4635 (33.1%)	1701.5
Cur@Cu/ZIF-8	25 (80%)	1620 (6.4%)	5414 (13.6%)	861.8

[d] *Numbers in parentheses indicate relative weights.*

previous computational chemistry study of bimetallic MOFs, such inter-metallic charge transfer processes are favorable between pair of cations of similar sizes [57]. ZIFs are characterized by fast recombination of charge carriers and weak absorption due to intra-linker excitation and the presence of redox inactive Zn^{2+}, respectively [58]. This situation gets reversed in Cu/ZIF-8 because Cu introduces empty 3d levels above the LUMO levels of ZIF facilitating the intermetallic-charge transfer and the presence of Cu^{II}/Cu^{I} redox pair facilitates light absorption. Next, we studied the fluorescence quenching behavior of Cur@Cu/ZIF system with respect to Cu/ZIF-8 (Figure 4.9.c). The steady state quenching is depicted in inset of Figure 4.9.c. There is a significant quenching in excited state lifetime of Cu/ZIF-8 after attachment with curcumin. Note that the average transient lifetime of free curcumin is very fast (~50 ps). So, we recorded the time-resolved fluorescence decay of free curcumin and found that it was much faster compared to Cur@Cu/ZIF-8. Hence, we attribute the faster fluorescence transient lifetime of Cur@Cu/ZIF-8 to the charge transfer process between Cu/ZIF and curcumin. This confirms greater interaction of curcumin with Cu^{2+} doped ZIF-8 system in which the empty d orbitals of Cu^{2+} ions interact with delocalized π-orbitals of curcumin. Moreover, the interaction of Cu^{2+} with keto-enol group of curcumin is much stable compared to Zn^{2+}. Our time-resolved data also suggests more covalent type of interaction between Cu/ZIF-8 and curcumin molecules. This also suggests surface adsorption followed by covalent linking or, 'molecular cross-talking' between Cu/ZIF-8 with ligand curcumin.

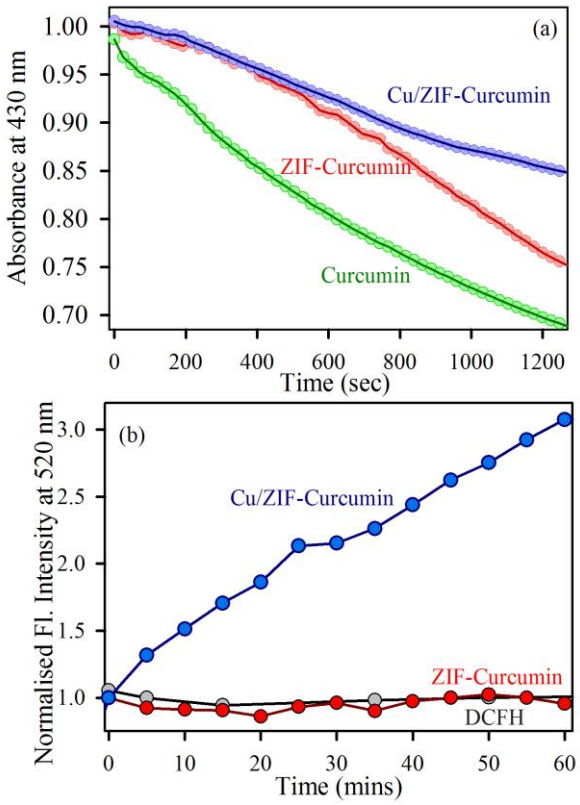

Figure 4.10. *(a) Aqueous Stability of Cur (green line), Cur@ZIF-8 (red line), Cur@Cu/ZIF-8 (blue line) (b) DCFH oxidation with time in presence of Cur@ZIF-8 (red line) and Cur@Cu/ZIF-8 (blue line) monitored through the emission intensity at 520 nm. The excitation was at 488 nm.*

Having characterized the Cur@Cu/ZIF-8 using microscopic and spectroscopic tools, we evaluated its potential as an active excipient under physiologically relevant condition. Comparison of the water-stability kinetics of Cur@Cu/ZIF-8 *versus* free curcumin was carried out by monitoring the UV-Vis absorption maxima at 430 nm for 10 mins. The stability curves were fitted with single exponential decay. Figure 4.10.a shows the stability curves of Cur@Cu/ZIF-8, Cur@ZIF-8, and free curcumin. They clearly demonstrate that the maximum stability of curcumin was attained *via* attachment to Cu/ZIF-8 crystals. The facilitated metal-curcumin interaction as observed from Cur@Cu/ZIF-8 might be a plausible reason for the observed increase in water stability. Also, the inherent stability of Cu/ZIF-8 system might also have contributed to the overall stability of Cur@Cu/ZIF-8 system. The drug loading capacity (DLC) and loading efficiency (DLE) of Cu/ZIF-8 were evaluated by monitoring the characteristic absorption

peak of curcumin at ~430 nm. The DLC and DLE of Cu/ZIF-8 were determined to be 22% and 83%. Such high DLC is crucial for therapeutic applications. Moreover, Cu/ZIF-8 increased the generation of ROS by several orders of magnitude relative to free curcumin (Figure 4.10.b). Generation of ROS depends on the tendencies of metals on peripheral O-H bond breaking and the subsequent release of singlet oxygen and hydrogen radical. For ZIF-8, only Zn^{2+} (d^{10}) interacts with curcumin and thus the tendency for peripheral O-H bond breaking is less, whereas in Cur@Cu/ZIF-8 system, both Zn^{2+} and Cu^{2+} interact with the keto enol group with additional possibility of bidentate binding. So, the breaking of peripheral O-H bond is easier in Cur@Cu/ZIF-8 systems. Figure 4.10.b depicts almost three times increase in ROS generation compared to Cur@ZIF-8.

Finally, we have employed Cur, ZIF-8, Cu/ZIF-8, Cur@ZIF-8 and Cur@Cu/ZIF-8 systems to check their anti-bacterial property. Figure 4.11.a depicts significant reduction in the number of colonies for the Cur@Cu/ZIF-8 treated samples compare to control (without any treatment) and Cur or Cur@ZIF-8 treated samples. The pristine ZIF-8 and Cu/ZIF-8 samples show no effects as shown in Figure 4.11.a. There is almost ten times reduction in number of colonies after treating with Cur@Cu/ZIF-8 sample. The enhanced ROS generation by the Cur@Cu/ZIF-8 samples are mainly responsible for the improved antibacterial effects. Then, we performed the dose dependent antibacterial effects for the Cur@Cu/ZIF-8 samples. It suggests that the doses C_1 (2.5 μM Cur), C_2 (2 μM Cur), C_3 (1.5 μM Cur) are highly effective (Figure 4.11.b). The bacterial mortality rate is lesser for lower doses as C_4 (1.0 μM Cur), C_5 (0.5 μM Cur), C_6 (0.25 μM Cur) but there is a significant effect compared to control cells in all the above concentrations. The reported IC_{50} value of curcumin is 15.9 μM [59] suggesting much greater activity of Cur@Cu/ZIF-8 at sufficiently lower concentration range. The high efficacy of Cur@Cu/ZIF-8 as an antibacterial agent motivates us to check its anti-biofilm effect.

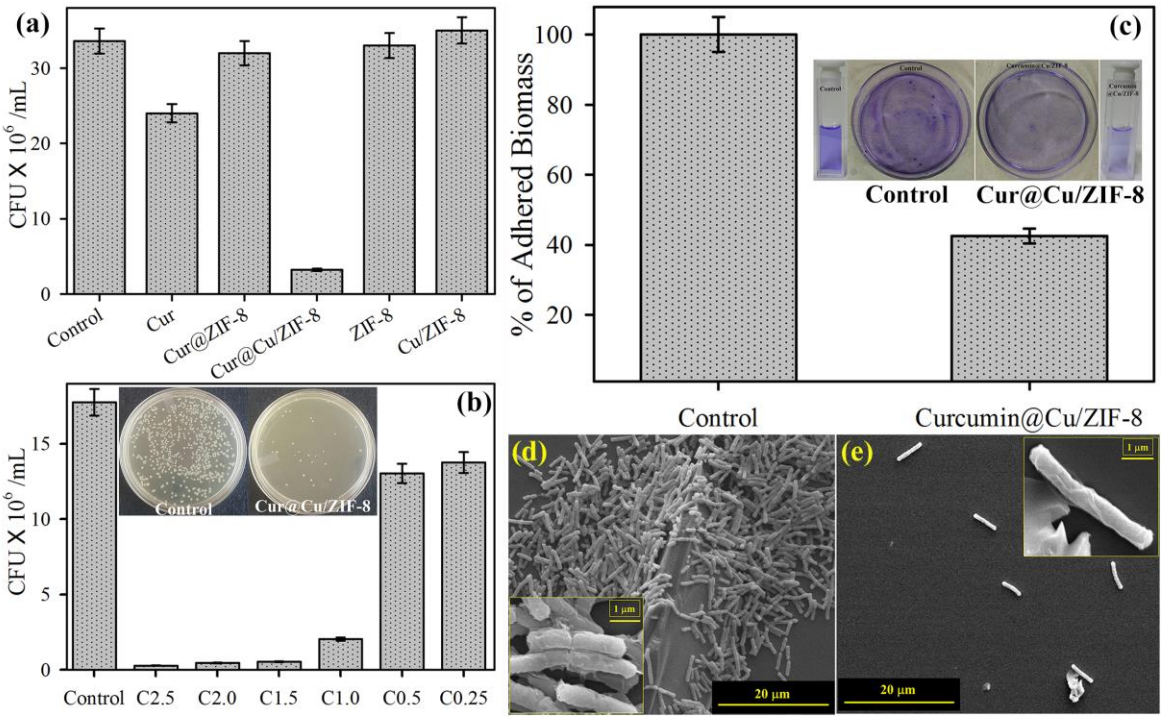

Figure 4.11. *(a) Bacterial viability after treatment with Cur, ZIF-8, Cu/ZIF-8, Cur@ZIF-8 and Cur@Cu/ZIF-8 tested in E. coli (b) The dose dependent antibacterial effect of Cur@Cu/ZIF-8 at curcumin concentrations ranging from 2.5 µM to 0.25 µM on E. coli. Upper panel depicts images of culture plates without treatment and after treatment with Cur@Cu-ZIF-8 (c) Adhesion efficiency of Cur@Cu/ZIF-8 treated E. coli biofilms. Inset shows visible colour change of crystal violet staining for biofilms without any treatment and treated with Cur@Cu/ZIF-8. SEM images of an E. coli biofilms (d) without treatment and (e) treated with Cur@Cu/ZIF-8. Inset shows magnified images of biofilms for clear visualization of surface of the biofilms.*

Biofims are communical structure of bacteria that form on living or non-living surfaces and remain protected by a slimy matrix of extracellular polymeric substances (EPS) [60]. Thus, we have employed the hybrid material for its potential anti-biofilm effects. Figure 4.11.c shows almost 60% decrease in adherent biomass after the Cur@Cu/ZIF-8 treatment as suggested by the CV staining assay. To unravel the structural and morphological changes in bacterial biofilm, SEM images were recorded. The typical communicable structure is seen in control set of *E. coli* in Figure 4.11.d. The inset shows magnified images of biofilms consisting of typical EPS. The number of bacteria, their adherence and the collective structure is completely lost (Figure 4.11.e) after Cur@Cu/ZIF-8 treatment. The zoomed image at the inset depicts complete distortion of typical biofilm structure. The

observations all together conclude great efficacy of Cur@Cu/ZIF-8 as an antibacterial and anti-biofilm agent due to its unprecedented ROS generation ability under dark condition.

4.3. Conclusion: In summary, we have synthesized and optically characterized the metallo-curcumin complexes of Cu(II) and Zn(II). The femtosecond resolved upconversion technique confirms excited state electron transfer processes from the ligand curcumin to the metal ions. 2,2-diphenyl-1-picrylhydrazyl (DPPH) assay in dark proved the enhanced antioxidant property of curcumin by incorporation of Cu(II) ion. The rejuvenating antioxidant properties of Cu(II)-curcumin have been illustrated, which reveal recyclability and highly efficient antioxidant property of the complex. Moreover, the complex shows greater antimicrobial effect for the inhibition of *E. coli* growth compared to that of free curcumin. To get more detailed mechanistic view, we performed dichlorofluorescin (DCFH) oxidation, which clearly shows ROS generation is more in case of Cu(II)-curcumin complexes. These results suggest that the presence of ROS induces the O-H bond breaking which is responsible for showing free-radical scavenging activity. Thus, the Cu(II)-curcumin complex behaves both as an anti-oxidant and anti-microbial agent. Moreover, to take care of both the factor of stability and activity of metallo-curcumin complexes, we propose a new method where aqueous stability is enhanced by Zn(II) complex and the activity can be increased by replacing Zn(II) with Cu(II) through a simple route prior to its use. The shift in absorbance spectra clearly demonstrates the replacement of metal ion at the reaction site. We believe that our study will effectively lead to the development of multifunctional, stable metallo-curcumin complexes having excellent potential to be used for *in-vivo* studies and as future medicines.

Additionally, we have illustrated a unique strategy for the co-amplification of bio-availability and functionality of curcumin using Cu^{2+}-doped ZIF-8 as a drug delivery system. We have shown that by incorporating a second transition metal

ion (Cu) in the tetrahedral site of Zn-based ZIF-8, it might be possible to tune its interaction with phenolic antioxidants/drugs, photo-absorption characteristics, recombination of charged carriers, antimicrobial effects, and thus its efficacy for therapeutic purposes. The resulting Cu/ZIF-8 possessed exceptional DLC, DLE, and efficiency against bacterial biofilms. Curcumin loaded onto Cu/ZIF-8 was more easily dispersible in water than free curcumin molecules and also stable in aqueous media. Besides, Cur@Cu/ZIF-8 exhibited a three-fold increase in generation of ROS. The simple and convenient synthetic method developed in this study can be extrapolated to synthesize other functional metal-organic hybrid systems with desired functionality for drug delivery and other biological applications. Further experimental and theoretical work is required to examine whether mixing of linkers within the framework can further enhance the charge-hole separation and photo-absorptivity of ZIF-based drug carrier systems.

References

[1] H.F. Ji, X.J. Li, H.Y. Zhang, Natural products and drug discovery: can thousands of years of ancient medical knowledge lead us to new and powerful drug combinations in the fight against cancer and dementia?, *EMBO Rep.,* 10 (2009) 194-200.

[2] S. Shishodia, G. Sethi, B.B. Aggarwal, Curcumin: getting back to the roots, *Ann. N. Y. Acad. Sci.,* 1056 (2005) 206-217.

[3] F. Yang, G.P. Lim, A.N. Begum, O.J. Ubeda, M.R. Simmons, S.S. Ambegaokar, P.P. Chen, R. Kayed, C.G. Glabe, S.A. Frautschy, Curcumin inhibits formation of amyloid β oligomers and fibrils, binds plaques, and reduces amyloid in vivo, *J. Biol. Chem.,* 280 (2005) 5892-5901.

[4] C.D. Mock, B.C. Jordan, C. Selvam, Recent advances of curcumin and its analogues in breast cancer prevention and treatment, *RSC Adv,* 5 (2015) 75575-75588.

[5] T. Esatbeyoglu, P. Huebbe, I.M. Ernst, D. Chin, A.E. Wagner, G. Rimbach, Curcumin—from molecule to biological function, *Angew. Chem.,* 51 (2012) 5308-5332.

[6] J. Wang, H. Wang, R. Zhu, Q. Liu, J. Fei, S. Wang, Anti-inflammatory activity of curcumin-loaded solid lipid nanoparticles in IL-1β transgenic mice subjected to the lipopolysaccharide-induced sepsis, *Biomaterials,* 53 (2015) 475-483.

[7] S.V. Jovanovic, C.W. Boone, S. Steenken, M. Trinoga, R.B. Kaskey, How curcumin works preferentially with water soluble antioxidants, *J. Am. Chem. Soc.,* 123 (2001) 3064-3068.

[8] B.B. Aggarwal, B. Sung, Pharmacological basis for the role of curcumin in chronic diseases: an age-old spice with modern targets, *Trends. Pharmacol. Sci.,* 30 (2009) 85-94.

[9] K. Indira Priyadarsini, Chemical and structural features influencing the biological activity of curcumin, *Curr. Pharm. Des.,* 19 (2013) 2093-2100.

[10] L. Nardo, R. Paderno, A. Andreoni, M. Másson, T. Haukvik, H.H. TØnnesen, Role of H-bond formation in the photoreactivity of curcumin, *J. Spectrosc,* 22 (2008) 187-198.

[11] K. Bairwa, J. Grover, M. Kania, S.M. Jachak, Recent developments in chemistry and biology of curcumin analogues, *RSC Adv,* 4 (2014) 13946-13978.

[12] H. Hatcher, R. Planalp, J. Cho, F. Torti, S. Torti, Curcumin: from ancient medicine to current clinical trials, *Cell. Mol. Life Sci.,* 65 (2008) 1631-1652.

[13] C. Banerjee, S. Maiti, M. Mustafi, J. Kuchlyan, D. Banik, N. Kundu, D. Dhara, N. Sarkar, Effect of encapsulation of curcumin in polymeric nanoparticles: how efficient to control ESIPT process?, *Langmuir,* 30 (2014) 10834-10844.

[14] D.K. Singh, R. Jagannathan, P. Khandelwal, P.M. Abraham, P. Poddar, In situ synthesis and surface functionalization of gold nanoparticles with curcumin and their antioxidant properties: an experimental and density functional theory investigation, *Nanoscale,* 5 (2013) 1882-1893.

[15] X. Fang, L. Fang, S. Gou, L. Cheng, Design and synthesis of dimethylaminomethyl-substituted curcumin derivatives/analogues: Potent antitumor and antioxidant activity, improved stability and aqueous solubility compared with curcumin, *Bioorg. Med. Chem. Lett.,* 23 (2013) 1297-1301.

[16] S. Wanninger, V. Lorenz, A. Subhan, F.T. Edelmann, Metal complexes of curcumin–synthetic strategies, structures and medicinal applications, *Chem. Soc. Rev.,* 44 (2015) 4986-5002.

[17] E. Ferrari, R. Benassi, S. Sacchi, F. Pignedoli, M. Asti, M. Saladini, Curcumin derivatives as metal-chelating agents with potential multifunctional activity for pharmaceutical applications, *J. Inorg. Biochem.,* 139 (2014) 38-48.

[18] B. Zebib, Z. Mouloungui, V. Noirot, Stabilization of curcumin by complexation with divalent cations in glycerol/water system, *Bioinorg. Chem. Appl.,* 292760 (2010) 1-8.

[19] S. Daniel, J.L. Limson, A. Dairam, G.M. Watkins, S. Daya, Through metal binding, curcumin protects against lead-and cadmium-induced lipid peroxidation

in rat brain homogenates and against lead-induced tissue damage in rat brain, *J. Inorg. Biochem.,* 98 (2004) 266-275.

[20] A. Valentini, F. Conforti, A. Crispini, A. De Martino, R. Condello, C. Stellitano, G. Rotilio, M. Ghedini, G. Federici, S. Bernardini, Synthesis, oxidant properties, and antitumoral effects of a heteroleptic palladium (II) complex of curcumin on human prostate cancer cells, *J. Med. Chem.,* 52 (2008) 484-491.

[21] M.H. Leung, D.-T. Pham, S.F. Lincoln, T.W. Kee, Femtosecond transient absorption spectroscopy of copper (II)–curcumin complexes, *Phys. Chem. Chem. Phys,* 14 (2012) 13580-13587.

[22] V. John, G. Kuttan, K. Krishnankutty, Anti-tumour studies of metal chelates of synthetic curcuminoids, *J. Exp. Clin. Cancer Res.,* 21 (2002) 219-224.

[23] L. Rossi, S. Mazzitelli, M. Arciello, C. Capo, G. Rotilio, Benefits from dietary polyphenols for brain aging and Alzheimer's disease, *Neurochem. Res.,* 33 (2008) 2390-2400.

[24] A. Barik, B. Mishra, A. Kunwar, R.M. Kadam, L. Shen, S. Dutta, S. Padhye, A.K. Satpati, H.-Y. Zhang, K.I. Priyadarsini, Comparative study of copper (II)–curcumin complexes as superoxide dismutase mimics and free radical scavengers, *Eur. J. Med. Chem.,* 42 (2007) 431-439.

[25] X. Mei, D. Xu, S. Xu, Y. Zheng, S. Xu, Novel role of Zn (II)–curcumin in enhancing cell proliferation and adjusting proinflammatory cytokine-mediated oxidative damage of ethanol-induced acute gastric ulcers, *Chem. Biol. Interact.,* 197 (2012) 31-39.

[26] H. Ahsan, N. Parveen, N.U. Khan, S. Hadi, Pro-oxidant, anti-oxidant and cleavage activities on DNA of curcumin and its derivatives demethoxycurcumin and bisdemethoxycurcumin, *Chem. Biol. Interact.,* 121 (1999) 161-175.

[27] H. Furukawa, N. Ko, Y.B. Go, N. Aratani, S.B. Choi, E. Choi, A.Ö. Yazaydin, R.Q. Snurr, M. O'Keeffe, J. Kim, Ultrahigh porosity in metal-organic frameworks, *Science,* 329 (2010) 424-428.

[28] H.-C. Zhou, J.R. Long, O.M. Yaghi, Introduction to metal–organic frameworks, *Chem. Rev.,* 112 (2012) 673-674.

[29] K. Vellingiri, A. Deep, K.-H. Kim, D.W. Boukhvalov, P. Kumar, Q. Yao, The sensitive detection of formaldehyde in aqueous media using zirconium-based metal organic frameworks, *Sens. Actuators. B Chem.,* 241 (2017) 938-948.

[30] T. Dutta, K.-H. Kim, R.J. Brown, Y.-H. Kim, D. Boukhvalov, Metal-organic framework and Tenax-TA as optimal sorbent mixture for concurrent GC-MS analysis of C1 to C5 carbonyl compounds, *Sci. Rep.,* 8 (2018) 5033.

[31] T. Rodenas, I. Luz, G. Prieto, B. Seoane, H. Miro, A. Corma, F. Kapteijn, F.X.L. i Xamena, J. Gascon, Metal–organic framework nanosheets in polymer composite materials for gas separation, *Nat. Mater.,* 14 (2015) 48.

[32] C. Guan, X. Liu, A.M. Elshahawy, H. Zhang, H. Wu, S.J. Pennycook, J. Wang, Metal–organic framework derived hollow CoS2 nanotube arrays: an efficient bifunctional electrocatalyst for overall water splitting, *Nanoscale. Horiz.,* 2 (2017) 342-348.

[33] P. Horcajada, T. Chalati, C. Serre, B. Gillet, C. Sebrie, T. Baati, J.F. Eubank, D. Heurtaux, P. Clayette, C. Kreuz, Porous metal–organic-framework nanoscale carriers as a potential platform for drug delivery and imaging, *Nat. Mater.,* 9 (2010) 172.

[34] S. Keskin, S. Kızılel, Biomedical applications of metal organic frameworks, *Ind. Eng. Chem. Res.,* 50 (2011) 1799-1812.

[35] A. Phan, C.J. Doonan, F.J. Uribe-Romo, C.B. Knobler, M. O'keeffe, O.M. Yaghi, Synthesis, structure, and carbon dioxide capture properties of zeolitic imidazolate frameworks, *Acc. Chem. Res,* 43 (2010) 58-67.

[36] O.M. Yaghi, M. O'keeffe, N.W. Ockwig, H.K. Chae, M. Eddaoudi, J. Kim, Reticular synthesis and the design of new materials, *Nature,* 423 (2003) 705.

[37] K.S. Park, Z. Ni, A.P. Côté, J.Y. Choi, R. Huang, F.J. Uribe-Romo, H.K. Chae, M. O'Keeffe, O.M. Yaghi, Exceptional chemical and thermal stability of zeolitic imidazolate frameworks, *Proc. Natl. Acad. Sci. U.S.A.,* 103 (2006) 10186-10191.

[38] H. Ren, L. Zhang, J. An, T. Wang, L. Li, X. Si, L. He, X. Wu, C. Wang, Z. Su, Polyacrylic acid@ zeolitic imidazolate framework-8 nanoparticles with ultrahigh drug loading capability for pH-sensitive drug release, *Chem. Comm,* 50 (2014) 1000-1002.

[39] D. Ge, H.K. Lee, Water stability of zeolite imidazolate framework 8 and application to porous membrane-protected micro-solid-phase extraction of polycyclic aromatic hydrocarbons from environmental water samples, *J. Chromatogr. A,* 1218 (2011) 8490-8495.

[40] Z. Wang, X. Tang, X. Wang, D. Yang, C. Yang, Y. Lou, J. Chen, N. He, Near-infrared light-induced dissociation of zeolitic imidazole framework-8 (ZIF-8) with encapsulated CuS nanoparticles and their application as a therapeutic nanoplatform, *ChemComm,* 52 (2016) 12210-12213.

[41] A. Tiwari, A. Singh, N. Garg, J.K. Randhawa, Curcumin encapsulated zeolitic imidazolate frameworks as stimuli responsive drug delivery system and their interaction with biomimetic environment, *Sci. Rep.,* 7 (2017) 12598.

[42] M. Zheng, S. Liu, X. Guan, Z. Xie, One-step synthesis of nanoscale zeolitic imidazolate frameworks with high curcumin loading for treatment of cervical cancer, *ACS Appl. Mater. Interfaces,* 7 (2015) 22181-22187.

[43] D. Bagchi, S. Chaudhuri, S. Sardar, S. Choudhury, N. Polley, P. Lemmens, S.K. Pal, Modulation of stability and functionality of a phyto-antioxidant by weakly interacting metal ions: curcumin in aqueous solution, *RSC Adv,* 5 (2015) 102516-102524.

[44] G.B. Kaufman, Inorganic chemistry: principles of structure and reactivity, 4th ed. (Huheey, James E.; Keiter, Ellen A.; Keiter, Richard L.), *J. Chem. Edu.,* 70 (1993) A279.

[45] A. Giri, N. Goswami, C. Sasmal, N. Polley, D. Majumdar, S. Sarkar, S.N. Bandyopadhyay, A. Singha, S.K. Pal, Unprecedented catalytic activity of Mn 3 O 4 nanoparticles: potential lead of a sustainable therapeutic agent for hyperbilirubinemia, *RSC Adv,* 4 (2014) 5075-5079.

[46] M.A. Addicoat, G.F. Metha, T.W. Kee, Density functional theory investigation of Cu (I)-and Cu (II)-curcumin complexes, *J. Comput. Chem.,* 32 (2011) 429-438.

[47] R. Adhikary, P. Mukherjee, T.W. Kee, J.W. Petrich, Excited-state intramolecular hydrogen atom transfer and solvation dynamics of the medicinal pigment curcumin, *J. Phys. Chem. B,* 113 (2009) 5255-5261.

[48] S. Chaudhuri, S. Batabyal, N. Polley, S.K. Pal, Vitamin B2 in nanoscopic environments under visible light: photosensitized antioxidant or phototoxic drug?, *J. Phys. Chem. A,* 118 (2014) 3934-3943.

[49] S. Chaudhuri, S. Sardar, D. Bagchi, S.S. Singha, P. Lemmens, S.K. Pal, Sensitization of an endogenous photosensitizer: electronic spectroscopy of riboflavin in the proximity of semiconductor, insulator, and metal nanoparticles, *J. Phys. Chem. A,* 119 (2015) 4162-4169.

[50] C.P. LeBel, H. Ischiropoulos, S.C. Bondy, Evaluation of the probe 2', 7'-dichlorofluorescin as an indicator of reactive oxygen species formation and oxidative stress, *Chem. Res. Toxicol.,* 5 (1992) 227-231.

[51] J. Nakamura, E.R. Purvis, J.A. Swenberg, Micromolar concentrations of hydrogen peroxide induce oxidative DNA lesions more efficiently than millimolar concentrations in mammalian cells, *Nucleic. Acids. Res.,* 31 (2003) 1790-1795.

[52] P. Malik, T.K. Mukherjee, Structure-function elucidation of antioxidative and prooxidative activities of the polyphenolic compound curcumin, *Chin. J. Biol,* 2014 (2014).

[53] T. Dutta, D. Bagchi, S.K. Pal, Bimetallic zeolitic imidazolate framework as an active excipient of curcumin under physiological condition, *Biomed. Phys. Eng. Express,* 4 (2018) 055004.

[54] S.R. Moulik, A. Ghatak, B. Ghosh, Study of surface chemistry and microstructure of TiO2 nanostructures on Pt (111)/Si wafer and FTO glass substrates: a comparative approach, *Surf. Sci.,* 651 (2016) 175-181.

[55] J. Cravillon, S. Mu̇nzer, S.-J. Lohmeier, A. Feldhoff, K. Huber, M. Wiebcke, Rapid room-temperature synthesis and characterization of nanocrystals of a prototypical zeolitic imidazolate framework, *Chem. Mater.,* 21 (2009) 1410-1412.

[56] D. Saliba, M. Ammar, M. Rammal, M. Al-Ghoul, M. Hmadeh, Crystal growth of ZIF-8, ZIF-67, and their mixed-metal derivatives, *J. Am. Chem. Soc.,* 140 (2018) 1812-1823.

[57] F. Trousselet, A.l. Archereau, A. Boutin, F.o.-X. Coudert, Heterometallic Metal–Organic Frameworks of MOF-5 and UiO-66 Families: Insight from Computational Chemistry, *J. Phys. Chem. C,* 120 (2016) 24885-24894.

[58] R. Grau-Crespo, A. Aziz, A.W. Collins, R. Crespo-Otero, N.C. Hernández, L.M. Rodriguez-Albelo, A.R. Ruiz-Salvador, S. Calero, S. Hamad, Modelling a linker mix-and-match approach for controlling the optical excitation gaps and band alignment of zeolitic imidazolate frameworks, *Angew. Chem.,* 128 (2016) 16246-16250.

[59] S. Gafner, S.-K. Lee, M. Cuendet, S. Barthélémy, L. Vergnes, S. Labidalle, R.G. Mehta, C.W. Boone, J.M. Pezzuto, Biologic evaluation of curcumin and structural derivatives in cancer chemoprevention model systems, *Phytochemistry,* 65 (2004) 2849-2859.

[60] G.D. Cagle, Fine structure and distribution of extracellular polymer surrounding selected aerobic bacteria, *Can. J. Microbiol.,* 21 (1975) 395-408.

Chapter 5

Experimental and Computational Studies on the Formation of Nanohybrid of a Medicinally Important Drug with Inorganic Nanostructure

5.1. Introduction: Herbal medicines with rich polyphenol content are attracting interest and are sometimes even preferred with respect to synthesised drugs due to their multiple functionalities, reduced side effects and cost effectiveness [1, 2]. The rising use of herbal medicines suggests an attention to the paramount issue of quality as it is directly related to safety and efficacy of the medicines [3]. Introduction of chemical toxins such as harmful pesticides, non-essential heavy metals (as Cd, Hg, Pb etc.) into these plant materials during harvesting or post-harvest collection and storage can lead to therapeutically less effective agents with some adverse action [4]. However, plants can execute some superficial mechanism by forming metal-ligand complexes in rhizosphere which can limit the uptake of metals by roots and help plants to tolerate a certain amount of toxic metals in the soil [5].

Turmeric, the golden yellow spice of India, is considered to be one of the most efficacious herbal plant due to its prolific content of natural phenols such as curcuminoids [6]. Curcumin is the principal curcuminoids of turmeric and used to be isolated from rhizomes of *Curcuma Longa* [7]. Besides the popularity of curcumin as spices, it exhibits varieties of medicinal applications including the use as anticancer agent [8, 9], anti-Alzheimer agent [10], anti-Parkinson disease neuroprotective agent [11], which emphasizes its significance as a herbal medicine. The behaviour of curcumin as a chelating ligand to bivalent metal ions such as zinc, copper, manganese, iron leading to formation of metallo-curcumin complexes

enhances both the solubility and activity of curcumin [12-15]. But this ligation property of curcumin has some contrasting effect as it can effectively chelates heavy metal ions [16] such as cadmium, lead, mercury, and arsenic. In recent literature it has been reported that contaminated curcumin can be a potential source of lead exposure [17]. Chronic exposure to curcumin may cause elevated blood lead levels (BLL) as it contains extremely high bio-accessible lead levels [18]. It is more alarming that this lead contamination affects children mostly due to high gastrointestinal uptake and the permeable blood-brain barrier [19]. The dietary supplement curcumin might contain elevated levels of mercury and arsenic contamination also [20]. Moreover, turmeric is profoundly used in cosmetics and applying the metal contaminated turmeric directly to the skin enhances the possibility of metal contamination in the body [21]. This necessitates the urgent requirement of a facile detection procedure of heavy metal conjugated curcumin. However, up to date no such attempt has been made, except conventional techniques [22].

Herein, we propose the use of ZnO nanorods (NR) for differentiating between pure curcumin (Cur) and metal attached curcumin (M-Cur). We have synthesized ZnO NR [23] which is environment friendly and less toxic than other semiconductor oxides [24] and its structural characterization was performed. In order to detect Cur and M-Cur distinctly, we have used Cur (as pure sample), synthesized Zn-Cur (as non-toxic M-Cur), and Hg-Cur (as toxic M-Cur). The samples are electrochemically deposited covering ZnO NR surfaces. The intrinsic defect state emission of the ZnO NR and its spectral overlap with the absorption spectrum of Cur and M-Cur samples reveals Förster Resonance Energy Transfer (FRET) from the surface of the NR to the attached moieties, confirming the close proximity between them. The variance in FRET distances for different samples suggest that Cur and M-Cur are attached to the ZnO NR surface through different binding sites. First-principle analysis of ground-state energies unveils that for Cur

and Zn-Cur, the NRs are attached through keto-enolic sites, whereas for Hg-Cur the attachment is through o-methoxy phenolic site. This result motivated us to fabricate a photovoltaic device using ZnO NRs sensitized with Cur or M-Cur as the active electrode to measure the photocurrent under visible light irradiation. The trend in photocurrent clearly shows an immense disparity suggesting that an electron recombination process is active in Cur and Zn-Cur systems which get hindered for the Hg-Cur sample. The slow back electron transfer process from the active layer (consisting of Hg-Cur) to the electrolyte justifies the observed photocurrent trend. To envisage the detailed mechanism responsible for the contrasting experimental behaviour of these samples, we have investigated the electronic structure of Cur-NR, Zn-Cur-NR and Hg-Cur-NR with the help of density functional calculations. Our study offers detailed physical insight and motivation for using ZnO NR as nanoprobes to characterize heavy-metal conjugated curcumin and is thus expected to find relevance in large scale, for daily consumer-based applications.

5.2. Results and Discussion:

5.2.1. Sensitized ZnO Nanorod Assemblies to Detect Heavy Metal Contaminated Phytomedicines: Spectroscopic and Simulation Studies [25]: The SEM images of synthesized nanoprobe ZnO NR are shown in Figure 5.1.a top view and 5.1.b side view. The ZnO NRs are found to be 2–3 μm in length and have diameters of 80–100 nm. The typical hexagonal surface of the NRs is shown in the inset of Figure 5.1.a. The synthesized Cur and M-Cur exhibit absorption in the region 430 nm in DMSO as shown in Figure 5.1.c. Curcumin shows an absorption peak at 430 nm [6] due to an electronic transition which is typically π-π* in nature. After successful attachment of the metal to curcumin, the absorption spectra slightly change. In case of Zn-Cur, the main peak is observed at 430 nm with a shoulder around 454 nm. The change in absorption spectra might be correlated with the formation of a new charge-transfer state by an electronic transition from the ligand curcumin to the metal ion. Hg-Cur shows slight blue shift in UV-Vis spectra with a peak maximum

at 422 nm (Figure 5.1.c). The inset depicts the emission spectra of Cur and M-Cur having similar OD at 430 nm, revealing a broader peak near 540 nm upon excitation at 430 nm.

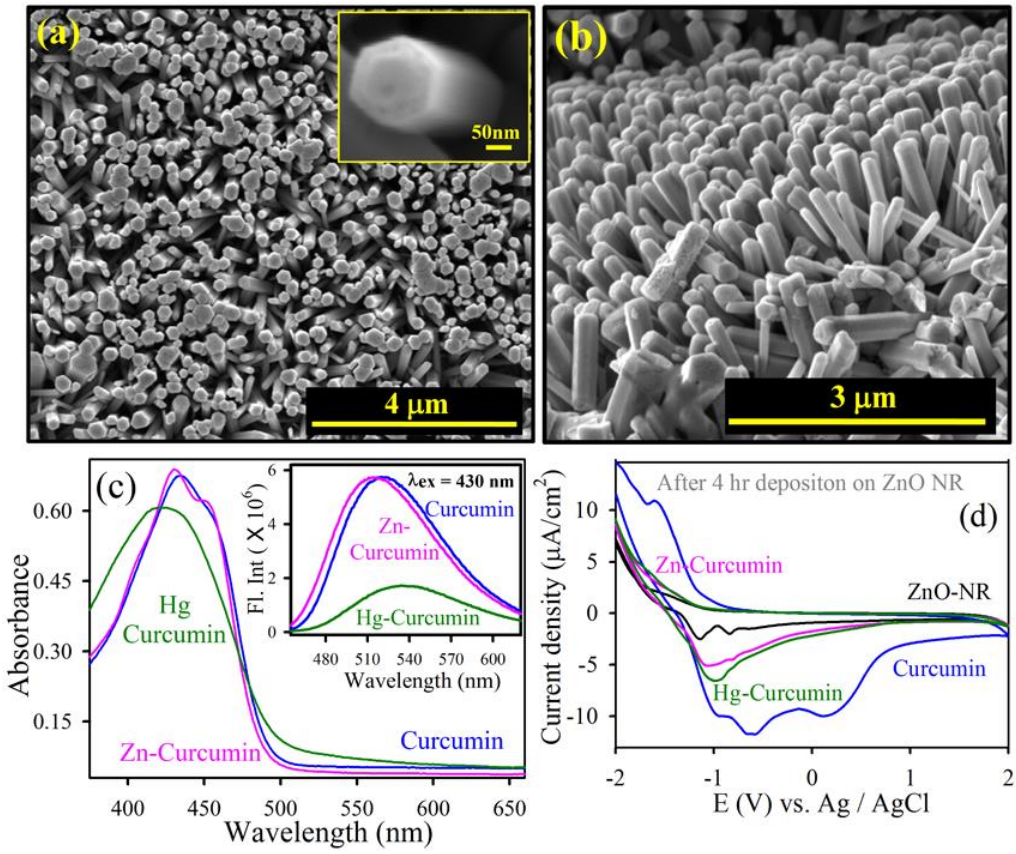

Figure 5.1. *(a) FEG-SEM of the ZnO nanorods (ZnO NR) on a glass plate. Inset shows magnified image of nanorod (b) Side view of ZnO NRs (c) Absorption spectra of Curcumin (blue), Zn-Curcumin (pink), Hg-Curcumin (dark green) in DMSO. Inset depicts emission spectra of Curcumin (blue), Zn-Curcumin (pink), Hg-Curcumin (dark green) in DMSO. The excitation wavelength is 430 nm (d) Cyclic voltammograms of Curcumin (blue), Zn-Curcumin (pink), Hg-Curcumin (dark-green) after 4 hrs open circuit deposition onto ZnO-NR fabricated on FTO plates. CV measurements were performed in PBS-aqueous KCl solution at 0.8 V s^{-1} scan rate and Ag/AgCl as reference electrode.*

Although there are changes in optical properties between Cur and M-Cur, but these differences are not enough to distinctly detect the presence of metals conjugated curcumin. In order to investigate the attachment of the Cur and M-Cur by electrochemical deposition to ZnO NR surface, cyclic voltammetry experiments were performed at different time intervals – initial, after 2 hrs and after 4hrs of

deposition. Figure 5.1.d shows comparative voltammograms after 4 hrs of deposition. The deposition of Cur or M-Cur onto the surfaces of the ZnO NRs significantly alters the interfacial charge transfer processes and greatly affects their electrochemical properties [26].

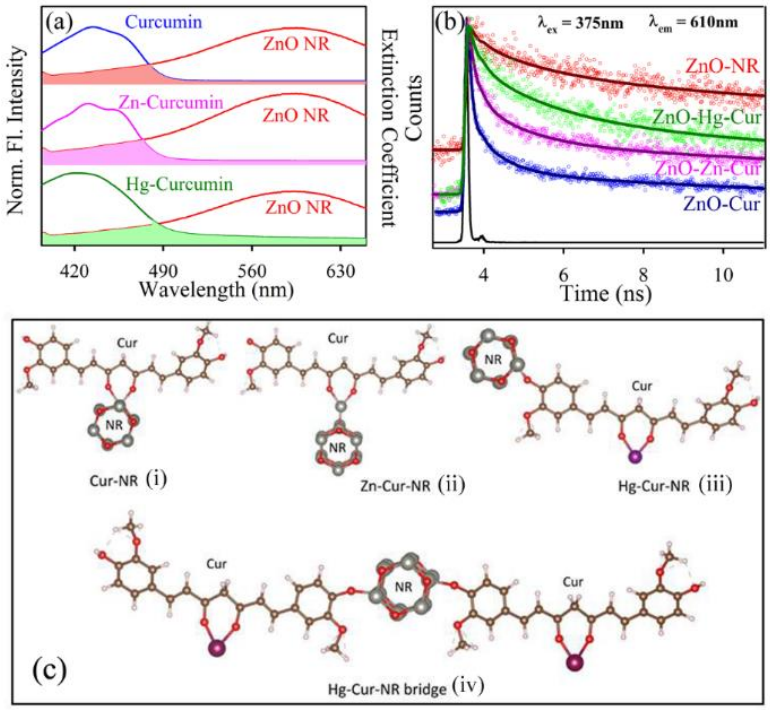

***Figure* 5.2.** *(a) Spectral overlaps of the emission of ZnO NRs and the absorption spectrum of Curcumin (red), Zn-Curcumin (pink), Hg-Curcumin (green) are shown (b) Picosecond resolved emission transients of ZnO NRs and composite systems, detected at 610 nm (c) Schematic ground state configuration of different structures (i) Cur-NR (ii) Zn-Cur-NR (iii) Hg-Cur-NR (iv) Hg-Cur-NR (bridge).*

As evident from previous reports, electro-oxidation of curcumin follows two consecutive steps via multiple intermediate formations which are essentially pH dependent. In the first step, phenolic hydroxyl group of curcumin is oxidized via formation of stable phenoxy radical at a peak 0.6 V followed by its conversion to quinone at 0.3 V [27]. The peak near 0.95 V might be correlated to oxidation of enolic hydroxyl group [28]. In case of Cur attached ZnO, the peaks are at 0.25 V, 0.63 V and 0.98 V which are in accordance with peak value of free curcumin. The redox potentials can be attributed to the binding of curcumin at the ZnO surface. The M-

Cur attached ZnO NRs depict a smaller (Zn-Cur- 0.98 V and Hg-Cur- 0.90 V) shift compare to curcumin, demonstrating lesser affinity towards attachment. The well-documented FTIR spectra of ZnO-Cur illustrate the attachment between the two moieties but the specific site of attachment is not properly recognized [29].

Table 5.1. *Picosecond-resolved fluorescence transient lifetime* [a]

System	τ_1 (ns)	τ_2 (ns)	τ_3 (ns)	τ_{avg} (ns)
ZnO NR	0.20 (23%)	1.73 (26%)	22.0 (51%)	11.70
ZnO-Curcumin	0.08 (73%)	0.72 (15%)	13.9 (11%)	1.70
ZnO-Zn-Curcumin	0.25 (59.8%)	1.80 (16.5%)	18.0 (23.7%)	4.70
ZnO-Hg-Curcumin	0.23 (35%)	1.95 (28%)	20.0 (37%)	7.90

[a] *Emission (monitored at 610 nm) was detected with 375 nm laser excitation. Numbers in parentheses indicate relative contributions.*

Table 5.2. *FRET parameters*

System	J (λ)	R_0 (Å)	E	r_{DA} (nm)
ZnO-Curcumin	0.497 X 10^{15}	13.80	0.854	1.03
ZnO-Zn-Curcumin	0.48 X 10^{15}	13.72	0.596	1.27
ZnO-Hg-Curcumin	0.69 X 10^{15}	14.57	0.320	1.66

To illustrate the feasibility of attachment of ZnO NR and Cur or M-Cur, we employed a FRET based spectroscopic method. The synthesized NR surfaces were observed to emit at 590 nm due to presence of intrinsic oxygen vacancies[30]. The broad NR emission is composed of two bands: a doubly charged vacancy centre (V_o^{++}) located at 610 nm (P_2), a singly charged vacancy centre (V_o^{+}) located at 550 nm (P1) [31, 32]. Figure 5.2.a illustrates the significant spectral overlap between emission of donor ZnO NR and absorption of acceptor Cur or M-Cur. The estimation of distances between two molecular units from FRET based calculation is extremely useful for many assignments [33]. The fluorescence decay profile of the donor ZnO NR in the presence and absence of the acceptors Cur or M-Cur were measured (Figure 5.2.b) upon excitation with 375 nm laser and monitored at 610 nm

(P_2) [34]. The excited-state lifetime of the ZnO NRs quenches after binding with Cur or M-Cur compared to that of bare ZnO NRs. In case of Cur, quenching is maximum followed by Zn-Cur and Hg-Cur. The details of the lifetime data with their relative contribution in the fluorescence decays are tabulated in Table 5.1. From FRET calculations (Table 5.2), the distance between the donor ZnO NR and acceptors Cur, Zn-Cur and Hg-Cur is found to be 1.0 nm, 1.3 nm and 1.7 nm, respectively. The energy transfer efficiency is calculated to be 85.4%, 59.6% and 32% for Cur, Zn-Cur and Hg-Cur, respectively. These results suggest a molecular level interaction between ZnO NR and Cur or M-Cur. The distance between M-Cur and ZnO NRs significantly increased with increase in the size of the metal ions which indicates the possibility of non-identical binding site for different systems.

Table 5.3. *Ground state energy per atom, HOMO LUMO Energy, Band Gap and relative shift of E_F of the systems with respect to Cur/M-Cur or NR*

System	Ground state energy/atom	Homo(eV), Lumo(eV)	Band-gap	Relative shift of EF with respect to the Cur/M-Cur
NR	-3.95	-0.62, 2.24	2.86	-
Cur	-6.40	-0.90, 2.21	3.11	-
Zn-cur	-6.27	0.01, 3.88	3.87	0.88
Hg-cur	-6.40	0.0, 3.53	3.53	0.54
Cur-NR	-5.67	-1.02, 1.33	2.35	-0.2
Zn-cur-NR	-5.54	-0.62, 2.22	2.84	-0.86
Hg-cur-NR	-5.50	0.33, 3.10	3.10	-1.59
Hg-bridge	-5.84	0.31, 3.19	3.19	-1.81

Table 5.4: *Lowest distances between the two moieties, calculated theoretically*

System	Lowest distance between two moieties (Å)
Cur-NR	2.0
Zn-Cur-NR	1.9
Hg-Cur-NR	3.6
Hg-Cur-NR-bridge	3.6

Thus, we have explored the ground state energy stability of four experimental control systems, *viz.*, ZnO nanorod (NR), pristine Curcumin (Cur), Zn-Curcumin (Zn-Cur) and Hg-Curcumin (Hg-Cur), which indicates that the

pristine system is energetically most stable (Table 5.3). Formation of M-Cur complexes materializes via diketo moiety, which acts as a chelating agent for complexation with metal ions [12]. For the formation of the NR attached complexes, depending upon the Cur system, there are two possible attachment sites. The NR may be chelating through the middle diketo site or via the o-methoxy phenolic group at the end of the Cur chain. A comparison of ground-state energies obtained from theoretical calculation, of the ground-state energies unveils that for Cur and Zn-Cur, NR is attached through the keto-enolic site, whereas for Hg-Cur the attachment is through the o-methoxy phenolic site. Interestingly, for Hg-Cur-NR assembly, there is an even lower-energy symmetric configuration, where two Hg-Cur chain get attached to the two opposite sides of a NR (Figure 5.2.c, iv), which will be referred as Hg-bridge. These energetically favourable ground state configurations, as suggested from our theoretical calculation, are depicted in Figure 5.2.c. Table 5.3 presents the number of atom-normalized total-energy, band-gap and relative Fermi level (E_F) shifts for all possible Cur-NR and M-Cur-NR complexes with respect to the component control systems. A comparison of total energy of the M-Cur-NR systems shows that Hg-Cur-NR and the Hg-bridge configurations are lowest in total energies. In Table 5.4, the optimized distances between two moieties, as obtained after ionic relaxation, are listed, which suggests highest distance for Hg-Cur-NR system. This trend is qualitatively similar to the experimentally obtained FRET distances. It may be mentioned that for the configuration with Hg-Cur attached to the NR via the middle diketo moiety, large structural distortions of the NRs lead to a break-up of the Hg-Cur-NR assembly with total energy of the system much higher than the stable configurations. Although, both Zn and Hg are d^{10} systems, larger size of the Hg^{2+} ion is mostly responsible for such structural distortion induced increase in ground state energy. In addition, an investigation of the binding energies (BE) of Cur/M-Cur-NR complexes reveals the fact that the order of decrease in BE of the systems are like: BE (Cur-NR) > BE (Zncur-NR) > BE (Hgcur-NR) > BE (Hg-bridge).

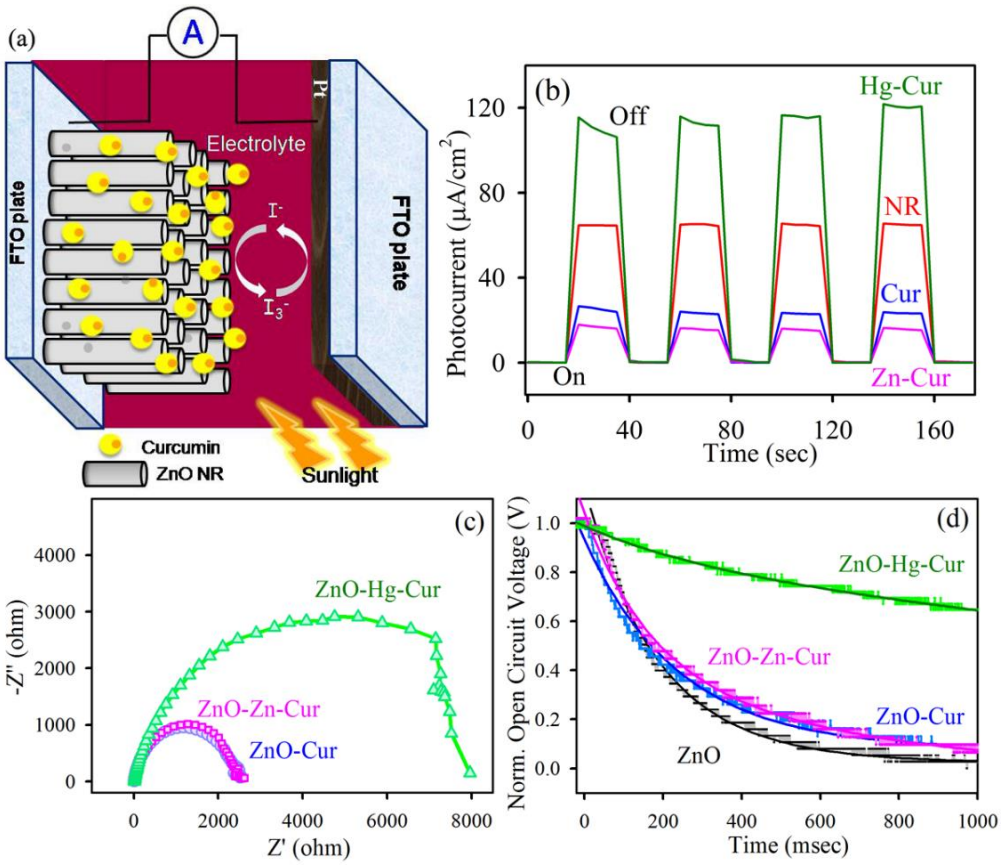

Figure 5.3. *(a) Schematic representation of photovoltaic device setup by using ZnO NRs fabricated on FTO as working electrode and Pt as counter electrode. Iodine-Triiodide was used as electrolyte solution (b) Photocurrent response of ZnO NR (red), ZnO-Curcumin (blue), ZnO-Zn-Curcumin (pink) and ZnO-Hg-Curcumin (Dark green) (c) Nyquist plots of different systems. Inset shows equivalent circuit model that was used to fit the EIS spectra (d) Open circuit voltage decay profiles of different systems.*

After confirmation of the attachment between Cur or M-Cur and ZnO NR, photocurrent measurements were performed in the fabricated photovoltaic devices. Figure 5.3.a is the schematic representation of the fabricated device using cur or M-Cur sensitized ZnO NR on FTO plates as photoanode and Pt as counter electrode and iodide/triiodide solution as electrolyte. The photocurrent response signal for ZnO NR with different cur or M-Cur remains similar under UV irradiation but under 1 sun illumination, it follows an interesting trend as shown in Figure 5.3.b. An enhanced photocurrent was observed for the Hg-Cur (110 μA) compared to the ZnO NR (60 μA) whereas Cur and Zn-Cur show a reduced photocurrent (20 μA). We have explored the different photo-induced processes involved at the interfaces

of the fabricated device to provide a detailed physical insight (scheme-5.1). Upon light illumination, the Cur or M-Cur experienced photo-excitation. The excited state electrons are readily injected to proximal ZnO NR. These electrons are passing through load and used for dye regeneration through iodine redox couple. But the interfacial back electron transport process from Fermi level of NR conjugated complex to electrolyte and/or the charge recombination to HOMO of Cur or M-Cur plays a significant role in photocurrent trend. Thus, to investigate these electronic and ionic processes, we use electrochemical impedance spectroscopic (EIS) method.

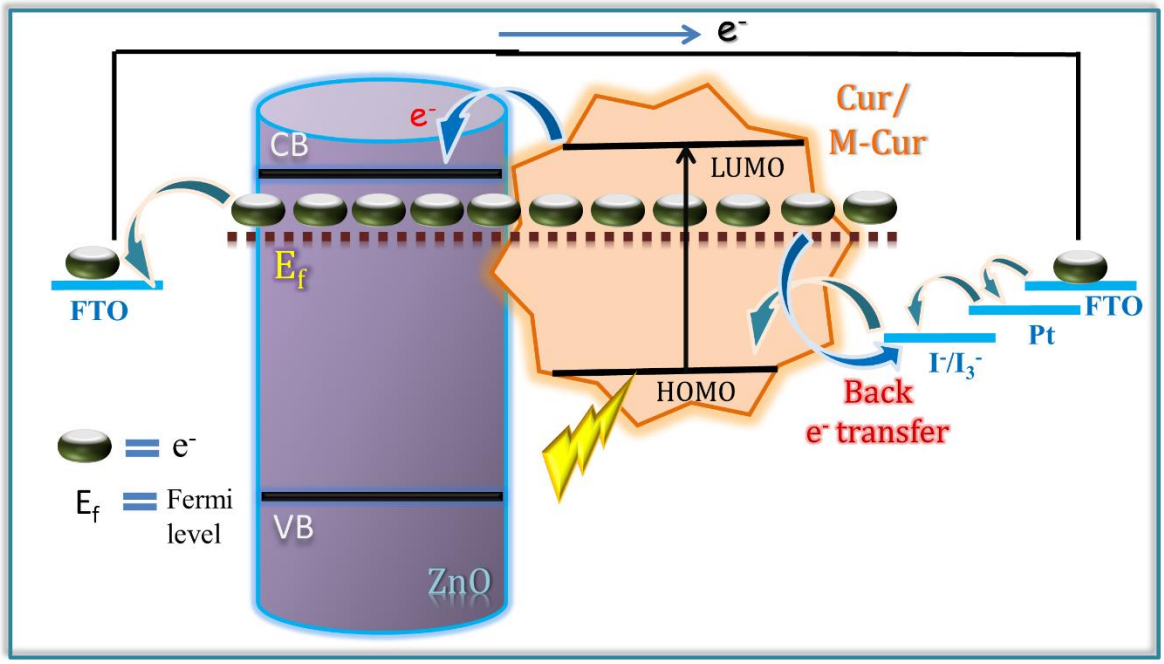

Scheme 5.1. *Schematic representation of the ultrafast dynamic processes in ZnO-NR-Cur/M-Cur composites under light illuminated conditions.*

As shown in Figure 5.3.c, the Nyquist plot features one semicircle, in the intermediate frequency region which is associated with the electron transport in the ZnO NR and back reaction at the NR conjugated complex /electrolyte interface [35]. The Nyquist plots are fitted using the equivalent circuit (where C_1 is capacitance and R is resistance) shown in the inset of the Figure 5.3.c and the parameters are summarized in Table 5.5. The R_1 value represents the interfacial recombination resistance at NR conjugated complex /electrolyte interface and is much higher for

Hg-Cur-NR than that of Cur-NR and Zn-Cur-NR. This suggests less charge recombination from Hg-Cur-NR photo-anode to the triiodide ions in the electrolyte.

Table 5.5. *EIS parameters of fabricated photovoltaic device using different active electrodes*

Active electrode	Rs (Ω)	R_1 (Ω)
ZnO-NR-Cur	14.09	2258
ZnO-NR-Zn-Cur	16.27	2283
ZnO-NR-Hg-Cur	13.44	3193

Table 5.6. *Dynamics of photovoltage transients of fabricated photovoltaic device using different active electrodes*

Active electrode	τ_1 (ms)	τ_2 (ms)	τ_{avg} (ms)
ZnO NR	154.7 (50%)	230 (50 %)	192.4
ZnO-NR-Cur	134.6 (55%)	552 (45%)	322.4
ZnO-NR-Zn-Cur	164 (59%)	711.6(41%)	388.5
ZnO-NR-Hg-Cur	-	12699.5 (100%)	12699.5

The lifetime of accumulated charges at the photo-anode can be monitored by taking the decay of the open circuit voltage in the dark following a brief period of illumination. Upon visible light illumination, the excited Cur or M-Cur injects electrons into ZnO NR. The accumulated electrons in the Fermi level moves to the more negative potential which reflects in the photovoltage enhancement. The forward electron injection is terminated upon stopping the illumination, thus discharging of electrons occurs through the back-electron transfer or recombination with the oxidized electrolytes. The open circuit voltage decay reflects the timescales for the recombination processes. Figure 5.3.d shows the decay profiles of different systems. The fitted timescales are presented in Table 5.6. The Hg-Cur-NR photo-anode exhibit a remarkably slow rate of voltage decay (12.7 s) compared to the other systems. This can be attributed to peripheral attachment of Hg-Cur to NR which contributes in lesser electron recombination processes.

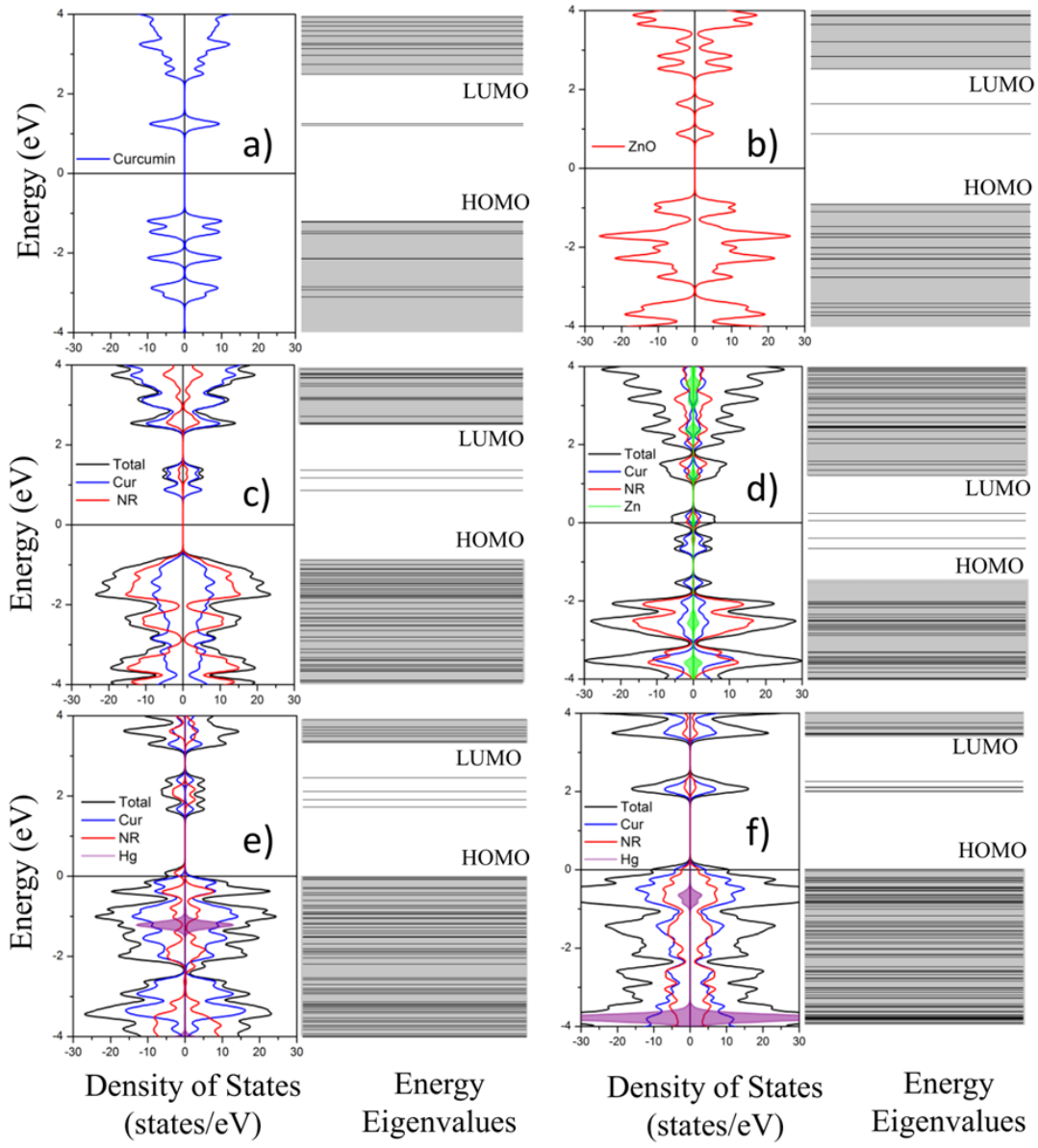

Figure 5.4. *Atom (APDOS) and orbital (OPDOS) projected Density of states (DOS) and corresponding energy eigenvalues of (a) Pure Cur (b) Pure ZnO NR (c) Cur-NR (d) Zn-Cur-NR (e) Hg-Cur-NR and (f) Hg-Cur-NR (bridge).*

The atom (APDOS) and orbital-projected density of states (OPDOS) and the corresponding energy eigenvalues of the NR conjugated complexes are displayed in Figure 5.4, along with the two control systems Cur and NR. Figure 5.4.a and b exhibit the total DOS of the Cur and NR systems with the respective highest occupied molecular orbital (HOMO) and lowest unoccupied molecular orbital (LUMO) levels. Both systems are found to be wide band gap semiconductors with

some gap states because of the dangling bonds at the surface. In Figure 5.4.c, for the cur-NR combined system, a shift of E_F with respect to the Cur and NR system is found to be 0.2 eV towards valence band (VB) and 1.36 eV towards conduction band (CB) respectively, implying a *p*(*n*)-type doping of the Cur(NR). This stipulates an obvious electron transfer from Cur to NR system, complementing the experimental indication. The DOS figures also show a strong O-2*p* of Cur to NR Zn-3*d* hybridization, including the filled states at the top of the VB (~ 0.7 eV below E_F) as well as the empty gap states (~ 0.65 eV above E_F). Figure 5.4.d for the Zn-Cur-NR assembly unveils that the charge transferred from Zn-Cur to NR fills up the empty O-2*p* dangling bond induced gap states both from Cur and NR, as present in 5.4.c, keeping the NR Zn-3*d* and Zn-Cur Zn-3*d* levels partially filled at E_F and Zn-3*d* induced donor levels created within 0.1 eV of CB. In a similar way as Cur-NR, there is a *p*(*n*) type doping of the Zn-Cur-NR system, indicating a charge transfer from Zn-Cur to NR. A comparison with Figure 5.4.c shows more localized and increased intensity of VB NR-DOS in comparison to the Cur-NR system. The relative shifts of E_F with respect to the Zn-Cur and NR systems are -0.86 eV and 1.58 eV, respectively. In comparison to Cur-NR, there is only a small shift of E_F by 0.22 eV towards CB in addition to a reduction of the HOMO-LUMO gap. Zn-Cur possesses almost similar E_F and similar amount of charge transfer from Zn-Cur to NR as Cur-NR system. From Bader analysis, the amount of electron transfer from Cur/Zn-Cur to NR is ~ 3e. This also explains similar photocurrent behaviour for these two systems.

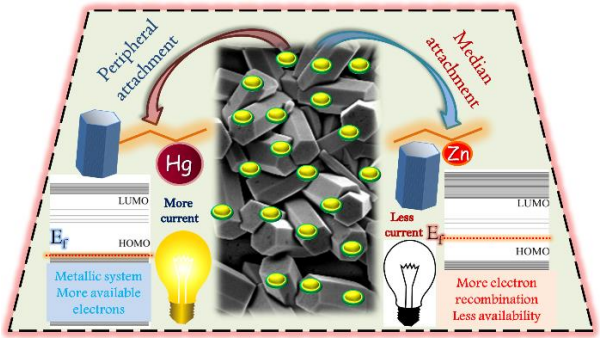

***Scheme* 5.2.** *Interfacial carrier dynamics of ZnO Nanoprobe assemblies for detection of heavy metal contaminated herbal medicine.*

As compared to the Cur-NR and Zn-Cur-NR systems, Hg-Cur-NR systems are energetically more favourable, as can be seen from the ground state total energy normalized by the number of atoms presented in Table 5.3. The Hg-bridge structure is lowest in normalized ground state energy. Due to its larger ionic radii, Hg^{2+} introduces more buckling and structural distortions within the system. The buckling angle between central C atoms for Hg-Cur-NR is 7.4°, which is much higher than Cur-NR and Zn-Cur-NR (3.6° and 0.4° respectively). While comparing the Fermi level shifts, large shift of Hg-Cur Fermi-level towards valence band for Hg-Cur-NR (-1.59 eV) and Hg-bridge (-1.81 eV) indicates huge charge transfer from Hg-cur to NR for both configurations. Bader partitioning analysis implies that the charge transfer from the Hg-cur to the NR can be quantified as ~ 3e and ~ 10e for Hg-Cur-NR and Hg-bridge configuration respectively. This transferred charge renders the Fermi-level to shift within valence band, imparting a metallic property within the system. The spin-polarized behaviour in case of Hg-Cur-NR system is subdued for the Hg-bridge system due to the symmetric nature of the charge transfer. In contrast to the Cur-NR and Zn-Cur-NR systems, inherent structural distortion of the Hg systems also generates NR and Hg-Cur induced shallow acceptor levels, which while overlapping with top of the VB are responsible for the metallic behaviour and better photocurrent for Hg-Cur-NR systems.

5.3. Conclusion: In summary, we have designed a facile detection procedure based on ZnO NR to estimate and characterize heavy-metal conjugated curcumin. ZnO NR of 2-3 μm of length and 80-100 nm diameters were synthesised using a hydrothermal method and characterised by electron microscopy (SEM). Three samples were employed namely Cur (pure), Zn-Cur (non-toxic M-Cur) and Hg-Cur (toxic M-Cur) for electrochemical deposition on ZnO NR surface and attachment is confirmed by cyclic voltammetry studies. To confirm the proximity of the ZnO NR to Cur or M-Cur at the molecular level, we have employed picosecond-resolved Förster resonance energy transfer (FRET) from the defect mediated emission of ZnO

NRs to Cur or M-Cur and the distance between the two is found to be dependent on the size of metal and the structure of the acceptor molecule. Computational investigation suggests variance of NR attachment sites due to the greater size of metal ions. We have fabricated a photovoltaic device based on molecular level interaction between ZnO and Cur or M-Cur, which shows higher photocurrent for Hg-Cur. The EIS and open circuit voltage decay profiles show remarkably slow rate of electron recombination from Hg-Cur-NR photo-anode to the oxidized electrolyte. DOS analysis suggests metallic behaviour of Hg-Cur-NR compare to all other systems is reasonable for its higher photo current generation. This work is expected to find relevance for fabricating more selective and sensitive sensors to detect heavy-metal contamination in different herbal medicines.

References

[1] D.S. Fabricant, N.R. Farnsworth, The value of plants used in traditional medicine for drug discovery, *Environ. Health Perspect.,* 109 (2001) 69-75.

[2] E. Haslam, T.H. Lilley, Y. Cai, R. Martin, D. Magnolato, Traditional herbal medicines--the role of polyphenols, *Planta medica,* 55 (1989) 1-8.

[3] H.H. Fong, Integration of herbal medicine into modern medical practices: issues and prospects, *Integr. Cancer. Ther,* 1 (2002) 287-293.

[4] K. Chan, Some aspects of toxic contaminants in herbal medicines, *Chemosphere,* 52 (2003) 1361-1371.

[5] A. Michalak, Phenolic compounds and their antioxidant activity in plants growing under heavy metal stress, *Pol J Environ Stud,* 15 (2006) 523.

[6] K.I. Priyadarsini, The chemistry of curcumin: from extraction to therapeutic agent, *Molecules (Basel, Switzerland),* 19 (2014) 20091-20112.

[7] B.B. Aggarwal, A. Kumar, A.C. Bharti, Anticancer potential of curcumin: preclinical and clinical studies, *Anticancer. Res.,* 23 (2003) 363-398.

[8] C.D. Mock, B.C. Jordan, C. Selvam, Recent advances of curcumin and its analogues in breast cancer prevention and treatment, *RSC Adv,* 5 (2015) 75575-75588.

[9] Q. Wen, X. Zhang, J. Cai, P.-H. Yang, A novel strategy for real-time and in situ detection of cytochrome c and caspase-9 in Hela cells during apoptosis, *Analyst,* 139 (2014) 2499-2506.

[10] F. Yang, G.P. Lim, A.N. Begum, O.J. Ubeda, M.R. Simmons, S.S. Ambegaokar, P.P. Chen, R. Kayed, C.G. Glabe, S.A. Frautschy, G.M. Cole, Curcumin inhibits formation of amyloid beta oligomers and fibrils, binds plaques, and reduces amyloid in vivo, *J. Biol. Chem.,* 280 (2005) 5892-5901.

[11] W. Fu, W. Zhuang, S. Zhou, X. Wang, Plant-derived neuroprotective agents in Parkinson's disease, *Am. J. Transl. Res.,* 7 (2015) 1189-1202.

[12] S. Wanninger, V. Lorenz, A. Subhan, F.T. Edelmann, Metal complexes of curcumin--synthetic strategies, structures and medicinal applications, *Chem. Soc. Rev.*, 44 (2015) 4986-5002.

[13] X.-Z. Zhao, T. Jiang, L. Wang, H. Yang, S. Zhang, P. Zhou, Interaction of curcumin with Zn(II) and Cu(II) ions based on experiment and theoretical calculation, *J. Mol. Struct.*, 984 (2010) 316-325.

[14] A.E. Schmitz, P.A. de Oliveira, L.F. de Souza, D.G. da Silva, S. Danielski, D.B. Santos, E.A. de Almeida, R.D. Prediger, A. Fisher, M. Farina, A.L. Dafre, Interaction of curcumin with manganese may compromise metal and neurotransmitter homeostasis in the hippocampus of young mice, *Biol. Trace. Elem. Res.*, 158 (2014) 399-409.

[15] S. Ghosh, J. Kuchlyan, D. Banik, N. Kundu, A. Roy, C. Banerjee, N. Sarkar, Organic additive, 5-methylsalicylic acid induces spontaneous structural transformation of aqueous pluronic triblock copolymer solution: a spectroscopic investigation of interaction of curcumin with pluronic micellar and vesicular aggregates, *J. Phys. Chem. B,* 118 (2014) 11437-11448.

[16] W.R. Garcia-Nino, J. Pedraza-Chaverri, Protective effect of curcumin against heavy metals-induced liver damage, *Food. Chem. Toxicol.,* 69 (2014) 182-201.

[17] K. Gleason, J.P. Shine, N. Shobnam, L.B. Rokoff, H.S. Suchanda, M.O. Ibne Hasan, G. Mostofa, C. Amarasiriwardena, Q. Quamruzzaman, M. Rahman, M.L. Kile, D.C. Bellinger, D.C. Christiani, R.O. Wright, M. Mazumdar, Contaminated turmeric is a potential source of lead exposure for children in rural Bangladesh, *J. Environ. Public. Health,* 2014 (2014) 730636.

[18] C.G. Lin, L.A. Schaider, D.J. Brabander, A.D. Woolf, Pediatric lead exposure from imported Indian spices and cultural powders, *Pediatrics,* 125 (2010) 828-835.

[19] L. Jarup, Hazards of heavy metal contamination, *Br. Med. Bull.*, 68 (2003) 167-182.

[20] S.P. Dolan, D.A. Nortrup, P.M. Bolger, S.G. Capar, Analysis of dietary supplements for arsenic, cadmium, mercury, and lead using inductively coupled plasma mass spectrometry, *J. Agric. Food. Chem.,* 51 (2003) 1307-1312.

[21] S. Borowska, M.M. Brzoska, Metals in cosmetics: implications for human health, *J. Appl. Toxicol.,* 35 (2015) 551-572.

[22] Y. Jung, J. Lee, H.K. Kim, B.C. Moon, Y. Ji, D.H. Ryu, G.-S. Hwang, Metabolite profiling of Curcuma species grown in different regions using 1H NMR spectroscopy and multivariate analysis, *Analyst,* 137 (2012) 5597-5606.

[23] B. Sunandan, D. Joydeep, Hydrothermal growth of ZnO nanostructures, *Sci. Technol. Adv. Mater.,* 10 (2009) 013001.

[24] R.J. Barnes, R. Molina, J. Xu, P.J. Dobson, I.P. Thompson, Comparison of TiO2 and ZnO nanoparticles for photocatalytic degradation of methylene blue and the correlated inactivation of gram-positive and gram-negative bacteria, *J. Nanopart. Res.,* 15 (2013) 1432.

[25] D. Bagchi, T.K. Maji, S. Sardar, P. Lemmens, C. Bhattacharya, D. Karmakar, S.K. Pal, Sensitized ZnO nanorod assemblies to detect heavy metal contaminated phytomedicines: spectroscopic and simulation studies, *Phys. Chem. Chem. Phys.,* 19 (2017) 2503-2513.

[26] X. Hou, L. Wang, G. He, J. Hao, Synthesis, optical and electrochemical properties of ZnO nanorod hybrids loaded with high-density gold nanoparticles, *CrystEngComm,* 14 (2012) 5158-5162.

[27] M.A. Manaia, V.C. Diculescu, E. de Souza Gil, A.M. Oliveira-Brett, Guaicolic spices curcumin and capsaicin electrochemical oxidation behaviour at a glassy carbon electrode, *J. Electroanal. Chem.,* 682 (2012) 83-89.

[28] G. Ziyatdinova, A. Nizamova, H. Budnikov, Voltammetric determination of curcumin in spices, *J. Anal. Chem.,* 67 (2012) 591-594.

[29] R.N. Moussawi, D. Patra, Modification of nanostructured ZnO surfaces with curcumin: fluorescence-based sensing for arsenic and improving arsenic removal by ZnO, *RSC Adv,* 6 (2016) 17256-17268.

[30] A. Djurišić, Y. Leung, K. Tam, L. Ding, W. Ge, H. Chen, S. Gwo, Green, yellow, and orange defect emission from ZnO nanostructures: Influence of excitation wavelength, *Appl. Phys. Lett.,* 88 (2006) 103107.

[31] K. Vanheusden, W. Warren, C. Seager, D. Tallant, J. Voigt, B. Gnade, Mechanisms behind green photoluminescence in ZnO phosphor powders, *J. Appl. Phys.,* 79 (1996) 7983-7990.

[32] A. van Dijken, E.A. Meulenkamp, D. Vanmaekelbergh, A. Meijerink, The kinetics of the radiative and nonradiative processes in nanocrystalline ZnO particles upon photoexcitation, *J. Phys. Chem. B,* 104 (2000) 1715-1723.

[33] S.K. Pal, J. Peon, A.H. Zewail, Biological water at the protein surface: dynamical solvation probed directly with femtosecond resolution, *Proc. Natl. Acad. Sci. USA,* 99 (2002) 1763-1768.

[34] K.K. Haldar, T. Sen, A. Patra, Au@ ZnO core− shell nanoparticles are efficient energy acceptors with organic dye donors, *J. Phys. Chem. C,* 112 (2008) 11650-11656.

[35] Q. Wang, J.-E. Moser, M. Grätzel, Electrochemical impedance spectroscopic analysis of dye-sensitized solar cells, *J. Phys. Chem. B,* 109 (2005) 14945-14953.

Chapter 6

Spectroscopic Studies on the Photosensitization of an Enzyme through Specific Molecular Recognition

6.1. Introduction: All crucial functions of living organisms are mediated by complex interconnected networks of functional units and associated proteins whose activity can be regulated by the application of internal and external stimuli. The majority of biological processes are controlled by chemical stimuli, such as ion concentrations and interactions with specific small-molecule effectors or inhibitors [1]. Molecular recognition, the ability of one molecule to 'recognize' another molecule through weak bonding interactions, is of fundamental importance to most processes within living systems [2]. The allosteric regulation of proteins by the binding of effector or inhibitor molecules at a site other than the active site is a powerful mechanism that drives complex biochemical reactions. Allosteric regulation is thus used to switch proteins from different conformational states to execute diverse functions [3]. The evolution of protein function is partially controlled by highly specific ligand binding sites that are crucial for the regulation of competing biological functions [4]. Furthermore, the reorganization of the chemical potential necessary for the action of a biochemical reaction can be attained by applying external stimuli. For example, changes in temperature can lead to the alteration of catalytic responses [5], and the application of mechanical forces can induce chemical transformations [6], among other reactions. Of the varied range of extrinsic stimuli, electromagnetic radiation is considered to be the most advantageous stimulus because it can precisely provide high spatio-temporal selectivity with strong dosage control [7].

Nature has evolved photo-responsive proteins such as rhodopsin, which is regulated by the *cis-trans* isomerization of its cofactor retinal [8]. These photo-

susceptible systems are generally composed of a photosensitive chromophore (photochromic molecule) that undergoes a chemical transformation (*e.g.*, photo-isomerization), subsequently controlling the conformation of the second functional unit (*e.g.*, a protein domain) [9]. A widely used approach to introduce a photochromic moiety is employed following the chemical modification of the protein [10].

Two fundamental classes of photoswitchable biomolecules have been developed: single-cycle and multicycle photoswitches. In single-cycle photoswitches, biomaterial is deactivated by the attachment of photosensitive chemical-protecting groups. Multicycle photoswitches can control enzymatic activities and ligand-binding affinities through the direct photoisomerization of chromophores and *via* the interactions of low-molecular-weight photochromic compounds with biomaterials [11]. These photoswitches enable either irreversible or reversible control of biological activities through biomolecular recognition events.

Mono-functional or bi-functional azobenzene derivatives and spiropyrans have been used as photoswitches to modulate biological activities. Reversible transitions of these compounds are mediated either through *cis*-*trans* or syn-anti isomerization [12]. Additionally, azobenzene derivatives have been shown to chemically modify peptides and proteins [13], altering the conformations and activities in a reversible manner in the presence of light [14-16]. In particular, photoswitchable proteins using azobenzene have been successfully employed to regulate protein function *via* light irradiation both *in vitro* [17] and *in vivo* [18]. Moreover, enzymes have been modified with mono-functional [7] or bi-functional azobenzene [9] derivatives in such a way as to enable the modulation of catalytic activity by light [19]. The photo-control of enzymatic activity offers opportunities to develop novel biotechnological applications and is considered as a promising area of research in near future.

In this chapter, we illustrate the photo-control of the enzymatic activity of the serine protease α-chymotrypsin (CHT) through a new class of photochromic material, dihydroindolizine (DHI) [20-22]. Photochromic DHI has received much attention owing to its remarkable photo-fatigue resistance and broad range of absorption [23]. Moreover, photochromic DHI is used to tether peptides and proteins *via* a maleimide functional group, which corresponds to absorption in the red region of the visible spectrum and in the near-IR spectral domain, indicating the potential for future use in *in vivo* applications [24, 25]. The basis of the photochromic behavior of DHI is light-induced reversible pyrroline ring opening, which transforms the molecule from a light yellow colored form (*cis*) to a red colored betaine form (*trans*) [26-28]. Betaines undergo a thermal back reaction to their corresponding DHI *cis* form by 1,5-electrocyclization [22, 29]. We have demonstrated that the recognition of photochromic DHI by CHT alters the enzymatic activity of CHT in a light-responsive manner. Circular dichroism (CD) spectra suggest that the protein structure remains unperturbed upon DHI recognition. To elucidate the position and orientation of the DHI moiety within CHT, Förster resonance energy transfer (FRET) strategy has been employed. 4-Nitrophenyl anthranilate (NPA), a covalently-attached chromophore at the active site of enzyme, has been used to obtain the distance between the active site and the DHI *cis*-isomer, which can then be correlated with the position of the DHI within CHT. In a similar manner, proflavin (PF) has been employed to measure the distance of the DHI *trans*-isomer from the CHT active site. Molecular docking has been utilized to specifically locate the position of both DHI isomers. The results of molecular docking correspond with our experimental findings. The molecular recognition of photochromic DHI by serine protease CHT leads to photo-responsive enzyme inhibition that could be used as a photo-controlled biological switch in numerous therapeutic applications.

6.2. Results and Discussion:

6.2.1. Allosteric Inhibitory Molecular Recognition of a Photochromic Dye by a Digestive Enzyme: Dihydroindolizine Makes Alpha-chymotrypsin Photo-responsive [30]: To elucidate the molecular recognition of photochromic DHI by CHT, we optically characterized the ligand. Figure 6.1.a shows the structures corresponding to the *cis*-isomer (present under dark conditions) and *trans*-isomer (present when the sample is exposed to UV-light) of the DHI ligand. In the presence of UV-light, ring opening of the *cis*-isomer *via* a cyclopropyl-allyl conversion leads to the formation of a colored *trans*-isomer (betaine). Subsequent slow thermal ring closure by 1,5-electrocyclization regenerates the *cis*-isomer [21]. The optical absorption spectrum of the *cis*-isomer shows a peak at 390 nm, which reduces in intensity when exposed to UV light, yielding a subsequent peak at 520 nm (Figure 6.1.b). These absorption bands can be assigned to the locally excited π-π* transition that occurs in the butadienyl-vinyl-amine chromophores. The inset demonstrates the visible color change of the sample from yellow to pink owing to the *cis* to *trans* conversion [23]. To evaluate the photochromic behavior of DHI, isomerization reaction kinetics are investigated in polar aprotic acetonitrile media. The *cis* to *trans* conversion is monitored by measuring the increase in absorbance at 520 nm. In a similar manner, the *trans* to *cis* conversion is followed by a decrease in absorbance at 520 nm. The rate constants for light triggered *cis* to *trans* conversion and *trans* to *cis* thermal relaxation have been depicted in Table 6.1.

Table 6.1. *Time constants of the isomerization reaction of DHI and CHT-DHI. The same lamp source is used for all the light triggered processes. Moreover, the temperature is maintained at 25°C.*

Systems	Time Constant (sec)	
	DHI (in acetonitrile)	CHT-DHI (in buffer)
Cis to *trans*	4.8	7.6
Trans to *cis*	53.3	342.9

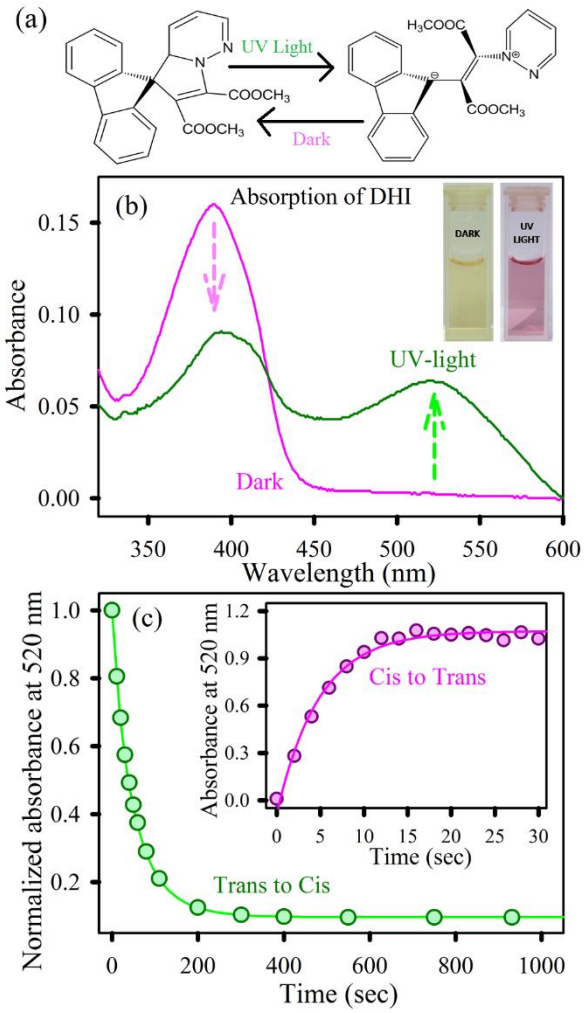

Figure 6.1. *(a) Structures of the cis and trans isomers of DHI (b) Absorption spectra of DHI: cis and trans isomers. The inset show visible color change from yellow to dark pink owing to conversion (c) Kinetics of the trans to cis conversion reaction of DHI in acetonitrile. Inset shows the corresponding cis to trans conversion rate.*

After the DHI and CHT interaction, the absorption spectra of CHT-DHI has a peak at 390 nm, indicative of the incorporation of DHI into CHT. This peak reduces its intensity and generates a peak at 520 nm when exposed to UV light (Figure 6.2.a), which is characteristic of the photoisomerization of DHI to the betaine form. The absorption spectra clearly suggest a reasonable recognition of DHI (in both *cis* and *trans* isomers) by CHT. To confirm the structural integrity of the enzyme, we performed CD experiments of CHT and CHT-DHI (in dark and light

conditions). Figure 6.2.a (inset) shows the CD spectra of CHT. These spectra indicate two minima at 202 nm and 232 nm, corresponding to the native secondary and tertiary structures of the protein, respectively [31]. Upon UV illumination, the CD spectrum of CHT (green line in Figure 6.2.a inset) shows no alteration. There is no perturbation observed with respect to these two peaks in CHT-DHI, suggesting the structural integrity of the protein after interaction with photochromic DHI. The photoisomerization rate of DHI when confined in the protein environment is drastically reduced. The *cis* to *trans* conversion rate of CHT-DHI in phosphate buffer is found to be decreased compared to free-DHI conversion (inset of Figure 6.2.b). The quantum yield of *cis* to *trans* conversion is calculated to be 0.34 for free-DHI,

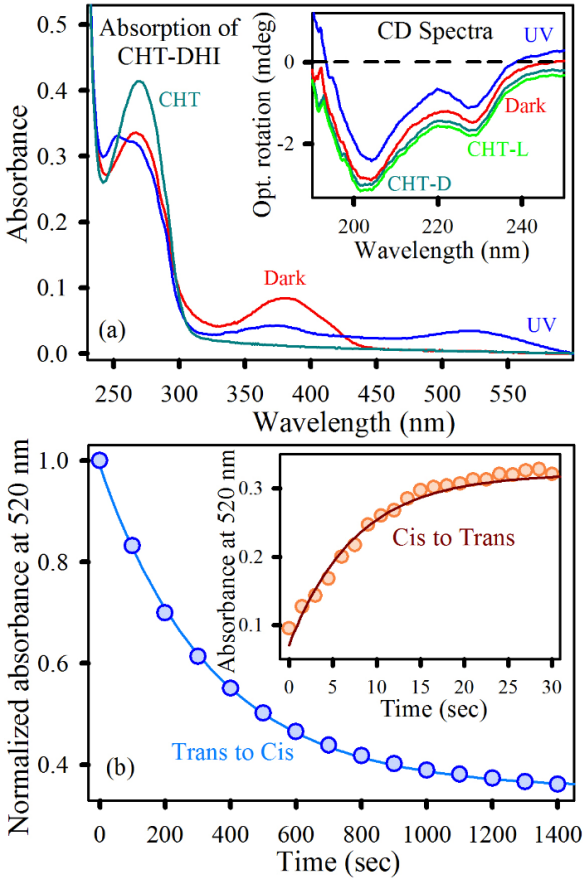

Figure 6.2. *(a) Absorption spectra of CHT and CHT-DHI. The inset shows the corresponding CD spectra (b) Kinetics of the trans to cis conversion reaction of CHT-DHI in phosphate buffer. Inset shows the corresponding cis to trans conversion rate.*

whereas, for CHT-DHI, it is 0.1. The values are consistent with solvent dependent quantum yield of photochromic ligands, available in literatures [32]. The significant reduction in *cis* to *trans* isomerization can be rationalized by the fact that the hydrophobic DHI *cis*-isomer can fit into various available hydrophobic binding sites present in the CHT structure [33]. The structural stability of the DHI *cis*-isomer into CHT might be increased by hydrophobic interactions resulting in a decreased isomerization rate. Moreover, the *trans* to *cis* conversion rate is decreased further compared to free-DHI (almost 50 times less), as shown in Figure 6.2.b. In the case of the DHI *trans*-isomer, stability further increases owing to the presence of several non-covalent interactions of the ionic *trans*-isomer with the more polar solvent (water), which significantly reduces the rate of *trans* to *cis* conversion.

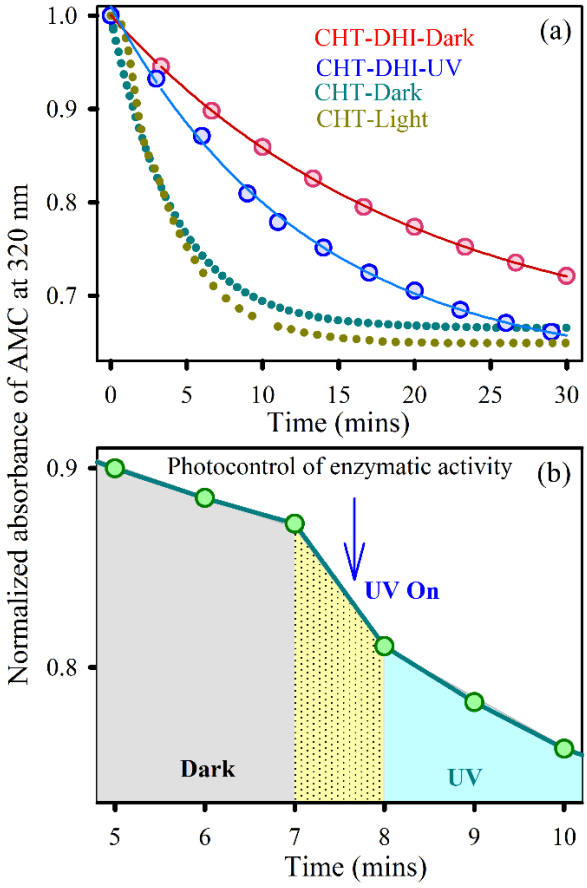

Figure 6.3. *(a) Enzymatic activity of CHT-DHI in absence and presence of UV light (b) Photo-control of enzymatic activity of CHT-DHI.*

After confirming the successful interaction between CHT and DHI in the dark and in the presence of UV light, we explored the corresponding enzymatic activities. Under both conditions, the enzymatic activities are inhibited compared to free-CHT, as shown in Figure 6.3.a. Under dark conditions, the activity is more hindered compared to the light-irradiated condition, indicating that the *cis*-isomer is more capable of inhibiting CHT activity compared to the *trans*-isomer. To evaluate the photo-control of enzymatic activity, we performed enzyme catalysis reactions both in dark and light conditions for 7-minute intervals. Figure 6.3.b clearly depicts the variation in reaction rate depending on the illumination condition. For the first 7 minutes in dark, the decay constant is much slower. However, for the next 7 minutes, the reaction rate increases in the presence of light (Table 6.2). Moreover, the photoresponsive enzymatic activity of CHT-DHI is recyclable for three consecutive cycles (data not shown) with a similar rate of reaction. This trend in enzymatic activity of CHT-DHI indicates that both the site of attachment and the conformational changes of DHI within the protein cavity are responsible for photo-controlled inhibition. Hence, the specific position of recognition and orientation of DHI in the protein cavity are two important parameters for an in-depth investigation of the molecular interactions.

Table 6.2. *Time constants of the enzymatic reaction of DHI and CHT-DHI. The same lamp source is used for all the light triggered processes. Moreover, the temperature is maintained at 25°C.*

Systems	Time Constant (min)	
	DHI (in acetonitrile)	CHT-DHI (in buffer)
CHT	4.0	4.0
CHT-DHI	100	5.0
	D1	L1
Dark then Light	100	4.8

Considering the hydrophobic nature of DHI, the possibility of interaction with the S1 pocket (active site) of CHT is more likely to take place and was hence investigated by the addition of the well-established fluorescent probes NPA and PF separately to the CHT-DHI complex. The simultaneous binding of DHI and either NPA or PF to CHT offers a unique opportunity to use Förster resonance energy transfer (FRET) as a tool to measure the relative position of the two probes one of which acting as a donor and the other as acceptor within the protein cavity. In this

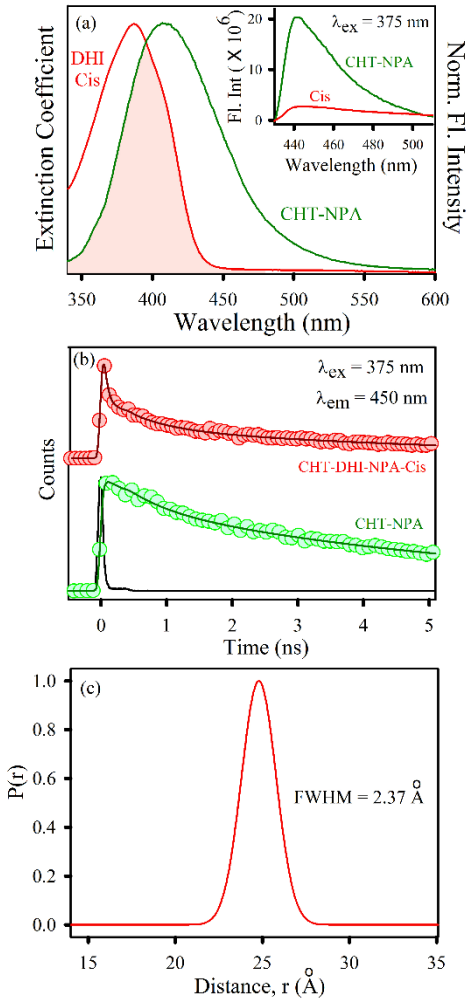

Figure 6.4. *(a) Overlap of the CHT-NPA emission and DHI cis absorption. Inset shows PL spectra of CHT-NPA and CHT-DHI-NPA upon excitation at 375 nm (b) The fluorescence transients of CHT-NPA (excitation at 375 nm) in the absence and in the presence of DHI cis collected at 450 nm are shown (c) Distribution of donor-acceptor distances between CHT-NPA and the DHI cis-isomer.*

case, CHT-NPA or CHT-PF is acting as the donor in the protein cavity and DHI acts as the acceptor. Figure 6.4.a shows a spectral overlap between CHT-NPA emission, and the absorption of the DHI *cis*-isomer suggests a possibility of FRET from CHT-NPA to DHI. The significant decrease in the steady-state emission of CHT-NPA upon DHI *cis*-isomer attachment is shown in the inset of Figure 6.4.a. The picosecond-resolved fluorescence decay profile of the donor CHT-NPA in the presence and absence of the acceptor DHI *cis*-isomer is obtained upon excitation with a 375-nm laser and is monitored at 450 nm (Figure 6.4.b). A shorter excited state lifetime of the CHT-NPA is clearly observed in the presence of the DHI *cis*-isomer. Details of the spectroscopic fitting parameters of the fluorescence transients are tabulated in Table 6.3. From FRET calculations, the distance between the donor CHT-NPA and acceptor DHI *cis*-isomer are determined to be 2.5 nm, and the energy transfer efficiency is calculated to be 79%. This observation confirms that the DHI *cis*-isomer attachment site is located at a distance of 2.5 nm from the NPA binding site. As documented in the literature, NPA binds at the hydrophobic active site of CHT [34], and it has been subsequently proven that the DHI *cis*-isomer binds at a site other than the S1 pocket. The distribution of donor–acceptor distances in the CHT-DHI (*cis)*-NPA (Figure 6.4.c) reveals an internal fluctuation with a full-width half-maximum (FWHM) of 2.37 Å. The relative position of the DHI *cis*-isomer is located at a distance of 25 ± 2.37 Å from the active site of CHT. The absorption spectra of the DHI *trans*-isomer overlaps with the emission of CHT-NPA and shows a faster excited state lifetime with an energy transfer efficiency of 74% (data not shown).

However, to confirm the sole contribution of the *trans*-isomer, we employed the simultaneous binding of PF and DHI in CHT, enabling the possibility of energy transfer from CHT-PF (donor) to the DHI *trans*-isomer (*i.e.*, when illuminated with UV light). The spectral overlap of the donor CHT-PF emission with the DHI *trans*-isomer absorption spectrum is shown in Figure 6.5.a. The steady-state fluorescence quenching of CHT-DHI (*trans*)-PF compared to CHT-DHI (*cis*)-PF is evident (Figure

6.5.a). The fluorescence decay profile of the donor CHT-PF in the absence of the acceptor DHI (Figure 6.5.b inset) and in the presence of the acceptor DHI in both isomers (Figure 6.5.b) are obtained upon excitation with a 375 nm laser and monitoring at 520 nm. The excited state lifetime of the CHT-PF quenches in the CHT-DHI (*trans*)-PF, indicating the presence of an energy transfer process.

Table 6.3. *Picosecond-resolved fluorescence transient lifetime* [a]

	System	τ_1 (ns)	τ_2 (ns)	τ_3 (ns)	τ_{avg} (ns)
Fluorescence transient lifetime	CHT-NPA		0.6 (29.6%)	5.9 (70.4%)	4.4
	CHT-DHI-NPA-*Cis*	0.04 (71.5%)	0.6 (14.7%)	5.7 (13.8%)	0.9
	CHT-DHI-NPA-*Trans*	0.07 (51%)	0.6 (31%)	5.1 (18%)	1.2
	CHT-PF		0.4 (16%)	4.8 (84%)	4.1
	CHT-DHI-PF-*Cis*		0.3 (29.1%)	4.5 (70.9%)	3.3
	CHT-DHI-PF-*Trans*	0.067 (40.5%)	1.0 (32.4%)	4.6 (27.1%)	1.6
FRET parameters	System	J (λ)	R_0 (Å)	Efficiency	r_{DA} (nm)
	CHT-DHI-NPA-*Cis*	1.426×10^{14}	31.1	79.3	2.5
	CHT-DHI-PF-*Trans*	0.488×10^{15}	35.56	61.2	3.3

[a] *The emission (monitored at 450 nm for NPA systems and at 520 nm for PF systems) was detected using an excitation laser at 375 nm. Numbers in parentheses indicate relative contributions. The reported lifetimes carry ~5% uncertainties.*

The details of the spectroscopic parameters and the fitting parameters of the fluorescence decays can be found in Table 6.3. From FRET calculations, the distance between the donor CHT-PF and acceptor DHI trans-isomer is determined to be 3.3 nm. The energy transfer efficiency is calculated to be 61%. Figure 6.5.c depicts the distribution of the donor–acceptor distances in the CHT-DHI (*trans*)-PF, revealing an internal fluctuation with a full-width half-maximum (FWHM) of 2.5 Å. PF is also

known to be an active site binding inhibitor [35] of CHT, and it can be suggested that the relative position of the DHI *trans*-isomer is at a distance of 33±2.5 Å from

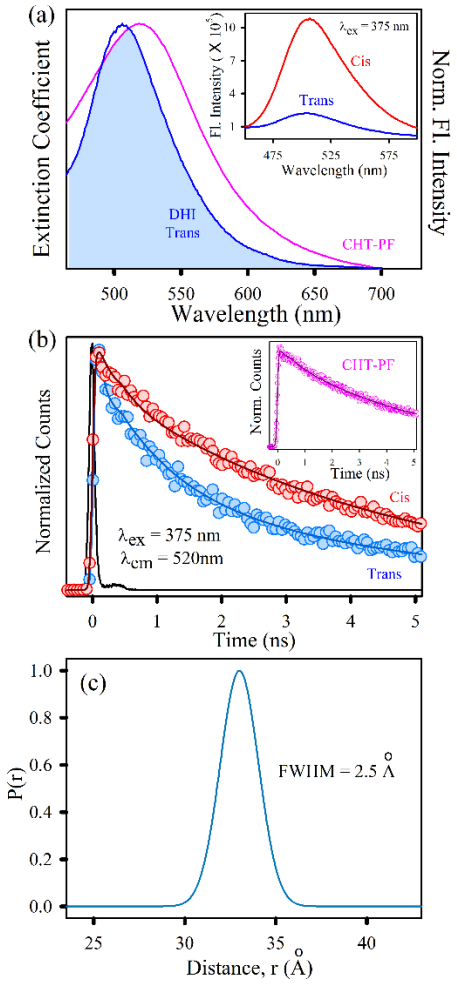

Figure 6.5. *(a) The overlap of the CHT-PF emission and DHI trans absorption. Inset shows the PL spectra of CHT-DHI-PF cis and CHT-DHI-PF trans upon excitation at 375 nm (b) The fluorescence transients of CHT-DHI-PF (excitation at 375 nm) in cis and in trans forms collected at 520 nm are shown. Inset depicts the fluorescence transients of CHT-PF (c) Indicates the distribution of donor-acceptor distances between the CHT-PF and DHI (trans).*

the CHT active site. Because enzymatic inhibition does not result from competition with the substrate at the Ser-195-His-57 active site, inhibition must result from other interactions with a control or allosteric site. This allosteric site may be hydrophobic in nature, and thus the hydrophobic inhibitor may bind *via* electrostatic and hydrophobic interactions. These interactions result in an unfavorable

conformational change at some different sites on the enzyme, significantly hampering its enzymatic activity [36].

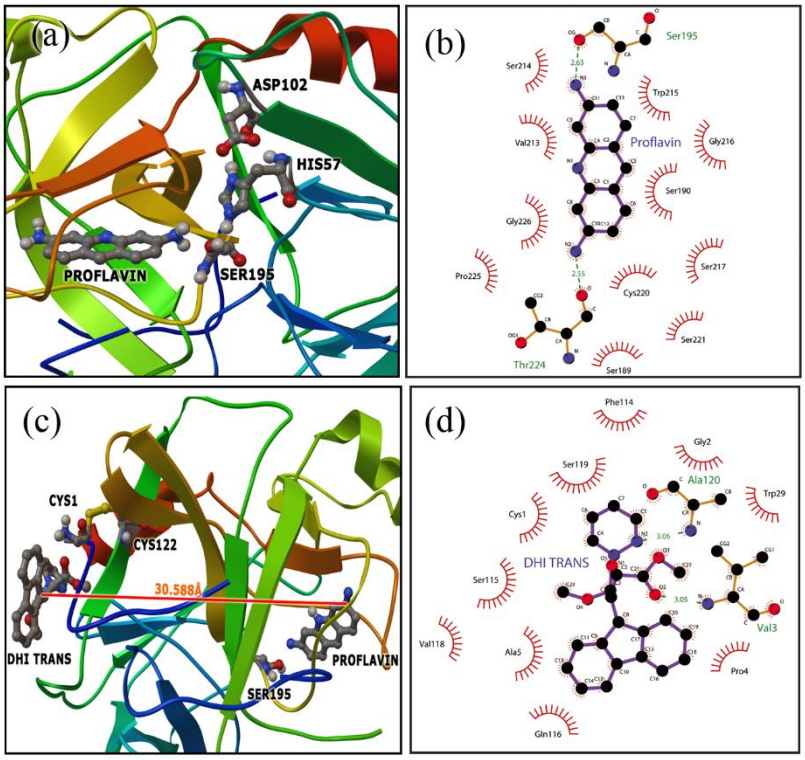

Figure 6.6. *(a) Relative position of PF in CHT cavity (b) Molecular contacts between the amino acid residues of CHT and PF (c) Relative position of the DHI trans-isomer in the CHT-PF cavity (d) Molecular contacts between the amino acid residues of CHT-PF and the DHI trans-isomer.*

To investigate the specific site of interactions between DHI and CHT, flexible docking studies were performed. We first employed PF as the ligand and CHT as the macromolecule. The most likely ligand binding modes are obtained by extracting the lowest energy conformation from the largest cluster (Figure 6.6.a). The flexible docking results clearly suggest that PF binds near the catalytic triad. Moreover, within the flexible docking binding sites of PF, there are possible hydrogen bond interactions between the N3 of PF and Ser-195 (2.63 Å) and between the N2 of PF and Thr 224 (2.55 Å) (Figure 6.6.b). Additionally, Trp-215, Ser-190, Gly-226, Val-213 and Cys-220 could provide additional hydrophobic force to stabilize the complex (Figure 6.6.b). The lowest energy structure obtained from CHT-PF in a blind docking calculation is considered to be the macromolecule for evaluating the

site of DHI interaction. Accordingly, the DHI *trans*-isomer is considered to be the flexible ligand and CHT-PF, the macromolecule. The lowest energy conformer occupies a site near the Cys-1-Cys-122 ANS binding hydrophobic site. The distance between the base of PF and DHI is measured to be 30.5 Å (Figure 6.6.c), which is consistent with our experimental findings. There are possible hydrogen bond interactions between the N2 of DHI and Ala-120 (3.06 Å) and between the O2 of DHI and Val-3 (3.05 Å). Additionally, Ser-119, Cys-1, Ala-5 and Gln-116 residues could provide extra hydrophobic force to stabilize the complex and several electrostatic interactions are also present.

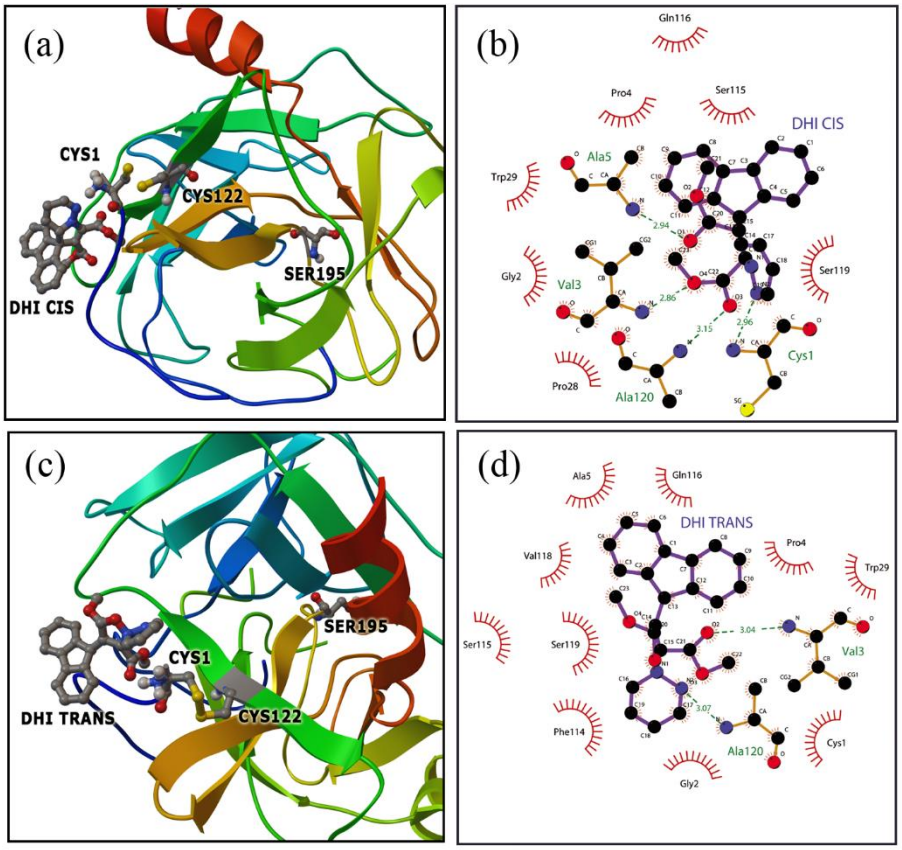

Figure 6.7. *(a) Relative position of the DHI cis-isomer in the CHT cavity (b) Molecular contacts between the amino acid residues of CHT and DHI cis-isomer (c) Relative position of the DHI trans-isomer in the CHT cavity (d) Molecular contacts between the amino acid residues of CHT and DHI trans-isomer.*

Finally, flexible docking using both DHI isomers separately as the ligand and CHT as the macromolecule suggests that both isomers of DHI are bound to the same

site in CHT (near the hydrophobic Cys-1-Cys-122). However, the difference in orientation and possible various interactions leads to dissimilarity with respect to enzymatic activities. There are four possible hydrogen bond interactions between the N2 of DHI and Cys-1 (2.96 Å), between the O4 of DHI and Val-3 (2.86 Å), between the O1 of DHI and Ala-5 (2.94 Å) and between the O3 of DHI and Ala-120 (3.15 Å) for the DHI *cis*-isomer, whereas the *trans*-isomer is able to form two hydrogen bonds between the O2 of DHI and Val-3 (3.04 Å) and between the N2 of DHI and Ala-120 (3.07 Å) (Figure 6.7). The corresponding electrostatic and hydrophobic interactions with various amino acid residues are also distinct in the case of both DHI isomers. The hydrophobic attachment of a molecule to a control site of an enzyme accompanying non-covalent interactions develops an unfavorable conformation, leading to a less effective active site for enzymatic action. In this study, the *cis*-isomer is more hydrophobic and interacts with the protein cavity to a greater extent compared to the *trans*-isomer. Therefore, a higher perturbation occurs with regard to its enzymatic activity (allosteric inhibition) compared to the *trans*-isomer, which is consistent with our experimental findings. Thus, the diversity in molecular recognition of a photochromic ligand under dark and light conditions leads to the photo-control of enzymatic action.

6.3. Conclusion: In summary, we investigated the molecular basis of the photo-control of serine protease α-chymotrypsin (CHT) enzymatic activity *via* the incorporation of a new class of synthesized photochromic material, dihydroindolizine (DHI). Photo-fatigue resistance DHI exhibits a broad range of absorption and possesses a variety of prospective applications. The light-induced reversible pyrroline ring opening, and the thermal back recovery reaction are responsible for photochromism. We have demonstrated that the recognition of photochromic DHI by CHT inhibits enzymatic activity in a light-responsive manner. Circular dichroism studies suggest no perturbation in the secondary structure of the enzyme structure upon interaction with DHI. Moreover, steady-state absorption studies suggest that DHI interacts with the protein cavity. To

elucidate the position and orientation of the DHI moiety within CHT under dark and UV-illuminated conditions, we applied Förster resonance energy transfer (FRET). A covalently attached chromophore at the active site of the enzyme 4-nitrophenyl anthranilate (NPA) was employed to obtain the distance between the active site and the DHI *cis*-isomer. A distance of 25 Å revealed the possible location of the DHI *cis*-isomer at an additional hydrophobic site rather than the catalytic center. In a similar manner, using the probe proflavin (PF), the distance of the DHI *trans*-isomer from the active site of CHT was estimated to be 33 Å. Finally, using molecular docking simulations, the locations of both DHI isomers were identified to be near the hydrophobic Cys-1-Cys-122 region. The relative orientations and variations in the electrostatic or hydrophobic interactions for both DHI isomers within the protein cavity are responsible for altering enzymatic activity. Thus, the diversity of the molecular recognitions of a photochromic ligand leads to photo-controlled enzymatic modulation, which could be relevant as a photo-controlled biological switch in the near future.

References

[1] R.S. Stoll, S. Hecht, Artificial light-gated catalyst systems, *Angew. Chem.,* 49 (2010) 5054-5075.

[2] R.E. Babine, S.L. Bender, Molecular recognition of protein-ligand complexes: applications to drug design, *Chem. Rev.,* 97 (1997) 1359-1472.

[3] R.A. Laskowski, N.M. Luscombe, M.B. Swindells, J.M. Thornton, Protein clefts in molecular recognition and function, *Protein. Sci.,* 5 (1996) 2438-2452.

[4] M.F. Dunn, Protein–ligand interactions: general description, in: eLS, 2007.

[5] M.E. Peterson, R.M. Daniel, M.J. Danson, R. Eisenthal, The dependence of enzyme activity on temperature: determination and validation of parameters, *Biochem. J.,* 402 (2007) 331-337.

[6] A. Piermattei, S. Karthikeyan, R.P. Sijbesma, Activating catalysts with mechanical force, *Nat. Chem.,* 1 (2009) 133-137.

[7] A. Goulet-Hanssens, C.J. Barrett, Photo-control of biological systems with azobenzene polymers, *J. Polym. Sci. A Polym. Chem.,* 51 (2013) 3058-3070.

[8] D.L. Farrens, C. Altenbach, K. Yang, W.L. Hubbell, H.G. Khorana, Requirement of rigid-body motion of transmembrane helices for light activation of rhodopsin, *Science,* 274 (1996) 768-770.

[9] B. Schierling, A.-J. Noël, W. Wende, E. Volkov, E. Kubareva, T. Oretskaya, M. Kokkinidis, A. Römpp, B. Spengler, A. Pingoud, Controlling the enzymatic activity of a restriction enzyme by light, *Proc. Natl. Acad. Sci. U.S.A.,* 107 (2010) 1361-1366.

[10] T. Shimoboji, E. Larenas, T. Fowler, S. Kulkarni, A.S. Hoffman, P.S. Stayton, Photoresponsive polymer–enzyme switches, *Proc. Natl. Acad. Sci. U.S.A.,* 99 (2002) 16592-16596.

[11] I. Willner, S. Rubin, Control of the structure and functions of biomaterials by light, *Angew. Chem.,* 35 (1996) 367-385.

[12] T.S. Zatsepin, L.A. Abrosimova, M.V. Monakhova, A. Pingoud, E.A. Kubareva, T.y.S. Oretskaya, Design of photocontrolled biomolecules based on azobenzene derivatives, *Russ. Chem. Rev.,* 82 (2013) 942-963.

[13] J.R. Kumita, D.G. Flint, G.A. Woolley, O.S. Smart, Achieving photo-control of protein conformation and activity: producing a photo-controlled leucine zipper, *Farad. Discuss.,* 122 (2003) 89-103.

[14] J.R. Kumita, O.S. Smart, G.A. Woolley, Photo-control of helix content in a short peptide, *Proc. Natl. Acad. Sci. U.S.A.,* 97 (2000) 3803-3808.

[15] U. Kusebauch, S.A. Cadamuro, H.J. Musiol, M.O. Lenz, J. Wachtveitl, L. Moroder, C. Renner, Photocontrolled folding and unfolding of a collagen triple helix, *Angew. Chem.,* 45 (2006) 7015-7018.

[16] F. Zhang, A. Zarrine-Afsar, M.S. Al-Abdul-Wahid, R.S. Prosser, A.R. Davidson, G.A. Woolley, Structure-based approach to the photocontrol of protein folding, *J. Am. Chem. Soc.,* 131 (2009) 2283-2289.

[17] S. Loudwig, H. Bayley, Photoisomerization of an individual azobenzene molecule in water: an on-off switch triggered by light at a fixed wavelength, *J. Am. Chem. Soc.,* 128 (2006) 12404-12405.

[18] M. Banghart, K. Borges, E. Isacoff, D. Trauner, R.H. Kramer, Light-activated ion channels for remote control of neuronal firing, *Nat. Neurosci.,* 7 (2004) 1381-1386.

[19] I. Willner, S. Rubin, A. Riklin, Photoregulation of papain activity through anchoring photochromic azo groups to the enzyme backbone, *J. Am. Chem. Soc.,* 113 (1991) 3321-3325.

[20] G. Hauck, H. Dürr, 1, 8a-Dihydroindolizines as Components of Novel Photochromic Systems, *Angew. Chem.,* 18 (1979) 945-946.

[21] H. Dürr, Perspectives in photochromism: a novel system based on the 1, 5-electrocyclization of heteroanalogous pentadienyl anions, *Angew. Chem.,* 28 (1989) 413-431.

[22] T.B. Shrestha, J. Melin, Y. Liu, O. Dolgounitcheva, V.G. Zakrzewski, M.R. Pokhrel, E. Gogritchiani, J.V. Ortiz, C. Turró, S.H. Bossmann, New insights in the

photochromic spiro-dihydroindolizine/betaine-system, *Photochem. Photobiol. Sci.,* 7 (2008) 1449-1456.

[23] S.A. Ahmed, Z.A. Hozien, A.-M.A. Abdel-Wahab, S.Y. Al-Raqa, A.A. Al-Simaree, Z. Moussa, S.N. Al-Amri, M. Messali, A.S. Soliman, H. Dürr, Photochromism of dihydroindolizines. Part 16: Tuning of the photophysical behavior of photochromic dihydroindolizines in solution and in polymeric thin film, *Tetrahedron,* 67 (2011) 7173-7184.

[24] T.B. Shrestha, M. Kalita, M.R. Pokhrel, Y. Liu, D.L. Troyer, C. Turro, S.H. Bossmann, H. Dürr, Maleimide-functionalized photochromic spirodihydroindolizines, *J. Org. Chem.,* 78 (2012) 1903-1909.

[25] T. Hartmann, T.B. Shrestha, S.H. Bossmann, C. Hübner, A. Renn, H. Dürr, A light-induced photochromic nanoswitch capable of non-destructive readout via fluorescence emission: cluster vs. single-molecule excitation of dihydroindolizines, *Photochem. Photobiol. Sci.,* 8 (2009) 1172-1178.

[26] O.F. Mohammed, S.A. Ahmed, E. Vauthey, E.T. Nibbering, Photoinduced ring-opening of a photochromic dihydroindolizine derivative monitored with femtosecond visible and infrared spectroscopy, *J. Phys. Chem. A,* 113 (2009) 5061-5065.

[27] A. Fernando, A.P. Malalasekera, J. Yu, T.B. Shrestha, E.J. McLaurin, S.H. Bossmann, C.M. Aikens, Refined insights in the photochromic spiro-dihydroindolizine/betaine system, *J. Phys. Chem. A,* 119 (2015) 9621-9629.

[28] S.A. Ahmed, I.I. Althagafi, B.H. Asghar, K.S. Khairou, H.A. Muathen, Photochromism of dihydroindolizines. Part XX: Synthesis and photophysical behavior of fluorenyldihydroindolizines photochromes based "Click" chemistry strategy, *J. Photochem. Photobiol. A,* 328 (2016) 163-170.

[29] A. Fernando, T.B. Shrestha, Y. Liu, A.P. Malalasekera, J. Yu, E.J. McLaurin, C. Turro, S.H. Bossmann, C.M. Aikens, Insights from theory and experiment on the photochromic spiro-dihydropyrrolo–pyridazine/betaine system, *J. Phys. Chem. A,* 120 (2016) 875-883.

[30] D. Bagchi, A. Ghosh, P. Singh, S. Dutta, N. Polley, I.I. Althagafi, R.S. Jassas, S.A. Ahmed, S.K. Pal, Allosteric inhibitory molecular recognition of a photochromic dye by a digestive enzyme: dihydroindolizine makes α-chymotrypsin photo-responsive, *Sci. Rep.,* 6 (2016) 34399.

[31] S.S. Narayanan, S.K. Pal, Structural and functional characterization of luminescent silver-protein nanobioconjugates, *J. Phys. Chem. C,* 112 (2008) 4874-4879.

[32] X. Chen, N.I. Islamova, R.V. Robles, W.J. Lees, Photochromic properties of a water-soluble methyl carboxylic acid indolylfulgimide, *Photochem. Photobiol. Sci,* 10 (2011) 1023-1029.

[33] D. Banerjee, S.K. Srivastava, S.K. Pal, Spectroscopic studies on ligand-enzyme interactions: complexation of α-chymotrypsin with 4', 6-diamidino-2-phenylindole (DAPI), *J. Phys. Chem. B,* 112 (2008) 1828-1833.

[34] R.P. Haugland, L. Stryer, A fluorescent probe at the active site of alpha-chymotrypsin, *Conf. Biopolym.,* 1 (1967) 321-333.

[35] A. Glazer, Spectral studies of the interaction of alpha-chymotrypsin and trypsin with proflavine, *Proc. Natl. Acad. Sci. U.S.A.,* 54 (1965) 171-176.

[36] R.N. Smith, C. Hansch, Hydrophobic interaction of small molecules with. alpha.-chymotrypsin, *Biochemistry,* 12 (1973) 4924-4937.

Chapter 7

Spectroscopic Studies on Photosensitization of a Drug Delivery Vehicle for Enhanced Biological Functionality

7.1. Introduction: Over the past two decades, photodynamic therapy has been harnessed in the treatment of a broad range of diseases [1, 2]. The therapeutic action is based on topical application of a photosensitive drug (photosensitizer) followed by irradiation usually in the ultraviolet-A (UVA: 320-400 nm) or visible (Vis: 400-720 nm) region of the spectrum [3, 4]. The photosensitizer will absorb the radiation and conduct the excitation energy into the tissue. This phenomenon leads to an array of photochemical-redox, and/or radical reactions [5]. The family of linear furocoumarins and their derivatives more customarily known as Psoralen (PSO), have been shown to be active dermal photosensitizing agents in presence of UVA [6-8]. PSO intercalates with DNA upon irradiation with UVA and subsequently it forms adduct with pyrimidine base of the opposite strands of DNA resulting in cross-linking in DNA strands [9, 10]. These result in inhibition of cell division and thus PSO followed by UV radiation is widely used for treatment of psoriasis [11, 12].

Efficacy of a drug depends on its penetration capability within the phospholipid membrane of the cell to reach their cellular targets [13]. The major difficulty of naturally occurring PSO is insolubility in water which leads to weak percutaneous permeability and poor deposition in the skin [14, 15]. The poor insolubility of the drug usually entails to frequent administration with the risk of adverse reactions [15]. Topical delivery of drugs by liposomal formulations has attracted considerable interest in recent decades because of the improved

therapeutic effects [16, 17]. However, classical liposomes are of little use as they cannot penetrate the cellular or bacterial membrane [18]. On the other hand, several research works indicate that ethosomes, which is in a class of liposomes containing some amount of ethanol in the core could be a better tool for sub-dermal delivery of macromolecules [19, 20]. Earlier it has been shown that increase in the concentration of ethanol from 20 to 45% in ethosome, the drug entrapment efficiency improves owing to an elevation in the fluidity of the membranes [21]. There are several *in vitro* and *in vivo* studies which demonstrate enhanced skin permeation and bioavailability of different therapeutic agents from biocompatible ethosomal formulation [22, 23]. For instance, Dubey et. Al, (2010) prepared an ethosomal formulation of Indinavir, an anti-HIV drug, and investigated their augmented transdermal delivery potential [24]. Previous studies report the delivery of significant photosensitizers using zinc oxide nanoparticles (ZnO NPs) as competent drug delivery vehicle where an increased efficacy of the phototherapeutic drugs upon conjugation with ZnO NPs has also been successfully determined [25-27].

Although, research studies have reported topical delivery of PSO via ethosomes [28], very little is known about the photoinduced dynamics of PSO encapsulated in the drug delivery vehicle. In the present study, we synthesized ethosomes of 110 nm vesicular size and entrapped PSO in the ethosomal formulation. PSO-ethosome was characterized by UV-Vis absorption and steady state fluorescence spectroscopic methods and dynamic light scattering (DLS) studies. Picosecond-resolved Förster Resonance Energy Transfer (FRET) was exploited to confirm the colocalization of PSO in ethosomes with crystal violet (CV), a well-known ethosome-binding organic dye [29]. After thorough characterisation of the interfacial events, PSO-ethosome was evaluated for its photoinduced antibacterial activities towards gram-negative *Escherichia coli* (*E. coli*) and gram-positive *Staphylococcus aureus* (*S. aureus*).

The life-threatening bacterial diseases originates due to the formation of biofilms, making the bacterial infections challenging to cure. The extracellular polymeric substances (EPS) comprising the biofilm prevent the penetration of drug into the biofilm [30, 31]. Thus, we finally employ PSO-ethosome to study eradication of biofilm as this requires efficient penetration and accumulation of the drug into the biofilm network. Crystal violet assay was used to assess the anti-biofilm activity of *E. coli* and *S. aureus* with PSO-ethosomes [32]. We further performed scanning electron microscopy to observe the morphological changes of the biofilm upon treatment with PSO-ethosome in presence of UVA. Therefore, our studies investigate a permeation enhancing carrier, ethosome, which facilitate the transport of PSO through the biological barrier, bacterial membrane or cell wall. This may result in an alternative use and an enhanced efficiency of ethosomes as drug delivery vehicle for antibiotic resistant biofilms.

7.2. Results and Discussion:

7.2.1. Essential Dynamics of an Effective Phototherapeutic Drug in a Nanoscopic Delivery Vehicle: Psoralen in Ethosome for Biofilm Treatment [33]: Ethosome is a soft vesicle composed of phospholipids (PC), high concentration of ethanol and water. In our study, we have synthesized ethosomal solutions having characteristic spherical droplets with an average hydrodynamic diameter of 110 nm which were measured from the DLS instrument (inset of Figure 7.1.a). Absorption spectra of PSO in water-ethanol mixture and in ethosome are shown in Figure 7.1.a, which shows that PSO in water-ethanol mixture (red) has three peaks at 244 nm, 294 nm and 340 nm. PSO encapsulated in ethosome (blue) also shows three peaks with a base line upliftment due to scattering of colloidal ethosome. The transitions at 294 nm and 340 nm are reported to be resulting from $n \rightarrow \pi^*$ transition of non-bonding electrons on the C-2 carbonyl group in PSO and $\pi \rightarrow \pi^*$ transition of π electrons of PSO ring system respectively [7]. We have estimated that 88.7 μM PSO is associated with 3.4 μM ethosome. In other words, 26 PSO are found to be attached with each

ethosome vesicle. Emission spectra of PSO in water-ethanol mixture (red) and PSO-ethosomes (blue) (Figure 7.1.b) show that fluorescence intensity of PSO is quenched

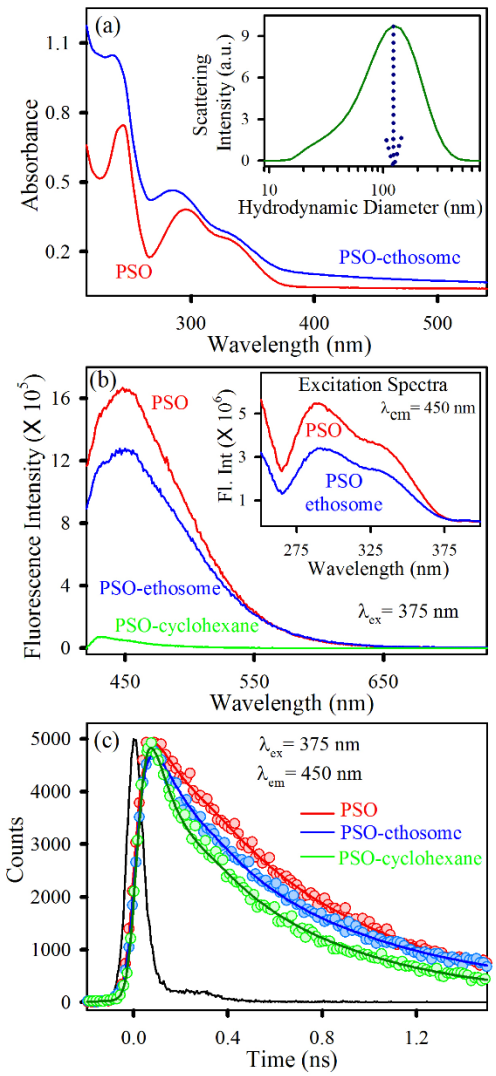

Figure 7.1. *(a) UV-Vis absorption spectra of PSO in water-ethanol mixture (red) and PSO-ethosome (blue). Inset shows hydrodynamic diameter of ethosome measured by DLS method (b) Room temperature emission spectra of PSO (red) and PSO-ethosome (blue) and PSO in cyclohexane (green). The excitation wavelength is 375 nm. Inset shows the excitation spectra of PSO (red) and PSO-ethosome (blue) (c) Shows the fluorescence transients of PSO in water-ethanol mixture (red), PSO-ethosome (blue) and PSO in cyclohexane (Green).*

upon encapsulation of PSO in the ethosomes. The emission quenching of PSO in a nonpolar medium, cyclohexane (green) is also shown in the Figure 7.1.b. The quantum yield of PSO in aqueous ethanol, ethosomes and cyclohexane are

estimated to be $1.0x10^{-2}$, $6.0x10^{-3}$ and $2.0x10^{-4}$ respectively consistent with the reported literature [34]. Studies on spectroscopic properties of PSO have reported that the energies of lowest excited states (singlet and triplet) of PSO are strongly dependent upon solvent polarity. With the increase in polarity of the solvent the energy level ordering of PSO is assumed to be changed and thereby fluorescence become predominant compared to non-radiative inter system crossing [34, 35]. Upon encapsulation into ethosome, polarity of the solvent around PSO decreases which results in quenching of fluorescence intensity without changing the emission maxima. The similarity of quantum yield of PSO in ethosomes with polar aqueous ethanol indicates the location of the probe at the interface. We have also recorded excitation spectra (Figure 7.1.b inset) of PSO in water-ethanol and PSO-ethosome, which are similar with corresponding absorption spectra. Figure 7.1.c shows picosecond resolved emission transients of PSO in various mediums including ethosomes. The numerical fitting of the transients reveals the average time constant 0.62 ns for aqueous ethanol and 0.34 ns for cyclohexane. In the ethosome the average time constant of 0.50 ns close to that of the aqueous ethanol revealing the location of PSO to be at the interface.

In order to study the co-localization of a model cationic drug with the hydrophobic DCM in the ethosome, we have used crystal violet (CV) and employed FRET strategy. Figure 7.2.a shows spectral overlap of energy donor DCM emission with the absorption spectrum of acceptor CV. A significant quenching in steady-state emission of DCM in presence of CV in the ethosome is observed, where DCM:CV concentration in the ethosomal mixture is 1:1 (inset of Figure 7.2.b). Picosecond-resolved fluorescence decay profile of DCM in absence (green) and in presence (blue) of CV was monitored at 620 nm upon excitation at 375 nm (Figure 7.2.b). The shorter component in decay profile suggests an excited state energy transfer process (Table 7.1). A FRET efficiency of ~75% with an average donor-acceptor distance of 5.8 nm was calculated for DCM–CV pair (Table 7.1). It is also

observed that the distance between DCM and CV is independent of detection wavelength by detecting fluorescence transients at different wavelengths (data not shown). This indicates the homogeneous distribution of DCM in ethosomal mixture. It is reported that the maximum thickness of phospholipid bilayer is 7.3 nm [36]. Therefore, the possible location of CV could be at the polar interface of the ethosome.

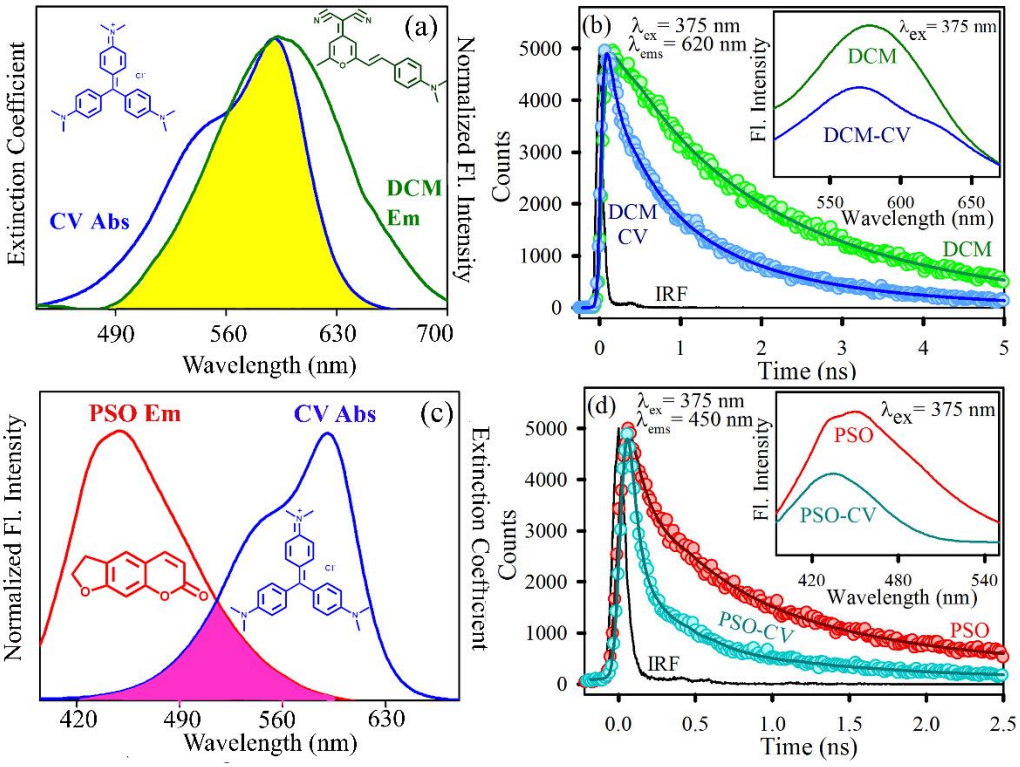

Figure 7.2. *(a) Shows the overlap of the DCM-ethosome emission and CV absorption in water (b) The picosecond-resolved fluorescence transients of DCM-ethosome (excited at 375 nm) in absence of CV (green) and in presence of CV (blue) are collected at 620 nm. Inset shows steady state emission spectra of DCM-ethosome in absence (green) and presence of CV (blue) (c) Shows the overlap of the PSO-ethosome emission and CV absorption in water (d) The picosecond-resolved fluorescence transients of PSO-ethosome (excited at 375 nm) in absence of CV (red) and in presence of CV (cyan) are collected at 450 nm. Inset shows steady state emission spectra of PSO-ethosome in absence (red) and in presence (cyan) of CV.*

After having an idea about the location of CV with respect to DCM, we exploited the spectral overlap of CV with PSO in order to study the localization of PSO in the ethosomes. A considerable spectral overlap of PSO emission with the absorption spectrum of CV is shown in Figure 7.2.c, where the concentration of PSO:

CV is 1:10, indicating possibility of FRET from PSO to CV in the ethosome. A significant quenching in steady-state emission of PSO in presence of CV in the ethosome is observed (inset of Figure 7.2.d). Picosecond-resolved fluorescence decay profile of PSO in ethosome in absence (red) and in presence (cyan) of CV was monitored at 450 nm upon excitation at 375 nm (Figure 7.3.d). The excited state lifetime (τ_{av}) of PSO reduces upon interaction with CV. The details of fitting parameters of the fluorescence decays are provided in Table 7.1. We have estimated the FRET efficiency to be ~84% and donor (PSO)-acceptor (CV) distance around 2.2 nm. The distance is almost independent of detection wavelength as there is no indication of change in lifetime by changing the detection wavelength. More details are provided in Table 7.1. Comparatively shorter donor-acceptor distance in case of PSO-CV can be attributed to the higher concentration of CV in the present case compared to former one.

Table 7.1. *Time-resolved fluorescence decay (excitation at 375 nm) and FRET data of PSO and DCM in ethosome in absence and presence of CV. Values in parentheses represent the relative weight percentage of the time component with a standard error of ca 10%.*

Fluorescence Transients	Wavelength (nm)	System	τ_1 (ns)	τ_2 (ns)	τ_3 (ns)	τ_{avg} (ns)	
	450	PSO	0.08 (51%)	0.58 (33%)	2.59 (16%)	0.65	
		PSO-CV	0.03 (83%)	0.22 (12%)	1.10 (05%)	0.11	
	620	DCM		0.72 (23%)	2.34 (77%)	1.97	
		DCM-CV	0.11 (36%)	0.61 (36%)	1.83 (28%)	0.77	
FRET parameters	Wavelength (nm)	System	Q_D	J(λ) (M^{-1} cm^{-1} nm^4)	E (%)	R_0 (nm)	R (nm)
	450	PSO-CV	6.0×10^{-3}	4.35×10^{15}	85	3.33	2.19
	620	DCM- CV	0.35	1.09×10^{16}	60	7.42	5.85

We have finally evaluated PSO-ethosome as an antimicrobial agent followed by a drug delivery system to inhibit the growth of bacterial biofilms. PSO-ethosome have employed as a potential photodynamic agent for the inhibition of growth of gram-negative *E. coli* and gram-positive *S. aureus*. For photodynamic therapy experiments, we have added PSO-ethosome (85 µM PSO) to bacterial cultures in the presence and absence of UV-A. The inhibition of bacterial growth after

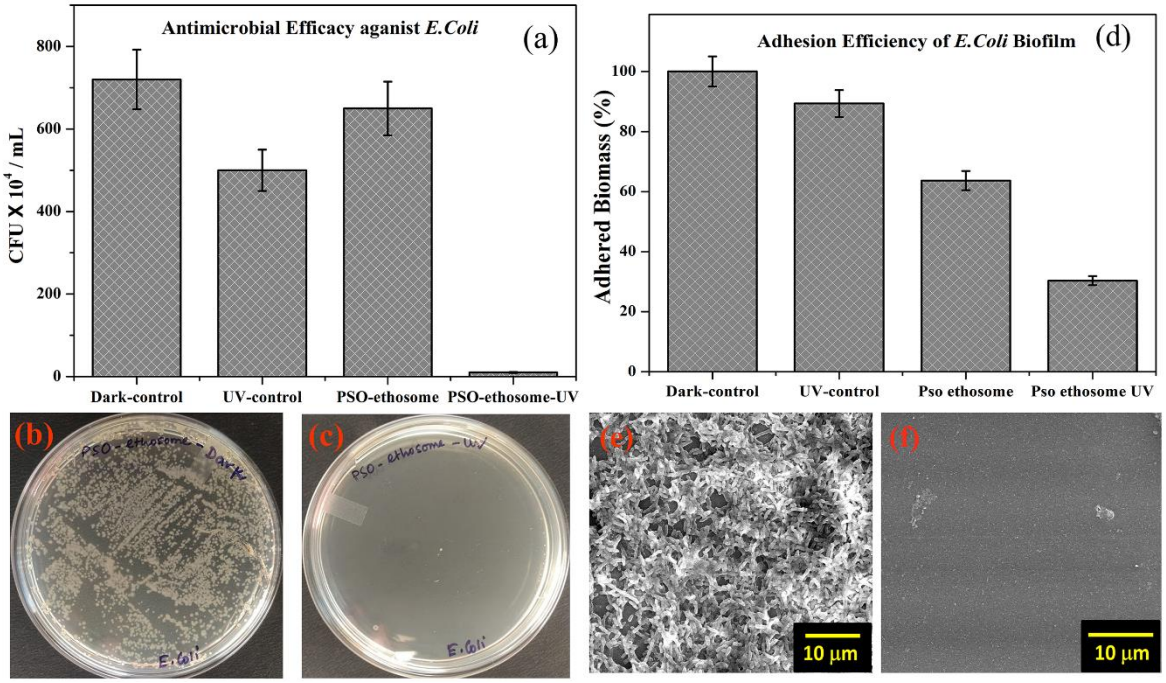

Figure 7.3. *(a) Antibacterial activity of PSO-ethosome against E. coli in the absence and presence of UVA (b) and (c) Shows images of PSO-ethosome treated E. coli. plates before and after UVA irradiation respectively (d) Adhesion efficiency of PSO-ethosome treated E. coli biofilms in absence and presence UVA irradiation. SEM images of biofilm of E. coli (e) without any treatment condition and (f) treated with PSO-ethosome followed by UVA illumination for 30 min.*

photodynamic treatment is clearly visible. For comparison, the colonies were counted for control and PSO-ethosome treated plates. The colony forming units (CFU) indicates insignificant antibacterial activity of PSO-ethosome in dark. In case of PSO-ethosome treated samples with UVA irradiation, the bacterial growth is inhibited sharply indicating immense photo-induced antimicrobial activity of PSO-ethosome. The maximum inhibition of *E. coli* is obtained for PSO-ethosome treated

samples where a 95% decrease in CFU is observed after photodynamic treatment (Figure 7.3.a). Figure 7.3.b and 7.3.c clearly indicate the pictures of *E. coli* cultures treated with PSO-ethosome in the absence and presence of UV-A light. The inhibition of bacterial growth after photodynamic treatment is clearly visible. The similar trend is observed for gram-positive bacteria *S. aureus* (Figure 7.4.a), demonstrating enormous photodynamic antibacterial activity of PSO-ethosome. The pictures of *S. aureus* cultured plates (Figure 7.4.b and 7.4.c) clearly show visual differences of PSO-ethosome treated bacteria in absence and presence of UVA. The control experiments using ethosome (no PSO) show no significant antibacterial effect.

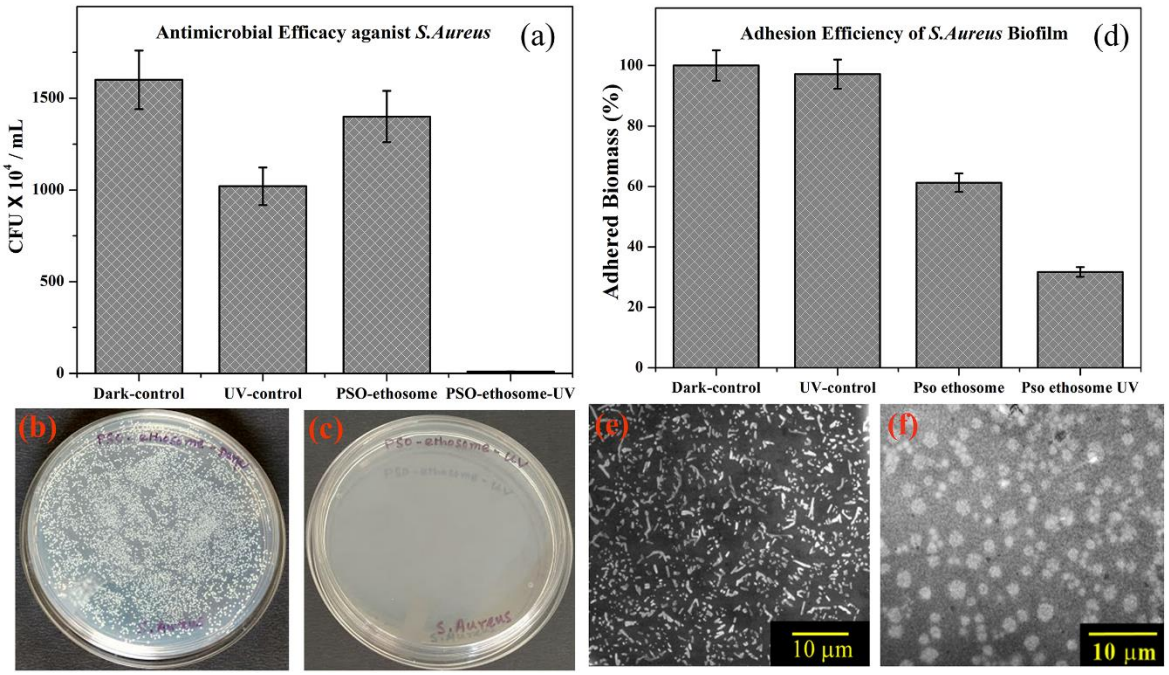

Figure 7.4. *(a) Antibacterial activity of PSO-ethosome against S. aureus in the absence and presence of UVA (b) and (c) Shows images of PSO-ethosome treated S. aureus plates before and after UVA irradiation respectively (d) Adhesion efficiency of PSO-ethosome treated S. aureus biofilms in absence and presence of UVA irradiation. SEM images of biofilm of S. aureus (e) without any treatment condition and (f) treated with PSO-ethosome followed by UVA illumination for 30 min.*

Biofilm is a microbial community that has a compact and complex structure and often encapsulated within a matrix of polymeric material that consists of intricate networks of cells attached to abiotic surfaces [37]. Upon formation of

biofilm microbes can resist antibiotics, immune cell challenge and can be deeply inserted into cracks and porosities of solid surfaces, metallic and non-metallic medical devices like catheters, implants, dental materials [38]. For our study, biofilm formation by *E. coli* and *S. aureus* was measured after 48 hours. Total adhered biomass of the biofilms was monitored through quantitative assay using crystal violet stain. There is a decrease in biomass (~ 30%) for both the bacteria (*E. coli* and *S. aureus*), treated with ethosome containing PSO. The bacterial biomass could be further reduced to ~60% when PSO-ethosome treated bacteria were exposed to UVA light for 30 min (Figure 7.3.d and 7.4.d). The structural and morphological changes of the biofilms are observed by taking SEM images [39]. Figure 7.3.e shows typical characteristics of *E. coli* biofilms and Figure 7.3.f shows samples treated with PSO-ethosome followed by UVA irradiation contain significantly less number of bacteria and the typical arrangement of biofilm is completely lost. The similar effect is observed for *S. aureus* biofilms (Figure 7.4.e and 7.4.f). The anti-biofilm activity of PSO-ethosome suggests ethanol entrapped in ethosome act as a permeation enhancer due to a synergistic mechanism between ethanol containing vesicles and bacterial membrane [40]. Our findings suggest that

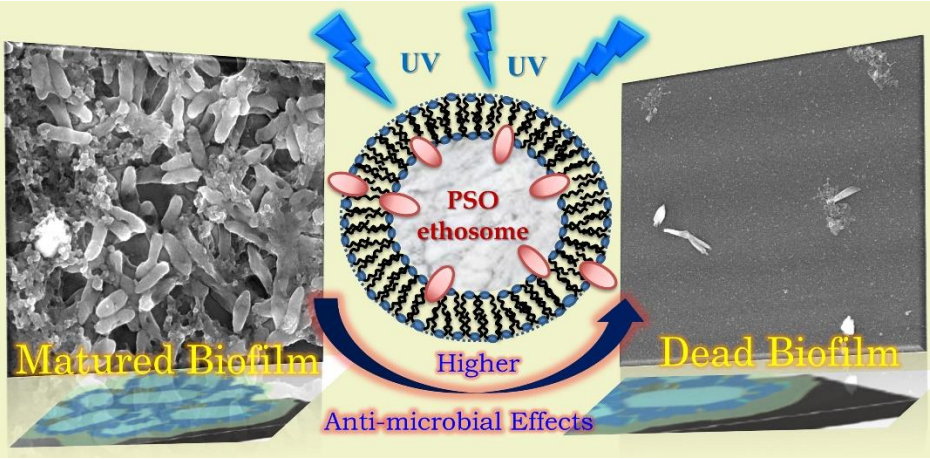

Scheme 7.1. *Photoinduced dynamics of Psoralen encapsulated in ethosomes favours destruction of bacterial infection.*

PSO-ethosome shows increased permeability and improved release rate as ethanol has fluidizing effect on phospholipid bilayers, which allow ethosome to more easily penetrate through bacterial cell wall. Therefore, drug containing ethosome shows more efficient photochemical activity for the inhibition of bacterial biofilm growth. The studies on photo-induced dynamics of PSO-ethosome as an efficient drug delivery vehicle will be helpful in designing future photodynamic agents.

7.3. Conclusion: In summary, we evaluated the photoinduced dynamics of Psoralen (PSO), a photobiologically important drug, upon encapsulation in ethosomes. We characterized PSO-ethosomes both structurally and spectroscopically. In addition, we performed time resolved studies to confirm the confined environments using model fluorophore. Picosecond-resolved Förster resonance energy transfer (FRET) technique revealed the binding of drug molecules in vesicles. It is inferred that there is a non-radiative energy transfer from PSO to crystal violet upon excitation with UVA light. Furthermore, the increase in cytotoxicity of PSO loaded ethosomes is found to be responsible for its better antimicrobial activities. The anti-biofilm activities in both the gram-negative and gram-positive bacteria are also confirmed. Hence, to our understanding the studies could pave the way in designing novel high potential therapeutic drugs with improved pharmacological efficacy to treat multi drug resistant bacteria induced diseases.

References

[1] T.J. Dougherty, C.J. Gomer, B.W. Henderson, G. Jori, D. Kessel, M. Korbelik, J. Moan, Q. Peng, Photodynamic therapy, *J. Natl. Cancer. Inst.,* 90 (1998) 889-905.

[2] M.R. Hamblin, T. Hasan, Photodynamic therapy: a new antimicrobial approach to infectious disease?, *Photochem. Photobiol. Sci.,* 3 (2004) 436-450.

[3] N. Mehraban, H.S. Freeman, Developments in PDT sensitizers for increased selectivity and singlet oxygen production, *Materials,* 8 (2015) 4421-4456.

[4] D.E.J.G.J. Dolmans, D. Fukumura, R.K. Jain, Photodynamic therapy for cancer, *Nat. Rev. Cancer.,* 3 (2003) 380-387.

[5] A.P. Castano, T.N. Demidova, M.R. Hamblin, Mechanisms in photodynamic therapy: part one—photosensitizers, photochemistry and cellular localization, *Photodiagnosis. Photodyn. Ther.* , 1 (2004) 279-293.

[6] S. Chimichi, M. Boccalini, B. Cosimelli, G. Viola, D. Vedaldi, F. Dall'Acqua, A convenient synthesis of psoralens, *Tetrahedron,* 58 (2002) 4859-4863.

[7] G.D. Cimino, Y.B. Shi, J.E. Hearst, Wavelength dependence for the photoreversal of a psoralen-DNA crosslink, *Biochemistry,* 25 (1986) 3013-3020.

[8] J.D. Laskin, E. Lee, E.J. Yurkow, D.L. Laskin, M.A. Gallo, A possible mechanism of psoralen phototoxicity not involving direct interaction with DNA, *Proc. Natl. Acad. Sci. U.S.A.,* 82 (1985) 6158-6162.

[9] F. Dall'Acqua, S. Marciani, G. Rodighiero, Inter-strand cross-linkages occurring in the photoreaction between psoralen and DNA, *FEBS Lett.,* 9 (1970) 121-123.

[10] J.E. Hearst, Psoralen photochemistry and nucleic acid structure, *J. Invest. Dermatol.,* 77 (1981) 39-44.

[11] A.B. Gottlieb, Psoriasis: emerging therapeutic strategies, *Nat. Rev. Drug. Discov.,* 4 (2005) 19-34.

[12] D.V. Briffa, A. Warin, Photochemotherapy in psoriasis: a review, *J. R. Soc. Med.,* 72 (1979) 440-446.

[13] Y.A. Hannun, L.M. Obeid, Principles of bioactive lipid signalling: lessons from sphingolipids, *Nat. Rev. Mol. Cell. Biol.,* 9 (2008) 139-150.

[14] B. Kammerau, U. Klebe, A. Zesch, H. Schaefer, Penetration, permeation, and resorption of 8-methoxypsoralen, *Arch. Dermatol. Res.,* 255 (1976) 31-42.

[15] D.J. dos Santos, L.A. Eriksson, Permeability of psoralen derivatives in lipid membranes, *Biophys. J.,* 91 (2006) 2464-2474.

[16] T.M. Allen, P.R. Cullis, Drug delivery systems: entering the mainstream, *Science,* 303 (2004) 1818-1822.

[17] A. Roy, N. Kundu, D. Banik, N. Sarkar, Comparative fluorescence resonance energy-transfer study in pluronic triblock copolymer micelle and niosome composed of biological component cholesterol: an investigation of effect of cholesterol and sucrose on the FRET parameters, *J. Phys. Chem. B,* 120 (2016) 131-142.

[18] R.M. Fielding, Liposomal drug delivery, *Clin. Pharmacokinet.,* 21 (1991) 155-164.

[19] E. Touitou, N. Dayan, L. Bergelson, B. Godin, M. Eliaz, Ethosomes — novel vesicular carriers for enhanced delivery: characterization and skin penetration properties, *J. Control. Release,* 65 (2000) 403-418.

[20] N. Dayan, E. Touitou, Carriers for skin delivery of trihexyphenidyl HCl: ethosomes vs. liposomes, *Biomaterials,* 21 (2000) 1879-1885.

[21] T. Parashar, R. Sachan, V. Singh, G. Singh, S. Tyagi, C. Patel, A. Gupta, Ethosomes: a recent vesicle of transdermal drug delivery system, *Int. J. Pharm. Life Sc.,* 2 (2013) 285-292.

[22] A. Ascenso, S. Raposo, C. Batista, P. Cardoso, T. Mendes, F.G. Praça, M.V.L.B. Bentley, S. Simões, Development, characterization, and skin delivery studies of related ultradeformable vesicles: transfersomes, ethosomes, and transethosomes, *Int. J. Nanomed.,* 10 (2015) 5837-5851.

[23] Y.-T. Zhang, L.-N. Shen, Z.-H. Wu, J.-H. Zhao, N.-P. Feng, Comparison of ethosomes and liposomes for skin delivery of psoralen for psoriasis therapy, *Int. J. Pharm.,* 471 (2014) 449-452.

[24] V. Dubey, D. Mishra, M. Nahar, V. Jain, N.K. Jain, Enhanced transdermal delivery of an anti-HIV agent via ethanolic liposomes, *Nanomedicine,* 6 (2010) 590-596.

[25] S. Sardar, S. Chaudhuri, P. Kar, S. Sarkar, P. Lemmens, S.K. Pal, Direct observation of key photoinduced dynamics in a potential nano-delivery vehicle of cancer drugs, *Phys. Chem. Chem. Phys.,* 17 (2015) 166-177.

[26] S. Chaudhuri, S. Sardar, D. Bagchi, S. Dutta, S. Debnath, P. Saha, P. Lemmens, S.K. Pal, Photoinduced dynamics and toxicity of a cancer drug in proximity of inorganic nanoparticles under visible light, *ChemPhysChem,* 17 (2016) 270-277.

[27] D. Bagchi, S. Chaudhuri, S. Sardar, S. Choudhury, N. Polley, P. Lemmens, S.K. Pal, Modulation of stability and functionality of a phyto-antioxidant by weakly interacting metal ions: curcumin in aqueous solution, *RSC Adv,* 5 (2015) 102516-102524.

[28] Y.-T. Zhang, L.-N. Shen, J.-H. Zhao, N.-P. Feng, Evaluation of psoralen ethosomes for topical delivery in rats by using in vivo microdialysis, *Int. J. Nanomed.,* 9 (2014) 669-678.

[29] S. Banerjee, N. Goswami, S.K. Pal, A potential carcinogenic pyrene derivative under Förster resonance energy transfer to various energy acceptors in nanoscopic environments, *ChemPhysChem,* 14 (2013) 3581-3593.

[30] L.-S. Wang, A. Gupta, V.M. Rotello, Nanomaterials for the Treatment of Bacterial Biofilms, *ACS Infect. Dis.,* 2 (2015) 3-4.

[31] D.G. Davies, M.R. Parsek, J.P. Pearson, B.H. Iglewski, J.t. Costerton, E. Greenberg, The involvement of cell-to-cell signals in the development of a bacterial biofilm, *Science,* 280 (1998) 295-298.

[32] M. Ishiyama, H. Tominaga, M. Shiga, K. Sasamoto, Y. Ohkura, K. Ueno, A combined assay of cell viability and in vitro cytotoxicity with a highly water-soluble tetrazolium salt, neutral red and crystal violet, *Biol. Pharm. Bull.,* 19 (1996) 1518-1520.

[33] D. Bagchi, S. Dutta, P. Singh, S. Chaudhuri, S.K. Pal, Essential dynamics of an effective phototherapeutic drug in a nanoscopic delivery vehicle: psoralen in ethosomes for biofilm treatment, *ACS Omega,* 2 (2017) 1850-1857.

[34] W.W. Mantulin, P.-S. Song, Excited states of skin-sensitizing coumarins and psoralens: spectroscopic studies, *J. Am. Chem. Soc.,* 95 (1973) 5122-5129.

[35] T.I. Lai, B.T. Lim, E. Lim, Photophysical properties of biologically important molecules related to proximity effects psoralens, *J. Am. Chem. Soc.,* 104 (1982) 7631-7635.

[36] C.-H. Huang, Phosphatidylcholine vesicles. Formation and physical characteristics, *Biochemistry,* 8 (1969) 344-352.

[37] R.J. Marano, H.J. Wallace, D. Wijeratne, M.W. Fear, H. San Wong, R. O'Handley, Secreted biofilm factors adversely affect cellular wound healing responses in vitro, *Sci. Rep.,* 5 (2015) 13296.

[38] X. Li, H. Kong, R. Mout, K. Saha, D.F. Moyano, S.M. Robinson, S. Rana, X. Zhang, M.A. Riley, V.M. Rotello, Rapid identification of bacterial biofilms and biofilm wound models using a multichannel nanosensor, *ACS Nano,* 8 (2014) 12014-12019.

[39] A.R. Granillo, M.G.M. Canales, M.E.S. Espíndola, M.A.M. Rivera, V.M.B. de Lucio, A.V.R. Tovar, Antibiosis interaction of Staphylococccus aureus on Aspergillus fumigatus assessed in vitro by mixed biofilm formation, *BMC Microbiol,* 15 (2015) 1-15.

[40] J.R. Morones-Ramirez, J.A. Winkler, C.S. Spina, J.J. Collins, Silver enhances antibiotic activity against gram-negative bacteria, *Sci. Transl. Med.,* 5 (2013) 190ra181.

Chapter 8

Spectroscopic Studies on a Hybrid Material of Red-light Active Dye with an Inorganic Oxide Material for Potential Photo-medicinal Application

8.1. Introduction: The utilization of nanomaterials for various biomedical aspects such as biosensors, drug-delivery, theranostics, and diagnosis is currently undergoing a dramatic expansion [1]. Nanomaterials, owing to their dimension driven unique physical and chemical properties, have appeared as a potential platform either being a delivery vehicle to transport drugs at the diseased site or as an active therapeutic agents [2]. However, the potential toxicity of nanomaterials upon long-term exposure is questionable and such treatments would be applied selectively for inhibiting the affected tissues while leaving the surrounding host cells healthy and intact [3]. This requires the nanoparticles (NPs) to be activated at the specific target organism [4]. Target specificity often depends on specific environmental signals such as temperature, pH, redox properties, enzymatic metabolism etc. which could be regulated through the application of external stimuli such as chemical stimuli (pH) or physical stimuli (light) [5, 6]. Hence, development of stimuli responsive nanomaterials is high on demand because of their multi-purpose and highly efficacious implementation [7-9].

Light mediated treatment namely photodynamic therapy PDT [10] involves a photosensitizers which could be activated by photon energy followed by production of light activated redox species (LARS) and/or reactive oxygen species (ROS) for therapeutics use. The spatial and temporal localization using light sources provides prevention to potential side effects of the therapies. Moreover, the investigation of the therapeutic efficacy of the photoactive drug using near-infrared

radiation can contribute avenues for using the biological window of optical transparency [11]. This often suggests implication of NIR absorbing dye molecule or nanomaterials as photosensitizer in PDT, which in-term improves the penetration potency of the light used [12, 13]. There are plenty of reports on multifunctional NIR agents for cancer targeting and imaging applications showing great potential for clinical use [14].

The emergence of pathogenic bacteria with acquired multi-drug resistance indicates the dawn of a post-antibiotic era, an alarming crisis worldwide [15, 16]. A recent report by the Centers for Disease Control and Prevention (CDC) suggests that each year at least 2 million people suffer from bacterial infection that are resistant to antibiotics in the United States alone [17]. Different nanomaterials, such as silver nanoparticle (Ag NPs) depict unprecedented anti-microbial activity and are often consider as nanoantibiotics (nAbts), a term that has been coined for the nanomaterials which show direct antimicrobial activity or improved effectiveness and safety of antibiotics administration [18]. nAbts are advantageous due to their sustained release and uniform distribution in the target tissue following enhanced cellular internalization, which minimized the possible side effects and patient-compliance [19]. However, to minimize the possible side-effects and complications introduced by nAbts, stimuli responsiveness is necessary [20]. In this aspect, antimicrobial PDT (aPDT) using nanomaterials show huge potential.

Moreover, healthcare-associated infections (HAIs) comprising medical device-related lower respiratory tract infections, catheter-associated urinary tract infections (CAUTIs) and surgical-site infections (SSIs) are often associated with gram-positive bacteria, such as *Staphylococcus aureus* and *Staphylococcus epidermidis* and their virulent biofilms [21]. Biofilms are dynamic communities of immobile bacteria encapsulated within a protective matrix of polysaccharides, proteins, nucleic acids and lipids, developing a compact structure typically attached to a surface or to each other [22]. The eradication of biofilm is challenging because the

extracellular polymeric substances (EPS) comprising the biofilm prevent the small-molecule therapeutics penetration into biofilms [23, 24]. This often suggests the desperate need for innovative nano-therapeutics [25]. The eradication of bacterial biofilms can be achieved through nanomaterial coating on implant surfaces [26]. The systematic interactions of the biofilms with nanomaterials through efficient penetration and accumulation of antimicrobial agents into the biofilm network provides an enhanced therapeutic efficacy [23].

The intrinsic acidic microenvironments of biofilms, chronic infections or wounds (pH values 4-7) could be exploited to fabricate pH sensitive nano-therapeutics [27]. The superior dissolution of zinc oxide nanoparticles (ZnO NPs) at lower pH inducted its use as nanocarriers for drug delivery application [28]. ZnO NPs also depict greater biocompatibility than other metal oxide NPs with size dependent anti-microbial property [29]. Despite the promising prospect of ZnO NPs as drug delivery vehicles due to their low cost and lesser cytotoxicity, the wide band gap (~ 3.3 eV) semiconducting nature suggests its activation only by UV light (λ ~ 375 nm) which eventually restricts its clinical applications [30]. The inorganic metal-oxide NPs conjugated with organic photosensitizers (visible-NIR absorption) forms new class of nanohybrids showing superior activity than the individual counterparts [31]. The enhanced photo-induced interfacial charge separation process often suggests greater activity.

The present chapter depicts the use of red-light absorbing dye Squaraine (SQ) as the photosensitizer for aPDT. The dye molecule has been conjugated to ZnO NPs surface, which has been confirmed using optical and vibrational (FTIR) spectroscopic tools. The nanohybrids employ both the stimuli responsive nature: acidic pH sensitivity due to ZnO and NIR light sensitivity due to SQ dye. The molecular level interaction between two moieties initiates the photoinduced excited state electron transfer process from dye to ZnO, which indeed improve the ROS generation capability. The improvement of *in-vitro* activity facilitates the dose

dependent killing of gram-positive bacteria (*S. aureus*) through cell membrane rapture and cellular internalization. We have also employed ZnO-SQ nanohybrid for the eradication of biofilms as this requires the efficient penetration and accumulation of the drug into the biofilm network. Crystal violet assay was used to assess the anti-biofilm activity. We have further performed scanning electron microscopy to observe the morphological changes of the biofilm upon photodynamic treatment. The material is eventually coated over titanium sheets (used to mimic implants [32]) and their anti-biofilm activity has been evaluated. The nanohybrids also exhibit low toxicity to mammalian cells and maintain high hemocompatibility.

In the next part of the chapter, we have examined ZnO-SQ nanohybrid for potential PDT application in cancer therapy. We have synthesised the surface modified ZnO NPs using the dye as the sensitizer. To check the integrity of nanohybrids formation, we have followed Förster resonance energy transfer (FRET) from donor ZnO to acceptor SQ molecule. The photo-induced electron transfer process is estimated using time-resolved fluorescence decay transients. The enhanced water stability, lesser aggregation, pH responsive delivery of drug in the nanohybrids has been monitored. We have tested and checked the light penetration efficacy through a mimic human tissue and evaluated the cytotoxicity of ZnO-SQ nanohybrids on human breast cancer cell line MCF-7. The present study depicts physico-chemical insight of an inorganic-organic hybrid material for potential biological effectivity.

8.2. Results and Discussion:

8.2.1. NIR Light Active ZnO Based Nanohybrids for Bacterial Biofilm Treatment [33]: The structure of the asymmetric squaraine dye (SQ) is depicted in Figure 8.1.a. A typical high-resolution transmission electron microscopic (HR-TEM) image of ZnO NPs is shown in Figure 8.1.b. The lattice fringes of ZnO NPs show an inter-

planar distance of 0.27 nm, which corresponds to the spacing between two (002) crystal planes. The size distribution of ZnO NPs is shown in the inset of Figure 8.1.b. The average particle size is found to be ~ 24 nm. To confirm the conjugation of SQ into ZnO NPs surfaces, Fourier transform infra-red (FTIR) technique has been used. The free SQ possess stretching frequencies at 1486 cm^{-1} which is attributed to C=C stretching in the four membered ring [34] and at 1700 cm^{-1}, the typical peak for the C=O stretching of an aromatic carboxylic group (Figure 8.1.c). This latter signal clearly disappears in ZnO-SQ conjugated system keeping other signals unaltered, suggesting that SQ is attached to the semiconductor surface through the peripheral COOH binding of SQ to ZnO.

The conjugation between SQ and the ZnO NPs can also be understood by using UV-Vis spectroscopy (Figure 8.1.d). The absorption spectra of SQ in DMSO

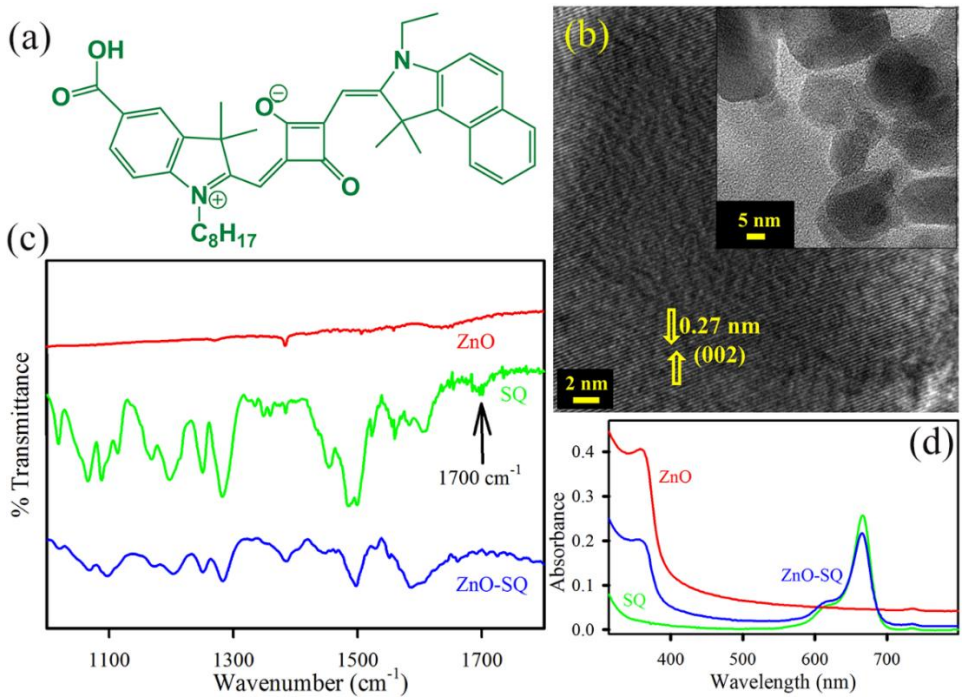

Figure 8.1: *(a) Structure of SQ (b) HRTEM image of ZnO NPs. Lattice fringes in the corresponding HRTEM image indicates high crystallinity. Inset shows the TEM images of ZnO NPs (c) FTIR spectra of ZnO NPs (red), SQ (green) and ZnO-SQ (blue) (d) UV-Vis absorption of ZnO NPs (red), SQ (green) and ZnO-SQ (blue) in DMSO.*

show the noticeable peak at 665 nm, which corresponds to π–π* charge-transfer process with a minor peak at 615 nm of dye aggregation [35]. The characteristic peaks of both SQ and ZnO are observed in the ZnO-SQ nanohybrids, which indicate the successful complexation between the two moieties. The steady-state emission spectra of SQ and ZnO-SQ in DMSO are shown in Figure 8.2.a and the corresponding excitation spectra are presented in the inset of Figure 8.2.a. SQ exhibits an emission peak at 673 nm upon excitation at 633 nm. The emission intensity is significantly reduced after attachment of SQ to the ZnO NPs. This observation indicates presence of the efficient non-radiative photoinduced processes from SQ to ZnO NPs. The excitation spectra depict two peaks for SQ which are similar to the corresponding absorption spectra. The ZnO-SQ nanohybrid shows 5 nm bathochromic shift in the excitation spectra, indicating molecular level interaction during the attachment process. To further study the electronic interactions, time-resolved fluorescence transient studies have been carried out [36]. The lower density sp orbital of Zn^{2+} in ZnO, interact with LUMO of dye (SQ) suggesting an ultrafast sub-picoseconds time-scale due to electron injection process [37]. The fluorescence decay profiles for free SQ and ZnO-SQ have obtained upon excitation at 633 nm and monitored at 670 nm (Figure 8.2.b) using DMSO as the solvent. The time constants for the excited state decay transients of SQ in DMSO show single exponential decay, with a lifetime of 580 ps. A very fast time component of 30 ps generates after attachment of SQ on ZnO surfaces, suggesting photoinduced electron transfer process from excited state of SQ (dye) to the conduction band of the ZnO NPs (semiconductor surface). The fitting parameter details of the fluorescence decays are provided in Table 8.1. As the ZnO NPs used in the present study have not shown any intrinsic defect state emission property, so there is no chance of energy transfer process associated with the faster time-scale present in the nanohybrids. Scheme 8.1 depicts band energy level diagram and charge separation path at the ZnO-SQ interface.

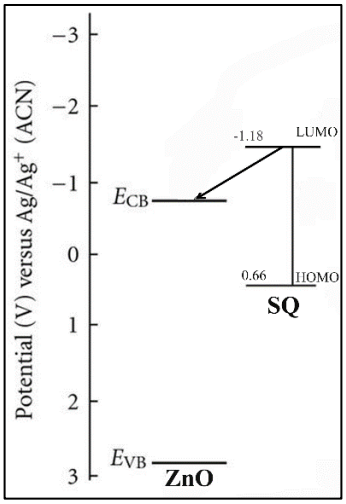

Scheme 8.1. *Schematic energy level diagram and charge separation path at the ZnO-SQ interface.*

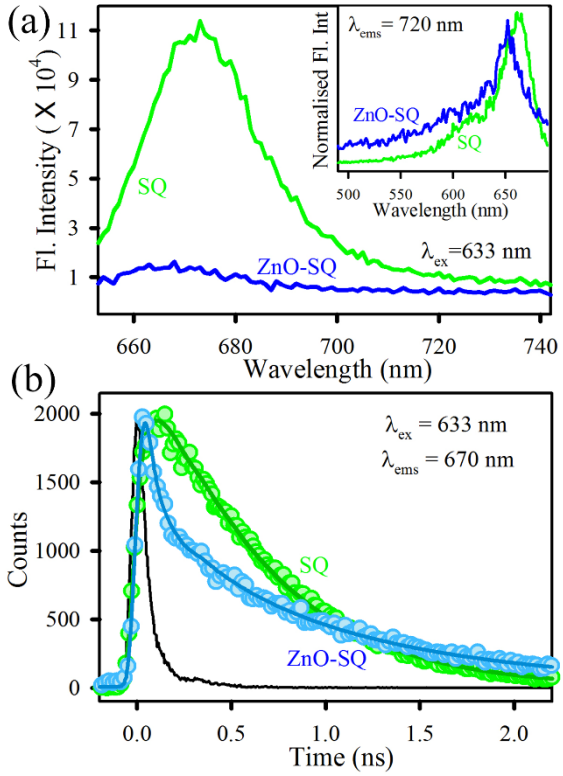

Figure 8.2. *(a) Room-temperature PL spectra (excitation at 633 nm) of SQ (green) and ZnO-SQ (blue). Inset shows the normalised excitation spectra of SQ (green) and ZnO-SQ (blue) at detection wavelength 720 nm (b) Fluorescence decay profiles of SQ (green) and ZnO-SQ (blue) at 670 nm (excitation at 633 nm).*

The efficient electron transfer process present in ZnO-SQ motivates us to investigate the photoinduced ROS generation capability of the nanohybrid. The ROS production ability of the sample has been evaluated using the DCFH assay in

which the oxidation of DCFH (non-fluorescent) into dichlorofluorescein DCF (fluorescent) through interaction with ROS is monitored [38]. The fluorescence emission intensity of DCF is recorded with respect to time (Figure 8.3.a). The highest enhancement of fluorescence intensity of DCF is obtained for ZnO-SQ nanohybrids under red light irradiation. ROS production increases three times compared to free dye SQ. The control experiments with DCFH and ZnO under red light irradiation show negligible increase in fluorescence intensity.

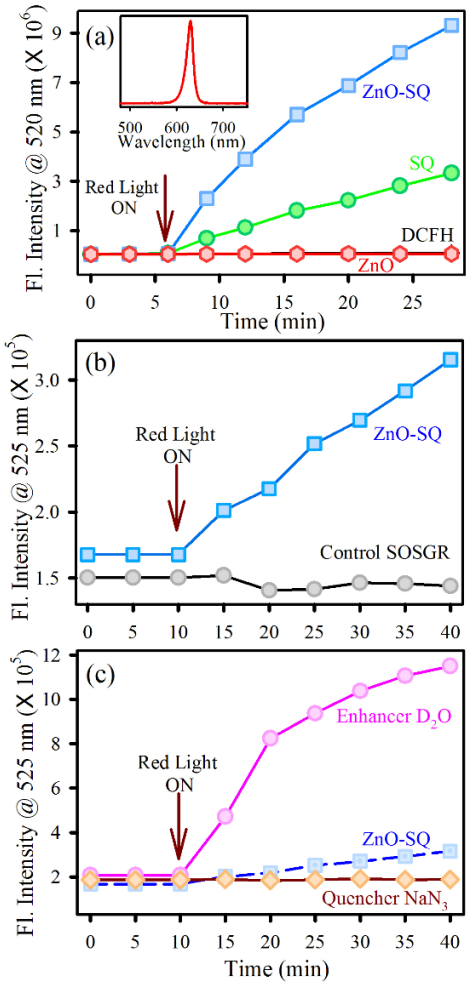

Figure 8.3. *(a) The DCFH oxidation with respect to time in the presence of SQ (green), ZnO-SQ (blue), ZnO (red) and only control DCFH (black) under dark followed by red light irradiation. The excitation was at 640 nm (b) Fluorescence response of SOSGR in presence of ZnO-SQ (blue) and control SOSGR (black) under dark followed by red light irradiation (c) Fluorescence response of SOSGR in presence of enhancer D_2O (pink) and quencher NaN_3 (dark red) with the sample ZnO-SQ under dark followed by red light irradiation. The dotted blue line shows the fluorescence response of SOSGR in presence of ZnO-SQ.*

This confirms the involvement of photoinduced interfacial dynamics in ZnO-SQ for enhancement of ROS production. However, DCFH assay is incompetent for the determination of specific nature of ROS. To confirm whether the generated ROS is singlet oxygen or not, we have performed singlet oxygen sensor green reagent SOSGR assay [39]. It also involves monitoring of the emission intensity at 525 nm with progressing time. Figure 8.3.b depicts significant increase in fluorescence intensity of SOSGR when exposed to ZnO-SQ under red light illumination. Furthermore, one quencher (NaN_3) and another enhancer (D_2O) of singlet oxygen species are added with SOSGR and ZnO-SQ under red light illumination. In case of D_2O, the fluorescence intensity increases many folds whereas for NaN_3, it reduces significantly (Figure 8.3.c). These results indeed confirm the generation of red light induced singlet oxygen by ZnO-SQ and signify its importance as a potential photodynamic agent for therapeutic action.

ZnO-SQ nanohybrid was evaluated for its antimicrobial activity as a potential photodynamic agent for the inhibition of growth of *S. aureus*. The effect of the sample with various concentrations (0-350 nM) on *S. aureus* growth has been examined using colony forming unit (CFU) assay under dark condition (Figure 8.4.a). The inhibition in bacterial growth was significant at a concentration range of ~ 200 nM, suggesting use of lower concentration for determining the photodynamic action. We have employed 140 nM of the sample and incubated the bacterial culture for 3 hrs in dark for cellular uptake of the drug followed by 30 mins red light illumination. The pictures of *S. aureus* cultures (Inset Figure 8.4.b) treated with sample in the absence and presence of red light depict the visible change in bacterial growth after photodynamic treatment, with significantly smaller number of colonies. In control and ZnO treated samples, the colony forming units (CFU) are almost same in the presence and absence of red light. The observation indicates the absence of antibacterial activity of the ZnO NP itself in our experimental concentration range (Figure 8.4.b). In the case of SQ treated samples, the bacteria

growth is inhibited up to 45% after photodynamic treatment. The maximum inhibition of bacterial growth is obtained for ZnO-SQ treated samples with a 95% decrease in CFU after photodynamic treatment. To elucidate the mechanism behind the enormous photodynamic killing efficiency of ZnO-SQ, we first evaluate its photoinduced bacterial membrane distortion capacity. The bacteria culture without sample treatment (under dark and with red light irradiation) and treated with ZnO-SQ (under dark and with red light irradiation), were stained with propidium iodide

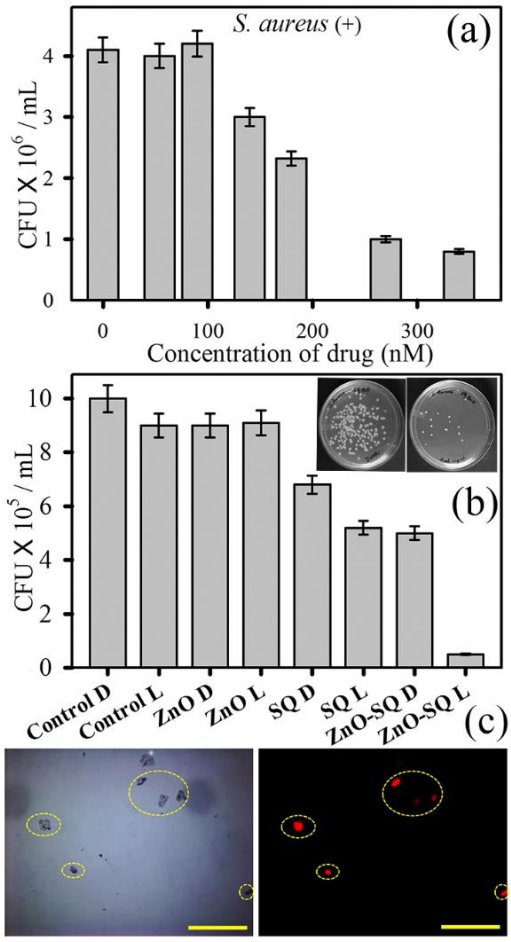

Figure 8.4. *The dose dependent antibacterial effect of ZnO-SQ at concentrations ranging from 0 nM to 400 nM on S.aureus under dark condition (b) Bacterial viability after treatment with 140 nM ZnO-SQ in presence and absence of red-light irradiation. Inset shows images of S. aureus plates treated with ZnO-SQ, before (left) and after (right) red light irradiation (c) Propidium iodide staining assays for cell membrane disruption of S. aureus. Microscopic images of S. aureus treated with ZnO-SQ under red light illumination: left panel-bright field and right panel-fluorescence. Scale bar is 100 μm.*

(PI) to check the integrity of bacterial membrane. PI only leaks into cells with compromised membranes, with concomitant enhanced fluorescence [40]. As shown in Figure 8.4.c, the observed strong red fluorescence only from bacterial cells treated with ZnO-SQ followed by red light illumination, indicating the integrity of bacterial membrane was indeed disrupted by photodynamic action of ZnO-SQ.

Further, we have evaluated the capability of ZnO-SQ to modulate the intracellular ROS generation which promote several cell death mechanisms. As shown in Figure 8.5.a, we noted that ZnO-SQ treated *S. aureus* induced about 2-fold increase in the intracellular ROS production under red light illuminated condition compared to the control group. Further extending our investigation, we have

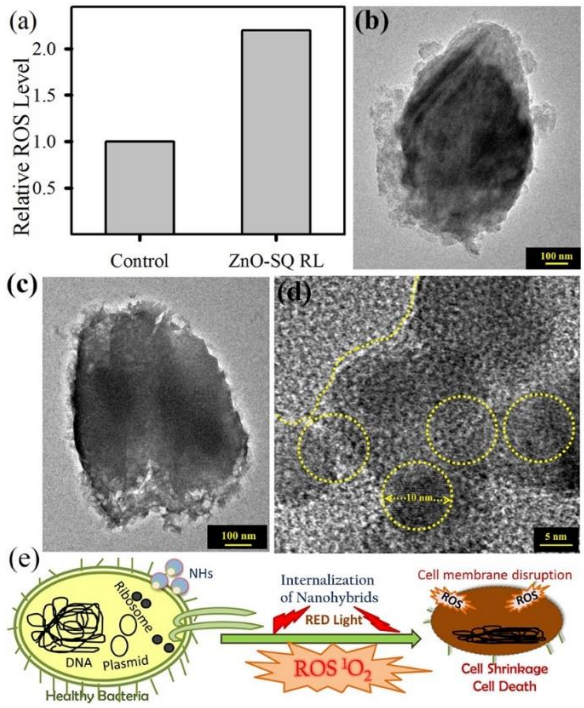

Figure 8.5. *The dose dependent antibacterial effect of ZnO-SQ at concentrations ranging from 0 nM to 400 nM on S.aureus under dark condition (b) Bacterial viability after treatment with 140 nM ZnO-SQ in presence and absence of red-light irradiation. Inset shows images of S. aureus plates treated with ZnO-SQ, before (left) and after (right) red light irradiation (c) Propidium iodide staining assays for cell membrane disruption of S. aureus. Microscopic images of S. aureus treated with ZnO-SQ under red light illumination: left panel-bright field and right panel-fluorescence. Scale bar is 100 µm.*

examined the bacterial morphology and NP internalization using transmission electron microscopy (TEM). As shown in Figure 8.5.b, *S. aureus* exhibits typical membrane structures. The morphology and membrane integrity of the bacteria were dramatically altered after photodynamic treatment with ZnO-SQ (Figure 8.5.c). The NPs randomly adsorbed on bacteria inducing noticeable changes in membrane morphologies. Significantly, the multi-layered peptidoglycan coating of gram-positive bacteria presumably passivates the interactions of NPs and bacterial membranes, leading to NPs penetration. ZnO NPs are believed to destruct lipids and proteins of the bacterial cell membrane, resulting in a leakage of intracellular contents and eventually the death of bacterial cells [41]. The HRTEM image (shown in Figure 8.5.d) at the cell membrane depicts internalization of highly crystalline ~ 10 nm ZnO NPs into the bacterial cell. The overall distribution of the NPs consisting of ~10 nm grain boundary in the cytoplasmic area clearly confirms cellular trafficking of the bigger NPs and embodiment of smaller NPs within the bacteria which are responsible for the drug-delivery and photoinduced intracellular ROS generation following cell death. The diverse cell death mechanism owe to photodynamic therapy by ZnO-SQ are pictorially depicted in Figure 8.5.e.

The diverse cell death mechanism leading to an exceptional stimuli responsive antimicrobial efficacy drives us to investigate the ability of ZnO-SQ to disrupt biofilm formation in a red light activated process. For our study, biofilm formation by *S. aureus* was measured after 48 hr. The total adhered biomass of the biofilms was monitored through quantitative crystal violet (CV) assay. There is a decrease of biomass (~20%) for the ZnO-SQ treated samples. The bacterial biomass could be further reduced to ~55% when ZnO-SQ treated bacteria were exposed to red light for 30 mins (Figures 8.6.a). The upper panel of Figure 8.6.a show photographs of crystal violet stain in the petri plates demonstrating visible reduction of biofilm adherence upon photodynamic treatment. The structural and morphological changes of the biofilms were observed by taking optical microscopic

and scanning electron microscopic images. Figure 8.6.b and 8.6.c depict the structure of *S. aureus* biofilm without any treatment and with ZnO-SQ red-light treatment respectively. The inherent colonization property of bacterial biofilms is significantly perturbed upon the treatment. Moreover, Figure 8.6.d shows typical characteristics of *S. aureus* biofilms comprising extracellular polymeric matrix, and Figure 8.6.e shows biofilm treated with ZnO-SQ followed by red light irradiation,

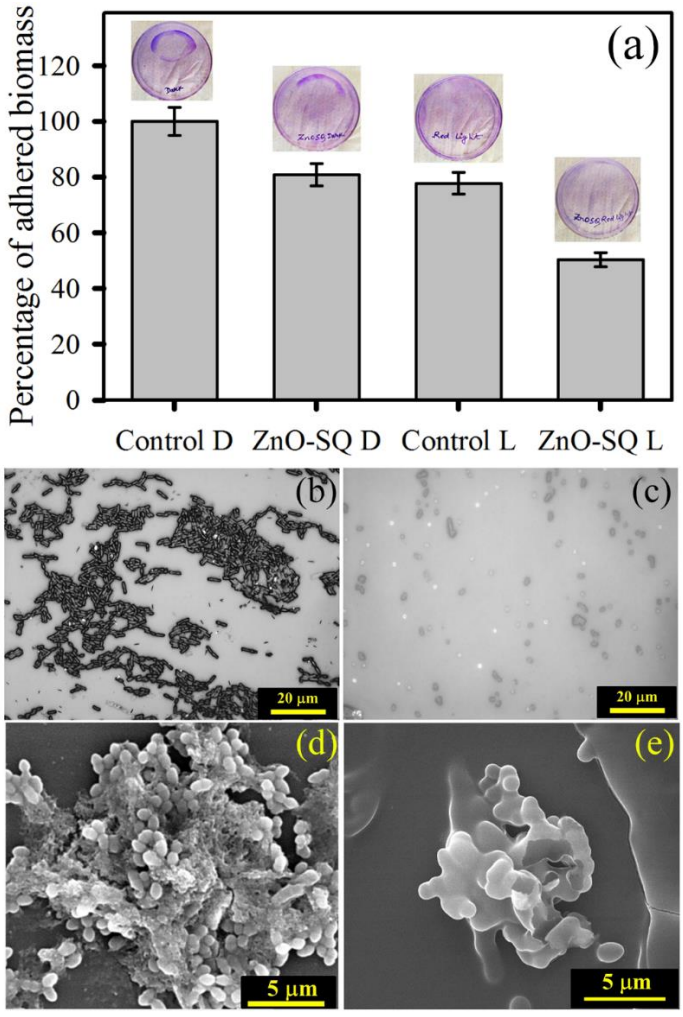

Figure 8.6. *(a) Anti-biofilm effects of ZnO-SQ on S. aureus biofilm in presence and absence of red-light illumination monitored by adhesion efficiency of biomass through crystal violet staining assay. The upper panel shows images of crystal violet stained plates. Microscopic images of (b) S. aureus biofilms and (c) after red light illumination on ZnO-SQ treated samples. Scale bar is 20 µm. FEGSEM images of (d) S. aureus biofilms and (e) after red light illumination on ZnO-SQ treated samples. Scale bar is 5 µm.*

which contain significantly fewer bacteria without the typical arrangement of a biofilm. Upon the treatment, both the adherence property and the characteristics morphology of biofilm were completely destroyed. The anti-biofilm activity of ZnO-SQ suggests that acidic pH responsive delivery vehicle ZnO act as a

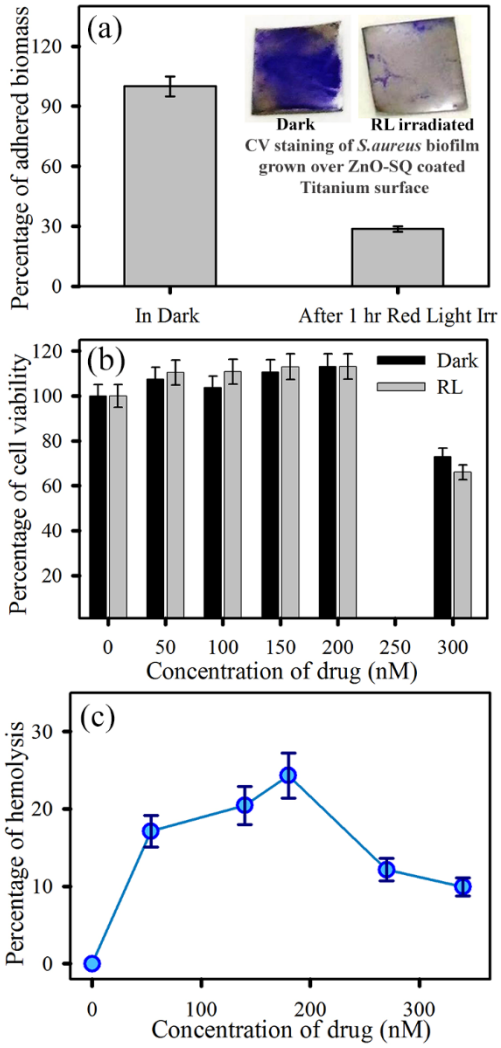

Figure 8.7. *(a) Anti-biofilm activity of ZnO-SQ sensitized model Titanium sheet in the absence and presence of red-light illumination. The upper panel depicts visual change in crystal violet staining after treatment with red light (b) Cytotoxicity assay in human bone cell MG-63 with different concentration of ZnO-SQ in the absence and presence of red-light illumination (c) Hemolysis assay study of ZnO-SQ at different concentration under dark condition.*

permeation enhancer followed by a synergistic mechanism of internalization of NPs within biofilms and generation of photoactive ROS disrupts the biofilm

structures completely. These findings suggest that ZnO-SQ should possess practical applicability for biofilm disruption on medical implants. To unravel the potential for clinical utilization, we have coated titanium sheets, the model for medical implants, with ZnO-SQ samples followed by 48 hrs incubation with *S. aureus* culture (OD_{600}=1). This generates bacterial biofilms over the coated titanium sheets, as indicated in Figure 8.7.a upper panel. The remarkable crystal violet staining over the coated titanium sheet demonstrates the presence of proliferating biofilms. However, as the sheet was illuminated under red light for 1 hr, there is a significant reduction in crystal violet staining suggesting disruption of biofilms due to photoinduced ROS generation by ZnO-SQ. This signifies the stimuli responsive targeted photodynamic killing and disruption efficacy of bacterial biofilms by ZnO-SQ suggesting future clinical prospect.

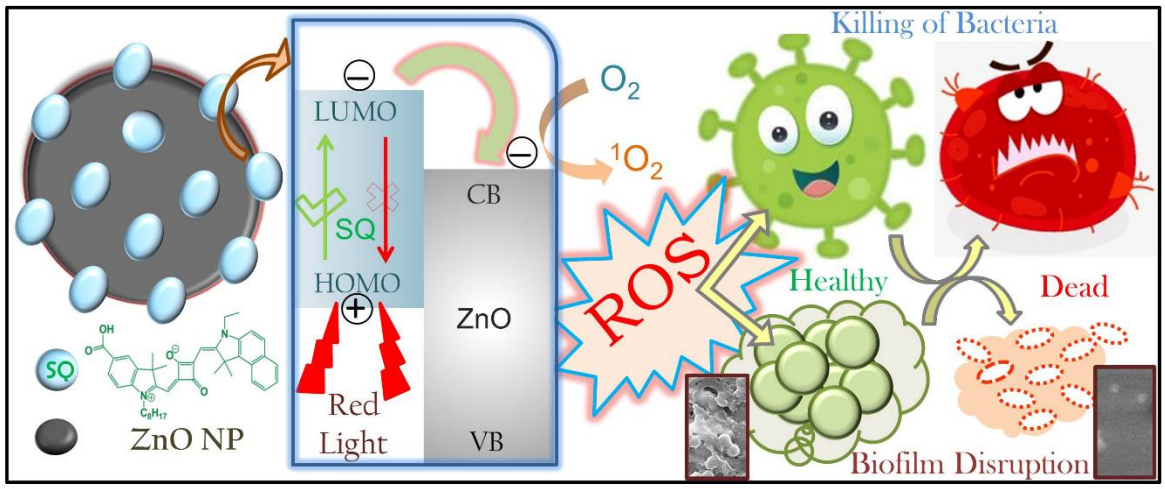

Scheme 8.2. *Red light activated biocompatible ZnO-SQ nanohybrids depict superior antimicrobial and anti-biofilm effect due to enhanced photo-induced ROS generation.*

Nevertheless, the toxicity of nanomaterials towards mammalian cells is one of the critical points for *in-vivo* application. To this end, we first studied the toxicity of the nanohybrids against human osteoblast cell line MG-63. We have specifically chosen the bone fibroblast cells to evaluate the cytotoxicity as microbial biofilm pathogens are the causative agents in chronic osteomyelitis. As depicted in Figure 8.7.b, MG-63 cells treated with a various concentration of nanohybrids had

negligible cytotoxicity as measured using MTT assay under both dark and red light irradiated conditions. The cell viability upon treatment with ZnO-SQ upto 200 nM concentration under both dark and red light illuminated condition, depict comparable cell viability (> 95%) with the control cells (Figure 8.7.b). The significant toxicity arises at 300 nM concentration (30% and 40% cell death in dark and light respectively) which is the double concentration used for the antimicrobial assays. This result confirms appreciable biocompatibility of ZnO-SQ nanohybrids. Moreover, the hemolytic activity of these NPs against human red blood cells (RBCs) was measured. As shown in Figure 8.7.c, at variable concentrations with highest dosing of twice the dose used for antimicrobial therapy, the NPs show no observable hemolytic activity, demonstrating the intrinsic biocompatibility of ZnO-SQ with human blood cells. The NPs are also biocompatible when exposed under red light (data not shown) suggesting the stimuli-responsive system as safe towards real-life implementation. These overall effects suggest ZnO-SQ as a stimuli responsive biocompatible antimicrobial and anti-biofilm agent which demonstrate achievable clinical applications.

Table 8.1. *Dynamics of picosecond-resolved luminescence transients* [a]

Sample	Excitation wavelength (nm)	Detection wavelength (nm)	τ_1 (ns)	τ_2 (ns)	τ_3 (ns)	τ_{avg} (ns)
SQ	633	670	580 (100%)			0.58
ZnO-SQ	633	670	30 (78.3%)	364.7 (6.7%)	1111.8 (14.9%)	0.21

[a]*Numbers in the parenthesis indicate relative weightages.*

8.2.2. Exploration of Interfacial Dynamics in Squaraine Based Nanohybrids for Potential Photodynamic Action [42]: We have synthesized ZnO NPs in ethanolic medium having typical dimension of 5-8 nm as depicted in Figure 8.8.a with uniform size distribution. Then, we have attached SQ to fabricate the nanohybrids. Inset of Figure 8.8.b shows absorption spectra of ZnO and ZnO-SQ in ethanolic

medium. Optical absorption of ZnO-SQ incorporates both the characteristics of ZnO

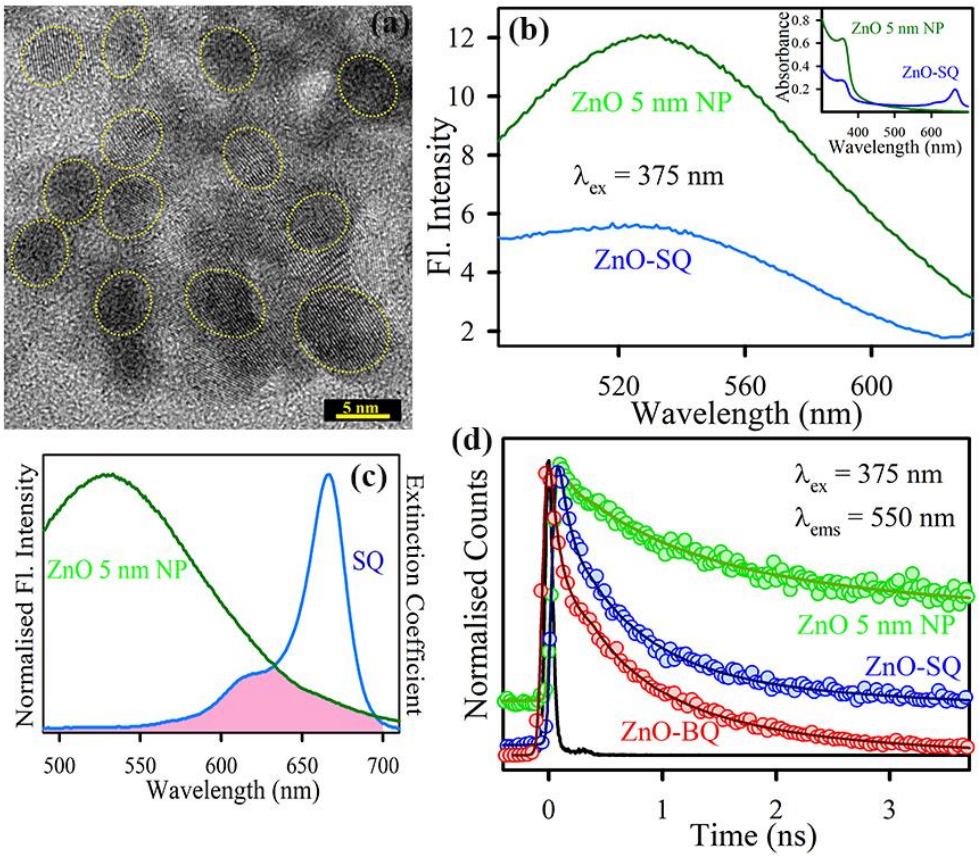

Figure 8.8. *(a) HRTEM images of ZnO nanoparticles (~5 nm) (b) Steady state fluorescence quenching of ZnO NPs after conjugation with SQ. The excitation wavelength is 375 nm. Inset shows the absorbance spectra (c) Spectral overlaps between the emission of ZnO NPs (5 nm) and the absorption spectrum of SQ is shown (d) Picosecond resolved emission transients of ZnO NPs (green), ZnO-SQ (blue) and ZnO-BQ (red) detected at 550 nm upon excitation at 375 nm.*

and SQ. The steady-state emission spectra of ZnO and ZnO-SQ is recorded next using excitation at 375 nm. Figure 8.8.b depicts quenching of fluorescence spectra of ZnO NPs upon SQ attachment. The room temperature PL spectrum of ZnO NP is comprised of broad emission bands upon excitation below the band-edge (λ_{ex} = 375 nm) as shown in Figure 8.8.b. The emission arises from the defect centres located near the nanoparticle surface [30]. The significant decrease in emission intensity of ZnO NPs upon SQ attachment can be attributed to the efficient non-radiative photoinduced processes from ZnO NPs to SQ. Herein, we anticipate Förster resonance energy transfer (FRET) from the donor ZnO NPs to the acceptor SQ. The

spectral overlap between the defect state emission of ZnO NPs (donor) and the absorption spectrum of SQ (acceptor) is shown in Figure 8.8.c [43]. The picosecond resolved fluorescence transients were recorded upon exciting with 375 nm laser source. The significant quenching in excited state lifetime of ZnO in presence of SQ provides a four-time faster average lifetime (Figure 8.8.d). The decay constants and their relative percentages are shown in Table 8.2. To eliminate the chance of charge transfer process, we elucidate the decay nature of ZnO in presence of benzoquinone BQ, a well-known electron acceptor [38]. Figure 8.8.d shows the fluorescence decay transients which clearly depicts that the lifetime of ZnO-BQ is much faster compare to ZnO-SQ, confirming the energy transfer process. We have calculated the FRET efficiency to be 76.8% and the donor-acceptor distance to be 2.23 nm. This confirms the molecular level interaction between ZnO and SQ in the ZnO-SQ nanohybrids through nanocrystal defect sites.

Next, we have used crystalline ZnO NPs of larger sizes and analysed its interaction with SQ molecules. The covalent conjugation through carboxylic group of SQ to defect state of ZnO NPs substantiate the formation of ZnO-SQ nanohybrid. Larger dimension nanoparticles are favourable for application as they are stable in aqueous dispersion whereas smaller particles are only stable in ethanol like solvents which is non-biocompatible in nature restricting its application. Figure 8.9.a depicts HRTEM image of ZnO NPs of size 20-30 nm with high crystallinity. The lattice fringes correspond to the (002) crystal plane which is mainly available at the surface of the NPs. Figure 8.9.b shows no significant change in size or crystallinity of ZnO NPs after SQ attachment. The observed absorption spectrum of ZnO-SQ nanohybrids indicates the presence of peaks at 350 nm (due to ZnO) and 663 nm with a shoulder around 610 nm (due to SQ) as shown in Figure 8.9.c. ZnO NPs shows absorption peak at 360 nm due to the wide band-gap nature of ZnO. 10 nm bathochromic shift of ZnO absorption maximum indicates formation of ZnO-SQ nanohybrids indeed modified the surface of ZnO NPs Then, we have monitored the

emission characteristics of the nanohybrids using excitation of 633 nm. The fluorescence quenching was obtained in steady-state fluorescence experiments (inset of Figure 8.9.d). We have checked the time-resolved photoluminescence decay of SQ in absence and presence of ZnO upon excitation at 633 nm laser sources (Figure 8.9.d). SQ depicts excited state lifetime of 560 ps which is remarkably quenched in ZnO-SQ with a new ultrafast time scale of 30 ps. The excited state lifetime study unveils presence of a photo-induced electron transfer process from LUMO of SQ to conduction band of ZnO.

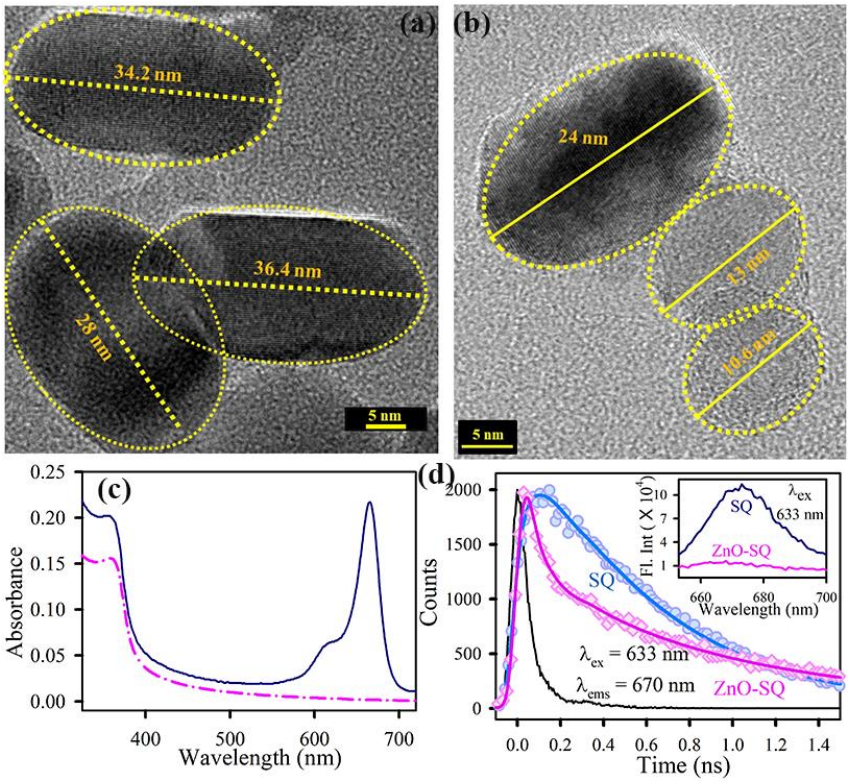

Figure 8.9. *HRTEM images of (a) ZnO nanoparticles (~30 nm) and (b) ZnO-SQ nanohybrids (c) UV-Vis absorption spectra of ZnO-SQ is shown (dark blue). The dotted pink curve depicts the absorption spectrum of ZnO NPs (d) Picosecond resolved emission transients of SQ (blue) and ZnO-SQ (pink), detected at 670 nm upon excitation at 633 nm. Inset shows steady state fluorescence quenching of SQ (blue) after conjugation with ZnO (pink). The excitation wavelength is 633 nm.*

Next, we have analyzed the aggregation behavior of SQ and ZnO-SQ with increasing water content in DMSO. The concentration is SQ is maintained ~ 45 μm in nanohybrid as well as control SQ to check its aggregation characteristics. Figure

8.10.a shows absorption spectra of SQ in pure DMSO (blue), 1:1 DMSO-water mixture (purple), 1:5 DMSO-water mixture (dark blue) and pure water (violet).

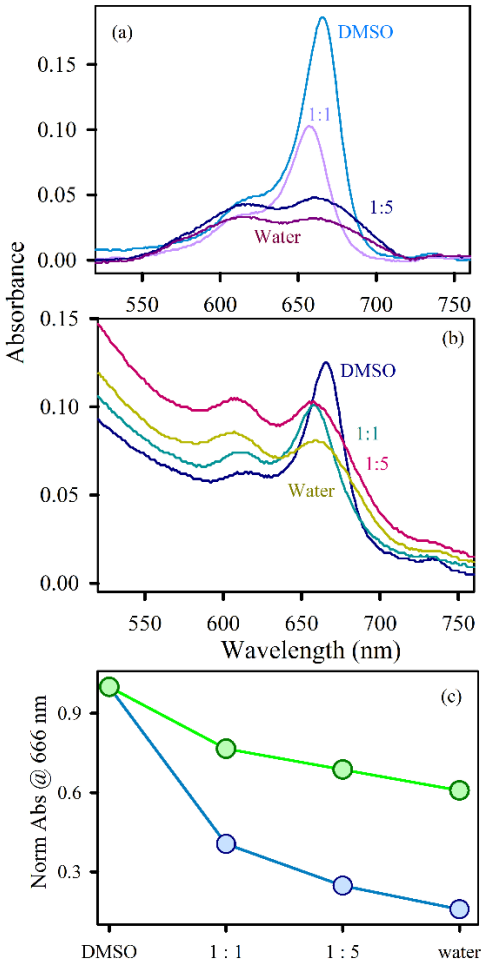

Figure 8.10: *Aggregation behavior of (a) SQ and (b) ZnO-SQ with increasing concentration of water: in DMSO, in 1:1 DMSO-water mixture, in 1:5 DMSO-water mixture and in water (c) Change in absorbance at 666 nm with increasing water content SQ (blue) and ZnO-SQ (green).*

Upon water addition the main absorption peak at 665 nm shows a 10 nm blue shift with a decrease in the magnitude of optical density. This suggests H-aggregate formation in presence of water. The low intensity, broad absorptions are features of the intermolecular interactions occurring within the Squaraine aggregates. With the increase in water content, the monomeric signature in the absorption significantly perturbed and the ratio between the monomer and aggregates keeps decreasing due

to enhancement in intermolecular charge transfer within the aggregates formed through both coulombic and H-bonding interaction. Figure 8.10.b shows that upon addition of water in ZnO-SQ, the 665 nm absorbance of SQ shifts to higher energy portion of the spectrum which is like the free SQ. However, the comparative decrease of 665 nm peak is much lesser compare to the free SQ solution. The blue shift in absorption spectra suggest H-aggregation of SQ moieties in presence of small amount of water. However, retention of similar spectral characteristics with increasing water content suggest lesser interaction between the aggregates due to orientational specificity of SQ molecule in ZnO nanoparticle surface. This observation suggests that presence of NPs surface diminishes the possibility of aggregation of SQ in water medium. The comparative kinetic plot (Figure 8.10.c) shows that change in monomeric peak is significantly lower in ZnO-SQ compare to SQ. The decay constants obtained by fitting the experimental data points suggest that the aggregation behavior is almost 2 times reduced in case of ZnO-SQ (Table 8.3).

Table 8.2. *Dynamics of picosecond-resolved luminescence transients* [a]

System (ex-375-ems-550)	τ_1 (ps)	τ_2 (ps)	τ_3 (ps)	τ_{ayg} (ns)
ZnO-5nm	100 (18.8%)	1025 (38.6%)	18310 (42.6%)	8.2
ZnO-5nm-SQ	85 (43.6%)	652 (41.02%)	10501 (15.4%)	1.9
ZnO-5nm-BQ	54 (61%)	448 (21%)	1421 (18%)	0.37
System (ex-633-ems-670)	τ_1 (ps)	τ_2 (ps)	τ_3 (ps)	τ_{ayg} (ns)
SQ	560 (100%)			0.56
ZnO-30nm-SQ	30 (77%)	355 (6%)	1005 (17%)	0.21

[a]*Numbers in the parenthesis indicate relative weightages.*

We further analyzed the precipitation rate of ZnO-SQ in different pH solutions. Figure 8.11.a suggests that the rate of precipitation of ZnO-SQ is much higher in pH 5 compare to pH 7. The precipitation rate is almost ten times faster in acidic condition with respect to neutral pH due to easy formation of Zn^{2+} ions in

acidic condition [44]. These observations impart the pH responsive drug-

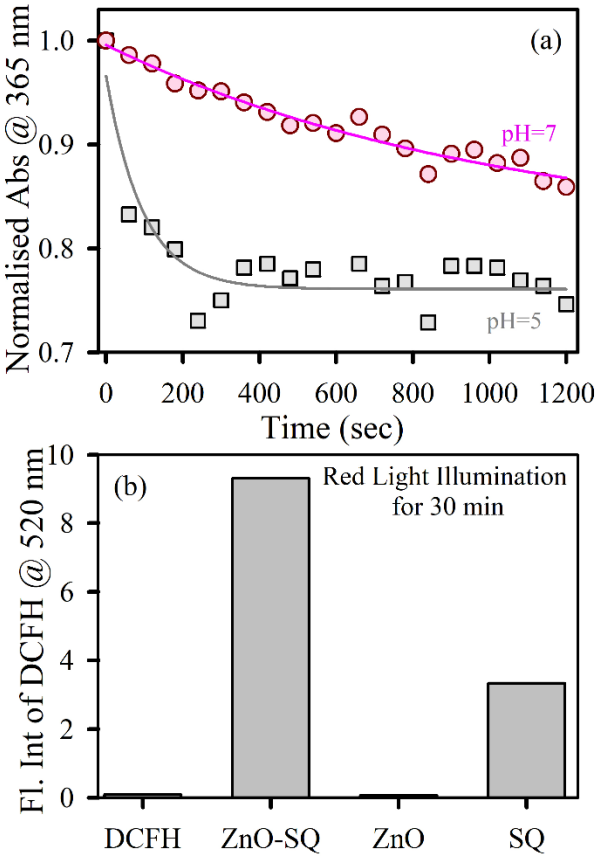

Figure 8.11: *(a) pH dependent precipitation kinetics of ZnO-SQ. The experimental values are represented by symbols, pH=7 (pink) and pH=5 (grey). The solid lines signify single exponential fitting curves (b) The fluorescence intensity of DCF in DCFH oxidation assay after 30 mins of red-light illumination time in the presence of ZnO-SQ, ZnO and SQ samples.*

effect of ZnO-SQ which facilitate anticancer effects as the infected cancerous tissues employed acidic cellular conditions whereas the normal cells have neutral intracellular pH. The presence of photo-induced charge transfer processes in the nanohybrid expected to improve the reactive oxygen species (ROS) generation. Thus, we have assessed the in-vitro ROS generation using the increment of DCF emission at 520 nm. Figure 8.11.b depicts the relative increase of DCF emission after 30 min of red-light illumination. ZnO-SQ nanohybrids shows three times increase in DCF emission suggesting improvement of photo-induced ROS generation due to presence of excited state electron transfer process in ZnO-SQ and lesser drug

aggregation. Hence, the synthesized ZnO-SQ nanohybrids show improvement in reducing dye aggregation, pH sensitive precipitation and photo-induced ROS generation compare to the bare photosensitizer SQ and suggest its potential for PDT examination.

Table 8.3. *Fitting parameters of aggregation behavior and precipitation kinetics of ZnO-SQ*

Aggregation behaviour		pH dependent precipitation	
Samples	Degradation percentage (%)	pH value	Rate constant (sec)
SQ	84	pH5	96
ZnO-SQ	40	pH7	1031

In view of biological applications firstly, we have checked the light penetration effect through human skin. Inset of Figure 8.12.a shows the fibre-optics based experimental design depicting one finger placed between white light illumination (400-1200 nm) from the source in one side and the spectrograph detector in the other end. The white light spectrum shows a broad spectrum from 400 to 1000 nm as shown in Figure 8.12.a (grey line). After placing the finger, the transmitted light spectrum is shown in dark red line in Figure 8.12.a. The light transmission starts from 595 nm and ends at 950 nm with highest peak at 695 nm. The ZnO-SQ peak maxima are well-matched and overlapped with the transmitted light spectrum. It is expected that the used light can be transmitted upto 3.6 mm which includes both the superficial dermis (upto 1.5 mm) and deep dermis (upto 3.0 mm).

Nowadays, PDT is experimentally used for treating breast cancer specially to treat recurrent breast cancers in the chest wall [12]. Thus, we have employed ZnO-SQ nanohybrids in human breast cancer cell-lines MCF-7 to observe its photodynamic action in malignant breast tissues. The photo-induced cytotoxicity was determined using MTT assay [45]. There is no change in cell viability using 30

mins of light irradiation suggesting no effect of the light dosimetry

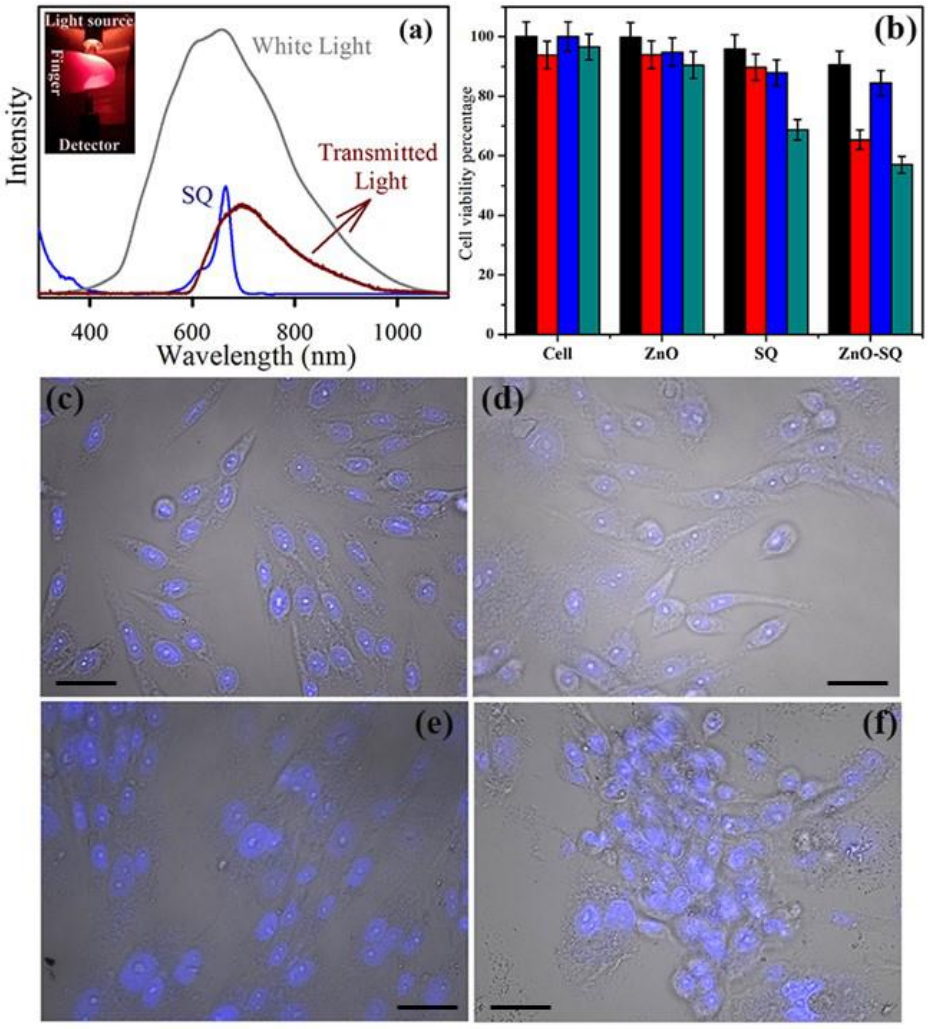

Figure 8.12: *(a) Penetration tendency of white light through human body: white light spectrum (grey colour), spectrum of transmitted light through finger (dark red) and absorption spectra of SQ (blue). Inset shows the experimental setup of measurement (b) In vitro cytotoxicity assay in MCF7 cells with ZnO-SQ, SQ, and ZnO with MTT as an indicator dye. Black bar and red bar represent dark and light irradiated conditions using 0.5 μm SQ as drug (SQ in ZnO-SQ is also 0.5 μm) and blue and cyan bar represent dark and light irradiated conditions using 1 μm SQ (SQ in ZnO-SQ is also 1 μm) as drug respectively. Microscopic images MCF7 cells without any treatment in the absence (c) and the presence (d) of red light and with ZnO-SQ treated samples in the absence (e) and the presence (f) of red light. Scale bar is 20 μm.*

in cell. We have evaluated two different concentrations of SQ for treatment purpose namely: 0.5 μm and 1 μm. For nanohybrid samples SQ concentration was set to 0.5 μm and 1 μm and corresponding ZnO concentration was determined using

absorption spectra. Cells treated with ZnO in presence or absence of red light depicts no cytotoxic nature (cell death < 10%). For nanohybrids corresponding to 0.5 μm concentration, there exist significant cytotoxicity (~35%) in light treated systems compare to cells treated under dark. For control SQ, very less effect is observed suggesting enhanced PDT action of nanohybrid even at low concentration. For nanohybrids corresponding to 1 μm concentration, PDT action further increases but significant dark toxicity also exists. The morphological changes of the cells have been observed using fluorescence microscopic images. The control cells (without any treatment) show typical adherence and morphology of cancer cells under both dark and red light illuminated conditions (Figure 8.12.c and 8.12.d). ZnO-SQ treated cells show no significant alteration of morphology suggesting lower dark toxicity (Figure 8.12.e). ZnO-SQ treated cells with red light illumination shows notable changes in morphology and adherence properties. Figure 8.12.f depicts rounded nuclei with lost cell adherence properties of MCF-7 cells treated with ZnO-SQ in presence of red-light suggesting ROS mediated cancer cell death. The observations suggest prospective use of ZnO-SQ nanohybrids for PDT based medicinal application.

8.3. Conclusion: An antimicrobial photodynamic therapy (aPDT) depends on target specificity of the drug and the penetration capability of the light used. In the present study, we have demonstrated the use of Squaraine (SQ) as the red light activated photosensitizer which can enhance the light penetration ability through tissue. SQ was successfully conjugated with ZnO NPs (~ 24 nm confirmed by TEM) to impart pH sensitivity followed by nano-dimension driven drug internalization. The attachment was confirmed using FTIR, UV-Vis, steady state fluorescence spectroscopic tools. The photoinduced excited state electron transfer process from dye to semiconductor was validated by time-resolved fluorescence transients and this process leads to greater extent of ROS generation. The ROS generated by ZnO-SQ is essentially singlet oxygen in nature as confirmed using SOSGR assay. The

photodynamic antibacterial effect on *S. aureus* was confirmed using CFU assay which suggest reduction of 95% colony after light activated drug treatment. The immense bacterial killing activity generated due to cell-membrane disruption confirmed by PI staining fluorescence microscopy-based assay, cellular internalization of NPs demonstrated using TEM and intracellular ROS generation. The tremendous stimuli responsive effectiveness of ZnO-SQ for killing bacteria drew our attention to check its efficacy to eradicate bacterial biofilms. The quantitative crystal violet assay depicted photo activated anti-biofilm effect of the nanohybrids. The loss of adherence property in biofilms as well as the structural disruption was confirmed using microscopic images. The ZnO-SQ nanohybrid was coated over titanium metal sheets, used as artificial implant mimic, was demonstrated to eradicate mature biofilms by application of external red illumination. The cytotoxicity assay using human bone cell line MG-63 and hemolysis assay on human RBCs show intrinsic biocompatibility of ZnO-SQ suggesting its overall clinical applicability. Hence, this enquiry could be translated to develop penetrable light activated nanoantibiotic agents to treat antibiotic resistant clinically isolated pathogens.

Next, we have employed ZnO NPs as the inorganic counterparts to obtain the inorganic-organic nanohybrids. ZnO NPs were synthesized and characterized using electron microscopic tools. The successful molecular level attachment of SQ on ZnO surfaces were determined using FRET strategy. The intermolecular distance was obtained as 22.3 Å. The nanohybrids then examined for dye aggregation in aqueous media, pH responsive delivery of the photosensitizers and improved ROS generation. The nanohybrids show betterment in stability, dissolution and activity compare to the bare SQ dye. The greater ROS efficacy is obtained due to photo-induced electron transfer process from excited state of SQ to conduction band of ZnO, which is determined using time-resolved fluorescence transients. The phototoxicity of ZnO-SQ was assessed in human breast cancer cell line MCF-7 which shows significant reduction in cell viability. The loss of adherence property

of cancer cells with rounded nucleus signify cell death through improved photodynamic action of ZnO-SQ nanohybrids. Overall, the novel physico-chemical properties of the nanohybrids are thoroughly evaluated for its potency to use in PDT.

References

[1] S. Davis, Biomedical applications of nanotechnology—implications for drug targeting and gene therapy, *Trends. Biotechnol.*, 15 (1997) 217-224.

[2] X. Zhu, A.F. Radovic-Moreno, J. Wu, R. Langer, J. Shi, Nanomedicine in the management of microbial infection - overview and perspectives, *Nano today,* 9 (2014) 478-498.

[3] C.M. Courtney, S.M. Goodman, J.A. McDaniel, N.E. Madinger, A. Chatterjee, P. Nagpal, Photoexcited quantum dots for killing multidrug-resistant bacteria, *Nat. Mater.,* 15 (2016) 529-534.

[4] J.J. Mekalanos, Environmental signals controlling expression of virulence determinants in bacteria, *J. Bacteriol.,* 174 (1992) 1-7.

[5] J.A. Edson, Y.J. Kwon, Design, challenge, and promise of stimuli-responsive nanoantibiotics, *Nano. Converg.,* 3:26 (2016) 1-13.

[6] S. Wang, P. Huang, X. Chen, Stimuli-responsive programmed specific targeting in nanomedicine, *ACS Nano,* 10 (2016) 2991-2994.

[7] C.I.C. Crucho, The attack of the smart particles: should bacteria be afraid?, *ACS Med. Chem. Lett.,* 9 (2018) 2-3.

[8] D.G. Meeker, S.V. Jenkins, E.K. Miller, K.E. Beenken, A.J. Loughran, A. Powless, T.J. Muldoon, E.I. Galanzha, V.P. Zharov, M.S. Smeltzer, J. Chen, Synergistic photothermal and antibiotic killing of biofilm-associated staphylococcus aureus using targeted antibiotic-loaded gold nanoconstructs, *ACS Infect. Dis.,* 2 (2016) 241-250.

[9] V. Biju, Chemical modifications and bioconjugate reactions of nanomaterials for sensing, imaging, drug delivery and therapy, *Chem. Soc. Rev.,* 43 (2014) 744-764.

[10] M.R. Hamblin, T. Hasan, Photodynamic therapy: a new antimicrobial approach to infectious disease?, *Photochem. Photobiol. Sci.,* 3 (2004) 436-450.

[11] J.-C. Boyer, M.-P. Manseau, J.I. Murray, F.C. van Veggel, Surface modification of upconverting NaYF4 nanoparticles with PEG− phosphate ligands for NIR (800 nm) biolabeling within the biological window, *Langmuir,* 26 (2009) 1157-1164.

[12] S. Luo, E. Zhang, Y. Su, T. Cheng, C. Shi, A review of NIR dyes in cancer targeting and imaging, *Biomaterials,* 32 (2011) 7127-7138.

[13] C. Wang, H. Tao, L. Cheng, Z. Liu, Near-infrared light induced in vivo photodynamic therapy of cancer based on upconversion nanoparticles, *Biomaterials,* 32 (2011) 6145-6154.

[14] K. Liu, X. Liu, Q. Zeng, Y. Zhang, L. Tu, T. Liu, X. Kong, Y. Wang, F. Cao, S.A. Lambrechts, Covalently assembled NIR nanoplatform for simultaneous fluorescence imaging and photodynamic therapy of cancer cells, *ACS Nano,* 6 (2012) 4054-4062.

[15] R. Laxminarayan, A. Duse, C. Wattal, A.K. Zaidi, H.F. Wertheim, N. Sumpradit, E. Vlieghe, G.L. Hara, I.M. Gould, H. Goossens, Antibiotic resistance—the need for global solutions, *Lancet. Infect. Dis.,* 13 (2013) 1057-1098.

[16] C.A. Arias, B.E. Murray, Antibiotic-resistant bugs in the 21st century—a clinical super-challenge, *N. Engl. J. Med.,* 360 (2009) 439-443.

[17] U.D.o. Health, H. Services, Antibiotic resistance threats in the United States, 2013, *Atlanta: CDC,* (2013) 1-114.

[18] A.J. Huh, Y.J. Kwon, "Nanoantibiotics": a new paradigm for treating infectious diseases using nanomaterials in the antibiotics resistant era, *J. Control. Release.,* 156 (2011) 128-145.

[19] H.M. Mansour, Y.-S. Rhee, X. Wu, Nanomedicine in pulmonary delivery, *Int. J. Nanomed.,* 4 (2009) 299-319.

[20] M.N. Karim, M. Singh, P. Weerathunge, P. Bian, R. Zheng, C. Dekiwadia, T. Ahmed, S. Walia, E. Della Gaspera, S. Singh, R. Ramanathan, V. Bansal, Visible-light-triggered reactive-oxygen-species-mediated antibacterial activity of peroxidase-mimic CuO nanorods, *ACS Appl. Nano. Mater.* , 1 (2018) 1694-1704.

[21] S.L. Percival, L. Suleman, C. Vuotto, G. Donelli, Healthcare-associated infections, medical devices and biofilms: risk, tolerance and control, *J. Med. Microbiol.,* 64 (2015) 323-334.

[22] H.-C. Flemming, J. Wingender, The biofilm matrix, *Nat. Rev. Microbiol.,* 8 (2010) 623-633.

[23] L.-S. Wang, A. Gupta, V.M. Rotello, Nanomaterials for the treatment of bacterial biofilms, *ACS Infect. Dis.,* 2 (2015) 3-4.

[24] C. Fux, J. Costerton, P. Stewart, P. Stoodley, Survival strategies of infectious biofilms, *Trends. Microbiol.,* 13 (2005) 34-40.

[25] B.M. Geilich, I. Gelfat, S. Sridhar, A.L. van de Ven, T.J. Webster, Superparamagnetic iron oxide-encapsulating polymersome nanocarriers for biofilm eradication, *Biomaterials,* 119 (2017) 78-85.

[26] D.K. Dennison, M.B. Huerzeler, C. Quinones, R.G. Caffesse, Contaminated implant surfaces: an in vitro comparison of implant surface coating and treatment modalities for decontamination, *J. Periodontol.,* 65 (1994) 942-948.

[27] R.C. Hunter, T.J. Beveridge, Application of a pH-sensitive fluoroprobe (C-SNARF-4) for pH microenvironment analysis in Pseudomonas aeruginosa biofilms, *Appl. Environ. Microbiol.,* 71 (2005) 2501-2510.

[28] Z.Y. Zhang, Y.D. Xu, Y.Y. Ma, L.L. Qiu, Y. Wang, J.L. Kong, H.M. Xiong, Biodegradable ZnO@ polymer core–Shell nanocarriers: pH-triggered release of doxorubicin in vitro, *Angew. Chem.,* 52 (2013) 4127-4131.

[29] K.R. Raghupathi, R.T. Koodali, A.C. Manna, Size-dependent bacterial growth inhibition and mechanism of antibacterial activity of zinc oxide nanoparticles, *Langmuir,* 27 (2011) 4020-4028.

[30] S. Chaudhuri, S. Sardar, D. Bagchi, S. Dutta, S. Debnath, P. Saha, P. Lemmens, S.K. Pal, Photoinduced dynamics and toxicity of a cancer drug in proximity of inorganic nanoparticles under visible light, *ChemPhysChem,* 17 (2016) 270-277.

[31] S. Sardar, S. Chaudhuri, P. Kar, S. Sarkar, P. Lemmens, S.K. Pal, Direct observation of key photoinduced dynamics in a potential nano-delivery vehicle of cancer drugs, *Phys. Chem. Chem. Phys.,* 17 (2015) 166-177.

[32] K. Page, M. Wilson, I.P. Parkin, Antimicrobial surfaces and their potential in reducing the role of the inanimate environment in the incidence of hospital-acquired infections, *J. Mater. Chem.,* 19 (2009) 3819-3831.

[33] D. Bagchi, V.S. Rathnam, P. Lemmens, I. Banerjee, S.K. Pal, NIR-Light-Active ZnO-Based Nanohybrids for Bacterial Biofilm Treatment, *ACS Omega,* 3 (2018) 10877-10885.

[34] J. Park, C. Barolo, F. Sauvage, N. Barbero, C. Benzi, P. Quagliotto, S. Coluccia, D. Di Censo, M. Gratzel, M.K. Nazeeruddin, G. Viscardi, Symmetric vs. asymmetric squaraines as photosensitisers in mesoscopic injection solar cells: a structure-property relationship study, *ChemComm,* 48 (2012) 2782-2784.

[35] J. Patwari, S. Sardar, B. Liu, P. Lemmens, S.K. Pal, Three-in-one approach towards efficient organic dye-sensitized solar cells: aggregation suppression, panchromatic absorption and resonance energy transfer, *Beilstein J. Nanotechnol.,* 8 (2017) 1705-1713.

[36] J. Kuchlyan, N. Kundu, D. Banik, A. Roy, N. Sarkar, Spectroscopy and fluorescence lifetime imaging microscopy to probe the interaction of bovine serum albumin with graphene oxide, *Langmuir,* 31 (2015) 13793-13801.

[37] N.A. Anderson, T. Lian, Ultrafast electron transfer at the molecule-semiconductor nanoparticle interface, *Annu. Rev. Phys. Chem.,* 56 (2005) 491-519.

[38] D. Bagchi, S. Chaudhuri, S. Sardar, S. Choudhury, N. Polley, P. Lemmens, S.K. Pal, Modulation of stability and functionality of a phyto-antioxidant by weakly interacting metal ions: curcumin in aqueous solution, *RSC Adv,* 5 (2015) 102516-102524.

[39] C. Flors, M.J. Fryer, J. Waring, B. Reeder, U. Bechtold, P.M. Mullineaux, S. Nonell, M.T. Wilson, N.R. Baker, Imaging the production of singlet oxygen in vivo using a new fluorescent sensor, singlet oxygen sensor green®, *J. Exp. Bot.,* 57 (2006) 1725-1734.

[40] X. Li, S.M. Robinson, A. Gupta, K. Saha, Z. Jiang, D.F. Moyano, A. Sahar, M.A. Riley, V.M. Rotello, Functional gold nanoparticles as potent antimicrobial agents against multi-drug-resistant bacteria, *ACS Nano,* 8 (2014) 10682-10686.

[41] Z. Huang, X. Zheng, D. Yan, G. Yin, X. Liao, Y. Kang, Y. Yao, D. Huang, B. Hao, Toxicological effect of ZnO nanoparticles based on bacteria, *Langmuir,* 24 (2008) 4140-4144.

[42] D. Bagchi, A. Halder, S. Debnath, P. Saha, S. K Pal, Exploration of interfacial dynamics in squaraine based nanohybrids for potential photodynamic action, *J. Photochem. Photobiol. A.,* (2019) doi.org/10.1016/j.jphotochem.2019.1005.1005.

[43] S. Chaudhuri, S. Sardar, D. Bagchi, S.S. Singha, P. Lemmens, S.K. Pal, Sensitization of an endogenous photosensitizer: electronic spectroscopy of riboflavin in the proximity of semiconductor, insulator, and metal nanoparticles, *J. Phys. Chem. A.*, 119 (2015) 4162-4169.

[44] R. Wahab, N.K. Kaushik, N. Kaushik, E.H. Choi, A. Umar, S. Dwivedi, J. Musarrat, A.A. Al-Khedhairy, ZnO nanoparticles induces cell death in malignant human T98G gliomas, KB and non-malignant HEK cells, *J. Biomed. Nanotechnol.,* 9 (2013) 1181-1189.

[45] P. Singh, S. Choudhury, S. Kulanthaivel, D. Bagchi, I. Banerjee, S.A. Ahmed, S.K. Pal, Photo-triggered destabilization of nanoscopic vehicles by dihydroindolizine for enhanced anticancer drug delivery in cervical carcinoma, *Colloids Surf B. Biointerfaces,* 162 (2018) 202-211.

Chapter 9

Spectroscopic Studies on a Porous Metal-organic Framework for Enhanced Drug Loading and Near Infra-red Sensitized Drug Activity

9.1. Introduction: Indiscriminate use of antibiotics in the field of medicine [1] as well as for agricultural purposes [2] has led to the emergence of multidrug resistant (MDR) infection. The indestructible superbugs pose a serious threat to global health indicating the inception of post-antibiotic era [3]. Antibiotic-resistant bacteria generate more than 2 million cases of severe illnesses, including 23000 annual deaths in the US alone [4]. Recent reports predict 10 million annual deaths from bacterial infections by 2050, which is way more than the deaths caused by cancer presently [5]. Despite rigid hygiene protocols followed within hospital environments, most life-threatening bacterial infections occur in healthcare settings such as hospitals and nursing homes commonly referred as healthcare-associated infections (HAIs) and its eradication requires prolonged antibiotic therapy with tissue debridement (i.e. surgical removal) in some cases, resulting in low patient compliance and excessive health-care costs [6]. HAIs are often associated with gram-positive bacteria, such as *Staphylococcus aureus* and *Staphylococcus epidermidis* infection and it has been reported that *S. aureus* solely causes 25 percent of nosocomial infections [7]. *S. aureus* often develops resistance against commonly used antibiotics as methicillin, vancomycin etc. These drug resistant strains are ranked fifth among eleven as highly threatening bacteria to human health in a recent report by WHO and requires urgent alternative medicinal approach [5].

As the development of resistance against antibiotic by the microbes is anticipated to continue in the coming years, a necessity exists for an immediate and

continual search for alternative methods against drug resistant bacteria towards which no resistance can develop easily. One of the most promising and innovative approaches in this respect is antimicrobial photodynamic therapy (aPDT) [8]. The therapeutic approach involves the administration of a photosensitizer (PS) which would be activated upon photo-irradiation to generate reactive oxygen species (ROS) that can kill the infected cells [9]. aPDT follows two types of mechanism to proceed photochemical reactions, namely type I or type II mechanism. Type I reactions generate radicals following triplet state electron transfer whereas in type II reactions PS reacts directly with molecular oxygen (O_2) and forms the highly reactive singlet oxygen ($^1O_2$) via $^3PS \rightarrow O_2$ energy transfer. Both type I and II reactions take place simultaneously during aPDT and the ratio of the occurrence of the two pathways depends on the type of PS and the microenvironment of application site [10]. Extent of aPDT induced cell damage is determined by several photophysical properties of the PS such as lipophilicity, extinction coefficient and quantum yield of the triplet state [11]. Again, therapeutic efficacy of PS activatable at the near-infrared region (650-900 nm) can contribute significantly due to greater light penetration through biological tissue [12]. There are several advantages related to aPDT such as lesser chance of resistance generation, more localized action of the treatment and lesser side effects to the surrounding healthy tissues [13]. However, the highly efficient PS are generally hydrophobic in nature which leads to self-aggregation of PS in aqueous solution, which is detrimental in view of PDT efficiency as it diminishes ROS generation capability [14]. Also, inefficient delivery of PS molecules specifically to the infected site enhances destruction possibilities of the surrounding normal tissues.

A possible approach to improve therapeutic efficacy of PS is to pinpoint its delivery to and into the bacteria using nanomaterials leading to lower systemic toxicity through minimal disturbance to the healthy tissue and cells [15]. Besides nanomaterials possessing a “sense and act” module triggered by signals found in

the microbial growth environment are preferential for site-specific delivery of antimicrobial agents [16]. Organic-based drug delivery systems (DDSs) includes lipid [17], protein and polymer-based systems which are already in use for clinical trial whereas use of inorganic nanomaterials in biological research is relatively new and constantly expanding as they possess tuneable properties, good biocompatibility, ease of functionalization, strong drug affinity and controllable release [18].

Recently, nanosized metal organic framework (NMOF) exhibiting the advantages of both organic and inorganic-based DDSs has been extensively exploited in a variety of biomedical applications due to its merits including high porosity, large specific surface area, and controllable composition [19]. Some recent reports depict that robust and crystallized NMOFs with well-defined pore structures can effectively encapsulate a large number of small molecules [20]. Also, porphyrin-based MOFs were prepared by using porphyrin derivatives as bridging ligands to coordinate with metal ions in periodic arrays, which greatly reduced the self-quenching of the porphyrin maintaining its PDT efficacy [21]. However, synthesis of this type of self-assembled system is often complicated involving multi-step reaction and largely depends on the anchoring group present in the PS. Thus, there is a huge demand for a facile and universal strategy to solve the solubility and bioavailability of hydrophobic PSs using NMOF as DDS maintaining monodispersed nanoparticle size, stability under physiological condition, inherent biocompatibility with ultrahigh drug loading following sustained and stimuli responsive drug release. Zeolitic imidazolate frameworks (ZIFs), a subclass of nano-porous MOFs composed via self-assembly of metal ions Zn^{2+} linked through nitrogen atoms of deprotonated imidazolate linker forming a sodalite topological crystal are shown to provide unique applicability in controlled anti-cancer drug delivery application [22]. ZIF-8 crystals can circulate in the bloodstream under physiological conditions and be slowly released after the accumulation in

intracellular organelles with lower pH (pH= 5−6) depicting its possibility to use as a pH-responsive DDS [22]. Recently, stable, highly-luminescent system was developed through trapping anionic complexes sensitized by tridentate pyridine-tetrazolate (pytz) ligands within the rigid framework of ZIF-8 which has huge application in medical diagnostic [23].

In this chapter, we have encapsulated squaraine SQ, a typical polymethyne dyes with donor−acceptor−donor (D−A−D) interaction [24] into zeolitic imidazolate framework-8 (ZIF-8) by a post-synthetic strategy. The insertion of SQ within ZIF-8 cavity is expected to lower free diffusion of SQ molecules in biological media and limit the SQ aggregation possibilities. Synthesized ZIF8-SQ nanoconjugates are characterized using electron microscopic techniques as SEM, TEM and XRD. Aggregation behaviour of SQ within ZIF-8 is critically analysed using steady-state and time-resolved spectroscopic methods. ZIF8-SQ nanoconjugate demonstrated acidic pH and red-light sensitive ROS generation due to molecular cross-talking and ease of diffusion of O_2 through porous ZIF. Next, ZIF8-SQ is examined for its aPDT action against methicillin resistant *Staphylococcus aureus* (MRSA) planktonic as well as in biofilm. Thus, this is the first account of fabricated photosensitizer-embedded MOFs showing unparallel aPDT action under red-light illumination keeping human cells unaffected.

9.2. Results and Discussion:

9.2.1. Nano MOF Entrapping Hydrophobic Photosensitizer for Dual-stimuli Responsive Unprecedented Therapeutic Action against Drug-resistant Bacteria [25]: Figure 9.1.a depicts the X-ray diffraction patterns of synthesized ZIF-8, ZIF8-SQ, and pure SQ. XRD patterns of both ZIF-8 and ZIF8-SQ revealed characteristic peaks at 2θ = 7.2°, 10.3°, 12.5°, 14.5°, 16.3° and 17.9°, which can be attributed to coherent diffraction from (011), (002), (112), (022), (013), (222) planes. The peaks are in well agreement with those reported in literature [26] confirming that the sample

has pure ZIF-8 phase pre and post drug encapsulation. Nonetheless, the PXRD

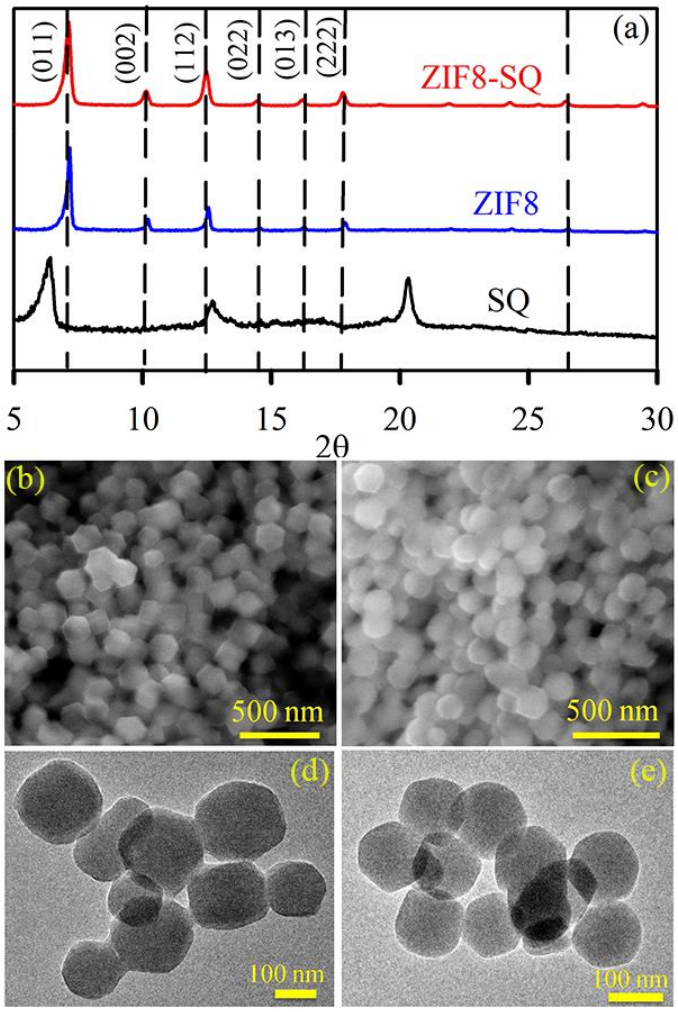

Figure 9.1. *(a) PXRD patterns of ZIF8 (blue), ZIF8-SQ (red) and SQ (black). SEM images of ZIF8 (b) and ZIF8-SQ (c) TEM images of ZIF8 (d) and ZIF8-SQ (e).*

pattern of ZIF8-SQ (red coloured in Figure 9.1.a) exhibits similar peaks to ZIF8 with slight deviation in the form of a peak broadening at lower values of 2θ in ZIF8-SQ compared to those of ZIF8. The observation indicates decrease in the crystal size according to Debye-Scherrer's equation [27]. The encapsulation of guest molecules SQ inside the micropores of ZIF8 is responsible for the change in inter-planer distance. In addition, the disappearance of a peak at 20.5^{o} in pure SQ after its encapsulation into ZIF-8 clearly suggests that ZIF8-SQ is a single-phase material devoid of free drug molecules that were present in some of the previous reports of

drug encapsulation inside the micropores of ZIF moiety [26]. The morphological analysis of the prepared nanoparticles of ZIF8 and ZIF8-SQ were carried out using SEM and TEM images as shown in Figure 9.1.b-e. SEM image of ZIF8 (Figure 9.1.b) depicts uniform rhombic dodecahedron crystals of around 170-200 nm dimension. The TEM image of ZIF8 (Figure 9.1.d) exhibits sharp edges of the dodecahedron structures with an average diameter of 180 nm. Encapsulation of SQ into ZIF8 alters the sharp crystalline nature of the dodecahedron. As shown in Figure 9.1.c, the SEM images of ZIF8-SQ illustrate change in edge sharpness compared to ZIF8 with a shrinkage of crystal size. TEM image depicts the similar change with a slight decrease of average diameter to 170 nm as shown in Figure 9.1.e. No apparent aggregation or destruction in crystal structure was observed by microscopy, which suggests that SQ molecules are encapsulated into the micropores inside or to the surface of ZIF8 framework [28].

The thermal stability is estimated using thermogravimetric analysis (TGA) and the resultant curves are illustrated in Figure 9.2.a. The first weight-loss profile around 10% before 400 °C corresponds to the removal of solvent and some guest molecules (e.g., 2-methyl imidazole) in ZIF-8. A sharp weight loss around 50% before 500 °C suggests the decomposition of the organic ligand and the collapse of the framework structure. Thus, ZIF8 is thermally stable up to around 450 °C. In case of ZIF8-SQ, the initial weight loss of about 10% occurs at the range of 300 °C, which corresponds to the departure of the solvent molecules. Additionally, ZIF8-SQ initiate decomposition at 400 °C and nearly 86% weight loss occurs within 500 °C. The initiation of thermal decomposition at an earlier temperature might be attributed to the dissociation of SQ molecules encapsulated within the ZIF8 framework [29]. We have calculated the drug loading percentage from TG curves considering the temperature range of 100 °C to 500 °C and the DL is found to be 31%. We have also estimated drug loading using difference between absorbance value of supernatant SQ before and after stirring with ZIF8 and the DL is found to be 39.2%. The ultrahigh drug loading is indicative of favourable molecular

orientation of SQ molecules into ZIF-8 porous structure. To further confirm structural stability and parity of ZIF-8 after SQ loading, we have performed Raman measurements of the systems. Figure 9.2.b shows the Raman spectra of ZIF8 and ZIF8-SQ. The Raman signal of ZIF8 is influenced by intense bands corresponding to methyl groups and imidazole ring vibrations. The band observed at 180 cm^{-1} was assigned to Zn−N stretching, while the bands obtained at 691, 1152, and 1462 cm^{-1} were designated to imidazolium ring puckering, C5−N stretching, and methyl bending, respectively [30]. The Raman modes of ZIF8-SQ samples are in the similar position and intensity, suggesting structural resemblance between ZIF8 and ZIF8-SQ [31].

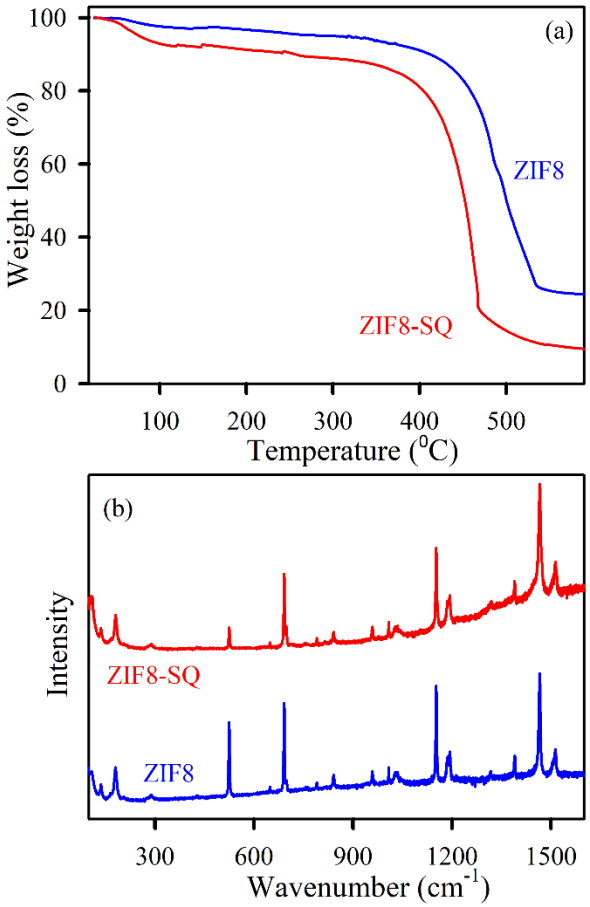

Figure 9.2. *(a) Thermogravimetric analysis profile of ZIF8 (blue) and ZIF8-SQ (red) (b) Raman spectra of ZIF8 (blue) and ZIF8-SQ (red).*

Then, we have evaluated aggregation behaviour of SQ within ZIF-8 cavity using absorbance in mixed solvent. Figure 9.3.a demonstrates absorption characteristics of SQ in mixed solvents. SQ shows a sharp absorbance nature in pure DMSO with a peak at 665 nm which is assigned as the isolated monomeric absorption from a single SQ molecule as there is an infinite separation between two adjacent SQ molecules. The shoulder peak around 610 nm can be attributed to vibronic monomeric transition [32]. With increasing water content, there is a hypsochromic shift in the spectra comprising broader profiles due to formation of aggregated states. The addition of a small amount of water generates a blue shift of 5 nm in SQ spectrum which corresponds to the formation of H-aggregates between two or more vertically stacked molecules [32]. With increasing water content, an inversion of peak intensities between the higher and lower energy state and a significant broadening of the peaks are observed. The plausible reasons for the alteration of absorption nature of SQ from DMSO to pure water is existence of three types of interactions including formation of H-aggregate (described earlier), J-aggregates that is associated with two or more horizontally aligned head-to-tail molecules and intermolecular charge transfer (ICT) process depending on the relative orientation of the SQ molecules in the stacked conformation [33]. In case of SQ encapsulated within the ZIF8 cavity, the spectrum is identical to that of free SQ molecules only when pure DMSO solvent was used. On the other hand, introduction of small amounts of water caused a 15 nm red shift in the monomeric peak which might be due to re-orientation of the SQ molecules resulting in lower energy J aggregate formation (Figure 9.3.b). However, with increasing water content there is no significant difference in the peak position or peak width which clearly suggests that the relative orientation of adjacent SQ molecules within the cavity is different from the free system. To explain this difference, it can be suggested that charge delocalisation led to zwitterionic stabilisation within the ZIF framework lowering the possibilities of aggregate formation or ICT process, which in turn improves aqueous stability of the aggregated forms. Thus, it may be

conjectured that ZIF8-SQ is the thermodynamically stabilised product in aqueous medium which may eventually facilitate its biologically relevant applications.

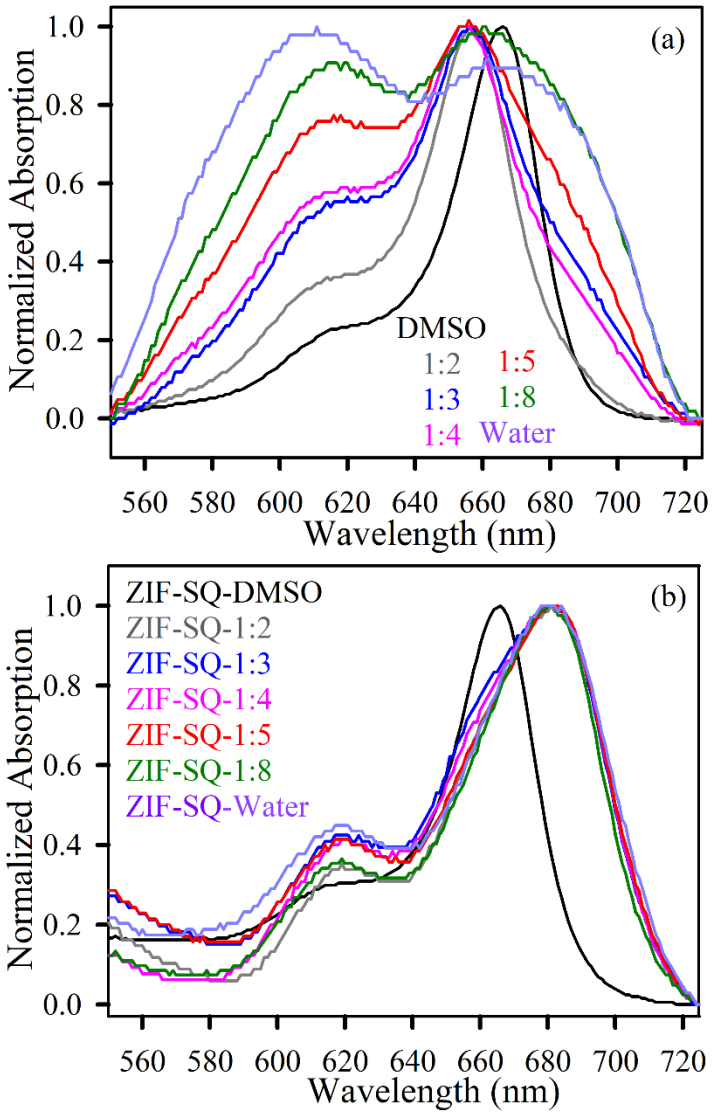

Figure 9.3. *Normalised absorption spectra of SQ (a) and ZIF8-SQ (b) in different solvent mixtures as pure DMSO (black), DMSO: water at 1:2 (grey), 1:3 (blue), 1:4 (pink), 1:5 (red), 1:8 (green) ratios and in pure water (purple).*

Thereafter, the time dependent precipitation of the ZIF8-SQ dispersion is monitored at different pH values (Figure 9.4.a). The dispersion is less stable in acidic aqueous solution (pH = 5) compared to that in neutral (pH = 7) solution. As microbial infections typically possess acidic environments owing to enhanced metabolic rates due to anaerobic fermentation, ZIF8-SQ is expected to be deposited

more in the infected site than normal tissues. The dissolution of the ZIF8-SQ at different pH values is also monitored and shown in Figure 9.4.b. At pH 5, 39% SQ was released from ZIF8-SQ whereas only 6.5% release took place at pH=7 buffer medium after 24 hr incubation time. These results indicate that ZIF8-SQ behaves as a pH responsive drug delivery template as the coordination between the zinc and imidazolate ions dissociates at pH ~ 5.0 which makes the drug release pH responsive and optimal for targeting bacterial infection [34].

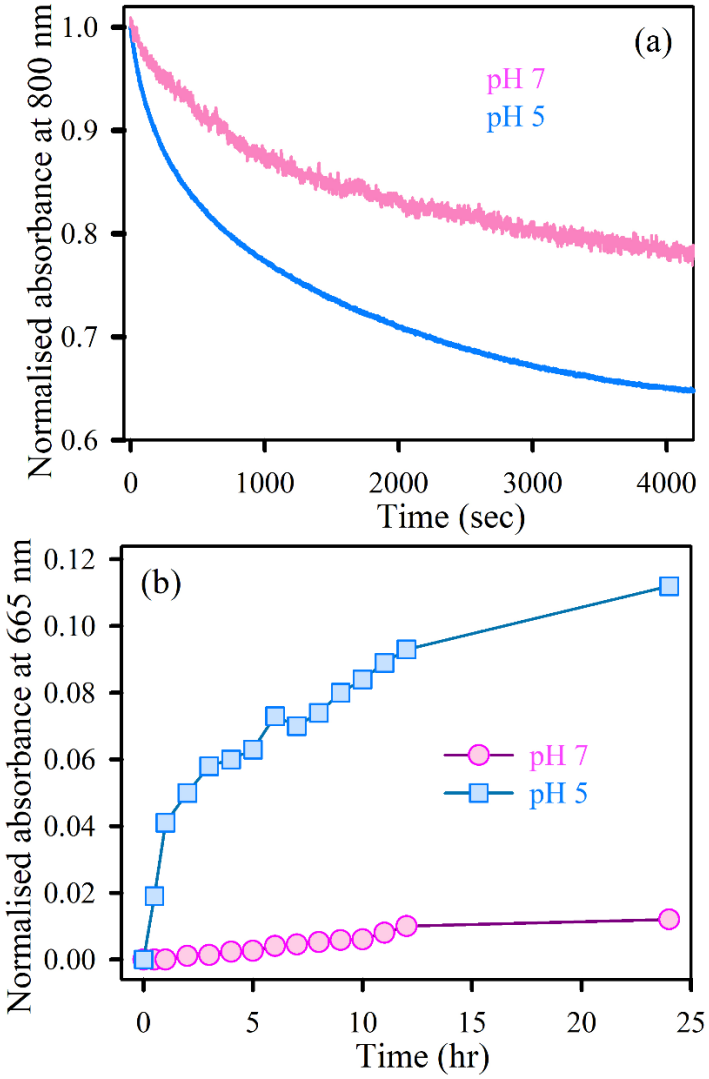

Figure 9.4. *(a) Precipitation of ZIF8-SQ dispersed in water at pH 7 and pH 5 obtained from absorbance at 800 nm (b) Dissolution of ZIF8-SQ in water at pH 5 and pH 7 obtained from the absorbance of the supernatant at 665 nm.*

Next, we have investigated the photoinduced ROS production capability of ZIF8-SQ and SQ. The ROS generation ability has been evaluated using the DCFH assay in which the oxidation of DCFH (non-fluorescent) to dichlorofluorescein (DCF, fluorescent) through interaction with ROS is observed. The fluorescence emission intensity of DCF is recorded as a function of time (Figure 9.5.a). The highest enhancement of the fluorescence intensity of DCF is obtained for ZIF8-SQ nanohybrids under red light illumination. ROS production increases ten times compared to that with free dye SQ. The control experiments with DCFH and ZIF8 under red light irradiation show negligible increase in fluorescence intensity. The huge photoinduced ROS production suggests ZIF8-SQ as a potential PDT agent. We have further analysed the reason behind such great increase in ROS. Besides the formation of stable aggregates in aqueous medium within ZIF framework structure, ZIF8-SQ depicts fluorescence quenching in aqueous medium compared to free SQ. To further study the electronic interactions, time-resolved fluorescence transient studies have been carried out. The fluorescence decay transients for free SQ and ZIF8-SQ have been collected upon excitation at 633 nm and detected at 670 nm (Figure 9.5.b) using water as the solvent. Steady state fluorescence quenching of SQ after encapsulation within ZIF-8 are shown in inset of Figure 9.5.b. The decay constants for the excited-state decay profiles of SQ in water show two time-scales, the faster one around 100 ps lifetime and a relatively longer component of 358 ps. The faster lifetime component is designated as the ICT process within SQ aggregated forms and the longer 358 ps component is ascribed to the excitonic coupling of monomeric transition. In case of ZIF8-SQ, a very fast time component of 30 ps predominantly exists, suggesting a photoinduced charge transfer process from the excited state of SQ to the ZIF8. The distinct change in lifetime of ZIF8-SQ indicates that different types of aggregation and orientation of SQ molecules might be co-existing within the framework structure increasing the overall electron residual time in the excited state that enhance the ROS generation. We anticipate

that conjugation of SQ with ZIF-8 leads to band gap reorientation of the whole system which favours photo induced charge transfer [35].

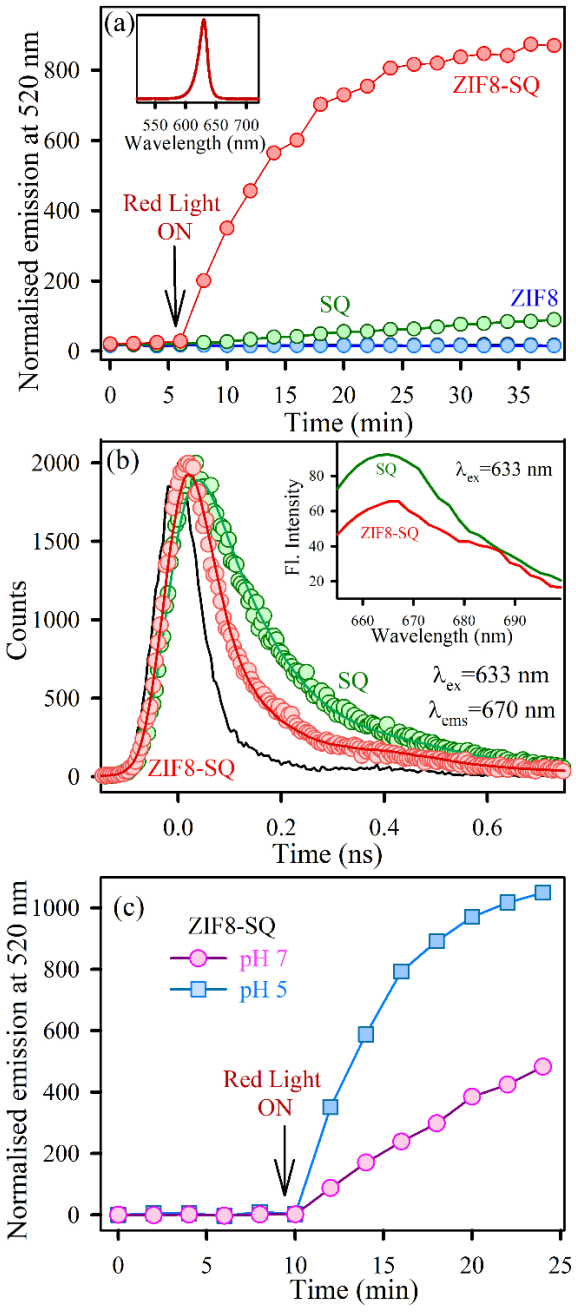

Figure 9.5. *(a) The DCFH oxidation with time in the presence of ZIF8-SQ (red), SQ (green), ZIF-8 (blue) and only DCFH (black) under red light irradiation. Inset shows the excitation spectrum of the red light (b) Fluorescence decay profiles of SQ (green) and ZIF8-SQ (red) at 670 nm (excitation at 633 nm). Black curve depicts the instrument response function IRF. Inset shows room-temperature PL spectra (excitation at 633 nm) of free SQ (green) and ZIF8-SQ (red) (c) The DCFH oxidation with time in the presence of ZIF8-SQ at two different pH solution (pH7: pink, pH5: blue).*

The ROS generation abilities of ZIF8-SQ are compared at two different pH conditions and it was found that ROS generation is much higher in acidic condition than at neutral pH. The greater precipitation rate of the nanohybrid can be correlated to the higher ROS generation at acidic environment. It is already reported that the reactivity of superoxide ion is more pronounced at lower pH due to its protonation and hence ZIF8-SQ shows greater ROS production at lower pH range [36]. To exclude the influence of SQ alone, we have checked ROS generation of SQ at two different pH condition (data not shown). The results depict no significant changes in ROS at various pH for only SQ which further confirms that ZIF8-SQ is acting as a pH responsive ROS generating nanohybrid. Also, at acidic pH, Zn-N bonds in ZIF-8 get unfasten and it can help diffusion of more molecular O_2 which helps in producing more ROS [37, 38].

Next, we have assessed the antimicrobial action of ZIF8-SQ towards methicillin resistant *S. aureus* (MRSA) under dark and red-light illumination. Variable concentrations of SQ and ZIF8-SQ (keeping SQ concentration same) ranging from 0 to 300 nM (0 nM, 25 nM, 50nM, 100 nM, 150 nM, 200nM, 250 nM and 300 nM) were examined using bacterial growth curve experiments. For SQ treated samples, no bacterial killing effect is observed under dark condition. However, after 30 mins of red-light irradiation, killing efficiency improved for concentrations greater than 150 nM. In case of ZIF8-SQ samples, dark toxicity is observed at 200 nM concentration up to which there is no effect of the sample (Figure 9.6.a). However, under red light illuminated condition, there is a drop in growth nature of MRSA even at lower concentrations of 25 nM and 50 nM. This trend is clearly indicative of superior effectivity of ZIF8-SQ even at very low concentration range. ZIF8-SQ is expected to adhere on bacterial cell membrane owing to its positively charged surface followed by intracellular uptake and consequent cell-death [34].

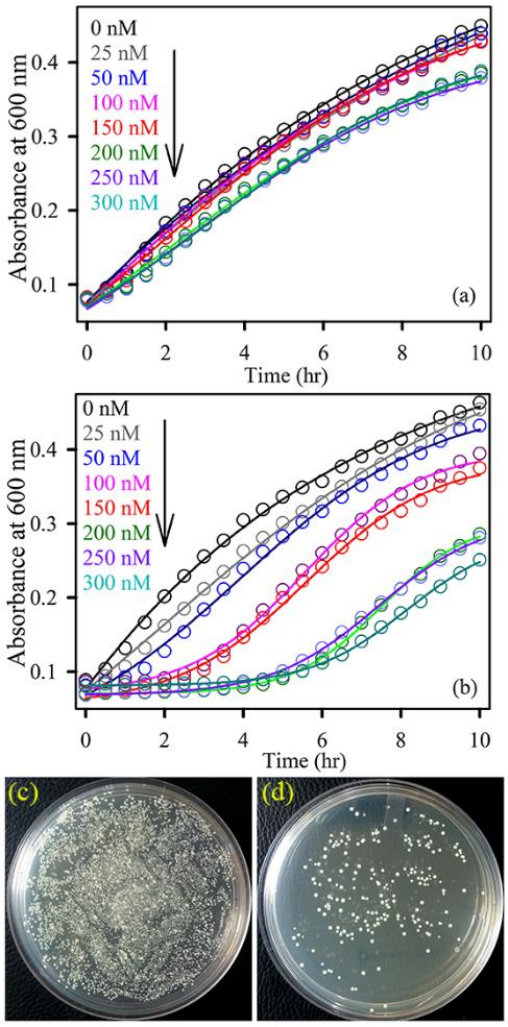

Figure 9.6. *Growth curves of MRSA in LB medium inoculated with 10^7 CFU of bacteria in the presence of different concentrations of ZIF8-SQ samples under dark condition (a) and with 30 mins of red light illuminated condition (b) Pictures of MRSA plates treated with 100 nM ZIF8-SQ under dark (c) and red light irradiated condition (d).*

Figure 9.6.b shows that at concentration ranges from 100 nM to 150 nM, the photo induced killing of MRSA by ZIF8-SQ is significantly pronounced. Higher concentration ranges as 200 nM, 250 nM and 300 nM of ZIF8-SQ provide even higher reduction in MRSA growth. Notably, there is no significant bacterial killing efficiency of ZIF-8 alone at the used concentration range. As increased concentration of SQ can provide dark toxicity which favours resistance generation, we have chosen 100 nM concentration for further experiments. Figure 9.6.c and d show MRSA plates treated with 100 nM ZIF8-SQ under dark and red light irradiated

conditions respectively. The visual difference in number of MRSA colonies after light illumination depicts specific photoinduced antibacterial effect (~86% colony reduction) of ZIF8-SQ nanoconjugate.

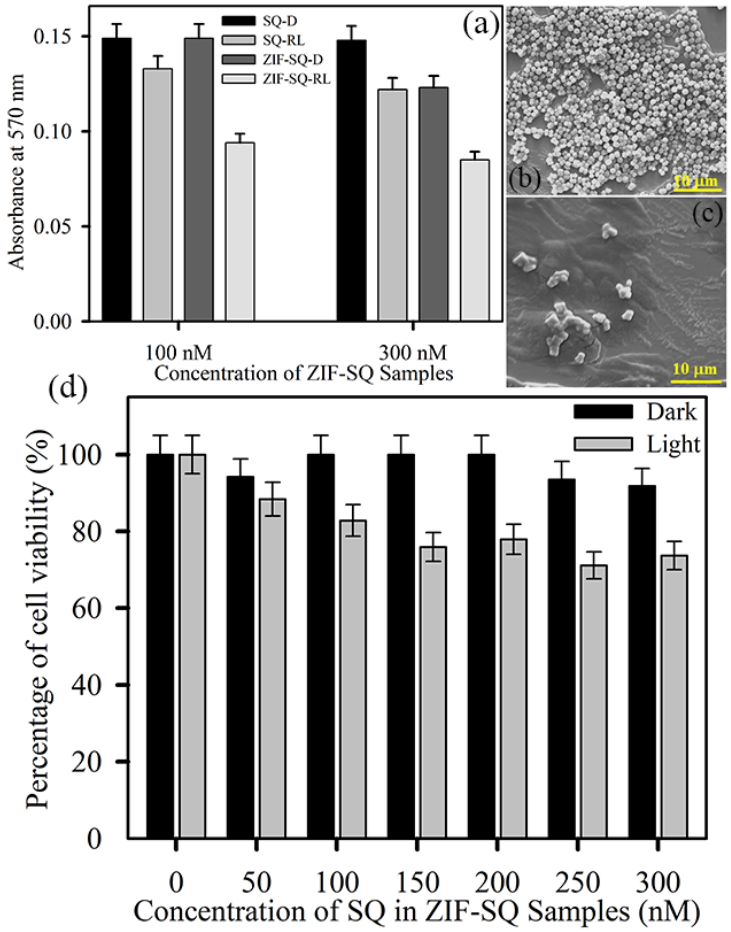

Figure 9.7. *(a) Adhesion efficiency of MRSA biofilms in presence of different dosage of SQ and ZIF8-SQ samples under dark and red-light irradiation. SEM images of an MRSA biofilm treated with ZIF8-SQ (b) under dark and (c) with 30 mins of red-light illumination (d) Cell viability assay using HEK-293 cells treated with different dosage of ZIF8-SQ in the absence (black) and presence of red-light illumination (grey).*

The exceptional photo active antimicrobial efficacy of ZIF8-SQ motivates us to investigate biofilm disruption capability of ZIF8-SQ. Biofilms are communicable structures of planktonic bacteria attached to a surface or with each other using extra polymeric substance (EPS) which is impenetrable by normal drugs [39]. The intrinsic acidic environment of biofilms motivates us to check destruction ability of ZIF8-SQ. The adhered biomass of 48 hr grown MRSA biofilms shows 13% and 40%

decrease in biomass for 100 nM SQ and ZIF8-SQ treated samples respectively under red light illuminated conditions. As depicted in Figure 9.7.a at higher concentration (i.e., 300 nM w.r.t SQ) ZIF8-SQ shows dark toxicity and hence a lower concentration range (100 nM) has been chosen for further studies. The morphological changes of the biofilms after treatment are demonstrated by SEM images. Figure 9.7.b and c depict the structure of the MRSA biofilms treated with ZIF8-SQ under dark and red light respectively. The inherent colonization effects of bacterial biofilms are significantly perturbed upon light treatment, as depicted by Figures 9.7.b and c. Figure 9.7.b shows typical characteristics of biofilms comprising extracellular polymeric matrix whereas Figure 9.7.c shows significantly lower number of bacteria without the typical arrangement of a biofilm. Magnified images show that the characteristic adherence and network structure of biofilms are completely destroyed upon red-light treatment. Biofilm perturbation nature of ZIF8-SQ got improved both by its pH responsive settlement and dissolution nature and hence it should be stated that biofilm destruction occurs by dual stimuli response: pH and light.

Nevertheless, the toxicity of nanomaterials toward mammalian cells is one of the crucial aspects associated with its real-life application [40]. ZIF8-SQ at very low dose (100 nM as used in aPDT) is expected to possess very less toxicity towards macrophages [34]. To evaluate the biocompatibility, we have evaluated the cytotoxicity of ZIF8-SQ against human embryonic kidney HEK-293 cells, which is a heterogeneous mix of all the types of cells present in the body. Figure 9.7.d represents result of MTT assay using variable concentration of ZIF8-SQ under dark and light irradiation. The cell viability upon treatment with ZIF8-SQ under dark almost remain similar except at 250 nM and 300 nM at which slight dark toxicity is present. In presence of light, for 100 nM concentration there is only 17% cell death which reaches to 25% for 250 and 300 nM concentration. Although the incubation and internalization of the nanohybrid is different in case of bacterial cell and human cell, even with highest concentration (300 nM) human cell viability is more than 75%

after red light irradiation. These observations confirm that ZIF8-SQ is non-toxic towards human cell at relatively lower concentration range which is highly effective against bacterial infections. More detail understanding of bacterial killing process by ZIF8-SQ using advanced bio-analytical techniques in *ex-vivo* and *in-vivo* condition is expected to provide significant real-life applicability of the fabricated nanoconjugates.

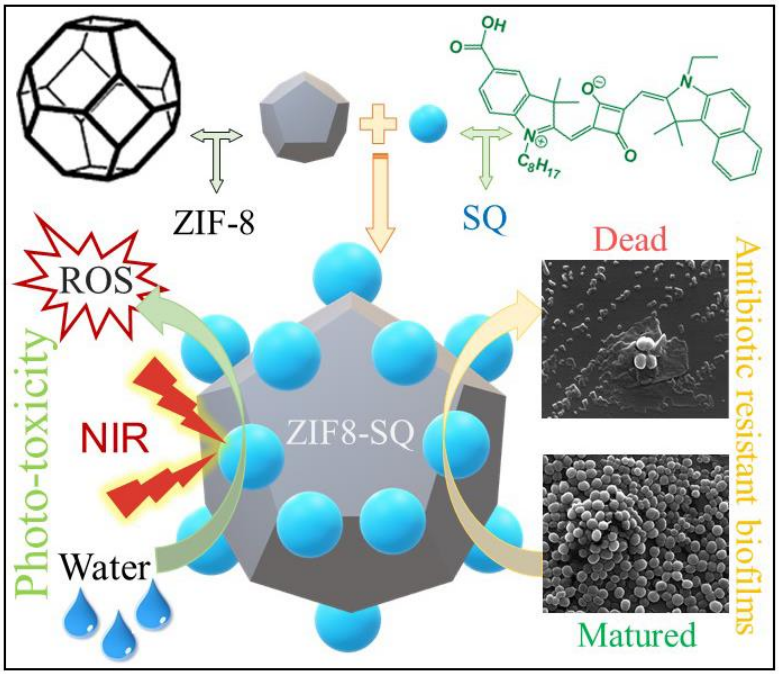

Scheme 9.1. *Squaraine incorporated nano-porous framework with improved NIR toxicity for fighting antibiotic-resistant bacterial infections.*

9.3. Conclusion: In summary, we present a post-synthetic approach for the synthesis of a Zn-based coordination polymeric system (ZIF-8) embedding a hydrophobic photosensitizing drug SQ while preserving its photodynamic action. The resultant nanoconjugate with the drug molecules entrapped within the well-defined porous cage structure of ZIF-8 ceases the self-aggregation behaviour of PS. It turns out that the PS molecules remain predominantly in monomeric forms within ZIF-8 cages due to an orientation driven energy stabilisation effect. ZIF8-SQ nanohybrid depicts enormous photoinduced ROS generation ability in pH responsive manner due to acidic pH driven pore expansion of ZIF-8 followed by

greater access of molecular O_2. Besides, ultrafast spectroscopic studies reveal that there is excited state charge transfer from SQ to ZIF that enhances excited state residual time of the activated species. The enormous aPDT effect of ZIF8-SQ towards MRSA even at distinctly lower concentration with no such toxicity towards human cell suggests its uniqueness and possibilities of real application. Overall, the present work demonstrates for the first time the retaining of photo-enabled action of hydrophobic SQ under physiological condition through encapsulation in a biodegradable therapeutic nano-platform for efficacious destruction of drug-resistant bacterial infections.

References

[1] C.A. Arias, B.E. Murray, Antibiotic-resistant bugs in the 21st century—a clinical super-challenge, *N. Engl. J. Med.,* 360 (2009) 439-443.

[2] B.M. Marshall, S.B. Levy, Food animals and antimicrobials: impacts on human health, *Clin. Microbiol. Rev.,* 24 (2011) 718-733.

[3] R. Laxminarayan, A. Duse, C. Wattal, A.K. Zaidi, H.F. Wertheim, N. Sumpradit, E. Vlieghe, G.L. Hara, I.M. Gould, H. Goossens, Antibiotic resistance—the need for global solutions, *Lancet. Infect. Dis.,* 13 (2013) 1057-1098.

[4] C.f.D. Control, Prevention, Antibiotic resistance threats in the united states, 2013. Atlanta: CDC; 2013, in, 2014, pp. 1-114.

[5] C. Willyard, The drug-resistant bacteria that pose the greatest health threats, *Nature News,* 543 (2017) 15.

[6] A. Gupta, S. Mumtaz, C.-H. Li, I. Hussain, V.M. Rotello, Combatting antibiotic-resistant bacteria using nanomaterials, *Chem. Soc. Rev.,* 48 (2018) 415-427

[7] S.L. Percival, L. Suleman, C. Vuotto, G. Donelli, Healthcare-associated infections, medical devices and biofilms: risk, tolerance and control, *J. Med. Microbiol.,* 64 (2015) 323-334.

[8] M.R. Hamblin, T. Hasan, Photodynamic therapy: a new antimicrobial approach to infectious disease?, *Photochem. Photobiol. Sci.,* 3 (2004) 436-450.

[9] T. Maisch, Anti-microbial photodynamic therapy: useful in the future?, *Lasers. Med. Sci.,* 22 (2007) 83-91.

[10] T. Maisch, R.-M. Szeimies, G. Jori, C. Abels, Antibacterial photodynamic therapy in dermatology, *Photochem. Photobiol. Sci.,* 3 (2004) 907-917.

[11] Y. Liu, R. Qin, S.A. Zaat, E. Breukink, M. Heger, Antibacterial photodynamic therapy: overview of a promising approach to fight antibiotic-resistant bacterial infections, *J. Clin. Transl. Res.,* 1 (2015) 140-167.

[12] T. Dai, Y.-Y. Huang, M.R. Hamblin, Photodynamic therapy for localized infections—state of the art, *Photodiagnosis. Photodyn. Ther.,* 6 (2009) 170-188.

[13] G. Jori, C. Fabris, M. Soncin, S. Ferro, O. Coppellotti, D. Dei, L. Fantetti, G. Chiti, G. Roncucci, Photodynamic therapy in the treatment of microbial infections: basic principles and perspective applications, *Laser. Surg. Med.,* 38 (2006) 468-481.

[14] Y. Feng, L. Liu, J. Zhang, H. Aslan, M. Dong, Photoactive antimicrobial nanomaterials, *J. Mater. Chem. B,* 5 (2017) 8631-8652.

[15] W. Gao, Y. Chen, Y. Zhang, Q. Zhang, L. Zhang, Nanoparticle-based local antimicrobial drug delivery, *Adv. Drug Deliv. Rev.,* 127 (2018) 46-57.

[16] C.I. Crucho, The attack of the smart particles: should bacteria be afraid?, *ACS Med. Chem. Lett*, 9 (2018) 2-3.

[17] D. Bagchi, S. Dutta, P. Singh, S. Chaudhuri, S.K. Pal, Essential dynamics of an effective phototherapeutic drug in a nanoscopic delivery vehicle: psoralen in ethosomes for biofilm treatment, *ACS Omega,* 2 (2017) 1850-1857.

[18] A.J. Huh, Y.J. Kwon, "Nanoantibiotics": a new Pparadigm for treating infectious diseases using nanomaterials in the antibiotics resistant era, *J. Control. Release,* 156 (2011) 128-145.

[19] M.X. Wu, Y.W. Yang, Metal–organic framework (MOF)-based drug/cargo delivery and cancer therapy, *Adv. Mater.,* 29 (2017) 1606134.

[20] J. Zhuang, C.-H. Kuo, L.-Y. Chou, D.-Y. Liu, E. Weerapana, C.-K. Tsung, Optimized metal–organic-framework nanospheres for drug delivery: evaluation of small-molecule encapsulation, *ACS Nano,* 8 (2014) 2812-2819.

[21] C.-W. Kung, T.-H. Chang, L.-Y. Chou, J.T. Hupp, O.K. Farha, K.-C. Ho, Post metalation of solvothermally grown electroactive porphyrin metal–organic framework thin films, *ChemComm,* 51 (2015) 2414-2417.

[22] C.-Y. Sun, C. Qin, X.-L. Wang, G.-S. Yang, K.-Z. Shao, Y.-Q. Lan, Z.-M. Su, P. Huang, C.-G. Wang, E.-B. Wang, Zeolitic imidazolate framework-8 as efficient pH-sensitive drug delivery vehicle, *Dalton Trans.,* 41 (2012) 6906-6909.

[23] F. Chen, L. Wang, Y. Xing, J. Zhang, Stable photoluminescence of lanthanide complexes in aqueous media through metal-organic frameworks nanoparticles with plugged surface, *J. Colloid Interface Sci.,* 527 (2018) 68-77.

[24] C. Zheng, A.R. Penmetcha, B. Cona, S.D. Spencer, B. Zhu, P. Heaphy, J.A. Cody, C.J. Collison, Contribution of aggregate states and energetic disorder to a squaraine system targeted for organic photovoltaic devices, *Langmuir,* 31 (2015) 7717-7726.

[25] D. Bagchi, A. Bhattacharya, T. Dutta, S. Nag, D. Wulferding, P. Lemmens, S.K. Pal, Nano MOF entrapping hydrophobic photosensitizer for dual-stimuli responsive unprecedented therapeutic action against drug-resistant bacteria, *ACS Appl. Bio Mater.,* 2 (2019) 1772-1780.

[26] N. Liédana, A. Galve, C.s. Rubio, C. Téllez, J. Coronas, CAF@ ZIF-8: one-step encapsulation of caffeine in MOF, *ACS Appl. Mater. Interfaces,* 4 (2012) 5016-5021.

[27] U. Holzwarth, N. Gibson, The Scherrer equation versus the'Debye-Scherrer equation', *Nat. Nanotechnol.,* 6 (2011) 534.

[28] A.R. Chowdhuri, B. Das, A. Kumar, S. Tripathy, S. Roy, S.K. Sahu, One-pot synthesis of multifunctional nanoscale metal-organic frameworks as an effective antibacterial agent against multidrug-resistant staphylococcus aureus, *Nanotechnology.,* 28 (2017) 095102.

[29] H. Nabipour, M.H. Sadr, G.R. Bardajee, Synthesis and characterization of nanoscale zeolitic imidazolate frameworks with ciprofloxacin and their applications as antimicrobial agents, *New J. Chem.,* 41 (2017) 7364-7370.

[30] G. Kumari, K. Jayaramulu, T.K. Maji, C. Narayana, Temperature induced structural transformations and gas adsorption in the zeolitic imidazolate framework ZIF-8: a Raman study, *J. Phys. Chem. A,* 117 (2013) 11006-11012.

[31] S. Tanaka, K. Fujita, Y. Miyake, M. Miyamoto, Y. Hasegawa, T. Makino, S. Van der Perre, J. Cousin Saint Remi, T. Van Assche, G.V. Baron, Adsorption and diffusion phenomena in crystal size engineered ZIF-8 MOF, *J. Phys. Chem. C,* 119 (2015) 28430-28439.

[32] G. De Miguel, M. Ziółek, M. Zitnan, J. Organero, S. Pandey, S. Hayase, A. Douhal, Photophysics of H-and J-aggregates of indole-based squaraines in solid state, *J. Phys. Chem. C,* 116 (2012) 9379-9389.

[33] N.J. Hestand, C. Zheng, A.R. Penmetcha, B. Cona, J.A. Cody, F.C. Spano, C.J. Collison, Confirmation of the origins of panchromatic spectra in squaraine thin films targeted for organic photovoltaic devices, *J. Phys. Chem. C,* 119 (2015) 18964-18974.

[34] H. Zheng, Y. Zhang, L. Liu, W. Wan, P. Guo, A.M. Nyström, X. Zou, One-pot synthesis of metal–organic frameworks with encapsulated target molecules and their applications for controlled drug delivery, *J. Am. Chem. Soc.,* 138 (2016) 962-968.

[35] G. Fan, J. Luo, L. Guo, R. Lin, X. Zheng, S.A. Snyder, Doping Ag/AgCl in zeolitic imidazolate framework-8 (ZIF-8) to enhance the performance of photodegradation of methylene blue, *Chemosphere,* 209 (2018) 44-52.

[36] W. He, Y.-T. Zhou, W.G. Wamer, M.D. Boudreau, J.-J. Yin, Mechanisms of the pH dependent generation of hydroxyl radicals and oxygen induced by Ag nanoparticles, *Biomaterials,* 33 (2012) 7547-7555.

[37] D. Xu, Y. You, F. Zeng, Y. Wang, C. Liang, H. Feng, X. Ma, Disassembly of hydrophobic photosensitizer by biodegradable zeolitic imidazolate framework-8 for photodynamic cancer therapy, *ACS Appl. Mater. Interfaces,* 10 (2018) 15517-15523.

[38] H. Wang, M. Jian, Z. Qi, Y. Li, R. Liu, J. Qu, X. Zhang, Specific anion effects on the stability of zeolitic imidazolate framework-8 in aqueous solution, *Microporous Mesoporous Mater.,* 259 (2018) 171-177.

[39] P.S. Stewart, J.W. Costerton, Antibiotic resistance of bacteria in biofilms, *Lancet.* , 358 (2001) 135-138.

[40] J. Bresee, C.M. Bond, R.J. Worthington, C.A. Smith, J.C. Gifford, C.A. Simpson, C.J. Carter, G. Wang, J. Hartman, N.A. Osbaugh, Nanoscale structure–activity relationships, mode of action, and biocompatibility of gold nanoparticle antibiotics, *J. Am. Chem. Soc.,* 136 (2014) 5295-5300.

List of Publications

(Peer-reviewed journals)

1. **D. Bagchi**, S. Chaudhuri, S. Sardar, S. Choudhury, N. Polley, P. Lemmens and S. K. Pal
"Modulation of stability and functionality of a phyto-antioxidant by weakly interacting metal ions: curcumin in aqueous solution"
RSC Advances 5 (2015) 102516.

2. **D. Bagchi**, T.Dutta and S. K. Pal
"Bimetallic zeolitic imidazolate framework as an active excipient of curcumin under physiological condition"
Biomedical Physics & Engineering Express 4 (2018) 055004.

3. **D. Bagchi**, T. K. Maji, S. Sardar, P. Lemmens, C. Bhattacharya, D. Karmakar and S. K. Pal
"Sensitized ZnO nanorod assemblies to detect heavy metal contaminated phytomedicines: spectroscopic and simulation studies"
Physical Chemistry Chemical Physics 19 (2017) 2503.

4. **D. Bagchi**, A. Ghosh, P. Singh, S. Dutta, N. Polley, I. I. Althagafi, R. S. Jassas, S. A. Ahmed and S. K. Pal
"Allosteric inhibitory molecular recognition of a photochromic dye by a digestive enzyme: dihydroindolizine makes alpha-chymotrypsin photo-responsive"
Scientific Reports (Nature Publications) 6 (2016) 34399.

5. **D. Bagchi**, S. Dutta, P. Singh, S. Chaudhuri and S. K. Pal
"Essential dynamics of an effective phototherapeutic drug in a nanoscopic delivery vehicle: psoralen in ethosome for biofilm treatment"
ACS Omega 2 (2017) 1850–1857.

6. **D. Bagchi**, V.S.S. Rathnam, P. Lemmens, I. Banerjee and S. K. Pal
"NIR light active ZnO based nanohybrids for bacterial biofilm treatment"
ACS Omega 3 (2018) 10877–10885.

7. **D. Bagchi**, A. Halder, S. Debnath, P. Saha and S. K. Pal
"Exploration of interfacial dynamics in squaraine based nanohybrids for potential photodynamic action"
Journal of Photochemistry and Photobiology A: Chemistry (doi.org/10.1016/j.jphotochem.2019.05.005).

8. **D. Bagchi**, A. Bhattacharya, T. Dutta, S. Nag, D. Wulferding, P. Lemmens and S. K. Pal
"Nano MOF entrapping hydrophobic photosensitizer for dual-stimuli responsive unprecedented therapeutic action against drug-resistant bacteria"
ACS Applied Bio Materials 2 (2019) 1772-1780.

9.* S. Chaudhuri, S. Sardar, **D. Bagchi**, S. Singha, P. Lemmens and S. K. Pal
"Sensitization of an endogenous photosensitizer: electronic spectroscopy of riboflavin in the proximity of semiconductor, insulator and metal nanoparticles"
The Journal of Physical Chemistry A 119 (2015) 4162.

10.* S. Chaudhuri, S. Sardar, **D. Bagchi**, S. Dutta, S. Debnath, P. Saha, P. Lemmens and S. K. Pal
"Photoinduced dynamics and toxicity of a cancer drug in proximity of inorganic nanoparticles under visible light"
ChemPhysChem 17 (2016) 270.

11.* A. Adhikari, N. Polley, S. Darbar, **D. Bagchi** and S. K. Pal
"Citrate functionalized Mn_3O_4 in nanotherapy of hepatic fibrosis by oral administration"
Future Science (OA) 2 (2016) FSO146.

12.* T. K. Maji, **D. Bagchi**, P. Kar, D. Karmakar and S. K. Pal
"Enhanced charge separation through modulation of defect-state in wide band-gap semiconductor for potential photocatalysis application: ultrafast spectroscopy and computational studies"
Journal of Photochemistry and Photobiology A: Chemistry 332 (2017) 391.

13.* P. Singh, S. Choudhury, S. Kulanthaivel, **D. Bagchi**, I. Banerjee, S. A. Ahmed, and S. K. Pal
"Photo-triggered destabilization of nanoscopic vehicles by dihydroindolizine for enhanced anticancer drug delivery in cervical carcinoma"
Colloids and Surfaces B: Biointerfaces 162 (2018) 202.

14.* P. Singh, **D. Bagchi** and S. K. Pal
"Ultrafast dynamics driven molecular recognition where fast activities dictates slow events"
Journal of Biosciences 43 (2018) 485-498.

(Book Chapters)

1. **D. Bagchi** and S. K. Pal
"Probing crucial interfacial dynamics of nanohybrids for emerging functionalities"
Edited by S. Sharma, Nanohybrids for Environmental and biomedical application, Edited by Surender Kumar Sharma, ***CRC Press (Taylor and Francis)*** Deanta, Dublin, Ireland, 2019.

* Not included in the thesis.

List of International/ National Conferences

1. Poster entitled as "Surface Engineering for Controlled Nanocatalysis: Key Dynamical Events from Ultrafast Electronic Spectroscopy" by **D. Bagchi** and S. K. Pal, was presented in the conference named ***DAE-BRNS Ultrafast Science (UFS-2015)*** held at S. N. Bose National Centre for Basic Sciences, Kolkata during 19-21 November 2015.

2. Poster entitled as "Nanoparticle Sensitization for Multifunctional Drugs: Prospective Future PDT Agents" by **D. Bagchi** and S. K. Pal, was presented in the conference named ***International Conference on Nanoscience and Technology (ICONSAT 2016)*** held at Indian Institute of Science Education and Research, Pune during 26 Feb-2 March 2016.

3. Poster entitled as "NIR Light Active Nano-antibiotic for Biofilm Treatment" by **D. Bagchi** and S. K. Pal, was presented in the conference named ***International Conference on Nanoscience and Technology (ICONSAT 2018)*** held at Indian Institute of Science, Bengaluru during 21-23 March 2018.

4. Oral presentation entitled as "Stimuli Responsive Nanomaterials for the Treatment of Bacterial Biofilms" by **D. Bagchi** and S. K. Pal, was delivered in the conference named ***International Conference on Current Trends in Materials Science and Engineering (CTMSE 2018)*** held at S. N. Bose National Centre for Basic Sciences, Kolkata during 19-20 January 2018.

5. Poster entitled as "Modulating effectivity of curcumin through metallation for its improved biological applications" by **D. Bagchi** and S. K. Pal, was presented in the conference named ***Gordon Research Conference on Drug Carriers in Medicine and Biology*** held at Mount Snow in West Dover, VT United States during 12-17 August 2018.

6. Poster entitled as "Metallation modulates the properties of Curcumin: An ultrafast dynamics overview" by **D. Bagchi** and S. K. Pal, was presented in the conference named ***256th ACS National Meeting & Exposition*** held at Boston, United States during 19-23 August 2018.

7. Attended the conference named ***Industry Academia Meet 2018*** held at S. N. Bose National Centre for Basic Sciences, Kolkata on 6 October 2018.